Imperial College of Science, Technology and Medicine
Department of Physics

The Influence of Electronic Temperature on Interatomic Forces in Warm Dense Matter

Thomas Yates

Submitted in part fulfilment of the requirements for the degree of
Doctor of Philosophy in Physics at Imperial College London, December 2023

Abstract

In this thesis, commonly used methods of calculating free energies and forces in warm dense matter are discussed. Mermin-Hohenberg-Kohn-Sham DFT (MHKS-DFT) is expected to be the most accurate, but is computationally prohibitive for large system sizes and high temperatures. Orbital-free DFT can partially overcome these computational limitations; however, the accuracy of the method is severely restricted by the requirement of a local pseudopotential and the choice of the approximation for the non-interacting free energy. Interatomic potentials are the most computationally efficient method, but require fitting to accurate *ab initio* data and are often restricted to a single electronic temperature. It is then proposed that the Atomic Cluster Expansion can be fit to MHKS-DFT data at finite electronic temperature and this is shown to predict free energies and forces accurate to a few percent of *ab initio* results for a fraction of the cost. This accuracy is maintained for all densities bounded by the training dataset and, by use of a simple linear interpolation scheme, intermediate electronic temperatures can also be probed without signifiant loss of accuracy. The many-body expansion, the form of which inspired the Atomic Cluster Expansion, is then used to investigate the importance of many-body interactions in warm dense aluminium. Finally, an experimentally realisable nonequilibrium system in which electronic-temperature dependence has appreciable effects is presented.

Acknowledgements

I would firstly like to express my thanks to Prof. Matthew Foulkes, who has been my primary source of academic guidance and support throughout my PhD. The many discussions we have had and the in-depth notes he has produced have been invaluable over the course of my PhD. I also offer my thanks to my second supervisor, Dr. Derek Lee, for his suggestions and mathematical assistance in the more technical parts of my PhD. A special thanks should be given to Prof. Mike Finnis, who has been a supervisor in all but name. His knowledge of interatomic forces is encyclopedic and his book has been an excellent starting point and reference for the work in this thesis. I would also like to thank Dr. Sam Azadi for his help and advice, especially his assistance with the DFT software at the start of my PhD. Without him, much of the work in this thesis would not have been possible. I am thankful to my international collaborators: Prof. Ralf Drautz, Dr. Matous Mrovec, and the entire research group at Ruhr-Universität Bochum for the discussions and help regarding the Atomic Cluster Expansion, which constitutes a large part of this thesis.

I am thankful to my family for their unending support during my entire academic life, and I hope that my mum can relax now that this thesis is complete. I wish to also thank all of my fellow students in the CMTH group and the Centre for Doctoral Training in Theory and Simulation of Materials for the lengthy discussions and words of encouragement. A special thanks to Chris Bradley, who has both listened to my complaints and provided his own, in equal measure. Finally, I would like to thank my girlfriend, Ling, who has quite literally been by my side for the majority of my PhD. I too often take for granted the joy she has brought to my life.

‘The man who asks a question is a fool for a minute, the man who does not ask is a fool for life.’

Confucius

The copyright of this thesis rests with the author. Unless otherwise indicated, its contents are licensed under a Creative Commons Attribution-Non Commercial 4.0 International Licence (CC BY-NC). Under this licence, you may copy and redistribute the material in any medium or format. You may also create and distribute modified versions of the work. This is on the condition that: you credit the author and do not use it, or any derivative works, for a commercial purpose. When reusing or sharing this work, ensure you make the licence terms clear to others by naming the licence and linking to the licence text. Where a work has been adapted, you should indicate that the work has been changed and describe those changes. Please seek permission from the copyright holder for uses of this work that are not included in this licence or permitted under UK Copyright Law.

Contents

Abstract **i**

Acknowledgements **iii**

1 Introduction **1**

1.1 Contributions 4

1.2 Data Availability 4

1.3 Statement of Originality 4

I Methods of Simulating Warm Dense Matter **5**

2 Density Functional Theory **6**

2.1 Hohenberg-Kohn Theorems 7

2.2 Born-Oppenheimer Approximation 11

2.2.1 Thermal Averages 12

2.3 Mermin-Hohenberg-Kohn-Sham DFT 12

2.4 Pseudopotentials 20

2.5 Hellmann-Feynman Theorem 22

2.6 Orbital-Free DFT 27

2.6.1 Thomas-Fermi Functional 30

2.6.2 VT84F 31

2.7 Periodic Boundary Conditions 33

2.7.1 Bloch Theorem 35

2.7.2 Electrostatics in a Periodic System 37

2.7.3 Evaluation in Reciprocal Space 39

2.7.4 Ewald Energy 40

2.7.5 Hartree Energy 42

2.7.6 Pseudopotential Energy 43

2.8 Scaling of computational resources in DFT 45

2.8.1 Scaling with electronic temperature 46

2.8.2 Scaling with system size 49

2.9 Summary 52

3 Developments of Finite-T DFT **54**

3.1 Finite-T Exchange-Correlation Functionals 56

3.1.1 Low-density aluminium 58

3.2 Pseudopotentials in Warm Dense Matter 60

3.2.1 Effect of material density 64

3.2.2 Effect of electronic temperature 67

3.3 Non-Local Free Energy Functionals 70

3.4 Extended First-Principles Molecular Dynamics 73

3.5 Summary 75

4 Interatomic Potentials **77**

4.1 Finite-T Interatomic Forces 79

4.2 Previous Finite-T Interatomic Potentials 83

4.2.1 DeePMD 85

4.2.2 Empirical potentials 89

4.2.3 Ground-state DOS approximation 93

4.3 Summary 95

5 Molecular Dynamics **97**

5.1 Calculating statistical quantities 98

5.2 Anatomy of a time step 99

5.3 Equilibration 100

5.4 Thermostat 104

5.5 Choosing a time step 109

5.6 Summary 111

6 Atomic Cluster Expansion **113**

6.1 Single-bond basis functions 114

6.2 Atomic bases 115

6.3 Nonlinear Atomic Cluster Expansion 117

6.4 Fitting a local potential to free energy 118

6.4.1 Electron gas contribution 119

6.5 Parameterisation . . . 123
6.5.1 Dataset . . . 123
6.5.2 Loss function and basis functions . . . 127
6.5.3 Optimisation considerations . . . 129
6.6 Results . . . 130
6.6.1 Free energy and forces . . . 130
6.6.2 Timing . . . 135
6.7 Summary . . . 138

7 Temperature Interpolation 139

7.1 Linear interpolation . . . 139
7.2 Future avenues . . . 143
7.2.1 ACE expansion coefficients . . . 143
7.2.2 Scaling of fluctuations with T_e . . . 143
7.3 Summary . . . 145

II Electronic-Temperature Effects on Interatomic Forces 146

8 Equation of State 147

8.1 Summary . . . 151

9 Many-body contributions to interatomic forces 152

9.1 Many-body expansion . . . 152
9.1.1 Embedding in an HEG environment . . . 155

9.2 n-body contributions in aluminium . . . 158

9.3 Summary . . . 162

10 Phonons at finite temperature **163**

10.1 Electronic-temperature effects on phonons . . . 165

10.2 Summary . . . 168

11 Two-temperature molecular dynamics **169**

11.1 The model . . . 170

11.1.1 Electron-ion coupling . . . 173

11.1.2 Surfaces . . . 174

11.1.3 Electronic thermal conductivity . . . 175

11.2 Laser-irradiated thin film . . . 178

11.3 Femtosecond electron diffraction . . . 181

11.4 Summary . . . 184

12 Conclusion **186**

12.1 Summary . . . 186

12.2 Future Work . . . 188

Bibliography **189**

A Finding the ground-state density **221**

A.1 Perturbative approach . . . 222

A.2 Direct minimisation . . . 227

B Error metrics **229**

C Phonons **231**

C.1 Calculating the interatomic force constants 232

C.1.1 'Direct' method 232

C.2 Finding the phonon frequencies 233

C.3 Thermodynamic properties 234

C.4 Anharmonicities 234

List of Tables

4.1 Force RMSE and MAE of the two DeePMD potentials. 86

6.1 Parameters of the ACE functional forms. 130

7.1 The electronic temperatures for which ACE potentials were fit. 140

7.2 Error in the predicted forces of $\rho = 2.37$ g/cm^3 aluminium when approximated by various methods. 141

List of Figures

2.1 The self-consistent loop in Kohn-Sham DFT. 17

2.2 The two approaches to finding the ground-state energy and density in orbital-free DFT. 27

2.3 The different methods for calculating the non-interacting free energy in Mermin-Hohenberg-Kohn-Sham (MHKS) and orbital-free (OF) DFT. . . . 28

2.4 An infinite crystal formed from periodic tiling of a unit cell. 34

2.5 The Ewald summation method. 41

2.6 The Fermi-Dirac distribution function. 47

2.7 The number of partially occupied orbitals per electron required to explicitly calculate all KS orbitals with an occupation greater than some chosen value. 48

3.1 KS band structures of low density fcc aluminium at $T = 5$ kK and $T = 20$ kK through a path of high symmetry points in k-space. 59

3.2 A snapshot of 2.37 g/cm^3 aluminium equilibrated at 100 kK with periodic boundary conditions. 61

3.3 A histogram of the interatomic nearest-neighbour distances within 2.37 g/cm^3 aluminium equilibrated at various T_{eq}. 62

3.4 A histogram of all of the interatomic distances within 2.37 g/cm^3 aluminium equilibrated at various T_{eq}. 63

3.5 Pressure of fcc aluminium at $T_e = 300$ K for varying ρ from DFT calculations performed in `Quantum Espresso`. 65

3.6 A pictorial representation of a 3e and 11e aluminium pseudopotential. . . . 67

3.7 Pressure of fcc aluminium for varying T_e from DFT calculations performed in `Quantum Espresso`. 69

3.8 The inverse of response functions at $T = 0$ K (left) and $T = 100$ kK (right). 72

4.1 The Lennard-Jones potential. 78

4.2 The force along the x-axis of a random sample of atoms within a 108 aluminium atom snapshot equilibrated at 10 kK and $\rho = 2.37$ g/cm^3. . . . 84

4.3 The force along the x-axis of each atom within a 108 aluminium atom snapshot equilibrated at 100 kK and with an electronic temperature $T_e = 1$ eV $= 11600$ K. 87

4.4 A system of four atoms and its description in terms of n-body interactions. 90

5.1 The total energy of a thermostatted MD simulation over time. 103

5.2 Mean square displacement against time for various choices of the collision frequency parameter $\tilde{\nu} = \nu \mathrm{d}t$. 106

5.3 Total energy throughout a microcanonical MD simulation for various time steps $\mathrm{d}t$ and 3000 iterations. 110

5.4 Total energy throughout a microcanonical MD simulation for permutations of the minimum and maximum density and temperature investigated in this thesis. 111

6.1 MHKS-DFT free energy for varying volume in fcc aluminium. 120

6.2 Chemical bond energy F_b for varying nearest neighbour distance d in fcc aluminium. 122

6.3 Scatter plot of energy and force RMSEs of a 10 kK ACE potential for different chosen values of κ. 127

6.4 RMSE and MAE of forces for various electronic temperatures at three different densities of aluminium. 131

6.5 RMSE and MAE of energies per atom for various electronic temperatures at three different densities of aluminium. 132

6.6 The normalised root-mean-square error of the forces for various electronic temperatures at three different densities of aluminium. 133

6.7 The difference in the x-direction force on atom i predicted by the many-body expansion in a 32 atom equilibrated aluminium snapshot at 10 kK. . 134

6.8 Wall time per MD step for various methods of simulating interatomic forces in aluminium at a range of temperatures. 136

8.1 Equation of state of warm dense aluminium for various material densities and 10 kK $< T_\mathrm{e} = T_\mathrm{i} <$ 100 kK. 149

9.1 Diagrammatic example of embedding a single aluminium atom of charge $Z_\mathrm{Al} = 3$ in an HEG. 156

9.2 Normalised root-mean-square errors in the forces for the many-body expansion at varying electronic temperature. 159

9.3 The sum of signed contributions to the normalised force RMSE for the many-body expansion at varying electronic temperature. 161

10.1 Phonon dispersion curves of fcc aluminium along a high symmetry path in the Brillouin zone. 167

11.1 A pictorial representation of a 2T-MD simulation of a 2D laser-irradiated thin film. 170

11.2 Snapshots of a 35×50×50 nm aluminium thin film that has been laser irradiated and is allowed to expand along its x axis. 178

11.3 Snapshots of a 35×50×50 nm aluminium thin film that has been laser irradiated and is allowed to expand along its x axis. 180

A.1 Heat plot of the thermal-equilibrium electron density for a periodic unit cell containing a bolonium ion, produced using our OF-DFT program. . . . 228

Chapter 1

Introduction

In the past few decades, warm dense matter has become readily accessible in inertial confinement fusion [1, 2], laser-irradiated solids [3, 4], and more [5, 6]. However, there is also interest in astrophysical processes, primarily in white dwarfs and large planetary cores [7, 8, 9], as these are expected to reach the temperatures and pressures required for sustained existence of warm dense matter. In the warm dense regime, the system cannot easily be described as simply quantum or classical; it is in an intermediate regime where both effects are important. Therefore, methods of simulating warm dense matter are typically extended from either condensed matter or plasma techniques. This extrapolation often leads to issues, though, as these methods are not formulated with warm dense matter in mind, causing both scaling and accuracy limitations.

In recent years, experimental methods have progressed to the level of providing precise measurements of static and transport properties of warm dense matter [10, 11, 12, 13, 14, 15, 16] that can act as benchmarks for theoretical predictions [17, 18]. Given a theoretical method or model that can reproduce the experimental findings, it will then be possible to make predictions using that model which can guide future experiments.

It is well known that increasing electronic temperature alters the interatomic forces felt by the ions, which can lead to phenomena such as softening of acoustic modes, ablation, and athermal melting, where the material melts at a much lower ionic temperature than

expected due to the weakening of the interatomic forces [19, 20, 21]. These phenomena have been observed in so-called 'two-temperature' laser-irradiated systems, where the electrons are in thermal equilibrium with each other, but not the ionic lattice [19, 22]. Laser-irradiation experiments can be simulated using an interatomic potential in the two-temperature molecular dynamics (2T-MD) method [23, 24], allowing for nonequilibrium effects to be observed. However, electronic-temperature-dependent potentials are rare [25, 26, 20, 27], with their use in 2T-MD simulations rarer still [28, 29, 30, 31, 32]. The change in the potential energy surface and interatomic forces due to the elevated electronic temperature is not accounted for when a zero-temperature potential is used.

The most commonly used technique for simulating the properties of warm dense systems is density functional theory (DFT) [33]. If the time scales, temperatures, and system sizes are small enough, accurate simulations can be performed using Mermin's finite-temperature extension [34] of Kohn-Sham DFT (MHKS-DFT) [35]. Simulations requiring longer time scales, and simulations of larger or hotter systems, must use orbital-free DFT (OF-DFT) [36] or other approximate reformulations of MHKS-DFT [37, 38]. It is commonly assumed that at the high temperatures ($\gtrsim$ 10 eV) where MHKS-DFT is no longer feasible, OF-DFT is relatively accurate [39, 40, 41, 42]. This is in contrast to its poor accuracy, without empirical tweaking, closer to zero temperature [43, 44]. The results of OF-DFT calculations of certain simple properties, such as the electronic pressure [45], static structure factor [46], and diffusion coefficient [17], can be compared with MHKS-DFT results. If the agreement is reasonably good, then OF-DFT is deemed acceptable for use in large systems.

There have also been attempts to fit interatomic potentials using OF-DFT data [46]. It is apparent that for this to provide meaningful results, the OF-DFT data for the given material must be accurate over the entire temperature and density range of the simulation in which the potential will be used. If the OF-DFT data used is satisfactory, these potentials should better reproduce quantum effects that may otherwise be missing in a classical interatomic potential [45].

The aim of this thesis is to test the accuracy and efficiency of the various methods used to simulate WDM, and provide a new electronic-temperature-dependent interatomic potential that is both more efficient than methods with comparable accuracy and more accurate than methods with comparable efficiency. Aluminium is used throughout this thesis as a test system, due to its free-electron-like electronic structure and the availability of experimental data in the warm dense regime [47, 48, 21, 49].

This thesis is split into two parts. The first part discusses the different methods of simulating warm dense matter and systems with elevated electronic temperature. The Atomic Cluster Expansion (ACE) [50] is used to fit interatomic potentials to MHKS-DFT data at electronic temperatures between 10 kK and 100 kK. The ACE potentials are shown to predict free energies that are accurate to within 0.1% of the MHKS-DFT results and forces that are accurate to within a few percent of the MHKS-DFT results. This is a significant improvement on the accuracy of the OF-DFT method, at a fraction of the cost. A linear interpolation scheme is introduced to allow for the ACE free energies and forces at intermediate electronic temperatures to be calculated. For the electronic temperature range investigated here, this produces forces with an error of approximately 1%, even though no data at the specified temperature is included in the training dataset used to fit the ACE potentials. Potential extensions are suggested which would allow for a single ACE potential to be fit to data at multiple electronic temperatures.

The second part investigates the effects that an elevated electronic temperature has on the interatomic forces. This is observed by using the newly fit ACE potentials to produce the equation of state for warm dense aluminium. This also provides a test of the linear interpolation scheme, with the accuracy and speed compared to MHKS-DFT and OF-DFT results. The importance of the many-body interactions in warm dense aluminium is then investigated using the many-body expansion. Phonon dispersion curves are discussed as a method for finding systems in which an elevated electronic temperature can cause athermal melting or bond hardening. Finally, laser-irradiated thin films are simulated using the two-temperature molecular dynamics method and the temperature-dependent ACE potential. These simulations show that correctly accounting for electronic-temperature effects is

crucial to reproducing accurate dynamics and nonequilibrium behaviours.

Atomic units are used in equations throughout this thesis and spin and relativistic effects will be ignored.

1.1 Contributions

I performed all of the work in this thesis, except for the initial fits of the ACE potential, which were fit by Ralf Drautz at Ruhr-Universität Bochum, or where stated in the text. My contributions to the software used in this thesis include adapting `PROFESS@QE` to allow for the use of the SDF functional in OF-DFT calculations, adapting `Quantum Espresso` to correctly use finite-temperature XC functionals from the `LibXC` library, and extending the two-temperature molecular dynamics module in `LAMMPS` to fix inefficiencies and use temperature-dependent inputs and interatomic potentials.

1.2 Data Availability

The data used in this thesis is available from the author upon request. The software adaptations presented in this thesis are available at `https://github.com/yatest/` and will hopefully be incorported into the main codebases in the future.

1.3 Statement of Originality

All of the work presented in this thesis is either my own or produced in tandem with my supervisors and collaborators, unless referenced.

Part I

Methods of Simulating Warm Dense Matter

Chapter 2

Density Functional Theory

For a system of N interacting electrons, the ground state (or thermal-equilibrium state) can be found by solving the Schrödinger equation [51]. For a time-independent Hamiltonian, the Schrödinger equation reads

$$\hat{H}\Psi_i\left(\mathbf{r}_1, ..., \mathbf{r}_N\right) = E_i\Psi_i\left(\mathbf{r}_1, ..., \mathbf{r}_N\right), \tag{2.1}$$

where Ψ_i is an N-electron eigenstate, E_i is the corresponding eigenvalue, and the Hamiltonian $\hat{H}$ is given as

$$\hat{H} = \underbrace{-\frac{1}{2}\sum_i^N \nabla_i^2}_{\hat{\mathcal{T}}} + \underbrace{\frac{1}{2}\sum_{i\neq j}^N \frac{1}{|\mathbf{r}_i - \mathbf{r}_j|}}_{\hat{V}_{\text{ee}}} + \underbrace{\sum_i^N V_{\text{ext}}(\mathbf{r}_i)}_{\hat{V}_{\text{ext}}}, \tag{2.2}$$

with $\hat{\mathcal{T}}$ the kinetic energy operator, $\hat{V}_{\text{ee}}$ the electron-electron interaction operator, $\hat{V}_{\text{ext}}$ the external potential operator, and $\mathbf{r}$ the position of an electron [52].

In practice, the Schrödinger equation is impossible to solve exactly in all but the simplest systems, due to Ψ_i being a function of the $3N$ spatial coordinates of the electrons. Therefore, a number of approximations or reformulations are commonly used to approach more complex problems [53, 54, 55, 56]. Perhaps the most successful and ubiquitous

reformulation of the many-electron problem is *density functional theory*.

2.1 Hohenberg-Kohn Theorems

In 1964, Hohenberg and Kohn showed that solving for the N-electron wavefunction Ψ in the many-electron problem could be avoided by expressing the total energy of the system as a functional of the electron density n[1][57, 33, 58, 59]. Since n is only a function of position $\mathbf{r}$, the dimensionality of the problem can be reduced from $3N$ spatial dimensions to only three spatial dimensions.

The proof that the total energy can be expressed as a functional of the electron density begins by showing how the ground-state density can be found using the Schrödinger equation. For a given $\hat{V}_{\text{ext}}$, the Schrödinger equation can be solved to find the eigenstates Ψ_i, including the ground-state Ψ_0. This relationship can be expressed as

$$\hat{V}_{\text{ext}} \rightarrow \Psi_i(\{\mathbf{r}\}) \rightarrow \Psi_0(\{\mathbf{r}\}) \rightarrow n_0(\mathbf{r}), \tag{2.3}$$

where $\{\mathbf{r}\}$ indicates the set of electronic positions $(\mathbf{r}_1, ..., \mathbf{r}_N)$, and the definition of the electron density for a normalised Ψ [57],

$$n(\mathbf{r}) = N \int \mathrm{d}\mathbf{r}_2 \cdots \int \mathrm{d}\mathbf{r}_N \, \Psi_i^* \left(\mathbf{r}, \mathbf{r}_2, ..., \mathbf{r}_N\right) \Psi_i \left(\mathbf{r}, \mathbf{r}_2, ..., \mathbf{r}_N\right), \tag{2.4}$$

gives the final relationship of Eq. 2.3.

The first Hohenberg-Kohn theorem states:

Theorem 2.1 *The external potential V_{ext} is uniquely defined, up to a constant shift, by the ground-state electron density n_0.*

[1]The Hohenberg-Kohn theorems are, in fact, applicable to any set of interacting particles; however, the discussion will be limited to an electronic system with an external potential arising from the nuclei in this thesis.

This theorem provides the missing link from n_0 to V_{ext}, forming a loop in Eq. 2.3. This leads to the corollary that all eigenstates Ψ_i of the N-electron wavefunction Ψ are, in theory, known, given a ground-state density n_0. Therefore, any observable of the system can be written as a functional of the ground-state density $F[n_0]$.

A functional can be thought of in a similar way to a function. Just as a function maps a scalar or vector to a number, for instance $n(\mathbf{r})$, a functional maps a function to a number. This is represented by using square brackets instead of parentheses, e.g., $F[n]$. Here, F is a functional of the density n, which in turn is a function of position $\mathbf{r}$. Further details on functionals can be found in Ref. [60].

The second Hohenberg-Kohn theorem states:

Theorem 2.2 *A universal functional of the density $F_{\text{HK}}[n]$ can be defined that is independent of the external potential V_{ext}. The exact ground-state energy and density of the system can then be found by minimising the total energy functional*

$$\begin{aligned} E_{\text{HK}}[n] &= \mathcal{T}[n] + E_{\text{ee}}[n] + \int \mathrm{d}\mathbf{r}\, V_{\text{ext}}(\mathbf{r}) n(\mathbf{r}) \\ &\coloneqq F_{\text{HK}}[n] + \int \mathrm{d}\mathbf{r}\, V_{\text{ext}}(\mathbf{r}) n(\mathbf{r}). \end{aligned} \tag{2.5}$$

Here, the energy arising from the interaction between the electrons and external potential has been written explicitly, and the kinetic and electron-electron density functionals have been defined as the expectation values of their respective operators,

$$\begin{aligned} \mathcal{T}[n] &= \int \mathrm{d}\mathbf{r}\, \Psi^*[n] \hat{\mathcal{T}} \Psi[n] \\ E_{\text{ee}}[n] &= \int \mathrm{d}\mathbf{r}\, \Psi^*[n] \hat{V}_{\text{ee}} \Psi[n]. \end{aligned} \tag{2.6}$$

From the second Hohenberg-Kohn theorem and the Rayleigh-Ritz variational principle, it is found that the minimum of $E_{\text{HK}}[n]$ is the exact ground-state energy of the system, and the density that minimises it is the exact ground-state density of the system. Importantly, this procedure only gives information about the ground-state properties of the system.

This method of minimising Eq. 2.5 to find the ground-state energy and density is called *density functional theory* (DFT). Primarily, DFT is used to solve systems at zero temperature, where the ground-state energy and density are the properties of interest. In warm dense matter, the system has a finite temperature and the internal energy is no longer the correct thermodynamic potential that must be minimised to find the thermal-equilibrium state.

Instead, for a system with constant particle number N, temperature T, and volume V (canonical ensemble), the Helmholtz free energy F is the variational energy of interest. If the particle number is allowed to fluctuate and the chemical potential μ is held constant (grand canonical ensemble), the grand canonical potential Ω must be minimised. Mermin DFT [34] rederives the Hohenberg-Kohn theorems for finite temperature, showing that it is Ω that must be minimised to find the thermal-equilibrium density. The universal density functional $F_{\mathrm{HK}}[n]$ in Mermin DFT also contains an entropic contribution that arises from the non-zero temperature.

The grand canonical Hamiltonian can be written as [52]

$$\hat{\Omega} = \hat{H} - T\hat{S} - \mu\hat{N}, \tag{2.7}$$

where $\hat{H}$ is the Hamiltonian defined in Eq. 2.2, $\hat{N}$ is the particle number operator, and $\hat{S}$ is the entropy operator, defined as [52]

$$\hat{S} = -k_{\mathrm{B}} \ln \hat{\rho}, \tag{2.8}$$

with $\hat{\rho}$ the grand canonical density operator.

At finite temperature, the thermal-equilibrium state is in fact an ensemble average, rather than a single microstate. Therefore, the grand canonical density operator is commonly used to describe the system,

$$\hat{\rho} = \frac{1}{Z_{\mathrm{G}}} \exp\Big[-\beta(\hat{H} - \mu\hat{N})\Big], \tag{2.9}$$

with $\beta = (k_{\mathrm{B}}T)^{-1}$, the grand canonical partition function

$$Z_{\mathrm{G}} = \exp[-\beta\Omega] = \mathrm{Tr}\exp\Big[-\beta(\hat{H} - \mu\hat{N})\Big], \tag{2.10}$$

and the grand potential

$$\Omega = \langle\hat{\Omega}\rangle = \mathrm{Tr}\,\hat{\rho}\,\hat{\Omega} = -k_{\mathrm{B}}TZ_{\mathrm{G}}. \tag{2.11}$$

The final equality can be found from either Eq. 2.10, or by evaluating $\langle\hat{S}\rangle$ using Eqs. 2.8 and 2.9.

In practice, periodic boundary conditions are often used in DFT calculations. For a constant V_{eff}, the number of atoms in a periodic unit cell (and therefore the number of electrons N) is fixed throughout the minimisation procedure. If N is allowed to vary whilst the number of atoms is fixed, charge neutrality will not be maintained. Whilst the instantaneous charge within a particular unit cell of a real solid may fluctuate, a periodic array of identical unit cells, each with non-zero total charge, would lead to an undefined Coulomb energy. Therefore, Ω must be minimised under the constraint that the correct N is found when integrating the electron density over the simulated unit cell.

In practice, this could be achieved by selectively picking out the results with the correct N; however, it is far simpler to minimise F for a chosen N. Effectively, the chemical potential μ is allowed to vary such that the correct N is always found in the thermal-equilibrium state. For a system in the thermodynamic limit (which is a reasonable assumption for any periodic calculation with a fine enough sampling of k-points), the minima of the canonical and grand-canonical potentials are found for the same thermal-equilibrium density.

2.2 Born-Oppenheimer Approximation

Until now, it has been implicitly assumed that the electronic and nuclear degrees of freedom in the wavefunction can be separated,

$$\Psi_{\text{total}}\left(\{\mathbf{r}\},\{\mathbf{R}\}\right) = \Psi_{\text{e}}(\{\mathbf{r}\}|\{\mathbf{R}\})\Psi_{\text{n}}(\{\mathbf{R}\}), \tag{2.12}$$

where Ψ_{e} represents the electronic wavefunction, Ψ_{n} the nuclear wavefunction, and $\{\mathbf{R}\}$ is the set of nuclear positions. The electronic wavefunction depends only parametrically on the fixed $\{\mathbf{R}\}$.

This separation of the wavefunction can be assumed as the nuclear mass is much greater than that of the electronic mass, and as such the nuclei move over a much longer timescale than the electrons. Analogously, throughout any change in the configuration of nuclear positions, the electronic system is expected to be found in its ground state. This decoupling of the electronic and nuclear wavefunctions is called the *Born-Oppenheimer approximation* [61]. It permits the solving of the electronic system, as in Eq. 2.1, by approximating the nuclear positions as fixed.

In DFT calculations, the Born-Oppenheimer approximation allows the nuclei to be treated as fixed classical particles that exert a static external potential on the electrons. The electronic system is then minimised, giving a ground-state energy and density for that particular nuclear configuration. The Born-Oppenheimer approximation is also essential to *ab initio* molecular dynamics, which will be discussed later in this thesis.

At finite temperature, the Born-Oppenheimer approximation may not always be valid. At a high enough temperature, the motion of the ions cannot be neglected during the equilibration of the electronic system. The system will therefore no longer evolve adiabatically. However, in the warm dense regime, the Born-Oppenheimer approximation is generally assumed to be valid [62].

2.2.1 Thermal Averages

The decoupling of the electronic and nuclear degrees of freedom is vital to simplifying the evaluation of thermal averages, such as Eq. 2.11. Since these thermal averages correspond to properties measured by experiments, it is important to be able to calculate thermal averages from a simulation or model.

Under the Born-Oppenheimer approximation, the canonical partition function can be expressed as

$$\begin{aligned} Z(\beta) &= \int \mathrm{d}\mathbf{R} \sum_i \left\langle \Psi_i \left| \exp\left[-\beta \left(\hat{H}_\mathrm{e}(\{\mathbf{R}\},\beta) + \frac{1}{2} M \dot{\mathbf{R}}^2 \right)\right] \right| \Psi_i \right\rangle \\ &= \int \mathrm{d}\mathbf{R} \exp\left[-\beta \left(F(\{\mathbf{R}\},\beta) + \frac{1}{2} M \dot{\mathbf{R}}^2 \right)\right], \end{aligned} \tag{2.13}$$

where $\hat{H}_\mathrm{e}$ is the Hamiltonian given by Eq. 2.2, Ψ_i is an electronic eigenstate for fixed $\{\mathbf{R}\}$, M is the mass of a nucleus, and the equation

$$\exp[-\beta F(\{\mathbf{R}\},\beta)] = \sum_i \left\langle \Psi_i \left| \exp\left[-\beta \hat{H}_\mathrm{e}(\{\mathbf{R}\},\beta)\right] \right| \Psi_i \right\rangle \tag{2.14}$$

has been used. This defines the thermal equilibrium free energy $F(\{\mathbf{R}\},\beta)$ for a given nuclear configuration and temperature.

A thermal average can then be calculated using

$$\langle \hat{O} \rangle = \frac{1}{Z(\beta)} \int \mathrm{d}\mathbf{R} \exp\left[-\beta \left(F(\{\mathbf{R}\},\beta) + \frac{1}{2} M \dot{\mathbf{R}}^2 \right)\right] O(\mathbf{R}), \tag{2.15}$$

where O is the property of interest.

2.3 Mermin-Hohenberg-Kohn-Sham DFT

Both the Hohenberg-Kohn and Mermin theorems provide proofs which are vital to zero-temperature and finite-temperature DFT; however, importantly, they do not give any

indication to the form of $F_{\mathrm{HK}}[n]$. Minimising Eq. 2.5 is therefore impossible without either an exact form for $F_{\mathrm{HK}}[n]$, or a suitable ansatz.

In 1965, Kohn and Sham proposed using an auxiliary system of non-interacting particles to generate the exact ground-state density of the fully interacting system [35]. Solving a non-interacting problem is a much easier task than solving the many-body problem as the electrons are no longer coupled, instead moving in an effective potential. The key assumption made by Kohn and Sham is that for every fully interacting ground-state density n_0, there exists a non-interacting ground-state density $n_{0,\mathrm{s}}$, such that $n_{0,\mathrm{s}} = n_0$. It should be noted that there is no general proof of the validity of this assumption.

To show how the non-interacting system can be used to solve the fully interacting system, the kinetic and electron-electron terms in Eq. 2.5 are first replaced by simpler, known approximations:

$$E_{\mathrm{HK}}[n] \approx \mathcal{T}_{\mathrm{s}}[n] + E_{\mathrm{H}}[n] + \int \mathrm{d}\mathbf{r}\, V_{\mathrm{ext}}(\mathbf{r}) n(\mathbf{r}), \tag{2.16}$$

where the subscript 's' indicates a non-interacting term, $E_{\mathrm{H}}[n]$ is the classical self-interaction energy of the electron density $n(\mathbf{r})$,

$$E_{\mathrm{H}}[n] = \frac{1}{2} \int \mathrm{d}\mathbf{r}\, \mathrm{d}\mathbf{r}' \, \frac{n(\mathbf{r}) n(\mathbf{r}')}{|\mathbf{r} - \mathbf{r}'|}, \tag{2.17}$$

and the non-interacting kinetic energy is defined as

$$\mathcal{T}_{\mathrm{s}} = \frac{1}{2} \sum_j \int \mathrm{d}\mathbf{r} |\nabla \phi_j(\mathbf{r})|^2, \tag{2.18}$$

where, from the non-interacting Schrödinger equation,

$$\left[-\frac{1}{2} \nabla^2 + V_{\mathrm{s}}(\mathbf{r}) \right] \phi_j(\mathbf{r}) = \varepsilon_j \phi_j(\mathbf{r}), \tag{2.19}$$

the ϕ_j are the single-particle eigenstates of an N-electron non-interacting system, with ε_j the eigenvalues, V_{s} the potential in which the non-interacting electrons move, and j the index that runs over the N fully occupied eigenstates.

By introducing a correction term E_{XC}, the equality in Eq. 2.16 is restored,

$$E_{\mathrm{HK}}[n] \coloneqq \mathcal{T}_{\mathrm{s}}[n] + E_{\mathrm{H}}[n] + E_{\mathrm{XC}}[n] + \int \mathrm{d}\mathbf{r}\, V_{\mathrm{ext}}(\mathbf{r}) n(\mathbf{r}), \tag{2.20}$$

where the *exchange-correlation* energy E_{XC} is defined such that it contains not only the missing exchange and correlation contributions from $E_{\mathrm{ee}} - E_{\mathrm{H}}$, but also the (hopefully small) difference in the fully interacting and non-interacting kinetic energies $\mathcal{T} - \mathcal{T}_{\mathrm{s}}$. The motivation behind this repartitioning of E_{HK} is that the explicit forms of all of the terms, bar E_{XC} which is assumed to be a small correction to the total energy, are now known.

In practice, there is no way of knowing the true form of $E_{\mathrm{XC}}[n]$ and approximations must be made. However, knowledge of exact exchange statistics gives a good starting point for an approximation to $E_{\mathrm{XC}}[n]$, and accurate many-body simulations of the homogeneous electron gas (HEG) can be used to estimate the correlation contributions, with small errors found for systems with a relatively smooth electron density distribution or without strong electron correlations.

One approximation that makes use of the HEG exchange-correlation energy is the *local-density approximation* (LDA). In the LDA, the exchange-correlation energy per electron ϵ_{XC} at each point in the system $\mathbf{r}$ is assumed to be that of the HEG with density $n(\mathbf{r})$. The total exchange-correlation energy of a system with electron density $n(\mathbf{r})$ is then

$$E_{\mathrm{XC}}^{\mathrm{LDA}}[n] = \int \mathrm{d}\mathbf{r}\, n(\mathbf{r}) \epsilon_{\mathrm{XC}}^{\mathrm{HEG}}(n(\mathbf{r})), \tag{2.21}$$

with $\epsilon_{\mathrm{XC}}^{\mathrm{HEG}}(n)$ the exchange-correlation energy per electron in the HEG. Accurate quantum Monte Carlo data [63] for the HEG exchange-correlation energy per electron has been parameterised [64] to give an analytic form for $\epsilon_{\mathrm{XC}}^{\mathrm{HEG}}$ as a function of arbitrary n.

Another commonly used paradigm is the *generalised gradient approximation* (GGA). This extends the LDA to also include the gradient of the density ∇n,

$$E_{\mathrm{XC}}^{\mathrm{GGA}}[n] = \int \mathrm{d}\mathbf{r}\, f(n(\mathbf{r}), \nabla n). \tag{2.22}$$

Like $\epsilon_{\mathrm{XC}}^{\mathrm{HEG}}$, the function f is chosen to be some parameterised analytic function [65].

There are also further levels of approximation [66] that incorporate various contributions important for strongly-correlated systems. Here, finite-temperature exchange-correlation functionals are of interest due to the elevated temperatures present in warm dense matter. Since the two finite-temperature functionals discussed in this thesis both use the LDA (see Section 3.1), functional forms of the extensions beyond the GGA will not be mentioned here.

With some chosen form for E_{XC}, Eq. 2.20 can now be cast in the form of the non-interacting picture, where $E_{\mathrm{ee}} = 0$ and F_{HK} is simply the non-interacting kinetic energy of the electrons. To find the minimum of E_{HK}, and therefore find the non-interacting ground-state density $n_{0,\mathrm{s}}$, the *Euler-Lagrange equation* can be used. The Euler-Lagrange equation is found by using the functional derivative of $E_{\mathrm{HK}}[n]$, with respect to the electron density, to minimise E_{HK} subject to the constraint of constant total electron number N,

$$\begin{aligned}\frac{\delta E_{\mathrm{HK}}[n]}{\delta n} &= \frac{\delta \mathcal{T}_{\mathrm{s}}[n]}{\delta n} + \frac{\delta E_{\mathrm{H}}[n]}{\delta n} + \frac{\delta E_{\mathrm{XC}}[n]}{\delta n} + V_{\mathrm{ext}}(\mathbf{r}) \\ &= \frac{\delta \mathcal{T}_{\mathrm{s}}[n]}{\delta n} + V_{\mathrm{eff}}(\mathbf{r}) = \mu,\end{aligned} \tag{2.23}$$

where μ is the Lagrange multiplier identified as the chemical potential. A local effective potential has also been defined,

$$V_{\mathrm{eff}}(\mathbf{r}) = \frac{\delta E_{\mathrm{H}}[n]}{\delta n} + \frac{\delta E_{\mathrm{XC}}[n]}{\delta n} + V_{\mathrm{ext}}(\mathbf{r}) = V_{\mathrm{H}}(\mathbf{r}) + V_{\mathrm{XC}}(\mathbf{r}) + V_{\mathrm{ext}}(\mathbf{r}). \tag{2.24}$$

Since the non-interacting kinetic energy is expressed not as an explicit functional of the density but rather as a functional of the single-particle eigenstates of the N-electron non-interacting system ϕ_j (see Eq. 2.18), to find its functional derivative the electron density must also be expressed using these eigenstates. The non-interacting electron density can be derived using Eq. 2.4 as

$$n_{\mathrm{s}}(\mathbf{r}) = \sum_j |\phi_j(\mathbf{r})|^2. \tag{2.25}$$

The chain rule is then used to find the functional derivative of $\mathcal{T}_{\mathrm{s}}[n]$ with respect to

electron density.

The solutions to the non-interacting problem are found by solving the single-particle Schrödinger equation

$$\left[-\frac{1}{2}\nabla^2 + V_{\text{eff}}(\mathbf{r})\right]\phi_j(\mathbf{r}) = \varepsilon_j\phi_j(\mathbf{r}), \tag{2.26}$$

with ε_j the eigenvalues, and $\phi_j(\mathbf{r})$ the single-particle eigenstates. The index j also includes the spin label, allowing for two opposite spin electrons to have the same energy. Note that the eigenstates are also sometimes referred to as orbitals or wavefunctions.

Eqs. 2.24, 2.25, and 2.26 are known as the *Kohn-Sham equations* and, given a form for $E_{\text{XC}}[n]$, can be used to find the ground-state energy and density of the fully interacting system. The effective potential $V_{\text{eff}}(\mathbf{r})$ can be calculated using Eq. 2.24 and the single-particle Schrödinger equation (Eq. 2.26) can be solved, given an input electron density $n_{\text{in}}(\mathbf{r})$. If the input density is the exact ground-state density, $n_{\text{in}}(\mathbf{r}) = n_0(\mathbf{r})$, the output density calculated from Eq. 2.25 would be equal to the exact ground-state density, $n_{\text{out}}(\mathbf{r}) = n_0(\mathbf{r})$.

For any realistic system, n_0 will not be known *a priori*. A reasonable choice for n_{in} must therefore be made, and the Kohn-Sham system solved *self-consistently*. This means that initially $n_{\text{in}} \neq n_{\text{out}}$, and n_{in} must be tuned over the subsequent cycles until $n_{\text{in}} = n_{\text{out}}$. The basic self-consistent cycle is shown in Fig. 2.1.

Different choices for the initial n_{in} are commonly used, such as the HEG or Gaussians centred on the nuclei. Furthermore, subsequent values of n_{in} are often constructed using mixing schemes, the most common of which is linear mixing. These schemes aim to improve the stability of the self-consistency loop and reduce the number of cycles required for convergence. In the linear mixing scheme, the input density for cycle c is defined as

$$n_{\text{in}}^{c} = \beta n_{\text{out}}^{c-1} + (1-\beta)n_{\text{in}}^{c-1}, \tag{2.27}$$

where β is the mixing factor.

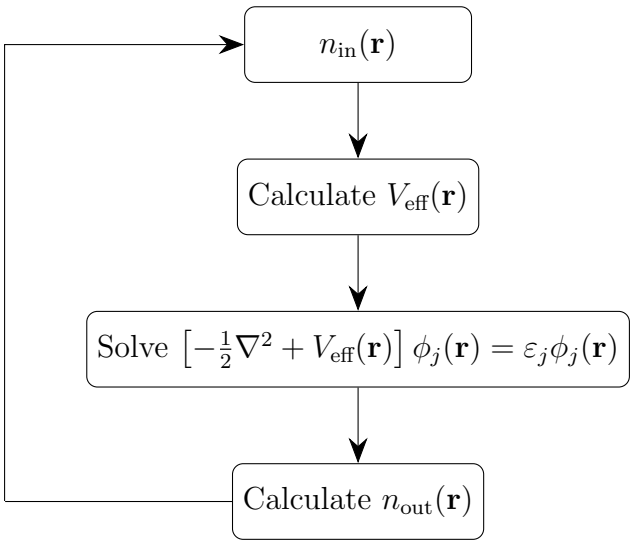

Figure 2.1: The self-consistent loop in Kohn-Sham DFT. In general, $n_{\text{out}}(\mathbf{r}) \neq n_{\text{in}}(\mathbf{r})$ and so n_{in} for the next cycle is changed by some amount, for example according to Eq. 2.27. The loop continues until $|n_{\text{out}}(\mathbf{r}) - n_{\text{in}}(\mathbf{r})| < \epsilon$, where ϵ is some chosen convergence tolerance.

At finite temperature, the Kohn-Sham method instead self-consistently calculates the thermal-equilibrium density. In addition, entropic contributions arising from the Fermi-Dirac smearing of the occupations contribute to the total energy, leading to the minimisation of a free energy rather than an internal energy.

For a system at zero temperature, the occupations of the single-particle Kohn-Sham eigenstates f_j are one if $\varepsilon_j \leq E_{\text{F}}$, where E_{F} is the Fermi energy, and zero otherwise. Therefore, only $M = N/2$ solutions of Eq. 2.26 must be calculated, where N is the number of electrons and it is assumed that the orbitals can be doubly occupied by opposite spin electrons[2]. In contrast, when $T \neq 0$ the occupations are instead governed by the well-known Fermi-Dirac distribution,

$$f_j = \frac{1}{\exp[(\varepsilon_j - \mu)/k_{\text{B}}T] + 1}, \tag{2.28}$$

with μ the chemical potential and k_{B} the Boltzmann constant. As discussed previously, μ is chosen such that $\sum_j f_j = N$.

[2]Both singly- and doubly-occupied orbitals/eigenstates will be used interchangeably in this thesis to refer to the solutions of the Kohn-Sham Schrödinger equation given by Eq. 2.26.

Calculating all states with a non-zero occupation at finite temperature would be impossible as there are now infinitely many of them. Therefore, a suitable total number of calculated states M must be chosen, dependent on the system. In practice, M is generally chosen such that all states with an occupation larger than some minimum occupation, $f_j > f_{\min}$, are included. This, in turn, requires a preliminary study of a simpler version of the system, e.g. a system with fewer atoms.

The choice of $f_{\min}$ is an empirical one, often motivated by some desired accuracy in the calculated properties. In an effort to reduce the number of costly convergence computations required to calculate M, the value of M in the non-interacting HEG, M_{HEG}, can be used as a preliminary guess. The key steps from the derivation of M_{HEG} in Ref. [67] will be shown here.

To begin, the Fermi-Dirac distribution is rearranged to give the energy at which Eq. 2.28 is equal to $f_{\min}$,

$$\varepsilon^* = \frac{1}{\beta} \ln \left[\frac{2}{f_{\min}} - 1 \right] + \mu, \tag{2.29}$$

with $\beta = (k_{\text{B}}T)^{1/2}$. The chemical potential of the HEG at finite temperature is given by [68]

$$\mu = \frac{1}{\beta} I_{1/2}^{-1} \left[\frac{2}{3} \theta^{-3/2} \right], \tag{2.30}$$

with $I_{1/2}^{-1}$ the inverse of the order 1/2 Fermi integral (Eq. 2.58) and $\theta = k_{\text{B}}T/E_{\text{F}}$ the dimensionless reduced temperature.

The total number of doubly-occupied states in the non-interacting HEG can be found by integrating the density of states up to ε^*,

$$M_{\text{HEG}} = \int_0^{\varepsilon^*} g(\varepsilon) \mathrm{d}\varepsilon = \frac{N}{2} \left(\frac{\varepsilon^*}{\varepsilon_F} \right)^{3/2}, \tag{2.31}$$

with $g(\varepsilon)$ the density of states and N the total number of electrons. Substituting in Eq. 2.29 and dividing by N gives the final result of

$$M^{\text{e}} \approx M_{\text{HEG}}^{\text{e}} = \frac{\theta^{3/2}}{2} \left(\ln \left[\frac{2}{f_{\min}} - 1 \right] + I_{1/2}^{-1} \left[\frac{2}{3} \theta^{-3/2} \right] \right)^{3/2}, \tag{2.32}$$

where M^{e} is the number of doubly-occupied states per electron (such that $N \times M^{\mathrm{e}} = M$), and $M^{\mathrm{e}}_{\mathrm{HEG}}$ is M^{e} for the homogeneous electron gas.

Using the definition of the Fermi-Dirac distribution (Eq. 2.28), the finite-temperature versions of the Kohn-Sham equations can be constructed. The total free energy (cf. Eq. 2.20) is written as

$$F([n], T) = F_{\mathrm{s}}([n], T) + E_{\mathrm{H}}[n] + F_{\mathrm{XC}}([n], T) + \int \mathrm{d}\mathbf{r}\, V_{\mathrm{ext}}(\mathbf{r}) n(\mathbf{r}), \tag{2.33}$$

where F now represents a free energy, not a universal functional, F_{s} is the non-interacting free energy, and F_{XC} is the exchange-correlation free energy. Explicit temperature dependence of the individual terms is shown to emphasise the differences from zero temperature; however, note that there is still implicit temperature dependence in the Hartree and external potential contributions due to the temperature dependence of the density (cf. Eq. 2.25),

$$n(\mathbf{r}) = \sum_{j=1}^{M} f_j |\phi_j(\mathbf{r})|^2. \tag{2.34}$$

The non-interacting free energy is expressed as the sum of the non-interacting kinetic and entropic energies,

$$F_{\mathrm{s}} = \mathcal{T}_{\mathrm{s}} - T S_{\mathrm{s}}, \tag{2.35}$$

with the non-interacting kinetic energy calculated as (cf. Eq. 2.18)

$$\mathcal{T}_{\mathrm{s}} = \frac{1}{2} \sum_{j=1}^{M} f_j \int \mathrm{d}\mathbf{r} |\nabla \phi_j(\mathbf{r})|^2, \tag{2.36}$$

and the non-interacting entropy as

$$S_{\mathrm{s}} = -k_{\mathrm{B}} \sum_{j=1}^{M} \{ f_j \ln f_j + (1 - f_j) \ln(1 - f_j) \}. \tag{2.37}$$

Eqs. 2.34 and 2.36 both maintain the correct behaviour as $T \to 0$, with the non-interacting entropy vanishing, as expected.

Throughout this thesis, HKS-DFT will be used to refer to the zero-temperature Hohenberg-Kohn-Sham DFT, and MHKS-DFT will be used to refer to the finite-temperature Mermin-Hohenberg-Kohn-Sham DFT method.

2.4 Pseudopotentials

The external potential V_{ext} for a system of electrons within a material is given by the sum of the Coulomb potentials of the nuclei. If working in a plane-wave basis without using any further approximations for V_{ext}, the computational requirements would quickly become intractable for all but the simplest systems.

The first issue with this treatment is that there will be many Kohn-Sham eigenstates with a non-zero occupation number and therefore many solutions of the non-interacting Schrödinger equation must be calculated and orthogonalised. Using aluminium as an example, there are $Z_{\text{Al}} = 13$ electrons per atom which require $Z_{\text{Al}}/2 \approx 7$ doubly-occupied eigenstates per atom at zero temperature. At finite temperature, the required number of eigenstates will be even higher due to the smearing of occupation numbers. To alleviate this problem, core electrons can be 'frozen' such that they are described together with the nuclei and only contribute through the external potential. This is a reasonable approximation (although its validity depends on the temperature), as the frozen-core electrons are generally chemically inactive, with the behaviour of the chemical bonding being dominated by the valence electrons.

Another problem with using the sum of nuclei-centred Coulomb potentials is that close to the origin the valence electrons have a rapidly oscillating wavefunction, due to the constraint of orthogonalisation, and therefore a large kinetic energy. Since the electronic wavefunction in the periodic DFT calculations presented in this thesis are represented by a plane-wave basis set (see Section 2.7.1), a large number of plane waves is required to accurately reproduce the rapidly oscillating wavefunction, leading to higher computational requirements. Defining a smooth *pseudopotential* that produces the same chemical be-

haviour as the true potential outside some core radius r_{core}, but with fewer oscillations of the wavefunction within r_{core}, allows the wavefunction to be represented by a significantly lower number of plane waves. Note that this approximation only holds so long as no two atoms' frozen cores overlap.

As an example, the functional form of a norm-conserving pseudopotential will be discussed. For the majority of the DFT calculations in this thesis a norm-conserving pseudopotential is used, making this a useful case study. The properties of a norm-conserving pseudopotential were first laid out by Hamann, Schluter, and Chiang [69]:

1. The true and pseudo eigenvalues ε_j agree for some reference atomic configuration.
2. The true and pseudo wavefunctions agree beyond r_{core}.
3. The integrated electron density within r_{core} is the same for the true and pseudo wavefunctions (hence, 'norm-conserving').
4. The logarithmic derivatives of the true and pseudo wavefunctions, as well as their first energy derivatives, match for all $r > r_{\text{core}}$.

Properties 1 and 2 ensure that the norm-conserving pseudopotential matches the true Coulombic potential for $r > r_{\text{core}}$, whilst Properties 3 and 4 are unique to norm-conserving pseudopotentials and improve the transferability of the pseudopotential.

In summary, a pseudopotential is used to both lower the number of electrons (and therefore orthogonal eigenstates) and decrease the required size of the plane-wave basis set used to represent the wavefunctions, significantly lowering computational demands. Further discussion on other types of pseudopotentials and the procedures used to ensure their accuracy and transferability is beyond the scope of this thesis; however, the validity of the pseudopotentials used throughout this thesis to generate DFT data in the warm dense regime will be explored where appropriate.

As an aside, throughout the derivation of density functional theory it has been assumed that the external potential can always be written as some local potential. In contrast,

a key finding of pseudopotential theory is that the pseudopotential that replaces the external potential must be non-local to achieve the highest quality results [70]. Whilst these two claims may seem at odds with each other, the core ideas of density functional theory can, in fact, be modified to allow a non-local external potential [71]. Due to the added computational complexity that this modification brings, it will not be discussed here, but it is enough to know that non-local external potentials do not pose an inherent problem in density functional theory.

As will be investigated later, the use of a particular pseudopotential is only valid up to some temperature. When the temperature is high enough to excite electrons from the frozen core states, the pseudopotential will no longer accurately describe the correct behaviour of the external potential. It is common to use pseudopotentials with fewer frozen core electrons at increasingly higher temperatures, until eventually an all-electron pseudopotential is required.

2.5 Hellmann-Feynman Theorem

DFT provides a way to calculate the ground-state (or thermal-equilibrium) density and energy of a system of atoms; however, during a molecular dynamics simulation the trajectories of the atoms are not directly governed by the energy of the system, but rather the interatomic forces. Furthermore, the absolute value of the energy is unimportant. For any system, a constant energy shift can be added to all calculated energies without affecting any other observable of the system. This is important when comparing the accuracy of different pseudopotentials, as they may not give the same absolute value for the ground-state energy, even when they have the same ground-state density.

The interatomic forces provide another way of testing the accuracy of different methods when constant energy shifts prevent direct comparison of total energies. The electronic finite-temperature effects in warm dense matter also manifest themselves as changes in the interatomic forces, a fact often ignored in interatomic potentials. Having a simple

formula to evaluate the forces is therefore essential if DFT is to be used to produce the data sets needed in Section 6.5.1.

The Hellmann-Feynman theorem provides this formula by relating the derivative of some variational energy to the expectation value of the derivative of the respective Hamiltonian. It can be derived starting from the definition of the energy,

$$E_\lambda = \left\langle \psi_\lambda \middle| \hat{H}_\lambda \middle| \psi_\lambda \right\rangle, \tag{2.38}$$

with E_λ and ψ_λ an eigenvalue and corresponding eigenstate of the Hamiltonian $\hat{H}_\lambda$. The subscript indicates the dependence of the terms on some parameter λ. Taking the derivative of both sides with respect to λ gives

$$\begin{aligned}
\frac{\mathrm{d}E_\lambda}{\mathrm{d}\lambda} &= \frac{\mathrm{d}}{\mathrm{d}\lambda} \left\langle \psi_\lambda \middle| \hat{H}_\lambda \middle| \psi_\lambda \right\rangle \\
&= \left(\frac{\mathrm{d}}{\mathrm{d}\lambda} \langle \psi_\lambda | \right) \hat{H}_\lambda |\psi_\lambda\rangle + \left\langle \psi_\lambda \middle| \left(\frac{\mathrm{d}}{\mathrm{d}\lambda} \hat{H}_\lambda \right) \middle| \psi_\lambda \right\rangle + \langle \psi_\lambda | \hat{H}_\lambda \left(\frac{\mathrm{d}}{\mathrm{d}\lambda} |\psi_\lambda\rangle \right) \\
&= \left\langle \psi_\lambda \middle| \frac{\mathrm{d}\hat{H}_\lambda}{\mathrm{d}\lambda} \middle| \psi_\lambda \right\rangle + E_\lambda \frac{\mathrm{d}}{\mathrm{d}\lambda} \langle \psi_\lambda | \psi_\lambda \rangle ,
\end{aligned} \tag{2.39}$$

where the two derivatives of the eigenstate on the second line have been combined to form the second term in the last line. If the eigenstates are normalised, $\langle \psi_\lambda | \psi_\lambda \rangle = 1$ and

$$\frac{\mathrm{d}}{\mathrm{d}\lambda} \langle \psi_\lambda | \psi_\lambda \rangle = 0; \tag{2.40}$$

however, for an incomplete basis set ψ_λ is not an exact eigenstate of $\hat{H}_\lambda$ and therefore

$$\hat{H}_\lambda |\psi_\lambda\rangle = E_\lambda |\psi_\lambda\rangle + |\chi_\lambda\rangle , \tag{2.41}$$

where $|\chi_\lambda\rangle$ is orthogonal to every function in the basis set. In this case, the first term in the second line of Eq. 2.39 becomes

$$\left(\frac{\mathrm{d}}{\mathrm{d}\lambda} \langle \psi_\lambda | \right) E_\lambda |\psi_\lambda\rangle + \left(\frac{\mathrm{d}}{\mathrm{d}\lambda} \langle \psi_\lambda | \right) |\chi_\lambda\rangle , \tag{2.42}$$

with the second term being the additional contribution arising from the incomplete basis set, referred to as the *Pulay correction*.

Although the plane-wave basis set that will be used for the DFT calculations in this thesis is, in practice, not complete (as an infinite number of plane wave contributions cannot be calculated and stored), the Hilbert space spanned by the plane-wave basis functions is independent of λ, so long as the reciprocal lattice vectors of the unit cell are also independent of λ. This leads to $\frac{\mathrm{d}}{\mathrm{d}\lambda}|\psi_\lambda\rangle$ occupying the same Hilbert space as the basis functions, which is by definition orthogonal to $|\chi_\lambda\rangle$, and so the Pulay corrections vanish exactly for a plane-wave basis set, no matter if it is complete or not. Further details of the plane-wave representation of the eigenstates can be found in Section 2.7.1.

From the definition of the forces on an atom at position $\mathbf{R}_\alpha$ as

$$\boldsymbol{\mathcal{F}}_\alpha = -\frac{\partial E}{\partial \mathbf{R}_\alpha}, \tag{2.43}$$

in Eq. 2.39 λ can be replaced by the atomic position $\mathbf{R}_\alpha$ to calculate the interatomic forces using the Hellmann-Feynman theorem,

$$-\frac{\partial E}{\partial \mathbf{R}_\alpha} = -\left\langle \psi \left| \frac{\partial \hat{H}}{\partial \mathbf{R}_\alpha} \right| \psi \right\rangle, \tag{2.44}$$

where the eigenstates are assumed to be normalised. At zero temperature, E is the total energy of the system as this is the variational energy that is minimised in the ground state.

The interatomic forces in a plane-wave DFT calculation can therefore be calculated as the expectation value of the derivative of the Hamiltonian with respect to the atomic positions [72]. The total Hamiltonian of the system of N electrons and M fixed ions is given by Eq. 2.2 with an additional ion-ion contribution:

$$\hat{H}_{\mathrm{tot}} = -\frac{1}{2}\sum_i^N \nabla_i^2 + \frac{1}{2}\sum_{i\neq j}^N \frac{1}{|\mathbf{r}_i - \mathbf{r}_j|} + \sum_i^N V_{\mathrm{ext}}(\mathbf{r}_i; \{\mathbf{R}\}) + \frac{1}{2}\sum_{\alpha\neq\beta}^M \frac{Z_\alpha Z_\beta}{|\mathbf{R}_\alpha - \mathbf{R}_\beta|}, \tag{2.45}$$

where Z_α is the nuclear charge of atom α. Taking the derivative with respect to an atomic position $\mathbf{R}_\gamma$, only the final two terms contribute to the force:

$$\boldsymbol{\mathcal{F}}_\gamma = -\frac{\partial E}{\partial \mathbf{R}_\gamma} = -\left\langle \psi \left| \frac{\partial \hat{H}}{\partial \mathbf{R}_\gamma} \right| \psi \right\rangle = -\int \mathrm{d}\mathbf{r}\, n_0(\mathbf{r}) \frac{\partial V_{\mathrm{ext}}(\mathbf{r}, \{\mathbf{R}\})}{\partial \mathbf{R}_\gamma} - \sum_{\alpha \neq \gamma}^{M} \frac{\partial}{\partial \mathbf{R}_\gamma} \frac{Z_\alpha Z_\gamma}{|\mathbf{R}_\alpha - \mathbf{R}_\gamma|}. \tag{2.46}$$

Therefore, the interatomic forces within some system can be easily calculated once the ground-state electron density n_0 has been found using DFT. For a non-local pseudopotential, the derivative of V_{ext} is less trivial; however, the forces can still be expressed analytically [73].

The extension of the Hellmann-Feynman theorem to finite temperature (canonical ensemble) is not immediately obvious, but is often assumed in MHKS-DFT calculations. Here, the Hellmann-Feynman theorem will be extended to the canonical ensemble following the derivation of Ref. [74]. The crucial difference at finite temperature is that the thermal-equilibrium state is found at the variational minimum of the Helmholtz free energy F, rather than the internal energy U as in a zero temperature system. The thermal-equilibrium state is also described by the partition function Z, which contains the statistical information about the ensemble. This is in contrast to the ground-state at zero temperature, which is given by only one microstate (ignoring possible degeneracies).

It is once again useful to describe the system using the density matrix operator, this time in the canonical ensemble it is given by

$$\hat{\rho}_\lambda = \frac{1}{Z_\lambda} \exp\left[-\beta \hat{H}_\lambda\right], \tag{2.47}$$

with the partition function defined as

$$Z_\lambda = \mathrm{Tr} \exp\left[-\beta \hat{H}_\lambda\right] = \sum_i \exp\left[-\beta E^i_\lambda\right], \tag{2.48}$$

where the final expression is given in the basis of eigenstates of $\hat{H}$ with corresponding many-electron eigenenergies E^i. The Helmholtz free energy can be defined in terms of Z_λ

as

$$F_\lambda = -\frac{1}{\beta} \ln Z_\lambda, \tag{2.49}$$

and its derivative with respect to some parameter λ is

$$\frac{\partial F_\lambda}{\partial \lambda} = -\frac{1}{\beta} \frac{\partial \ln Z_\lambda}{\partial \lambda} = \frac{1}{Z_\lambda} \sum_i \exp\left[-\beta E_\lambda^i\right] \frac{\partial E_\lambda^i}{\partial \lambda}. \tag{2.50}$$

Using Eq. 2.39, with the Pulay forces assumed to be zero, taking the negative of the entire equation, and substituting $\mathbf{R}_\gamma$ for λ gives

$$\boldsymbol{\mathcal{F}}_\gamma = -\frac{\partial F}{\partial \mathbf{R}_\gamma} = -\frac{1}{Z} \sum_i \exp\left[-\beta E^i\right] \left\langle \psi^i \middle| \frac{\partial \hat{H}}{\partial \mathbf{R}_\gamma} \middle| \psi^i \right\rangle. \tag{2.51}$$

On comparison to the zero-temperature forces given by Eq. 2.44, and using the definition of an ensemble average,

$$\langle \hat{O} \rangle = \operatorname{Tr} \hat{\rho}\, \hat{O} = \frac{1}{Z} \sum_i \exp\left[-\beta E^i\right] \left\langle \psi^i \middle| \hat{O} \middle| \psi^i \right\rangle, \tag{2.52}$$

the forces at finite temperature can be interpreted as the ensemble average of $\frac{\partial \hat{H}}{\partial \mathbf{R}_\gamma}$ at temperature T. Any other property that is defined by a derivative of the total energy, e.g. stress, can also be calculated by analogous equations derived using the Hellmann-Feynman theorem.

At finite temperature, the system is represented by a statistical ensemble of systems in different quantum states, so there is no single correct value of the 'force'. Atoms belonging to different systems in the thermal ensemble will be experiencing different forces and accelerating at different rates. The forces defined here, which are derivatives of the free energy, are thermal averages of the forces experienced by members of the ensemble and are not physical things. This is discussed further in Section 4.1.

These average forces are, however, useful in molecular dynamics simulations (see Chapter 5). For a molecular dynamics simulation in a canonical ensemble at temperature T, if the above method is used to calculate the interatomic forces, and assuming that the dynamics

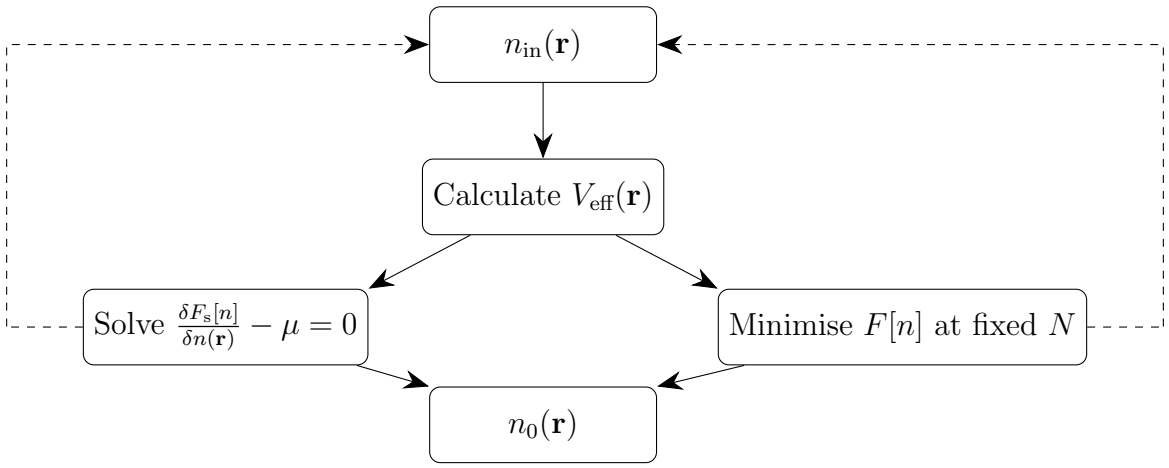

Figure 2.2: The two approaches to finding the ground-state energy and density in orbital-free DFT. The left hand method solves the Euler-Lagrange equation, whilst the right hand method minimises the total free energy functional directly. Both methods require constraints on the density $n(\mathbf{r})$ such that the total number of electrons is constant and the density is non-negative everywhere. The dashed arrows indicate that the density is iteratively changed according to the minimisation scheme until the minimum is found.

are ergodic and the Born-Oppenheimer approximation is valid, the atomic configurations visited will sample, in a statistical sense, the canonical probability density

$$p = \frac{\exp[-\beta F(\{\mathbf{R}\})]}{\operatorname{Tr}\exp[-\beta F(\{\mathbf{R}\})]}. \tag{2.53}$$

Thus, by averaging over measurements made along such trajectories, correct expectation values, or thermal averages, in the canonical ensemble are found. This is true, even though the observed dynamics of the simulation may not represent any physical trajectory.

2.6 Orbital-Free DFT

Orbital-free DFT (OF-DFT) removes the need for the single-particle orbitals in HKS- and MHKS-DFT by approximating the non-interacting free energy explicitly as a functional of the electron density. As there are no longer any KS orbitals, the self-consistent loop is instead replaced by a direct minimisation of the total energy with respect to the electron

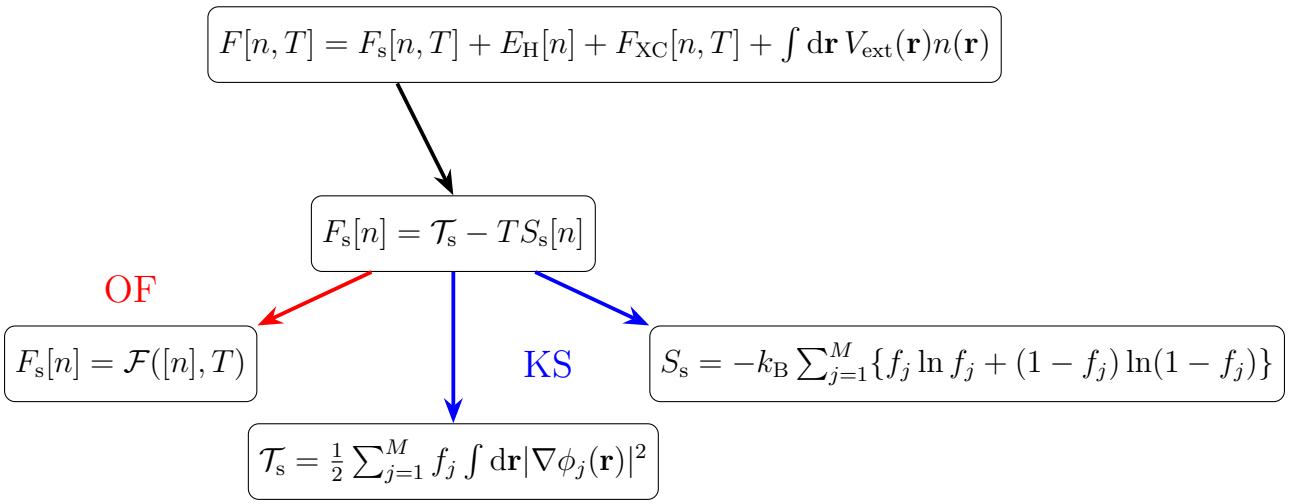

Figure 2.3: The different methods for calculating the non-interacting free energy in Mermin-Hohenberg-Kohn-Sham (MHKS) and orbital-free (OF) DFT. In MHKS-DFT, the non-interacting free energy is calculated using the single-particle orbitals of an auxiliary non-interacting system. In OF-DFT, the non-interacting free energy is calculated as an explicit functional of the electron density.

density. This can be achieved by solving the Euler-Lagrange equation

$$\frac{\delta F_\mathrm{s}[n]}{\delta n(\mathbf{r})} = \mu, \tag{2.54}$$

where the functional derivative of $F_\mathrm{s}[n]$ can be analytically calculated and the chemical potential μ ensures a constant number of electrons. Alternatively, the ground-state energy and density can be found by using an optimiser to directly minimise Eq. 2.33. The two methods for minimising the total energy and density in OF-DFT are shown in Fig. 2.2.

Since there are no orbitals in OF-DFT, the costly orthogonalisation is avoided. Furthermore, since the computational and time requirements of OF-DFT do not explicitly increase with temperature, the speed of high temperature calculations can be orders of magnitude faster than their MHKS-DFT counterparts, as well as requiring no more memory than at low temperature. The contrasting approaches to calculating the non-interacting free energy in MHKS-DFT and OF-DFT are shown in Fig. 2.3.

Here, a brief introduction to some of the non-interacting free energy functionals $F_\mathrm{s}[n] = \mathcal{F}([n],T)$ will be given. A simple program was also written to aid in the understanding of the OF-DFT method, and a few key implementation details from the code's development

will be outlined in Section 2.7. However, the majority of the OF-DFT calculations in this thesis were performed using `PROFESS` [75, 76], due to the availability of a wide range of functionals in the software and a useful structure for extending the code to allow for non-local free energy functionals. Furthermore, the code has been thoroughly tested and optimised throughout its years of development.

During the last decade, there has been a renewed interest in OF-DFT, in particular to simulate the high temperatures found in warm dense matter which the computational limitations of MHKS-DFT prohibit. To this end, more accurate and non-empirical functionals have been developed [77]; however, the accuracy of static (e.g., equilibrium volume and bulk modulus) and dynamic (e.g., dynamic structure factor) properties predicted by OF-DFT still remain inadequate compared to MHKS-DFT, especially at lower temperatures [45] and when tested on a wide range of systems (e.g. semiconductors, simple metals, transition metals) [78].

Another issue in OF-DFT is the requirement of a local pseudopotential, due to the lack of orbitals. Local pseudopotentials are generally less accurate than their non-local counterparts, commonly used in MHKS-DFT, further limiting the overall accuracy of the OF-DFT method [79]. The lack of orbitals in OF-DFT also prevents direct calculation of dynamical properties, such as the electronic conductivity and X-ray absorption near-edge structure [80]. Instead, the KS orbitals and eigenenergies must be calculated using the minimised OF-DFT electron density and atomic configuration, which are then used as the input to the Kubo-Greenwood formula [17]. Although this does not completely circumvent using MHKS-DFT, no self-consistent cycle is required and the computational requirements for the calculation of dynamical properties are reduced.

Much like exchange-correlation functionals, the non-interacting free energy functional can be local (LDA), semi-local (GGA), or non-local. It is well known that without at least gradient corrections, of which the von Weizsäcker correction [81] is the most ubiquitous, molecules cannot bond [82]; therefore, purely local functionals fail to reproduce even the most simple systems at lower temperatures. Here, the local Thomas-Fermi-Dirac func-

tional is introduced as a pedagogical example; however, it also acts as a core component of the subsequent semi-local and non-local functionals. A relatively recent semi-local functional that will later be used to benchmark the accuracy and efficiency of OF-DFT is then discussed.

2.6.1 Thomas-Fermi Functional

The non-interacting kinetic energy density proposed by Thomas and Fermi [57] is

$$\tau_{\mathrm{TF}} = \frac{3}{10}\left(3\pi^2\right)^{2/3} n^{5/3}(\mathbf{r}), \tag{2.55}$$

which is used in the local density approximation (LDA) to give a total kinetic energy of

$$\mathcal{T}_{\mathrm{TF}}[n] = C_{\mathcal{T}} \int n^{5/3}(\mathbf{r})\,\mathrm{d}\mathbf{r}, \tag{2.56}$$

with $C_{\mathcal{T}} = \frac{3}{10}\left(3\pi^2\right)^{2/3}$. Eq. 2.55 can be easily derived by expressing the kinetic energy of a HEG as a k-space integral over the Fermi sphere of radius k_{F}.

The zero-temperature Thomas-Fermi kinetic energy can be extended to finite temperature [83], giving the Thomas-Fermi non-interacting free energy

$$F_{\mathrm{TF}}([n], T) = \int \mathrm{d}\mathbf{r}\, \frac{\sqrt{2}}{\pi^2}\beta^{-5/2}\left[-\frac{2}{3}I_{3/2}(\eta) + \eta I_{1/2}(\eta)\right], \tag{2.57}$$

with $\beta = (k_{\mathrm{B}}T)^{-1}$, I_α the Fermi integral of order α given by

$$I_\alpha(z) = \int_0^\infty \mathrm{d}y\, \frac{y^\alpha}{\exp\left[y - z\right] + 1}, \quad \alpha \geq -\frac{1}{2}, \tag{2.58}$$

and η being defined through the equation

$$n = \frac{\sqrt{2}}{\pi^2}\beta^{-3/2} I_{1/2}(\eta). \tag{2.59}$$

Zero-temperature exchange effects can also be included through the Dirac exchange [84],

which gives a contribution to the total energy of

$$E_{\mathrm{X}} = C_{\mathrm{X}} \int n^{4/3}(\mathbf{r})\,\mathrm{d}\mathbf{r}, \tag{2.60}$$

with $C_{\mathrm{X}} = -\frac{3}{4}\left(\frac{3}{\pi}\right)^{1/3}$; however, from the formulation of OF-DFT shown in Fig. 2.3 it can be seen that both DFT methods define the exchange-correlation contribution in the same way. Therefore, the more accurate exchange-correlation functionals originally derived for use in (M)HKS-DFT can be used in OF-DFT without any adjustment (assuming an exchange-correlation functional that takes KS orbitals as input is not used). Furthermore, in warm dense matter finite-temperature exchange-correlation contributions are often required to accurately describe the system. Finite-temperature exchange-correlation functionals are therefore introduced in Section 4.1.

2.6.2 VT84F

VT84F [42] is a non-empirical semi-local functional with the form

$$F_{\mathrm{s}}^{\mathrm{VT84F}}([n], T) = \int \mathrm{d}\mathbf{r}\, \tau_{\mathrm{TF}}(n) \left[\xi(t) F_\tau(s_\tau) - \zeta(t) F_\sigma(s_\sigma)\right], \tag{2.61}$$

where τ_{TF} is the zero-temperature Thomas-Fermi kinetic energy density defined in Eq. 2.55, ξ and ζ are known functions of Fermi-Dirac integrals [68], $t = \frac{k_{\mathrm{B}}T}{E_{\mathrm{F}}}$ is the reduced temperature, F_τ and F_σ are kinetic and entropic enhancement factors, and s_τ and s_σ are the kinetic and entropic reduced density gradients, defined as

$$\begin{aligned} s_\tau(n, \nabla n, t) &= s(n, \nabla n)\sqrt{\frac{\tilde{h}(t) - t\mathrm{d}\tilde{h}(t)/\mathrm{d}t}{\xi(t)}} \\ s_\sigma(n, \nabla n, t) &= s(n, \nabla n)\sqrt{\frac{t\mathrm{d}\tilde{h}(t)/\mathrm{d}t}{\zeta(t)}}, \end{aligned} \tag{2.62}$$

with the zero-temperature reduced density gradient

$$s(n, \nabla n) = \frac{1}{2(3\pi^2)^{1/3}} \frac{|\nabla n|}{n^{4/3}}, \tag{2.63}$$

and

$$\tilde{h}(t) = -3\frac{I_{1/2}(\beta\mu)I_{-3/2}(\beta\mu)}{I^2_{-1/2}(\beta\mu)}, \tag{2.64}$$

where $\mu = \left.\frac{\delta F_{\mathrm{TF}}([n],T)}{\delta n}\right|_{n(\mathbf{r})}$ is the chemical potential of a non-interacting HEG with density $n(\mathbf{r})$.

The kinetic enhancement factor $F_\tau(s)$ is chosen to fulfil three constraints [42],

1. In the small-s limit, the second-order gradient expansion is recovered, $F_\tau(s) \approx 1 + (5/27)s^2$. This ensures that densities close to, and at, the uniform limit are accurately described. [68]

2. The Pauli potential is non-negative for all $\mathbf{r}$. The Pauli potential is given by $v_\theta([n];\mathbf{r}) = \frac{\delta(F_{\mathrm{s}}([n],T=0)-T_{\mathrm{vW}}[n])}{\delta n(\mathbf{r})}$, with $T_{\mathrm{vW}}[n] = \int \mathrm{d}\mathbf{r}\tau_{\mathrm{TF}}(n)(5s^2/3)$ the von Weizsäcker functional. This constraint ensures that atoms can bind to form molecules and solids [85, 86].

3. In the large-s limit, the von Weizsäcker behaviour is recovered. This is required as the von Weizsäcker correction is known to exactly describe the density matrix far from a nucleus, which is dominated by the highest occupied molecular orbital [87]. The highest occupied molecular orbital is, itself, exact, by the ionisation potential theorem [88].

These constraints motivate the choice of functional form similar to that of the GGA exchange functional VT{8,4} [89],

$$F_\tau(s) = 1 - \frac{\mu s^2 \exp[-\alpha s^2]}{1+\mu s^2} + \left(1 - \exp\left[-\alpha s^{m/2}\right]\right)\left(s^{-n/2} - 1\right) + \frac{5s^2}{3}, \tag{2.65}$$

with $m = 8$, $n = 4$, $\mu = 2.778$, and $\alpha = 1.2965$. The entropic enhancement factor is then defined by $F_\sigma(s_\sigma) = 2 - F_\tau(s_\sigma)$, which is exact for the second-order gradient expansion [68].

Both the finite-temperature Thomas-Fermi functional and VT84F are implemented in

PROFESS through the PROFESS@QE package [90], which was developed to couple the OF-DFT method to a molecular dynamics module.

2.7 Periodic Boundary Conditions

OF-DFT is, conceptually, a far simpler method than MHKS-DFT, thanks to the direct minimisation of the free energy functional and the explicit functional form of $F_\mathrm{s}[n]$; however, there are also terms that appear unchanged between the two methods (see Fig. 2.3). These are the Hartree (or electron-electron) term, the external potential (or electron-ion) term, and the (until now, ignored) ion-ion term, collectively called the electrostatic terms.

Any real material of interest will contain of order $\mathcal{O}(10^{23})$ atoms. Defining $V_\mathrm{ext}(\mathbf{r}) = \sum_I Z_I/|\mathbf{r} - \boldsymbol{\tau}_I|$, with $\{\boldsymbol{\tau}_I\}$ the atomic positions, I the atomic index, and ignoring any issues from the singularity in the Coulomb potential, it is apparent that a vast number of non-negligible terms must be included in the sum to calculate $V_\mathrm{ext}(\mathbf{r})$, due to the long range of the Coulomb interaction. This sum would be computationally intractable for a macroscopic system. Instead, the crystalline nature of many materials can be exploited by modelling the system as a single unit cell that is then periodically repeated in all directions, such that there are identical unit cells at each Bravais lattice vector $\mathbf{R}$. An example system is shown in Fig. 2.4.

In a conventional face-centred cubic (fcc) structure, for example, this reduces the number of atoms that must be explicitly simulated from $\mathcal{O}(10^{23})$ to four. Even in the case where the material is not perfectly periodic, e.g. if it is partially liquid or contains dislocations and defects, etc., the approximation made by modelling a non-periodic system by a periodically repeated simulation cell becomes better as the simulation cell is made larger. Often, the simulation cell is chosen to be a supercell, which is the unit cell produced from combining multiple primitive unit cells, with the primitive unit cell the smallest possible unit cell that can be periodically repeated to create the chosen crystalline structure.

In a periodic system of atoms, the ions (which can either be bare nuclei or a combination

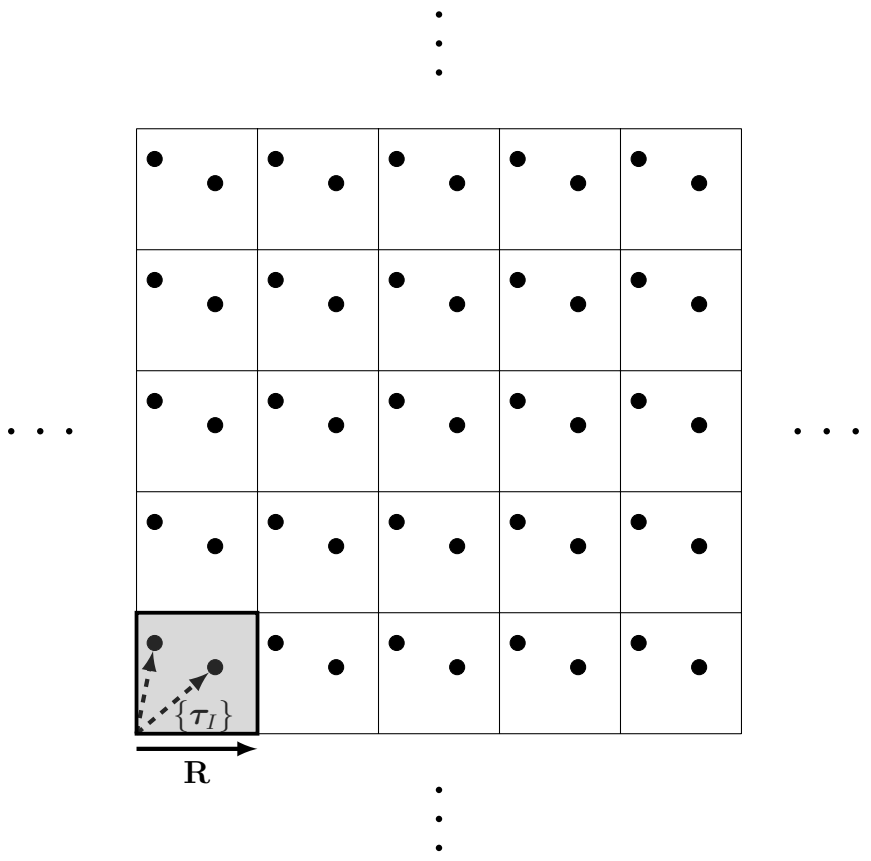

Figure 2.4: An infinite crystal formed from periodic tiling of a unit cell. The two atom atomic basis $\{\boldsymbol{\tau}_I\}$ and the periodic part of the Bloch state $u_{n,\mathbf{k}}$, defined in Eq. 2.72, are periodic with the Bravais lattice vector $\mathbf{R}$. As there are an infinite number of periodically repeated unit cells in the crystal, the allowed values of $\mathbf{k}$ are continuous, and the per unit cell values are calculated as integrals over $\mathbf{k}$ within the Brillouin zone. When modelling a non-periodic system (e.g., liquids) by a periodic simulation cell, the unit cell is replaced by the simulation cell and $\mathbf{R}$ is replaced by the simulation cell lattice vector $\mathbf{R}^{\mathrm{s}}$.

of nuclei and frozen-core electrons in the form of a pseudopotential) are fixed in position in the unit cell, whilst the 'smoothed' electron density is allowed to vary under the constraint that it has the periodicity of the unit cell. To calculate the electrostatic terms, the contributions from the interactions with all of the other charges, both inside and outside the unit cell, must be taken into account.

The focus here will be on how enforcing periodicity affects the (M)HKS-DFT and OF-DFT methods. To this end, the Bloch state will be introduced as the periodic solution of the single-particle Schrödinger equation used in (M)HKS-DFT, Eq. 2.26, and to show how

plane waves and Fourier transforms can be used to simplify periodic systems. Then, the approach for calculating the electrostatic terms in the total energy for a periodic system will be detailed, which were implemented in my OF-DFT program.

2.7.1 Bloch Theorem

A unit cell is defined such that translating by a Bravais lattice vector

$$\mathbf{R} = n_1\mathbf{a}_1 + n_2\mathbf{a}_2 + n_3\mathbf{a}_3, \tag{2.66}$$

with $\mathbf{a}_i$ the primitive lattice vectors of the unit cell and n_i positive or negative integers, leaves the configuration of atoms unchanged. A reciprocal lattice vector can be defined as

$$\mathbf{G} = m_1\mathbf{b}_1 + m_2\mathbf{b}_2 + m_3\mathbf{b}_3, \tag{2.67}$$

with $\mathbf{b}_i$ the primitive reciprocal lattice vectors of the unit cell and m_i positive or negative integers, such that

$$\mathbf{a}_i \cdot \mathbf{b}_j = 2\pi\delta_{ij}. \tag{2.68}$$

Any function that is periodic with the unit cell satisfies the relationship

$$f(\mathbf{r}) = f(\mathbf{r} + \mathbf{R}), \tag{2.69}$$

and can be expanded in a plane-wave basis as a sum over its reciprocal lattice vectors,

$$f(\mathbf{r}) = \sum_{\mathbf{G}} f(\mathbf{G}) \exp\left[\mathrm{i}\mathbf{G} \cdot \mathbf{r}\right], \tag{2.70}$$

where $f(\mathbf{G})$ are the Fourier coefficients for each $\mathbf{G}$ vector which are given as

$$f(\mathbf{G}) = \frac{1}{\Omega}\int_{\Omega} f(\mathbf{r}) \exp\left[-\mathrm{i}\mathbf{G} \cdot \mathbf{r}\right] \mathrm{d}\mathbf{r}, \tag{2.71}$$

with $\Omega = \mathbf{a}_1 \cdot (\mathbf{a}_2 \times \mathbf{a}_2)$ the volume of a periodic unit cell. Since the atomic configuration is periodic with $\mathbf{R}$, so too is the Hamiltonian and, therefore, the effective potential $V_{\text{eff}}(\mathbf{r})$ in Eq. 2.26. The solutions of the single-particle Schrödinger equation are then *Bloch waves* or *states*. These take the form

$$\phi_{n,\mathbf{k}}(\mathbf{r}) = \exp\left[\mathrm{i}\mathbf{k} \cdot \mathbf{r}\right] u_{n,\mathbf{k}}(\mathbf{r}), \tag{2.72}$$

with $\mathbf{k}$ a wavevector, n the band index denoting the different solutions to the Schrödinger equation for a particular $\mathbf{k}$, and $u_{n,\mathbf{k}}(\mathbf{r})$ a periodic function such that $u_{n,\mathbf{k}}(\mathbf{r}+\mathbf{R}) = u_{n,\mathbf{k}}(\mathbf{r})$. In words, Bloch's theorem states that the single-particle eigenstates consist of a periodic function modulated by a plane wave.

The periodic function $u_{n,\mathbf{k}}$ is often expanded in a plane-wave basis using Eq. 2.70,

$$u_{n,\mathbf{k}}(\mathbf{r}) = \sum_{|\mathbf{G}| \leq G_{\max}} c_{n,\mathbf{k}}(\mathbf{G}) \exp\left[\mathrm{i}\mathbf{G} \cdot \mathbf{r}\right], \tag{2.73}$$

with $c_{n,\mathbf{k}}(\mathbf{G})$ the Fourier coefficients and

$$G_{\max} = |\mathbf{G}_{\max}| = \sqrt{2E_{\text{kin}}^{\text{cut}}} \tag{2.74}$$

the highest energy plane wave contained within the basis set. The kinetic energy cutoff $E_{\text{kin}}^{\text{cut}}$ is treated as a convergence parameter within DFT calculations. As $E_{\text{kin}}^{\text{cut}}$ is increased, so too is the size of the basis set used to represent the KS eigenstates. The variational principle then dictates that the increase in basis set size leads to a systematic improvement in the accuracy of the calculations. An additional benefit to using a plane-wave basis is the lack of dependence on the atomic positions.

One of the consequences of Bloch's theorem is that there is now a set of possible solutions, indexed by $\mathbf{k}$, all satisfying the Schrödinger equation. Whilst the modulating plane wave $\exp\left[\mathrm{i}\mathbf{k} \cdot \mathbf{r}\right]$ is not necessarily periodic on translation by an arbitrary lattice vector $\mathbf{R}$, from the definitions of $\mathbf{G}$ and $\mathbf{R}$, given in Eqs. 2.67 and 2.66, it is known that the plane wave

$\exp[\mathrm{i}\mathbf{G}\cdot\mathbf{r}]$ is periodic with $\mathbf{R}$. Any Bloch state with an arbitrary wavevector $\mathbf{q}$ lying outside the first Brillouin zone can be written as

$$\begin{aligned}\phi_{n,\mathbf{q}}(\mathbf{r}) &= \exp[\mathrm{i}\mathbf{q}\cdot\mathbf{r}]\, u_{n,\mathbf{q}}(\mathbf{r}) \\ &= \exp[\mathrm{i}(\mathbf{k}+\mathbf{G})\cdot\mathbf{r}]\, u_{n,\mathbf{q}}(\mathbf{r}) \\ &= \exp[\mathrm{i}\mathbf{k}\cdot\mathbf{r}]\, u_{n,\mathbf{k}}(\mathbf{r}),\end{aligned} \tag{2.75}$$

where $\mathbf{k}$ has been enforced to be within the first Brillouin zone, and $u_{n,\mathbf{k}}(\mathbf{r}) = \exp[\mathrm{i}\mathbf{G}\cdot\mathbf{r}]\, u_{n,\mathbf{q}}(\mathbf{r})$ is manifestly periodic with $\mathbf{R}$. Therefore, any $\phi_{n,\mathbf{q}}(\mathbf{r})$ with $\mathbf{q}$ lying outside the first Brillouin zone is equivalent to $\phi_{n,\mathbf{k}}(\mathbf{r})$ with $\mathbf{k} = \mathbf{q} - \mathbf{G}$ lying within the first Brillouin zone. Thus, it suffices to consider only Bloch states $\phi_{n,\mathbf{k}}(\mathbf{r})$ where $\mathbf{k}$ is within the first Brillouin zone.

With an infinitely periodic system, any total energy or number of particles will be infinite. The more useful values are per unit cell properties which can be compared or minimised, as needed. To calculate a per unit cell value, the average over all possible $\mathbf{k}$ must be taken. For a finite system, there will be N_{cell} different $\mathbf{k}$ points at which the value is sampled, where N_{cell} is the number of unit cells in the entire system. As the finite system becomes infinite, the sum over $\mathbf{k}$ becomes an integral over the first Brillouin zone,

$$\bar{f} = \lim_{N_{\mathrm{cell}}\to\infty} \frac{1}{N_{\mathrm{cell}}} \sum_{\mathbf{k}} f(\mathbf{k}) = \frac{\Omega}{(2\pi)^3} \int_{\mathrm{BZ}} \mathrm{d}\mathbf{k}\, f(\mathbf{k}). \tag{2.76}$$

The variation of the eigenvalues of the single-particle Schrödinger equation $\varepsilon_{n,\mathbf{k}}$ against $\mathbf{k}$ is called the *band structure*.

2.7.2 Electrostatics in a Periodic System

Accounting for the periodic images of the unit cell is also essential to calculating the electrostatic terms in the DFT total energy. The periodicity of the unit cell leads to $V_{\mathrm{eff}}(\mathbf{r})$ being periodic, as well as the electron density $n(\mathbf{r})$. It has already been shown that any periodic function can be expressed in a plane-wave basis using Eqs. 2.70 and 2.71,

and here this will be exploited to demonstrate how integrals that are intractable in real space can be readily evaluated in reciprocal space.

Any system of interest in DFT must ensure charge neutrality for a number of reasons; however, the most important is that if there is a net charge within the unit cell, when the periodicity is accounted for in the thermodynamic limit there would be an infinitely charged system and the total energy would diverge. The total charge density is therefore defined as

$$n_{\text{tot}}(\mathbf{r}) = n^{+}(\mathbf{r}) + n(\mathbf{r}), \tag{2.77}$$

with the periodic unit cell containing the same amount of positive and negative charge, such that

$$\int_{\Omega} n_{\text{tot}}(\mathbf{r})\,\mathrm{d}\mathbf{r} = 0, \tag{2.78}$$

where n^{+} is the positive charge density, primarily constituted of point charges, such that

$$n^{+}(\mathbf{r}) = n_{\text{H}} + \sum_{I}\sum_{\mathbf{R}} Z_I \delta(\mathbf{r} - (\boldsymbol{\tau}_I + \mathbf{R})), \tag{2.79}$$

with Z_I the ion's charge, $\boldsymbol{\tau}_I$ the ion's position within the unit cell, n_{H} the homogeneous background into which the atoms are embedded, and n the negative charge density. For the vast majority of DFT calculations, $n_{\text{H}} = 0$ and can be ignored; however, it is included here to prove the applicability of the DFT method to the systems of interest in Chapter 9. The ionic sum over I is restricted to only include ions within the unit cell, and no constraints are placed on the form of the negative charge n, other than it integrating to $-\int_{\Omega} n^{+}(\mathbf{r})\,\mathrm{d}\mathbf{r}$ in each unit cell and being relatively smooth.

The Coulomb energy per unit cell is calculated through the usual Coulomb formula

$$\begin{aligned} U &= \frac{1}{2}\int_{\mathbf{r}\in\Omega}\int_{\mathbf{r}'<\infty} \frac{n_{\text{tot}}(\mathbf{r})n_{\text{tot}}(\mathbf{r}')}{|\mathbf{r}-\mathbf{r}'|}\,\mathrm{d}\mathbf{r}\,\mathrm{d}\mathbf{r}' \\ &= \frac{1}{2}\int_{\mathbf{r}\in\Omega}\int_{\mathbf{r}'\in\Omega}\sum_{\mathbf{R}} \frac{n_{\text{tot}}(\mathbf{r})n_{\text{tot}}(\mathbf{r}'+\mathbf{R})}{|\mathbf{r}-(\mathbf{r}'+\mathbf{R})|}\,\mathrm{d}\mathbf{r}\,\mathrm{d}\mathbf{r}', \end{aligned} \tag{2.80}$$

where in the first line $\mathbf{r}$ is integrated over the unit cell volume Ω and $\mathbf{r}'$ over all space. In

the second line, the sum over all space has been replaced by a sum over Bravais lattice vectors $\mathbf{R}$ and an integration of $\mathbf{r}'$ over Ω. Substituting in the density $n_{\text{tot}}(\mathbf{r})$, removing the spurious ionic self-interaction terms, and separating the Coulomb energy into three terms, gives

$$\begin{aligned} U &= E_{II} + E_{\text{ext}} + E_{\text{H}} \\ &= \frac{1}{2}\sum_{I}\sum_{\substack{J \\ (J\neq I)}}\sum_{\mathbf{R}}\frac{Z_I Z_J}{|\boldsymbol{\tau}_I - (\boldsymbol{\tau}_J + \mathbf{R})|} + \frac{1}{2}\sum_{I}\sum_{\mathbf{R}\neq\mathbf{0}}\frac{Z_I^2}{|-\mathbf{R}|} \\ &+ \int_{\Omega}\sum_{I}\sum_{\mathbf{R}}\frac{(n(\mathbf{r}) + n_{\text{H}})Z_I}{|\mathbf{r} - (\boldsymbol{\tau}_I + \mathbf{R})|}\,\mathrm{d}\mathbf{r} \\ &+ \frac{1}{2}\int_{\Omega}\int_{\Omega}\sum_{\mathbf{R}}\frac{(n(\mathbf{r}) + n_{\text{H}})(n(\mathbf{r}') + n_{\text{H}})}{|\mathbf{r} - (\mathbf{r}' + \mathbf{R})|}\,\mathrm{d}\mathbf{r}'\,\mathrm{d}\mathbf{r}, \end{aligned} \tag{2.81}$$

with E_{II} the ion-ion energy and $E_{\text{ext}} = \int \mathrm{d}\mathbf{r}\, V_{\text{ext}}(\mathbf{r})n(\mathbf{r})$ the external potential interaction energy.

2.7.3 Evaluation in Reciprocal Space

Eq. 2.81 now provides a form for the total Coulomb energy of a charge neutral periodic unit cell with point-like ionic charges. However, each term still contains a sum over an infinite number of lattice vectors $\mathbf{R}$, and each term only drops off as $1/r$. If all of the positive and negative charges are included in the summation, it is conditionally convergent [91], meaning that the result depends on which order the contributions are summed, and so an alternative method to calculate each term must be found.

It has been alluded to that, due to the periodicity of the problem, one can calculate many of the terms in reciprocal space as a simple sum over $\mathbf{G}$ vectors. As will be shown later, when the Coulomb potential is Fourier transformed into reciprocal space, the long-tail convergence problem in real space becomes a singularity at $\mathbf{G} = \mathbf{0}$. At first glance, this seems to have not solved the issue; however, the fact that the zero of a potential is arbitrary allows the $\mathbf{G} = \mathbf{0}$ components of the potential to be removed (or effectively set to zero). The reason for this is that the $\mathbf{G} = \mathbf{0}$ Fourier component of a real space function

is simply its average value over a periodic unit cell, as can be seen from Equation 2.71. The $\mathbf{G} = \mathbf{0}$ component of the Coulomb potential is therefore also arbitrary, and will be set to zero to remove the singularity. In addition, the requirement of charge neutrality ensures that the $\mathbf{G} = \mathbf{0}$ component of the total charge density is also zero.

Finally, the implementation of this theory commonly uses Fast Fourier Transforms (FFTs) to quickly move between real and reciprocal spaces. This is a technique that uses Discrete Fourier Transforms and a divide and conquer approach that is most efficient when the number of grid points is a power of two [92]. Although the definition given in Eq. 2.70 (Eq. 2.71) for the (inverse) Fourier transform will be followed here, it is important to note that there are many different conventions in the literature.

2.7.4 Ewald Energy

The first line in the final equality of Eq. 2.81 corresponds to E_{II}. The most common method for evaluating this term is the Ewald summation [57, 91]. Whilst the mathematical derivation will not be covered here, the method is shown in Fig. 2.5 and involves adding two equal, but opposite sign, Gaussians of charge over each point ion to screen the interactions and maintain the correct total charge. The Coulomb potentials due to the point charges and the cancelling Gaussians centred on them die off rapidly away from the point charges and are calculated in real space; the other Gaussians make up a smooth periodic charge density, the potential of which is easily calculated in reciprocal space.

Since the system considered in E_{II} only contains positive ions, and the added Gaussian charges cancel, the entire system is not charge neutral. Therefore, a uniform cancelling background must be included such that the $\mathbf{G} = \mathbf{0}$ component of the total charge density can be ignored, avoiding singularities. As the total system (electrons and ions) is charge neutral, the uniform cancelling background required to evaluate the individual components of Eq. 2.81 cancel out when added together, leaving the total Coulomb energy U unchanged.

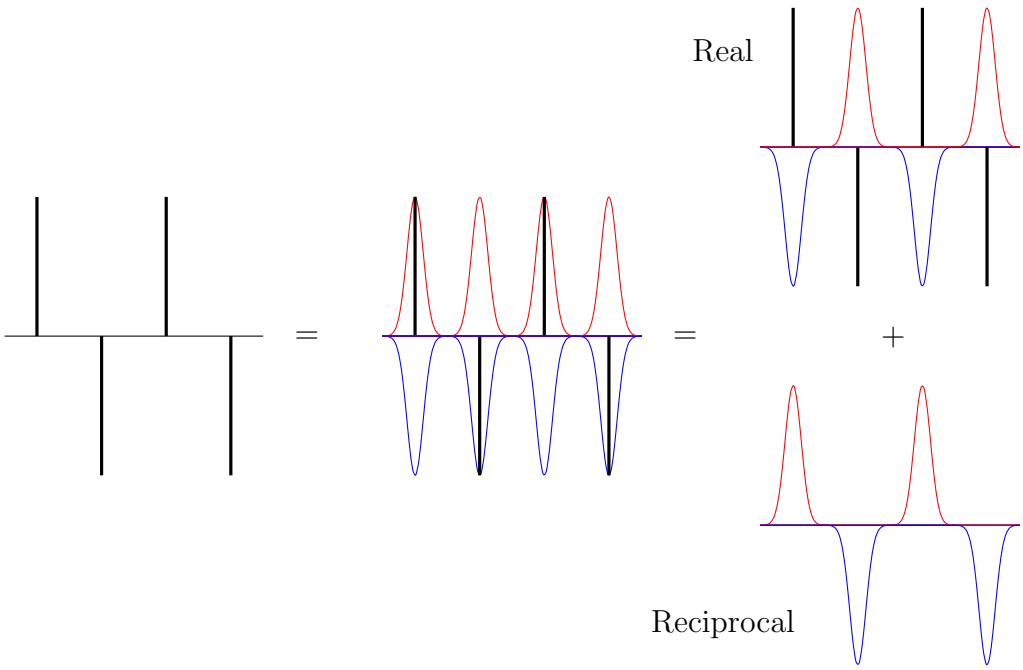

Figure 2.5: The Ewald summation method which is used for calculating the electrostatic energy of a charge-neutral infinitely periodic system. The left hand side of the first equality shows the initial system with vertical lines representing positive (above the horizontal axis) and negative (below the horizontal axis) point charges. The positive (red) and negative (blue) Gaussians are then added to the system, maintaining charge neutrality. The system can then be split into two charge-neutral terms: the first contains the point charges and the oppositely charged Gaussians that then screen the point charge Coulomb interactions, whilst the second removes the additional contributions from the screening Gaussians. The first term is then evaluated in real space, and the second term in reciprocal space. Here, the system is shown to be charge neutral throughout, with each individual term also charge neutral. This avoids a divergent result when the terms are evaluated. However, in practice the negative charges (electrons) are represented as a density, rather than point charges, and are evaluated using a separate method.

The Ewald potential at a point $\mathbf{r}$ due to a point charge at position $\mathbf{r}_j$ in every unit cell is given by the formula [93]

$$v_E(\mathbf{r},\mathbf{r}_j) = \sum_{\mathbf{R}} \frac{\operatorname{erfc}(\gamma^{\frac{1}{2}}|\mathbf{r}-(\mathbf{r}_j+\mathbf{R})|)}{|\mathbf{r}-(\mathbf{r}_j+\mathbf{R})|} - \frac{\pi}{\Omega\gamma} + \frac{4\pi}{\Omega}\sum_{\mathbf{G}\neq\mathbf{0}} \frac{\exp\left[-G^2/4\gamma\right]}{G^2}\exp\left[\mathrm{i}\mathbf{G}\cdot(\mathbf{r}-\mathbf{r}_j)\right], \tag{2.82}$$

where erfc is the complementary error function, and γ is a convergence parameter. The value of γ affects the real and reciprocal sums in opposite ways. This means a larger γ will require fewer $\mathbf{R}$ vectors to converge the real space sum, whereas the reciprocal sum would require more $\mathbf{G}$ vectors. There is, therefore, a compromise that must be struck to allow both sums to converge at a reasonable rate. This is often chosen as $\gamma = (2.8/\Omega^{1/3})^2$, since

this value minimises the computational cost for many Bravais lattices [94]. No matter the choice of γ, the real and reciprocal space sums are, in this form, absolutely convergent, and the calculated value of $v_E(\mathbf{r}, \mathbf{r}_j)$ is independent of γ.

The primary use of the Ewald summation is to allow the interactions between periodic charges to be evaluated. Therefore, an expression for the Ewald potential at an ionic position, $\mathbf{r} = \boldsymbol{\tau}_I$, is required. This is found by summing the Ewald potentials due to all of the other ions in the unit cell with that from the periodic images of ion I. Mathematically, this is written as

$$v(\boldsymbol{\tau}_I) = \sum_{\substack{J \\ J \neq I}} q_J v_E(\boldsymbol{\tau}_I, \boldsymbol{\tau}_J) + q_I v_M, \tag{2.83}$$

where q_I is charge at $\boldsymbol{\tau}_I$ and the Madelung constant v_M is defined as

$$\begin{aligned} v_M &= \lim_{\mathbf{r} \to \boldsymbol{\tau}_I} \left(v_E(\mathbf{r}, \boldsymbol{\tau}_I) - \frac{1}{|\mathbf{r} - \boldsymbol{\tau}_I|} \right) \\ &= \sum_{\mathbf{R} \neq \mathbf{0}} \frac{\operatorname{erfc}(\gamma^{1/2} R)}{R} - \frac{2\gamma^{1/2}}{\pi^{1/2}} - \frac{\pi}{\Omega \gamma} + \frac{4\pi}{\Omega} \sum_{\mathbf{G} \neq \mathbf{0}} \frac{\exp\left[-G^2/4\gamma\right]}{G^2}, \end{aligned} \tag{2.84}$$

which is the potential acting on ion I from its own periodic images, but excluding itself (hence there is no $\mathbf{R} = \mathbf{0}$ term).

Using Eq. 2.83, the ion-ion Coulomb energy can then be expressed as

$$\begin{aligned} E_{II} &= \frac{1}{2} \sum_I \sum_{\substack{J \\ J \neq I}} q_I q_J v_E(\boldsymbol{\tau}_I, \boldsymbol{\tau}_J) + \frac{1}{2} \sum_I q_I^2 v_M \\ &= \frac{1}{2} \sum_I \sum_{\substack{J \\ J \neq I}} q_I q_J (v_E(\boldsymbol{\tau}_I, \boldsymbol{\tau}_J) - v_M), \end{aligned} \tag{2.85}$$

where the charge neutrality, $q_I + \sum_{(J \neq I)}^{J} q_J = 0$, has been exploited in the second line.

2.7.5 Hartree Energy

For a smooth, continuous, and periodic charge density, it is easiest to make use of reciprocal space sums to evaluate the interaction energy. Starting from the third line of Eq.

2.81 as the expression for E_{H}, and defining $\tilde{n}(\mathbf{r}) = n(\mathbf{r}) + n_{\mathrm{H}}$,

$$\begin{aligned} E_{\mathrm{H}} &= \frac{1}{2}\int_{\Omega}\int_{\Omega}\sum_{\mathbf{R}}\frac{\tilde{n}(\mathbf{r})\tilde{n}(\mathbf{r}')}{|\mathbf{r}-(\mathbf{r}'+\mathbf{R})|}\,\mathrm{d}\mathbf{r}'\,\mathrm{d}\mathbf{r} \\ &= \frac{1}{2}\int_{\Omega}\int_{\Omega}\tilde{n}(\mathbf{r})\left(\sum_{\mathbf{G}\neq\mathbf{0}}\frac{4\pi}{\Omega G^2}\exp\left[\mathrm{i}\mathbf{G}\cdot(\mathbf{r}-\mathbf{r}')\right]\right)\tilde{n}(\mathbf{r}')\,\mathrm{d}\mathbf{r}'\,\mathrm{d}\mathbf{r} \\ &= \frac{1}{2\Omega}\sum_{\mathbf{G}\neq\mathbf{0}}\left(\int_{\Omega}\tilde{n}(\mathbf{r})\exp\left[\mathrm{i}\mathbf{G}\cdot\mathbf{r}\right]\,\mathrm{d}\mathbf{r}\right)\frac{4\pi}{G^2}\left(\int_{\Omega}\tilde{n}(\mathbf{r}')\exp\left[-\mathrm{i}\mathbf{G}\cdot\mathbf{r}'\right]\,\mathrm{d}\mathbf{r}'\right) \\ &= \frac{\Omega}{2}\sum_{\mathbf{G}\neq\mathbf{0}}\tilde{n}(-\mathbf{G})\frac{4\pi}{G^2}\tilde{n}(\mathbf{G}) = \frac{\Omega}{2}\sum_{\mathbf{G}\neq\mathbf{0}}n(-\mathbf{G})\frac{4\pi}{G^2}n(\mathbf{G}), \end{aligned} \tag{2.86}$$

where Eqs. 2.70 and 2.71 have been used to transform the Coulomb potential and density into reciprocal space, the magnitude of a reciprocal lattice vector has been defined as $G = |\mathbf{G}|$, and the final expression arises due to the exclusion of the $\mathbf{G} = \mathbf{0}$ Fourier components, setting the n_{H} contributions to zero. The Fourier transform of the Coulomb potential should contain a convergence factor, commonly of the form $\exp\left[-\epsilon\mathbf{G}^2\right]$, in a rigorous mathematical derivation; however, it has not been included here for brevity.

2.7.6 Pseudopotential Energy

The final electrostatic term to calculate is E_{ext}. In practice, an approximation is made by the introduction of a pseudopotential. As mentioned previously, pseudopotentials replace the ionic Coulomb potential and have many benefits computationally, such as removing the asymptotic $1/r$ behaviour as $r \to 0$ and smoothing out the functional form within some core radius. This then means that fewer $\mathbf{G}$ vectors, and therefore plane waves, are needed to accurately represent the Kohn-Sham eigenstates. It is important, however, that at large r the pseudopotential tends towards the normal Coulombic form, and different pseudopotential constructions will ensure that particular values within the core region are the same as for an all-electron calculation.

Here, the pseudopotential is assumed to be local, to simplify the derivation. Beginning

at Equation 2.81, a pseudopotential v_{ps}^I can be substituted in for the Coulomb potential,

$$\begin{aligned} E_{\text{ext}} &= \int_\Omega \sum_I \sum_{\mathbf{R}} \frac{(n(\mathbf{r}) + n_{\text{H}}) Z_I}{|\mathbf{r} - (\boldsymbol{\tau}_I + \mathbf{R})|} \, \mathrm{d}\mathbf{r} \\ &= \int_\Omega \sum_I \sum_{\mathbf{R}} (n(\mathbf{r}) + n_{\text{H}}) v_{\text{ps}}^I(\mathbf{r} - (\boldsymbol{\tau}_I + \mathbf{R})) \, \mathrm{d}\mathbf{r} \\ &= \frac{1}{\Omega} \int_\Omega (n(\mathbf{r}) + n_{\text{H}}) \sum_I \left(\sum_{\mathbf{G}} v_{\text{ps}}^I(\mathbf{G}) \exp\left[\mathrm{i}\mathbf{G} \cdot (\mathbf{r} - \boldsymbol{\tau}_I)\right] \right) \mathrm{d}\mathbf{r}, \end{aligned} \tag{2.87}$$

where Equation 2.70 has been used to find the Fourier sum for $v_{\text{ps}}^I(\mathbf{r})$, with the superscript I indicating that it contains the factor of Z_I.

The $\mathbf{G} = \mathbf{0}$ component of the Ewald potential for the total charge density is set to zero by choice. Here, however, the Coulomb interaction between the electrons and nuclei has been replaced by a pseudopotential and so care must be taken since the pseudopotential's $\mathbf{G} = \mathbf{0}$ component is not equal to that of the Coulomb potential. Therefore, the difference between the components $v_{\text{ps}}^I(\mathbf{G} = \mathbf{0}) - v_{\text{Coulomb}}^I(\mathbf{G} = \mathbf{0})$ must be added when the $\mathbf{G} = \mathbf{0}$ components are removed. Even though both $\mathbf{G} = \mathbf{0}$ terms diverge individually, their difference is finite. Therefore, Δv_{ps}^I is defined as the integral of the difference between the pseudopotential and the Coulomb potential,

$$\Delta v_{\text{ps}}^I(\mathbf{G} = \mathbf{0}) = \int_{\mathbf{r}<\infty} \left(v_{\text{ps}}^I(\mathbf{r}) - \frac{Z_I}{r} \right) \mathrm{d}\mathbf{r}. \tag{2.88}$$

By splitting up the sum over $\mathbf{G}$ vectors in E_{ext}, setting all the $\mathbf{G} = \mathbf{0}$ components to zero, and substituting in the Fourier expansion for the density, the external energy can be expressed as

$$\begin{aligned} E_{\text{ext}} &= \frac{1}{\Omega} \int_\Omega n(\mathbf{r}) \sum_I \left(\sum_{\mathbf{G}\neq\mathbf{0}} v_{\text{ps}}^I(\mathbf{G}) \exp\left[\mathrm{i}\mathbf{G} \cdot (\mathbf{r} - \boldsymbol{\tau}_I)\right] + \Delta v_{\text{ps}}^I \right) \mathrm{d}\mathbf{r} \\ &= \sum_{\mathbf{G}\neq\mathbf{0}} n(-\mathbf{G}) \sum_I v_{\text{ps}}^I(\mathbf{G}) \exp\left[-\mathrm{i}\mathbf{G} \cdot \boldsymbol{\tau}_I\right] + \frac{1}{\Omega} \int_\Omega \sum_I \Delta v_{\text{ps}}^I n(\mathbf{r}) \, \mathrm{d}\mathbf{r} \\ &= \sum_{\mathbf{G}\neq\mathbf{0}} n(-\mathbf{G}) \sum_I v_{\text{ps}}^I(\mathbf{G}) \exp\left[-\mathrm{i}\mathbf{G} \cdot \boldsymbol{\tau}_I\right] + \frac{N}{\Omega} \sum_I \Delta v_{\text{ps}}^I, \end{aligned} \tag{2.89}$$

in which N is defined as the number of electrons in the unit cell, and the process of defining a new density has been skipped by immediately setting n_{H} to zero.

Expressions for all of the terms in the Coulomb energy, Eq. 2.81, are now known, each of which requires (at least some) evaluation in reciprocal space. Given that the density is relatively smooth, the size of $n(\mathbf{G})$ will drop off quickly as G increases. Combined with the factors of $1/G^2$ present in some of the summations, the reciprocal-space energy contributions in Eqs. 2.85, 2.86, and 2.89 converge rapidly as G increases. The real-space contribution to the Ewald sum also converges rapidly if γ is chosen sensibly. Hence, using periodic boundary conditions and a plane-wave basis set has been shown to be an effective approach to including the effect of interactions from charges throughout all space $\mathbf{r}$, whilst avoiding the convergence problems that arise from the Coulomb potential.

2.8 Scaling of computational resources in DFT

MHKS-DFT provides a general method that can simulate zero-temperature systems and warm dense matter on the same footing, as well as calculate accurate interatomic forces for use in molecular dynamics simulations. This allows the electronic-temperature effects on the forces to be easily discerned. Furthermore, the explicit orbitals allow for the calculation of electrical conductivities and phonons using the response function formalism [95, 96, 97]. However, for the calculation of, for example, ablation dynamics, systems with hundreds of thousands, if not millions, of atoms are required to observe behaviours that match qualitatively with experimental results. To study most of the warm dense regime, MHKS-DFT calculations at electronic temperatures up to $T_{\mathrm{e}} \approx 10^6$ K must be computationally possible.

The limiting factor which prevents arbitrarily large and hot systems from being simulated using MHKS-DFT is the scaling of the computational time and memory requirements with the number of KS orbitals. The KS orbitals must be orthogonalised to calculate the eigenenergies and eigenstates, with the computational time for this procedure scaling as

[98]

$$t^{\mathrm{KS}} \propto N_{\mathrm{occ}}^3, \tag{2.90}$$

with N_{occ} the number of partially occupied KS orbitals. The memory requirements of orthogonalisation also increase with N_{occ}. Some algorithms will store intermediate steps in the diagonalisation process on disk or recalculate previous results when needed, capping the required memory [99]. However, this then comes at the cost of a longer computational time. As such, it is difficult to precisely define the scaling of the memory requirements.

Therefore, the focus will primarily be on the scaling of the computational time with N_{occ}, although it is safe to assume that any calculation that is limited by computational time will likely also be limited by memory requirements. The value of N_{occ} in a MHKS-DFT calculation is determined by the electronic temperature and system size. A discussion on how N_{occ} scales with each of these parameters follows.

2.8.1 Scaling with electronic temperature

The scaling with electronic temperature T_{e} is especially important when there is a varying T_{e} throughout the simulation, such as when heating or dissipative effects are included, as although low temperature calculations may be computationally inexpensive, poor scaling may lead to the highest temperatures becoming inaccessible. In MHKS-DFT, as the temperature increases the Fermi-Dirac distribution flattens, as shown in Fig. 2.6, leading to more KS orbitals with a non-negligible occupation. As mentioned in Section 2.3, the choice of a 'non-negligible' occupation is empirical and generally determined by some specified accuracy in the calculated properties. The number of partially occupied orbitals approximately scales as

$$N_{\mathrm{occ}} \propto T_{\mathrm{e}}^{3/2}, \tag{2.91}$$

with T_{e} the electronic temperature [67].

A simple derivation of this scaling behaviour can be found by approximating the density of states of the warm dense system as the density of states of a free electron system. This

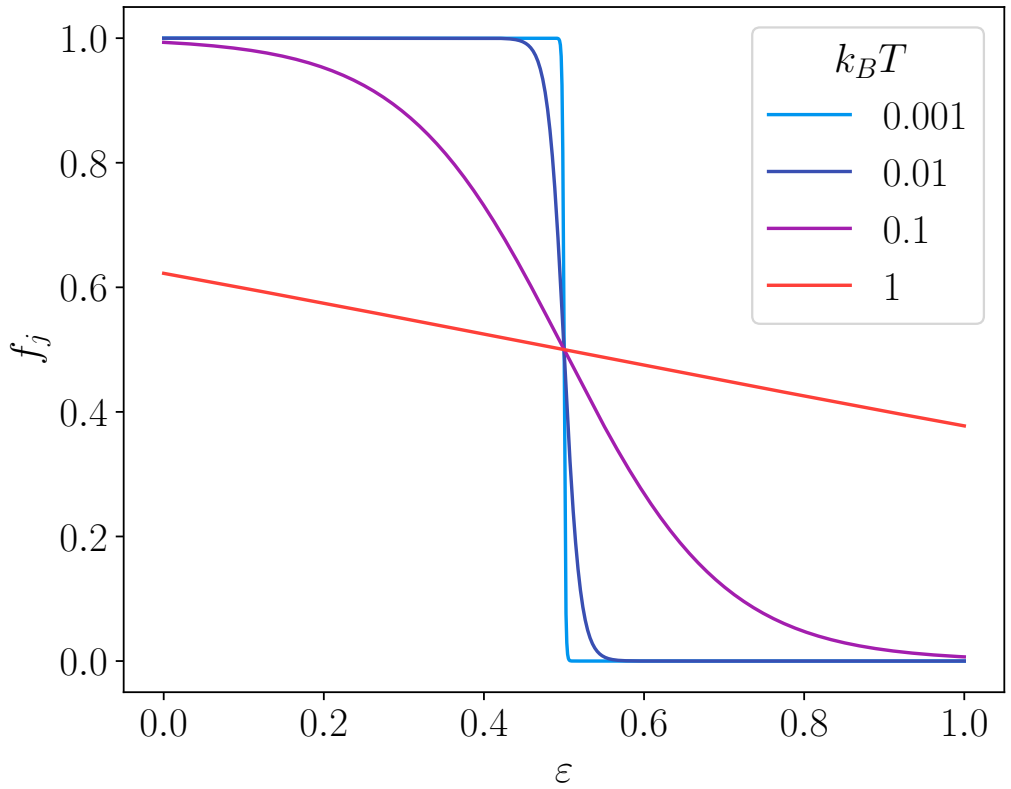

Figure 2.6: The Fermi-Dirac occupation f_j against energy ε as given by Eq. 2.28 with arbitrary units. The chemical potential is fixed at $\mu = 0.5$ for all temperatures. As the temperature T increases, the Fermi-Dirac distribution becomes smoother, the occupation of the higher ε states increases, and the occupation of the lower ε states decreases. The units of all parameters are arbitrary.

approximation is more accurate for certain materials, e.g. aluminium, but is also more accurate at the higher temperatures found in warm dense systems. The density of states in the free electron model is

$$g(\varepsilon) \propto \sqrt{\varepsilon}, \tag{2.92}$$

with ε the energy of a particular state. To find N_{occ}, such that all partially occupied KS orbitals are included in the calculation, the density of states is integrated up to the maximum orbital energy ε_{max} chosen to satisfy some convergence criteria:

$$N_{\text{occ}} \propto \int^{\varepsilon_{\text{max}}} \sqrt{\varepsilon}\, \mathrm{d}\varepsilon \sim \varepsilon_{\text{max}}^{3/2}. \tag{2.93}$$

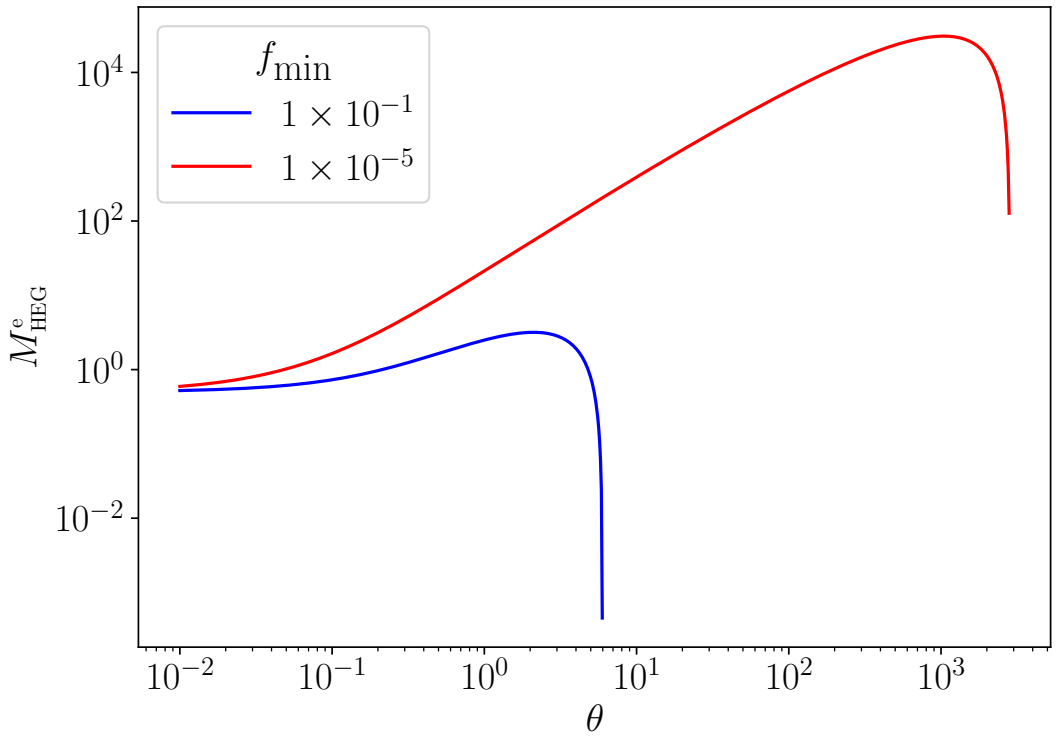

Figure 2.7: The number of partially occupied orbitals per electron $M^{\mathrm{e}}_{\mathrm{HEG}}$ required to explicitly calculate all KS orbitals with an occupation greater than $f_{\min}$ for the non-interacting HEG at reduced temperature $\theta = k_{\mathrm{B}}T/\varepsilon_{\mathrm{F}}$, given by Eq. 2.32. The total number of orbitals required for N_{at} atoms contributing Z_{val} valence electrons each can be calculated using Eq. 2.95. Two different values of $f_{\min}$ are plotted, showing that a larger $f_{\min}$ leads to the maximum in $M^{\mathrm{e}}_{\mathrm{HEG}}$ occurring at a lower θ. The seemingly unphysical drop in $M^{\mathrm{e}}_{\mathrm{HEG}}$ at large θ is explained in Section 2.8.2.

According to the equipartition theorem, $\varepsilon_{\max} \sim k_{\mathrm{B}}T_{\mathrm{e}}$ and therefore

$$N_{\mathrm{occ}} \propto T_{\mathrm{e}}^{3/2}, \tag{2.94}$$

giving the expected scaling. A more rigorously derived relationship between N_{occ} and T_{e} is given by Eq. 2.32 and is shown in Fig. 2.7.

Current MHKS-DFT programs do not allow for a fluctuating value of N_{occ}, meaning that, within a single simulation, minimisations at low temperature must be performed with the same computational time cost as those at high temperature. To avoid this, an adaptive scheme could be implemented for $N_{\mathrm{occ}}(T_{\mathrm{e}})$; however, convergence tests should, in theory,

be performed when moving between electronic temperatures. A more naive approach would be to restart the simulation for each step. Although only the scaling has been discussed here, each calculation also entails a prefactor cost that is independent of the scaling behaviour. In MHKS-DFT, this prefactor includes the cost from setting up the FFT grids, parallelisation, etc., which the program performs at the start of any simulation. For repeated, small calculations, this will quickly become the dominant limitation.

OF-DFT does not use orbitals, eliminating the scaling with T_e and making it an attractive method to simulate systems with either a varying, or arbitrarily high, T_e. Interestingly, there have been previous studies that show a slight decrease in the computational time of OF-DFT for increasing T_e [77]. It has been postulated that this may be due to an increasing homogeneity of the electron density with T_e.

2.8.2 Scaling with system size

The second scaling consideration is the scaling with the number of atoms N_at (or the number of electrons N) and material density ρ. In DFT simulations, supercells are often used to model liquids or investigate phononic properties. For instance, in warm dense matter entropic contributions dominate and the vast majority of systems are found in a liquid phase. The lack of long-range order requires the introduction of a supercell, which is then periodically repeated. To reduce the effects of this unphysical translational symmetry, which is introduced for technical reasons only, large supercells are required to reach convergence with experimental results. Often, the initial configuration of these supercells is chosen to be multiple primitive unit cells of some perfect crystal lattice, before being equilibrated.

When studying phonons, these supercells will have a small perturbation to the position of one atom and the change in the interatomic forces from equilibrium can be calculated. Predicting the computational resources required for a supercell can be made easier if the scaling with N_at for a constant material density ρ is known. Other applications for

which favourable scaling with the number of atoms is essential include simulations of non-equilibrium experiments, such as the laser heating of a thin film in Chapter 11. These simulations often allow for expansion of the system into the surrounding vacuum, which requires systems containing millions of atoms to reproduce the correct ablation dynamics upon heating and allow for creation of voids in the film [100].

The scaling with ρ is relatively unimportant for simulations of ablation, where the material density ρ is often close to the material density at room temperature and pressure ρ_0. However, for equation of state calculations, or when attempting to span the entire warm dense regime, the material density can be far from ρ_0. Therefore, the scaling with respect to the material density can limit a method's applicability [67].

In (M)HKS-DFT, for a system with constant material density ρ and a single elemental species, the required number of orbitals is given by

$$N_{\mathrm{occ}} = M^{\mathrm{e}} Z_{\mathrm{val}} N_{\mathrm{at}}, \tag{2.95}$$

with M^{e} the number of partially occupied orbitals per electron and Z_{val} the number of valence electrons per atom. As is apparent from the form of Eq. 2.32, the number of partially occupied orbitals per electron is independent of N_{at}. According to Eq. 2.95, it follows that

$$N_{\mathrm{occ}} \propto N_{\mathrm{at}}. \tag{2.96}$$

To derive the scaling of N_{occ} with ρ, Eq. 2.32 along with the definition of the Fermi energy,

$$E_{\mathrm{F}} = \frac{1}{2}(3\pi^2 n)^{2/3} = \frac{1}{2}\left(3\pi^2 \frac{N}{V}\right)^{2/3}, \tag{2.97}$$

can once again be used, this time with N held constant and V allowed to vary. Both V and θ increase as ρ decreases, with Fig. 2.7 showing the final effect as an increase in M^{e}, in general. Interestingly, M^{e} is not monotonically increasing, as at extremely high temperatures and low densities it begins to decrease. Mathematically, this arises from the

inverse Fermi integral of order 1/2 in Eq. 2.32 (equal to $\mu_{\mathrm{HEG}}/k_{\mathrm{B}}T$) becoming increasingly negative.

Physically, N_{occ} cannot become zero (or negative) as the electrons must be found somewhere; however, this behaviour indicates that the chosen f_{min} is too large for the given θ. For example, under the HEG approximation, at a large enough θ and f_{min} the occupation predicted by the Fermi-Dirac distribution f_i for all orbitals i would be less than f_{min}. Therefore, the 'correct' number of orbitals to use would be $N_{\mathrm{occ}} < 1$, which is physically impossible. This is observed in Fig. 2.7, as at high temperatures M^{e} tends to zero in order of decreasing f_{min}.

The high temperatures (and low densities) at which $\theta \gg 1$ and N_{occ} starts to decrease are beyond the warm dense regime and are not of interest here. Therefore, the general rule is that systems with a higher material density require fewer KS orbitals. Importantly, N_{occ} is not the only convergence parameter and systems with a high material density can encounter issues with the overlapping of pseudopotential cores, discussed in Section 3.2.

OF-DFT improves on the (M)HKS-DFT scaling with N_{at}, thanks to its direct representation of the electron density on a grid of points. The limiting factor is therefore the FFTs used to transform the density to and from reciprocal space [44], which leads to a scaling of

$$t^{\mathrm{OF}} \propto N_{\mathrm{at}} \ln N_{\mathrm{at}}, \tag{2.98}$$

for a calculation at constant material density ρ and fixed cutoff energy. The computational time of OF-DFT does not depend on N_{at} if the volume is fixed and the FFT grid is left unchanged as the density of atoms is increased. If the volume of the unit cell is increased with a fixed N_{at}, an equivalent scaling law to Eq. 2.98 is found with N_{at} replaced by V. Once again, this arises due to the use of FFTs to move between real and reciprocal space.

In addition, for the evaluation of the FFT to be maximally efficient, 2^n grid points are needed, with n an integer. Therefore, the number of grid points is always rounded up to the nearest power of two, often leading to a overly fine mesh for the electron density

and a slower minimisation. Even with this limitation, OF-DFT avoids the cubic scaling inherent to the orthogonalisation of the KS orbitals, expressed in Eq. 2.90, and therefore scales better than (M)HKS-DFT with both N_{at} and $1/\rho$.

The final consideration, touched upon earlier, is the prefactor (i.e., the cost of a calculation for a single atom at zero temperature), which dominates the low temperature and small system size behaviour. Empirical examples of the prefactor will be shown in Section 6.6.2, but for large-scale simulations at high temperature the scaling of the method with electronic temperature and system size is generally the limiting factor on whether a method is computationally feasible or not.

Overall, MHKS-DFT is limited by its scaling with electronic temperature, the number of atoms, and the inverse material density. Often, a balance must be struck between these three parameters to ensure reasonable computational requirements. For example, a simulation at high temperature will be limited to only a few atoms or an extremely high material density. Conversely, the computational cost of an OF-DFT simulation is independent of temperature, allowing arbitrarily high temperatures to be simulated, and the scaling with system size is close to linear, vastly improving the efficiency of large-scale simulations. This is the motivation behind the recent interest in finite-temperature OF-DFT functionals; however, accuracy of the approximate functionals, and the local pseudopotentials that must be used, currently limit the systems for which OF-DFT can produce data with an accuracy on par with MHKS-DFT.

2.9 Summary

In this chapter, DFT has been introduced as a method to find the ground state of the many-electron problem for periodic systems. The use of the Born-Oppenheimer approximation allows the electronic and ionic degrees of freedom to be treated separately, vastly reducing the dimensionality of the problem. The Kohn-Sham scheme then provides a method to calculate the ground state of the fully interacting electronic system using an

auxiliary non-interacting ensemble of electrons.

The finite-temperature analogue of ground-state DFT, introduced by Mermin, allows for the calculation of free energies and forces in warm dense matter on the same footing as ground-state DFT calculations. The core alteration required for the finite-temperature extension is the varying occupation of the KS orbitals according to Fermi-Dirac statistics.

Pseudopotentials have been introduced as a way to avoid convergence issues and to improve the computational efficiency of DFT calculations with negligible effect on the accuracy.

OF-DFT was shown to avoid the poor scaling with temperature and system size inherent to MHKS-DFT, thanks to the representation of the non-interacting free energy as an explicit functional of the electron density; however, the limitations of the approximations for the non-interacting free energy functional and the local pseudopotentials that must be used in OF-DFT simulations severely restrict the accuracy and transferability of the method.

Chapter 3

Developments of Finite-T DFT

In this chapter, extensions to the finite-temperature DFT methods will be discussed. These can be categorised into two types. The first aim to improve the accuracy of the approximations used in finite-temperature DFT. As DFT is primarily used as a method to solve zero-temperature systems, the approximations of the exchange-correlation energy and psuedopotentials are generally formulated for zero temperature. Therefore, consideration of where zero-temperature approximations, often used at finite temperature without further validation, are applicable and where they break down is vital to ensuring the accuracy of finite-temperature DFT calculations. Furthermore, approximations that have shown success at zero temperature can often be extended to finite temperature with only slight modifications, e.g., by incorporating entropic contributions.

The second type of developments aim to speed up and improve the computational efficiency of the high temperature calculations required to simulate warm dense matter. The poor scaling of the run time of MHKS-DFT calculations as the temperature is increased, caused by the increasing number of partially occupied KS orbitals, prevents calculation of arbitrarily high temperature systems. One approach that avoids this prohibitively poor scaling is OF-DFT, introduced earlier. Non-interacting free energy functionals used in OF-DFT can be constructed such that their evaluation time does not scale with temperature; however, these functionals often have poor transferability and struggle to describe

a wide range of systems. An alternative approach to speed up high-temperature MHKS-DFT calculations, without completely forgoing the use of KS orbitals, is to treat the high energy orbitals in MHKS-DFT as a continuum, the effect of which can be approximated using the explicitly calculated low energy orbitals.

The accuracy of finite-temperature approximations is important for generating reliable DFT data to be used in the fitting of an interatomic potential in Chapter 6. It is also important for modelling the correct dynamics in laser-irradiated thin film simulations which require an accurate description of the electronic-temperature effects, as shown in Chapter 11. The efficiency of high temperature calculations is vital for generating a large and varied dataset of the free energies and forces in WDM aluminium. To ensure the transferability of any interatomic potential fit to the dataset, free energies and forces of snapshots with different densities and temperatures are required. When simulating laser-irradiated thin films, systems with up to 10^8 atoms are required to observe void formation and ablation dynamics that match experimental data [100, 20].

This chapter is structured as follows. First, the developments aimed at improving the accuracy of finite-temperature DFT are discussed. This includes a recent finite-temperature exchange-correlation functional and its implementation in `Quantum Espresso`, a (M)HKS-DFT program. A simple example system will be investigated to show the importance of electronic-temperature effects in the warm dense regime. Then, the temperature and density regime for which zero-temperature pseudopotentials can be used in finite-temperature DFT calculations will be studied.

The second type of developments, aimed at improving the efficiency of high-temperature DFT calculations, will then be introduced. The first is a non-local functional for the non-interacting free energy in OF-DFT, created as the finite-temperature extension of a preexisting zero-temperature functional. I implemented this in `PROFESS@QE` to allow for the comparison of semi-local and non-local OF-DFT functionals later in Section 6.6. Finally, it will be shown how the poor scaling of MHKS-DFT with temperature can be avoided by use of the extended first-principles molecular dynamics model.

3.1 Finite-T Exchange-Correlation Functionals

In Chapter 2, the finite-temperature versions of the non-interacting contributions to the free energy were discussed. The temperature dependence of these terms could be expressed by exact analytic forms. However, the XC contribution is generally calculated using a function that has been fit to empirical data. Extending this fit to finite temperature therefore requires the generation of data at various temperatures and densities of interest, and a temperature-dependent functional form to be chosen.

For most condensed matter systems, the temperature dependence of the XC functional is negligible compared to the other thermal terms. Zero-temperature XC (ZTXC) functionals are therefore commonly used in DFT calculations at elevated temperatures [79, 21]. In recent years, accurate quantum Monte Carlo simulations have shown discrepancies between free energies calculated using a ZTXC functional and the 'true' free energies in the WDM regime [101]. This has spurred on the research and development of accurate finite-temperature XC (FTXC) functionals.

Recently, two almost identical FTXC LDA functionals have been published, differing only by the quantum Monte Carlo data for the HEG to which they are fit. Both use a Padé representation for the XC free energy per particle of the form [102]

$$f_{\mathrm{XC}}(r_s,\theta) = -\frac{1}{r_s}\frac{a(\theta)+b(\theta)\sqrt{r_s}+c(\theta)r_s}{1+d(\theta)\sqrt{r_s}+e(\theta)r_s}, \tag{3.1}$$

where $r_s = [3/(4\pi n)]^{1/3}$, $\theta = k_{\mathrm{B}}T/E_{\mathrm{F}}$ is the reduced temperature, $a(\theta)$–$e(\theta)$ are fitted Padé formulae, and it has been assumed that the spins are unpolarised. A Padé form was chosen as f_{XC} can be obtained from the exact electron-electron energy per electron u_{ee} by a thermodynamic relation, and it has previously been shown that u_{ee} can be approximated well by a Padé formulae [103]. The form of f_{XC} as a ratio of two polynomials also allows for derivatives and functional derivatives to be expressed analytically, improving the computational efficiency of their evaluation. For instance, the exchange-correlation

potential V_{XC}, required in Eq. 2.24, can be expressed as

$$V_{\mathrm{XC}}([n],\mathbf{r}) = \frac{\delta\left(\int \mathrm{d}\mathbf{r}\, n(\mathbf{r}) f_{\mathrm{XC}}(r_s,\theta)\right)}{\delta n(\mathbf{r})} = f_{\mathrm{XC}}(r_s,\theta) - \frac{r_s}{3}\frac{\partial f_{\mathrm{XC}}(r_s,\theta)}{\partial r_s} - \frac{2\theta}{3}\frac{\partial f_{\mathrm{XC}}(r_s,\theta)}{\partial \theta}. \quad (3.2)$$

The two different fits for Eq. 3.1 are the GDSMFB functional, by Groth et al. [102], and the KSDT functional, by Karasiev et al [103, 104]. The KSDT functional will be used throughout this thesis when finite-temperature XC effects are important; however, there is very little difference between the two functionals over a wide range of the warm dense regime.

All of the MHKS-DFT calculations in this thesis used `Quantum Espresso` [105, 106], a suite of tools that can perform electronic-structure calculations. Many MHKS-DFT codes, including `Quantum Espresso`, implement XC functionals via the `LibXC` library [107, 108]. Calls to the external library involve arguments for the name of the function, the type of function (LDA, GGA, MGGA, etc.), as well as the local density and, in the case of the two FTXC functionals, the local temperature.

The core difference between using the ZTXC and FTXC functionals is that for the FTXC functionals the electronic temperature must be set independently through a separate function call, after the initialisation call. If not, the program assumes the default value of 0 K. This second function call is missing in version 6 of `Quantum Espresso`[1]. This was fixed in a local version with all MHKS-DFT calculations in this thesis produced using this fixed version. Similar care must be taken for any OF-DFT program that uses the `LibXC` library.

Since the finite-temperature effects on the XC functional are, in most cases, expected to be negligible [101], it is not surprising that the incorrect implementation of FTXC functionals can often be overlooked. The correct method to call FTXC functionals using `LibXC` has been outlined previously [109]. Whilst the exact functions and arguments

[1]It is important to note that only the XC functional's temperature is not being set correctly; the temperature of the system overall that is used for the smearing of occupations and calculation of the entropic contribution is correct. In WDM simulations, both temperatures ought to be the same, although they are set in different modules within the program.

are now outdated, the general procedure still holds. These functionals see only rare use though, and the incorrect implementation is only obvious in specific circumstances, such as in the low-density aluminium system discussed next.

3.1.1 Low-density aluminium

The low density fcc aluminium system put forward in Ref. [101] is considered here. This particular system is chosen due to the noticeable finite-temperature XC effects on its Kohn-Sham band structure, which makes any issues with the implementation of FTXCs in `Quantum Espresso` apparent.

Both the KSDT and GDSMFB functionals are designed in such a way that they recover the behaviour of the Perdew-Zunger (PZ) ZTXC functional [64] at zero temperature. In addition, the PZ functional is one of the archetypal LDA XC functionals whose accuracy has been heavily tested, making it a good comparison. Therefore, by comparing the PZ and KSDT band structures at various temperatures, the FTXC effects can be separated from the implicit finite-temperature contributions that are present regardless of the XC functional, as shown in Fig. 3.1.

At 5 kK, using a ZTXC functional is reasonably justified, as seen by the almost identical band structure of the PZ and KSDT functionals. However, at 20 kK there are notable differences between the two band structures. Since the energy shift from including finite-temperature XC effects is not constant for all of the bands, the band gaps and transport properties are also dependent on the electronic temperature. The finite-temperature XC effects are therefore essential to accurately describe hot diffuse systems, such as WDM, and tests should also be performed for systems with a lower temperature or higher density before assuming the use of a ZTXC functional is satisfactory.

Aluminium samples melt at temperatures much lower than those encountered in the warm dense regime, so the atoms in warm dense aluminium are not arranged in an fcc structure. The computations reported here are not irrelevant, however, as irradiating a thin film of

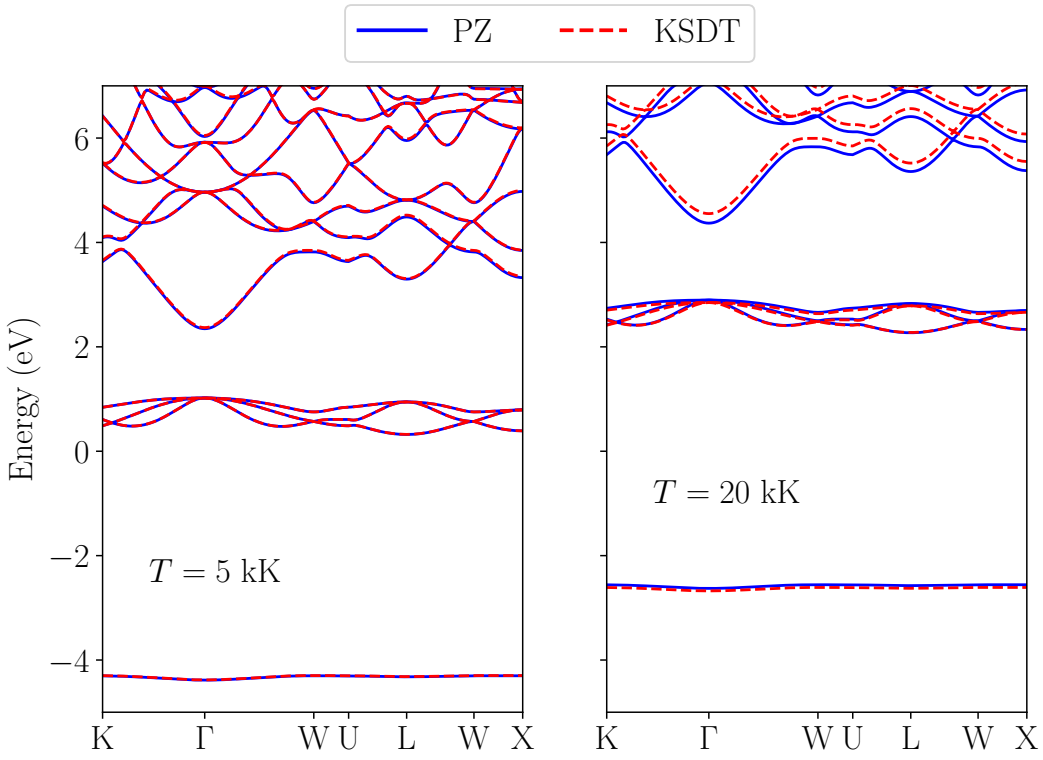

Figure 3.1: KS band structures of low density fcc aluminium at $T = 5$ kK (left) and $T = 20$ kK (right) through a path of high symmetry points in k-space. All of the calculated band structures were produced using `Quantum Espresso`. The aluminium system has a density of 0.2 g/cm^3 and the energies are plotted relative to to their respective chemical potentials. The blue curves are the bands calculated using the zero-temperature PZ XC functional, whilst the red dashed curves are calculated using the finite-temperature KSDT XC functional. There is little observed difference between the ZTXC and FTXC bands at 5 kK; however, the difference at 20 kK is pronounced and cannot be approximated by a constant shift. This figure is a recreation of Fig. 5 from Ref. [101].

cold aluminium with a powerful laser raises the electronic temperature whilst leaving the ionic temperature close to zero and the crystal lattice almost unaltered [110, 111, 23, 26]. This is due to the discrepancy between the ionic and electronic coupling to the pumping laser. Furthermore, the time taken for the hot electrons to equilibrate thermally with each other, which is of order 10-100 fs, is much shorter than the time required for the ionic and electronic systems to equilibrate with each other, which takes of order 1 ps. This allows experimental measurements to be taken in the regime considered here, when the ions are cold and crystalline but the electrons are hot [112, 113]. Finite-temperature effects in laser-irradiated thin films will be investigated further in Chapter 11.

3.2 Pseudopotentials in Warm Dense Matter

In Chapter 2, the pseudopotential was introduced as a way of improving the computational efficiency of DFT calculations, without affecting any of the calculated properties. A pseudopotential achieves this by reducing the number of electrons that are explicitly considered and smoothing out the all-electron wavefunction, thereby requiring fewer Fourier components to accurately model the pseudo-wavefunction.

Since the MHKS-DFT forces will be used later in the thesis as a benchmark, it must be ensured that any inaccuracy due to the pseudopotential is minimised. In pseudopotential studies of aluminium, a 3 valence electron (3e) pseudopotential is often used [114, 115]. This means that the 3s and 3p electrons are accounted for exactly using KS orbitals, whilst the 1s, 2s, and 2p electrons are frozen in the pseudopotential core. Since the 2s and 2p electrons are at relatively low-lying energies, this serves as a good approximation for standard density and low temperature calculations. On the other hand, if extreme states of matter are investigated, an 11e pseudopotential, that also explicitly considers the 2s and 2p states, may be required to attain accurate results due to pressure and thermal ionisation of the frozen-core electrons.

Use of a pseudopotential with fewer frozen electrons will generally incur two computational penalties. The first is a smaller core cutoff radius r_{core}, which leads to an increase in the number of plane waves in the basis set required to accurately describe the pseudo wavefunction. The second is a greater number of KS orbitals with non-negligible occupation, due to the increased number of valence electrons. The number of KS orbitals required to achieve a chosen precision in the computed properties (see Section 2.3) also becomes more pronounced at high temperature due to the flattening of the Fermi-Dirac distribution.

Since the warm dense regime encompasses a wide range of temperatures and densities, care must be taken to ensure that a chosen pseudopotential can accurately describe all possible states of the system during a simulation. This is generally checked using a convergence

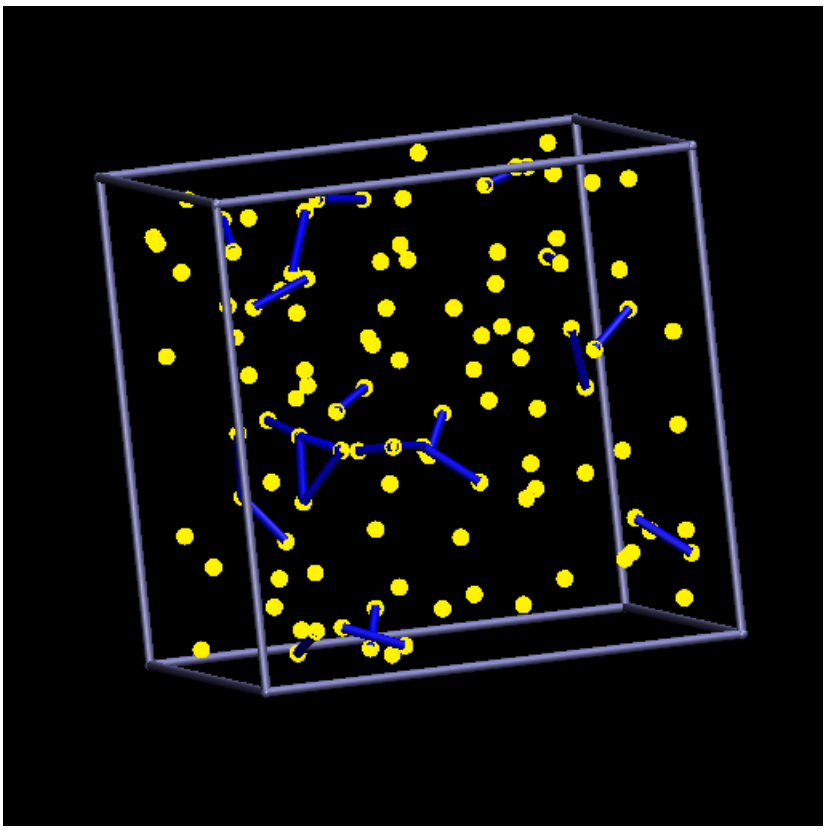

Figure 3.2: A snapshot of 2.37 g/cm^3 aluminium equilibrated at 100 kK using an embedded atom model potential and with periodic boundary conditions. The yellow spheres represent the Al atoms, whilst the blue bonds show where $r_{IJ} < 2\,r_{\text{core}}$. The size of the yellow spheres is chosen solely for visual clarity.

test, where the properties of a simpler system calculated using pseudopotentials with different numbers of valence electrons and different values of r_{core} are compared. Here, an investigation into the material densities and electronic temperatures for which a chosen pseudopotential is applicable is undertaken.

As the ionic temperature and material density increases, the likelihood of two pseudo-atoms (the combination of an ionic core and its frozen-core electrons) having an inter-atomic separation of $r_{IJ} < 2\,r_{\text{core}}$ increases. This can be seen in Fig. 3.2, which is a snapshot of a $T_{\text{eq}} = 100$ kK molecular dynamics simulation at $\rho = 2.37$ g/cm^3 using a classical potential, where T_{eq} is defined as the equilibration temperature of the molecular dynamics simulation. In Fig. 3.2, the blue bonds indicate pairs of pseudo-atoms separated by distances less than $2\,r_{\text{core}}$. In the perfect fcc lattice, there are no overlapping pseudo-atoms. It is assumed throughout the molecular dynamics simulation that the electrons

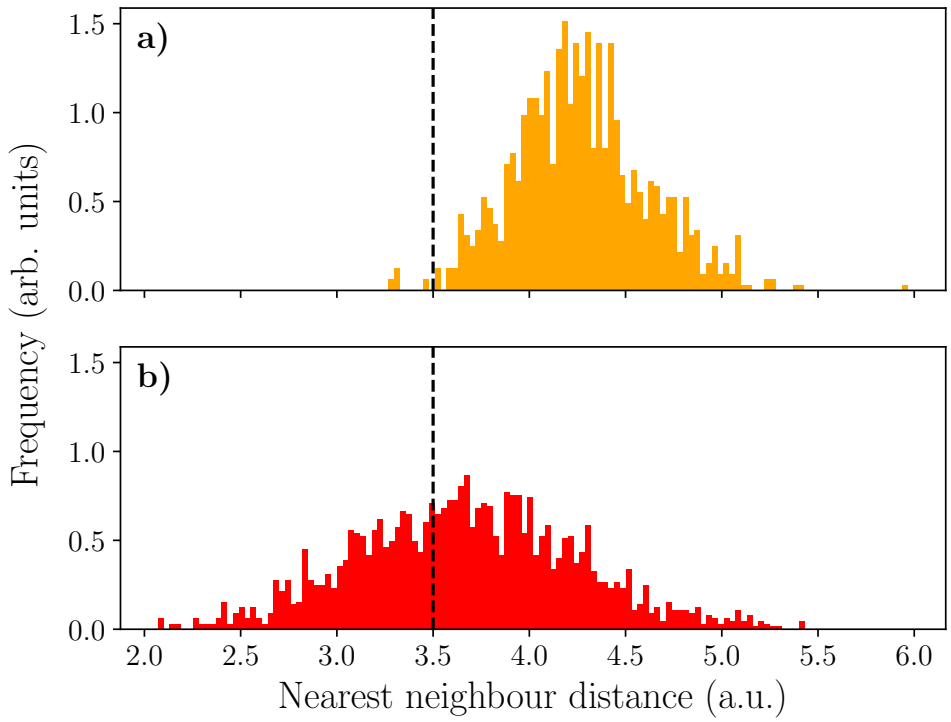

Figure 3.3: A histogram of the interatomic nearest-neighbour distances of multiple snapshots for 2.37 g/cm^3 aluminium equilibrated at various T_{eq}. **a)** $T_{\text{eq}} = 10$ kK. **b)** $T_{\text{eq}} = 100$ kK. The vertical dashed lines represent $2\,r_{\text{core}}$ for the pseudopotential used. The data is normalised such that both histograms contain the same total area.

and ions are in thermal equilibrium, i.e., $T_{\text{i}} = T_{\text{e}}$.

In Fig. 3.3, a histogram of interatomic nearest-neighbour distances from multiple snapshots at a given T_{eq} is plotted. For $T_{\text{eq}} = 10$ kK, only a few of the pseudo-atoms overlap, with the average overlap being relatively small. At $T_{\text{eq}} = 100$ kK, there are now a non-negligible number of $r_{IJ} < 2\,r_{\text{core}}$ separations and the overlap of the frozen cores is severe. The large number of small interatomic nearest-neighbour distances shown here is primarily due to the high temperature: the correspondingly high kinetic energy allows the ions to overcome the core repulsion and move close to their neighbours. Core overlap can also be increased by raising the density.

It is, however, important to note that Fig. 3.3 only plots the nearest-neighbour distances. Fig. 3.4 plots all of the interatomic distances of the ions within the snapshots, and allows one to assess the number of pairs of ions with overlapping cores as a fraction of the total

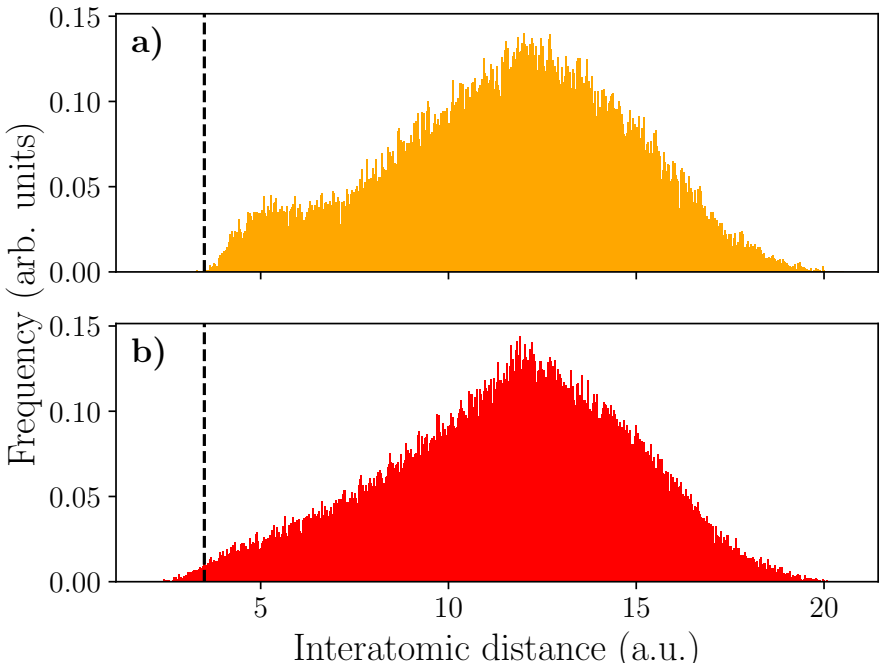

Figure 3.4: A histogram of all of the interatomic distances within multiple snapshots for 2.37 g/cm^3 aluminium equilibrated at various T_{eq}. **a)** $T_{\text{eq}} = 10$ kK. **b)** $T_{\text{eq}} = 100$ kK. The vertical dashed lines represent $2\,r_{\text{core}}$ for the pseudopotential used. The data is normalised such that both histograms contain the same total area.

number of pairs. If the range of pairwise interactions was also known, a better picture of how many of these pairwise interactions actually contribute to the interatomic forces and, consequently, the importance of accurately modelling the interactions from overlapping cores could be found.

Whilst it may seem that these interactions involving the frozen cores will not be accurately represented, due to the fixed approximate nature of the wavefunction and potential within the core radius, it has previously been shown that for low temperature systems, norm-conserving pseudopotential cores can overlap by up to 1 a.u. without affecting calculations of aluminium significantly [114]. It is argued that the continued accuracy may be due to the close matching of the pseudo and all-electron wavefunctions, even within the core radius. The effect of overlapping frozen cores is discussed further in the next section.

3.2.1 Effect of material density

Previous studies, using both PAW [116, 40, 117] and norm-conserving [114, 118] pseudopotentials, have often used the accuracy of the calculated electronic pressure to determine whether a pseudopotential is suitable for use at elevated density. In Fig. 3.5, the pressure of an fcc aluminium lattice with increasing density is shown for two 3e Optimized Norm-Conserving Vanderbilt (ONCV) pseudopotentials from `PseudoDojo` [119], using either the LDA (PZ [64]) or GGA (PBE [65]), along with an 11e ONCV LDA pseudopotential generated locally using `ONCVPSP` [120]. Whilst the convergence and transferability of the 11e pseudopotential have not been thoroughly investigated, its pressure-density curve was compared to that of the well-tested 11e ONCV PBE pseudopotential from the SG15 library [121]. The SG15 and 11e ONCV LDA pressure-density curves are practically indistinguishable, so only the 11e ONCV results are shown in Fig. 3.5.

The predominant difference between the two 11e pseudopotentials is that the SG15 pseudopotentials are generated using the PBE XC functional. A 3e PBE pseudopotential is also plotted to show the expected effects due to the choice of XC potential. The almost exact match of the LDA and PBE 11e pseudopotentials is therefore surprising; however, the difference in the LDA and PBE 3e pseudopotentials may be due to how susceptible they are to errors from overlapping frozen cores. This is evidenced by the similarity between the pressure-density curves generated using the 3e LDA and GGA pseudopotentials at lower density, where core overlap is not a problem.

In Ref. [114], Tambe et al. investigated how changing the number of valence electrons in the Al pseudopotential changed the pressure-density curve. They found that including the 2s and 2p states in the frozen core produced noticeable effects above 1200 GPa, which is in good agreement with Fig. 3.5, even though an ultrasoft 11e pseudopotential was used in that work.

To assess the importance of core overlaps on the accuracy of a pseudopotential, a metric

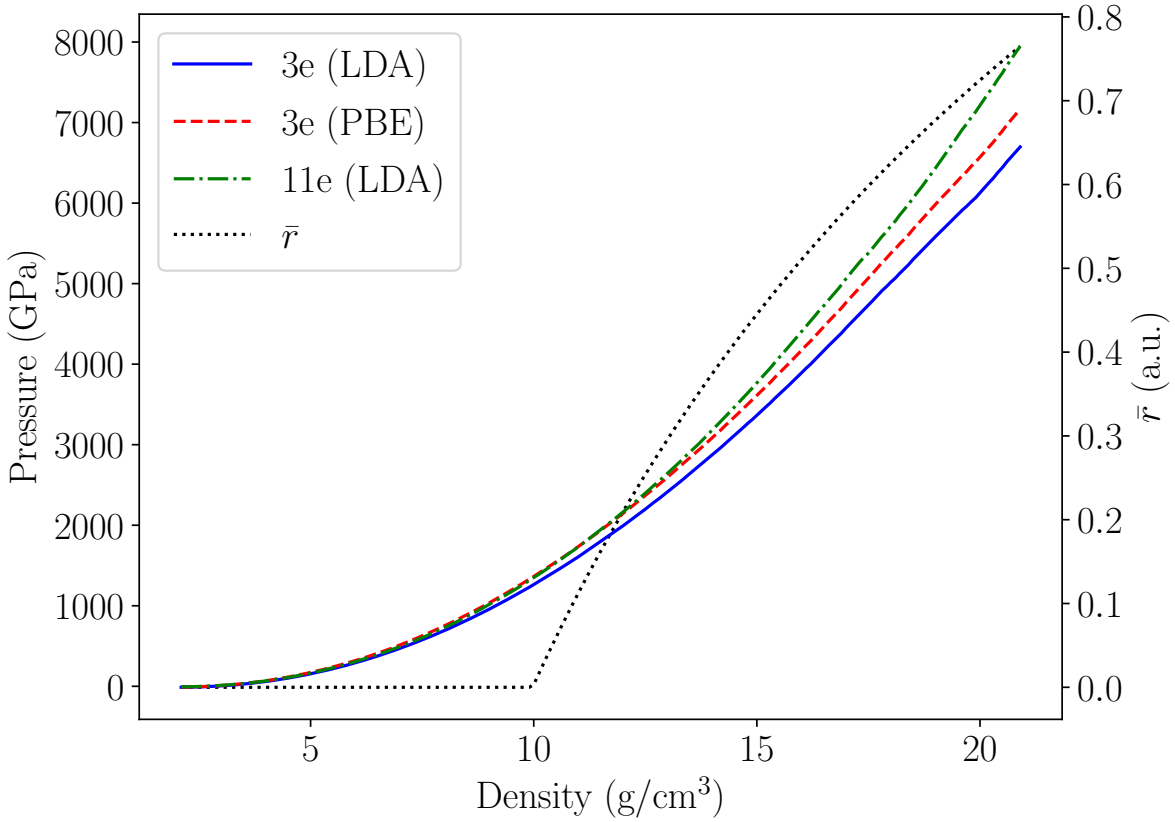

Figure 3.5: Pressure of fcc aluminium at $T_e = 300$ K for varying ρ from DFT calculations performed in `Quantum Espresso`. All pseudopotentials are norm-conserving and produce an equilibrium density of 2.6 g/cm^3 $< \rho_0 <$ 2.8 g/cm^3. The 3e LDA pseudopotential used in this study can be seen to match the more accurate 11e LDA pseudopotential up to around 10 g/cm^3. The dotted black line shows the weighted average size of core overlap for a given density, as defined in Eq. 3.3.

can be defined as

$$\bar{r} = \frac{1}{2N_{IJ}} \sum_{I' \neq J'} 2\, r_{\text{core}} - r_{I'J'}, \tag{3.3}$$

where I' and J' are any pair of atoms whose separation is less than $2\, r_{\text{core}}$ and N_{IJ} is the total number of atomic pairs in the structure. This expression measures the weighted average size of the core overlap for a random pair of atoms in a particular structure. In Fig. 3.5, this metric is plotted on the right-hand axis. The smoothness of the curve is due to the symmetry of the fcc structure used in this convergence test. The divergence in the 3e and 11e pseudopotential pressures aligns well with the overlapping of the frozen cores. This lends credence to the prediction that the main cause of inaccuracies for increasing

density is the overlapping cores.

Assuming that a 3e pseudopotential which predicts accurate pressures in fcc aluminium will also predict accurate energies and forces, the highest densities studied in this thesis ($\rho = 9.67$ g/cm^3) will be at the upper limit of the accurate density range. Here, it has been assumed that the temperature has no effect on the accurate density range; however, this will be investigated in Chapter 8.

To ensure that an fcc lattice can be used to predict the effects of overlapping cores in a stochastic equilibrated configuration of aluminium (which will be referred to in this thesis as a 'snapshot'), the number and severity of overlapping cores in both structures should be similar[2]. In fact, as can be seen in Fig. 3.5, at $\rho = 9.67$ g/cm^3 no cores overlap in the fcc crystal; however, at a slightly higher density of $\rho = 9.97$ g/cm^3 the frozen cores of each atom and its 12 nearest neighbours begin to overlap. This amounts to 11% of the interatomic separations being less than $2\,r_{\mathrm{core}}$. This stepwise increase in the number of overlapping cores is due to the symmetry of the fcc lattice, something that will not be present in the snapshots.

For an average $\rho = 9.67$ g/cm^3 snapshot equilibrated at a temperature between 10-100 kK, the fraction of overlapping cores is approximately 4%. This fraction has only a slight dependence on equilibration temperature for this density. Since the volume per atom should be approximately equal in the $\rho = 9.97$ g/cm^3 fcc crystal and $\rho = 9.67$ g/cm^3 snapshots, the severity of the core overlaps will therefore be greater in the snapshots (in fact, the fcc 'overlapping' cores are only touching at this density).

As discussed above, pseudopotentials with slightly overlapping cores can still produce accurate results. This is observed in Fig. 3.5, as the 3e pseudopotential pressure is not immediately inaccurate at $\rho = 10$ g/cm^3, but rather gradually becomes worse as the over-

[2]In fact, a few snapshots with densities higher than this are used in the training of the ACE potential in Chapter 6. Although there is no reason to expect these snapshots to produce accurate data, these are included to ensure that small interatomic separations are qualitatively correct and do not produce spurious anomalies in the final fit. MHKS-DFT data from densities higher than 10 g/cm^3 are only used for comparison in the equation of state in Chapter 8, and the effects of using a 3e pseudopotential to simulate high densities are discussed there.

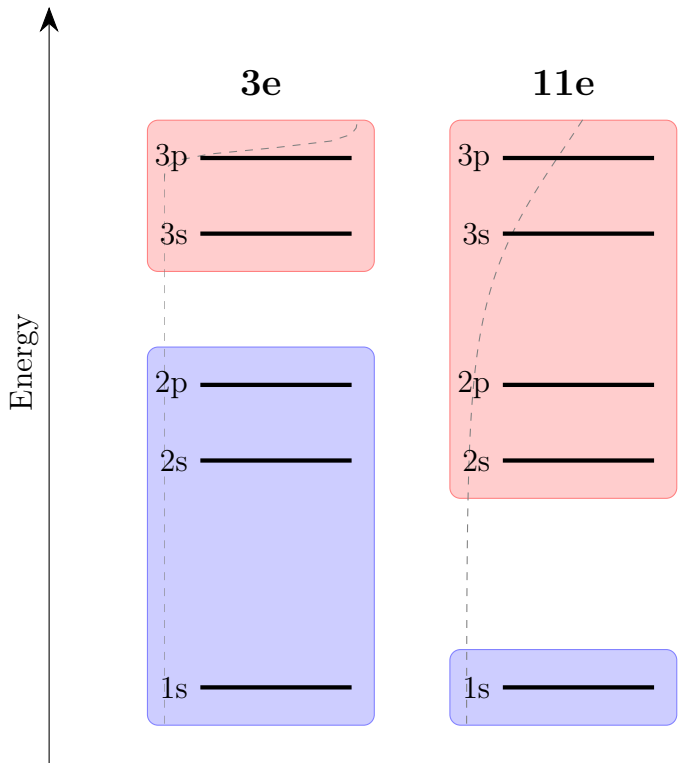

Figure 3.6: A pictorial representation of a 3e and 11e aluminium pseudopotential. The blue boxes represent the states that are frozen in the pseudopotential. The red boxes represent the valence states that are explicitly treated by the electron density n. The dashed grey lines show Fermi-Dirac distributions f for which the respective pseudopotentials should be used. States for which $f < 1$ will incur some thermal depopulation with the electrons excited into higher energy states. If the thermally depopulated state is in the frozen core, the pseudopotential will not be able to accurately describe the excitation.

lapping of the cores becomes more severe. Whether the fewer, more severely overlapping cores of the high density snapshots will affect the accuracy of the calculated properties more than the many, small overlaps of the fcc systems at a similar density is an open question.

3.2.2 Effect of electronic temperature

In theory, a finite-temperature pseudopotential should be used in any simulation of warm dense matter where the ionisation of the core electrons is expected to be non-negligible. A finite-temperature pseudopotential should incorporate temperature effects arising from both the electronic and ionic temperatures, with ionisation of the core electrons properly modelled. However, finite-temperature psuedopotentials are rare and not commonly used

[122]; instead, pseudopotentials with fewer frozen-core electrons, but no explicit temperature dependence, are used for increasing electron temperature, until it is necessary to use an all-electron pseudopotential [47].

Rather than approximating the temperature dependence of the core electrons as an explicit function of temperature, as would be achieved by a finite-temperature pseudopotential, a pseudopotential with fewer frozen-core electrons simply increases the number of valence electrons that are explicitly treated by the Kohn-Sham orbitals. The temperature-induced ionisation of the core electrons then arises naturally from the smearing of the Fermi-Dirac distribution. At $T_\mathrm{e} = 0$ K, the highest frozen-core energy eigenvalue (2p) in the 3e LDA pseudopotential is -70 eV. At $T_\mathrm{e} = 100$ kK ≈ 8 eV, the highest temperature of interest in the warm dense regime, and assuming the temperature dependence of the eigenvalues is negligible, the thermal depopulation of the 2p eigenvalue is approximately 3×10^{-4} [101]. For the purposes of this thesis, and taking into account both the other approximations made (e.g. simulating a liquid in a periodic unit cell) and the computational limitations present, this level of core excitation should be acceptable; however, for higher temperatures, or the study of properties that require a very strict convergence with respect to the number of orbitals, an 11e (or all-electron) pseudopotential should be used. The effect of thermal ionisation on the accuracy of the frozen core approximation is shown in Fig. 3.6.

To investigate the suitability of a 3e pseudopotential for simulating WDM, the pressure of fcc aluminium as the electronic temperature is increased is plotted in Fig. 3.7. At the highest temperature of 100 kK, the difference between the 3e and 11e pseudopotentials is 3%. As in Fig. 3.5, the LDA and PBE 11e pseudopotentials are practically indistinguishable. The pressure difference is therefore assumed to arise from the different number of frozen-core electrons in each pseudopotential. Comparing with Fig. 3.5, the effects from temperature ionisation are small compared to those from pseudopotential core overlaps. As mentioned previously, the severity of the temperature ionisation effects may change with the density, and this will be studied further in Chapter 8.

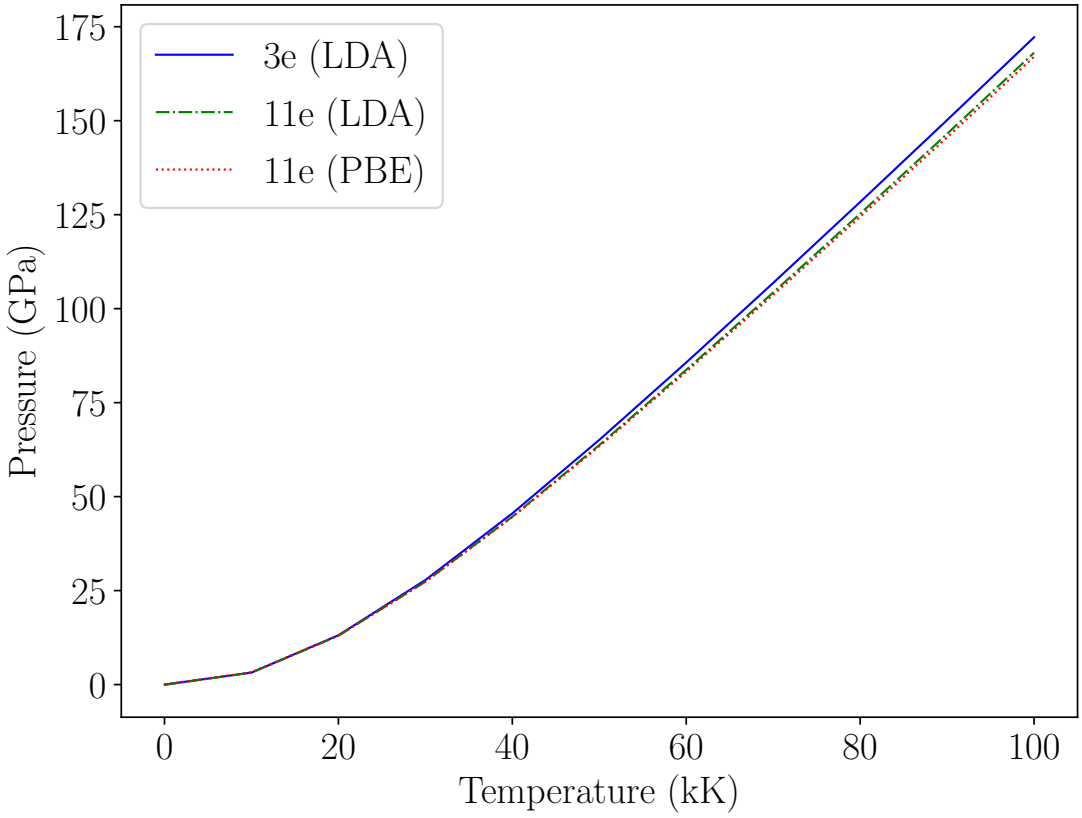

Figure 3.7: Pressure of fcc aluminium for varying T_e from DFT calculations performed in `Quantum Espresso`. All pseudopotentials are norm-conserving and the structures were relaxed such that the pressure is zero for zero temperature. This produced an equilibrium density within the range 2.6 g/cm^3 $< \rho_0 <$ 2.8 g/cm^3.

Throughout this thesis, unless stated otherwise, the 3e aluminium ONCV LDA pseudopotential will be used with a minimum plane-wave cutoff of 60 Ry, such that the total free energies are converged to within 0.01% at all temperatures. Although the use of a pseudopotential with fewer frozen core electrons and a smaller core cutoff radius r_{core} would be preferable at higher electronic temperatures and material densities, current computational limitations prevent this.

For the 3e pseudopotential, the required plane-wave cutoff for convergence was found to be independent of the electronic temperature for the temperatures investigated here. A few calculations used a higher plane-wave cutoff of 100 Ry, but this is not expected to affect any of the results. The densities investigated will be limited to a maximum of 10

g/cm^3 and the temperatures to a maximum of 100 kK. This allows for the study of a large portion of the warm dense regime of aluminium, whilst balancing computational issues and excessive errors.

3.3 Non-Local Free Energy Functionals

Local (Thomas-Fermi) and semi-local (VT84F) non-interacting free energy functionals have previously been implemented in `PROFESS@QE` and were introduced earlier in Section 2.6. Here, a non-local functional is discussed and implemented in `PROFESS@QE` to allow for the comparison of the three different levels of functional approximation.

SDF [123] is a non-local functional for the non-interacting free energy formulated such that the density-density response,

$$\chi_0(\mathbf{r}-\mathbf{r}',T,n_0) = -\left(\left.\frac{\delta^2 F_{\mathrm{s}}([n],T)}{\delta n(\mathbf{r})\delta n(\mathbf{r}')}\right|_{n_0}\right)^{-1}, \tag{3.4}$$

of the non-interacting homogeneous electron gas with the same average electron density n_0 reproduces the exact Lindhard density-density response [124]. The non-interacting free energy is expressed as

$$F_{\mathrm{s}}^{\mathrm{SDF}}([n],T) = F_{\mathrm{TF}}([n],T) + {}_{\beta}F_{\mathrm{vW}}([n],T) + F_{a,b}([n],T), \tag{3.5}$$

with F_{TF} the finite-temperature Thomas-Fermi free energy functional defined in Eq. 2.57, ${}_{\beta}F_{\mathrm{vW}}$ the von Weizsäcker gradient correction, which has been altered to prevent infinitely negative energies in the large q limit [125], and $F_{\mathrm{a,b}}$ the finite-temperature extension of the non-local Wang and Teter functional [126]. The non-local von Weizsäcker free energy is defined as

$${}_{\beta}F_{\mathrm{vW}}([n],T) = \frac{1}{2}\int\int \mathrm{d}\mathbf{r}\,\mathrm{d}\mathbf{r}'\,\left[\left(\nabla n^{1/2}(\mathbf{r})\right)\cdot\left(\nabla n^{1/2}(\mathbf{r}')\right)\right]\times\left[\delta(\mathbf{r}-\mathbf{r}')+\beta(|\mathbf{r}-\mathbf{r}'|,T)\right], \tag{3.6}$$

and the non-local free energy is defined as

$$F_{a,b}([n],T) = \int\int \mathrm{d}\mathbf{r}\,\mathrm{d}\mathbf{r}'\, n^a(\mathbf{r}) w(|\mathbf{r}-\mathbf{r}'|,T) n^b(\mathbf{r}'), \tag{3.7}$$

with $\beta(|\mathbf{r}-\mathbf{r}'|,T)$ and $w(|\mathbf{r}-\mathbf{r}'|,T)$ kernels discussed later.

The SDF functional is the most recent of the functionals studied here and was not available in PROFESS. Therefore, PROFESS@QE was extended to allow for the calculation of energies, forces, and pressures using the SDF functional. This first required implementing the finite-temperature Lindhard function, which in reciprocal space takes the form [124]

$$\tilde{\chi}_0(q,T,n_0) = \int_0^\infty \mathrm{d}E\, \frac{\tilde{\chi}_0(q,T=0,n_0)|_{E_\mathrm{F}=E}}{4k_\mathrm{B}T\cosh^2\left(\frac{E-\mu(T)}{2k_\mathrm{B}T}\right)}, \tag{3.8}$$

with q the magnitude of a wavevector, and the zero-temperature Lindhard function is defined as

$$\tilde{\chi}_0(q,T=0,n_0) = -\frac{k_\mathrm{F}}{\pi^2}\left[\frac{1}{2} + \frac{1-\nu}{4\nu}\ln\left|\frac{1+\nu}{1-\nu}\right|\right], \tag{3.9}$$

where $\nu = q/(2k_\mathrm{F})$ is a dimensionless wavevector and $k_\mathrm{F} = (3\pi^2 n_0)^{1/3}$.

The Thomas-Fermi response function is well known:

$$\tilde{\chi}_\mathrm{TF}(T) = -\frac{1}{2\pi^2}\left(\frac{2}{\beta}\right)^{1/2} I_{-1/2}(\beta\mu_0), \tag{3.10}$$

with $\mu_0 = \left.\frac{\delta F_\mathrm{TF}([n],T)}{\delta n}\right|_{n_0}$ the non-interacting chemical potential and where the explicit dependence on n_0 has been dropped for readability. The standard von Weizsäcker response function can be easily found from $\tilde{\chi}_\mathrm{TF}$ [127]; however, fixing the large q behaviour of the SDF functional requires adding a non-linearity to the von Weizsäcker term, leading to a response function of the form

$$\tilde{\chi}_\mathrm{vW}(q,T) = -\frac{4k_\mathrm{F}^3}{3\pi^2 q^2}\left(\frac{1}{1+\tilde{\beta}(q,T)}\right), \tag{3.11}$$

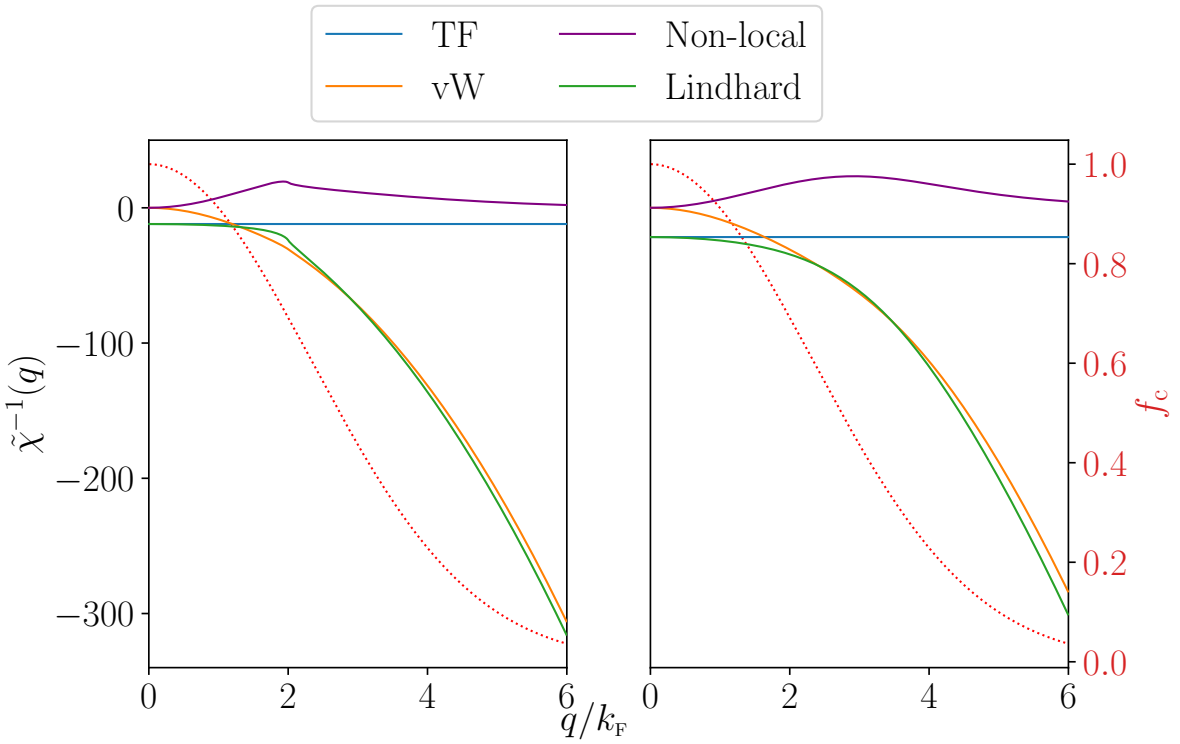

Figure 3.8: The inverse of response functions at $T = 0$ K (left) and $T = 100$ kK (right). The Thomas-Fermi response gives the correct behaviour in the small q limit, whilst the standard semi-local von Weizsäcker response (not shown) gives the correct behaviour in the large q limit. For $T = 0$ K, there is a discontinuity in the Lindhard function at $q = 2k_\mathrm{F}$ due to the logarithm in Eq. 3.9. The cutoff function, Eq. 3.13, is shown by the red dotted line.

where $\tilde{\beta}(q,T)$ is the von Weizsäcker kernel, chosen to have the form

$$\tilde{\beta}(q,T) = (f_\mathrm{c}(q) - 1)\frac{-\tilde{\chi}_0^{-1}(q,T) + \tilde{\chi}_\mathrm{TF}^{-1}(T) + \tilde{\chi}_\mathrm{vW}^{-1}(q,T)}{\tilde{\chi}_\mathrm{vW}^{-1}(q,T)}, \tag{3.12}$$

with the cutoff function

$$f_\mathrm{c}(q) = \exp\left[-q^2/(16k_\mathrm{F}^2)\right], \tag{3.13}$$

to ensure that the non-local kernel $\tilde{w}(q,T)$ tends to zero at large q. Note that the symbol β standing alone represents the inverse temperature, while the symbol β followed by parentheses expressing dependence on a real space vector $\mathbf{r}$ or reciprocal space vector $\mathbf{q}$ stands for the von Weizsäcker kernel. For completeness, the non-local response function can be defined as

$$\tilde{\chi}_{a,b}(q,T) = -\left[2abn_0^{(a+b-2)}\tilde{w}(q,T)\right]^{-1}; \tag{3.14}$$

however, what is actually needed to calculate $F_{a,b}$ is the non-local kernel

$$\tilde{w}(q,T) = f_c(q)\frac{-\tilde{\chi}_0^{-1}(q,T) + \tilde{\chi}_{\mathrm{TF}}^{-1}(T) + \tilde{\chi}_{\mathrm{vW}}^{-1}(q,T)}{2abn_0^{a+b-2}}. \tag{3.15}$$

The various inverses of the response functions $\tilde{\chi}^{-1}$ at zero temperature and 100 kK are shown in Fig. 3.8.

To calculate $I_{-1/2}$, the Fermi integral of order $-\frac{1}{2}$, the Fortran 90 implementation by Fukushima [128] was used, and `QUADPACK` [129] was used to solve the semi-infinite integral in Eq. 3.8. The $\tilde{w}$ and $\tilde{\beta}$ kernels calculated using my implementation of the SDF functional agreed with the figures from the supplementary material of Ref. [123].

The SDF functional has shown good agreement with MHKS-DFT properties at both zero temperature and warm dense conditions [123], and was used to investigate transport properties in warm dense hydrogen and aluminium [17]. The accuracy of the functional is shown to be better than that of the local VT84F functional in Section 6.6.

3.4 Extended First-Principles Molecular Dynamics

A recent method that aims to speed up high temperature MHKS-DFT calculations, without sacrificing the accuracy gained from using the auxiliary Kohn-Sham system, is the extended first-principles molecular dynamics (extended FPMD) model [37]. The extended FPMD model uses the fact that the KS orbitals from Eq. 2.72 approximate single plane waves when the one-electron eigenvalue is high and that their density of states is similar to that of a shifted Fermi gas. The sum over discrete high energy levels in a traditional MHKS-DFT calculation is then replaced by an analytic integral over the density of states, which significantly reduces the size of the matrix of orbitals and speeds up calculations at higher temperature.

The shifted density of states of a Fermi gas is given by

$$D(\varepsilon) = \frac{\sqrt{2}\Omega}{\pi^2}\sqrt{\varepsilon - U_0}, \tag{3.16}$$

where Ω is the volume of the unit cell and U_0 is a constant shift. Three different methods of determining U_0 have been suggested [130] and will be presented here. The first way to evaluate U_0 is as the average of the difference in eigenvalues ε and kinetic energy ε^{K},

$$U_0^{\mathrm{K}} = \frac{1}{\Delta N}\sum_{n=(N_c-\Delta N)}^{N_c}\sum_{\mathbf{k}}\omega_{\mathbf{k}}\left(\varepsilon_{\mathbf{k},n} - \varepsilon^{\mathrm{K}}_{\mathbf{k},n}\right), \tag{3.17}$$

over the ΔN highest energy orbitals, where N_c is the highest energy orbital explicitly treated by MHKS-DFT, n indexes the orbitals, and $\omega_{\mathbf{k}}$ is the weight of sampling point $\mathbf{k}$. The second way to evaluate U_0 replaces the kinetic energy by the Fermi energy $\varepsilon^{\mathrm{F}}_n$ in Eq. 3.17,

$$U_0^{\mathrm{K}} = \frac{1}{\Delta N}\sum_{n=(N_c-\Delta N)}^{N_c}\sum_{\mathbf{k}}\omega_{\mathbf{k}}\left(\varepsilon_{\mathbf{k},n} - \varepsilon^{\mathrm{F}}_{n}\right). \tag{3.18}$$

The final method evaluates U_0 as the average of the MKS effective potential V_{eff} over the unit cell,

$$U_0^{V} = \frac{1}{\Omega}\int \mathrm{d}\mathbf{r} V_{\mathrm{eff}}(\mathbf{r}). \tag{3.19}$$

The standard MHKS-DFT expressions for free energies, internal energies, entropies, and forces then consist of a discrete sum over low energy states plus an integral over the high energy density of states; for example, the non-interacting entropy (cf. Eq. 2.37) is calculated as

$$\begin{aligned} S_{\mathrm{s}} = &- k_{\mathrm{B}}\sum_{j=1}^{N_{\mathrm{c}}}\{f_j \ln f_j + (1-f_j)\ln(1-f_j)\} \\ &- k_{\mathrm{B}}\int_{E_{\mathrm{c}}}^{\infty}\mathrm{d}\varepsilon\, D(\varepsilon)\{f_j \ln f_j + (1-f_j)\ln(1-f_j)\}, \end{aligned} \tag{3.20}$$

with N_{c} the index of the highest energy explicit Kohn-Sham orbital and E_{c} its respective energy.

Testing of the extended FPMD method was performed in `Quantum Espresso` Version 6, which required adaptation of the Version 5 patch produced by Zhang et al. [37] to work with the updated modules present in Version 6. Version 5 of `Quantum Espresso` could not be used for the calculations in this thesis due to the lack of support for finite-temperature XC functionals. Each time the extended FPMD method was used, a convergence test for ΔN and N_c was first performed such that the free energies, forces and pressures generated were consistent with those from converged calculations using standard MHKS-DFT.

Whilst the extended FPMD method provides access to arbitrarily high electronic temperatures (albeit with a larger prefactor), molecular dynamics simulations of large systems are still computationally intractable due to the poor scaling with system size, given by Eq. 2.90. The extended FPMD method, therefore, is not a suitable technique for simulating ablation dynamics or other behaviours that require more than a few hundred atoms in a unit cell.

3.5 Summary

In this chapter, various improvements for the study of WDM using the finite-temperature DFT method have been discussed and implemented.

FTXC functionals were introduced as the finite-temperature generalisation of the more commonly used ZTXC functionals. Whilst the finite-temperature XC effects are negligible for many systems, those with a reduced temperature $\theta \approx 1$, often found in WDM, can show noticeable discrepancies in the calculated properties when using FTXC and ZTXC functionals. The implementation of two FTXC functionals in `Quantum Espresso` was fixed to ensure finite-temperature exchange-correlation effects are properly accounted for in the WDM simulations presented later in this thesis.

The use of pseudopotentials at finite temperature was investigated, with limits placed on the material density and temperature at which they should be used. As at zero temperature, a balance must be struck between the accuracy of calculated properties

and computational efficiency. A pseudopotential with fewer frozen core electrons and a smaller r_{core} allows for the accurate simulation of systems with higher densities and temperatures; however, the increased number of KS orbitals and plane-wave coefficients can make MHKS-DFT calculations inefficient in all but the smallest systems.

A recent non-local free energy functional (SDF) for the non-interacting free energy in OF-DFT was introduced. It was implemented in `PROFESS@QE` and allows for the comparison of local, semi-local, and non-local approximations for the non-interacting free energy. The accuracy of the method will be investigated further in Section 6.6.

Finally, a MHKS-DFT method that scales independently of temperature was detailed. The extended FPMD method approximates the high energy orbitals by a shifted Fermi gas, allowing for arbitrarily high temperatures to be simulated with no added cost. However, the poor scaling with system size limits the use of the method to small periodic systems, preventing the simulation of large-scale WDM systems using the method.

Chapter 4

Interatomic Potentials

One of the simplest models of interatomic forces is an empirical interatomic potential, such as the Lennard-Jones potential [131] shown in Fig. 4.1. Interatomic potentials are, in theory, an attempt to integrate out the electronic degrees of freedom of a system such that it can be described by only the ionic positions (and potentially a few other parameters). This vastly reduces the number of degrees of freedom of the problem, but sometimes misses important aspects of the physics within a system.

Interatomic potentials are generally fit to DFT or experimental data with the aim of being transferable to different systems and environments. Whilst their relatively simple form significantly speeds up complex calculations, it also limits their use to specific situations. For instance, the Lennard-Jones potential works well for noble gases [132], where dispersion forces dominate, but predicts an hcp structure for the noble gas solids, which is inconsistent with the experimentally observed fcc structure of Ne, Ar, and Kr [133]. Moreover, the elastic constants of any material with a cubic crystal structure and modelled using a pair potential must obey the Cauchy relation $C_{12} = C_{44}$ [134]; however, the elastic constants of most real materials do not.

Pair potentials can, though, produce important insight into interactions and accurately describe some systems, such as plasmas [135]. It is therefore important to analyse the trade-offs between efficiency and accuracy of the various approaches and approximations

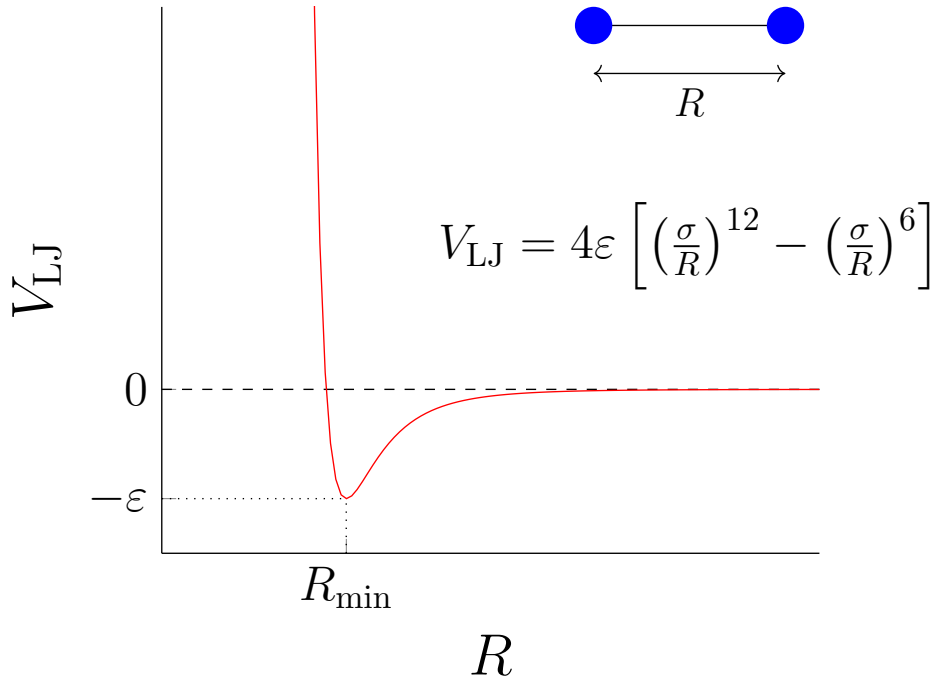

Figure 4.1: The Lennard-Jones potential. The two blue circles represent particles at a distance R with a pairwise interaction. The Lennard-Jones potential has a minimum energy of $-\varepsilon$ at $R_{\mathrm{min}} = 2^{1/6}\sigma$. As $R \to \infty$, the potential $V_{\mathrm{LJ}} \to 0$.

for interatomic potentials (pairwise or not) used to simulate warm dense matter under different conditions.

To this end, the interatomic forces calculated using an interatomic potential should be compared with those from an *ab initio* method that explicitly calculates the electronic effects. A comparison can also be made for any other property that the empirical potential should accurately reproduce. Whilst most *ab initio* methods cannot be used for system sizes much more than a few thousand electrons, they provide relatively accurate results to contrast against and are commonly used to fit interatomic potentials as it is much easier to generate large quantities of simulation data than experimental data. Furthermore, simulations provide access to variables that cannot be measured experimentally, such as entropy.

This chapter will begin by exploring what an interatomic potential aims to approximate, particularly at finite temperature. Then, previously developed finite-temperature interatomic potentials will be introduced and their strengths and weaknesses for simulating WDM will be discussed.

4.1 Finite-T Interatomic Forces

For a system of ions with zero electronic temperature, the interatomic forces $\boldsymbol{\mathcal{F}}$ are calculated as the derivatives of the internal energy U (see Section 2.5),

$$\boldsymbol{\mathcal{F}}_\alpha = -\frac{\partial U(\mathbf{R})}{\partial \mathbf{R}_\alpha}, \tag{4.1}$$

with $\mathbf{R}_\alpha$ the ionic position of ion α, $\mathbf{R} = (\mathbf{R}_1, \mathbf{R}_2, \dots)$ the set of all ionic positions, and U the internal energy of the system for a fixed set of ionic positions. These forces are often used in the integration of the equations of motion for the ions during a molecular dynamics simulation. Importantly, this assumes the electronic subsystem is at zero temperature, which, while not strictly true in any molecular dynamics simulation (at zero temperature the ions would not move), is generally a good approximation for up to a few thousand Kelvin.

For finite electronic temperature, a contribution from the electronic entropy must be added. A free energy is therefore used, rather than an internal energy. This free energy is given by

$$F = F_\mathrm{e} + U_\mathrm{i} = U_\mathrm{e} - T_\mathrm{e} S_\mathrm{e} + U_\mathrm{i}, \tag{4.2}$$

where the subscripts 'e' and 'i' indicate electronic and ionic terms, respectively, and U_i does not contain a contribution from the ionic kinetic energy due to the fixed ionic positions. This is not the total free energy, as the ionic kinetic energy and entropy are missing, but rather the free energy for a fixed set of ionic positions.

The finite-temperature interatomic forces are then calculated as

$$\boldsymbol{\mathcal{F}}_\alpha = -\frac{\partial F}{\partial \mathbf{R}_\alpha}. \tag{4.3}$$

The motion of the ions under these forces reproduces the thermodynamics of the full electron-ion system at finite electronic temperature, just as the forces derived from the internal energy reproduce the thermodynamics at zero electronic temperature. The aim

of a finite-temperature interatomic potential is to accurately predict F, and therefore the interatomic forces, given an approximate functional form.

Statistical mechanics can be used to give a different perspective on what an interatomic potential is trying to approximate. The partition function contains all of the statistical information required to describe a specific system in a chosen ensemble, and can be used to calculate thermodynamic properties. For a system of electrons and ions, with the ions treated classically and the electronic eigenstates obtained for fixed ionic positions within the Born-Oppenheimer approximation, the partition function can be written as

$$Z(\beta) = \int \mathrm{d}\mathbf{P}\mathrm{d}\mathbf{R} \sum_j \left\langle \Psi_j \middle| \exp\left[-\beta\left(\hat{H}_\mathrm{e}(\mathbf{R}) + U_\mathrm{i}(\mathbf{R}) + \frac{\mathbf{P}^2}{2M}\right)\right] \middle| \Psi_j \right\rangle, \tag{4.4}$$

with $\hat{H}_\mathrm{e}$ the electronic Hamiltonian, $|\Psi_j\rangle$ a normalised electronic eigenstate, and $\mathbf{P} = (\mathbf{P}_1, \mathbf{P}_2, \dots)$ the set of all ionic momenta. Comparing with Eq. 2.48, the partition function of the electronic subsystem, Eq. 4.4 also contains the integral over all possible states of the ionic subsystem.

By defining the effective potential experienced by the ions F_el as

$$\exp[-\beta F_\mathrm{el}(\mathbf{R}, \beta)] = \sum_j \left\langle \Psi_j \middle| \exp\left[-\beta \hat{H}_\mathrm{e}(\mathbf{R})\right] \middle| \Psi_j \right\rangle, \tag{4.5}$$

the canonical partition function can be written

$$Z(\beta) = \int \mathrm{d}\mathbf{P}\mathrm{d}\mathbf{R} \exp\left[-\beta\left(F_\mathrm{el}(\mathbf{R}, \beta) + U_\mathrm{i}(\mathbf{R}) + \frac{\mathbf{P}^2}{2M}\right)\right], \tag{4.6}$$

where it can be seen that $F_\mathrm{el} = U_\mathrm{e} - TS_\mathrm{e}$ from Eq. 4.2. The effective potential experienced by the ions $F_\mathrm{el} + U_\mathrm{i}$ describes the electronic degrees of freedom, as well as the ionic electrostatics. The explicit dependence of F_el on the (inverse) temperature β is due to the finite-temperature electronic effects. The ionic positions $\mathbf{R}$ then evolve according to $F_\mathrm{el} + U_\mathrm{i}$.

An interatomic potential, or *ab initio* method, aims to approximate the true behaviour of

F_{el} regarded as a function of the ionic positions $\mathbf{R}$ and inverse temperature β. Generally, interatomic potentials ignore the electronic-temperature dependence in their functional form, $F_{\mathrm{el}}(\mathbf{R}, \beta) \approx F_{\mathrm{el}}(\mathbf{R})$; however, this approximation breaks down for any system where the electronic excitations are severe enough to alter the forces on the ions significantly. This is the case for the high electronic temperatures encountered in the warm dense regime.

Before introducing examples of finite-temperature interatomic potentials, it is worth discussing the physical interpretation of the interatomic forces defined by the thermodynamic method above along with the various ways that the interatomic forces at finite temperature can be calculated. In the above, the ions are treated classically and the electrons quantum mechanically within the Born-Oppenheimer approximation. A true thermodynamic ensemble for this mixed quantum-classical system would include realisations of the system with the electrons in different quantum states and the classical ions in different positions. Even if the ionic positions were constrained to a particular configuration $\mathbf{R}$, there would be different realisations with different electronic states. The interatomic forces found in each of the realisations would then differ. Therefore, there is no such thing as a 'true' interatomic force, only averages over the possible electronic states for a given set of $\mathbf{R}$.

The interatomic forces calculated from F_{el}, as defined above, are uniquely determined by the set of ionic positions $\mathbf{R}$. There will therefore be no fluctuation in the forces arising from the different possible electronic quantum states; however, if the forces calculated from F_{el} are used in an ergodic molecular dynamics simulation, the ensemble of ionic positions obtained reproduces the true quantum-classical partition function. Since the interatomic forces are fixed for a given set of $\mathbf{R}$, their measurement in any ensemble should be equivalent. Although it has been argued earlier that the same thermal-equilibrium density will be found when minimising the grand canonical potential Ω or the Helmholtz free energy F using DFT, it can further be shown that the interatomic forces in all ensembles are identical at electronic equilibrium.

The grand canonical potential can be defined as the Legendre transform of the Helmholtz free energy,

$$\Omega_{\mathrm{el}}(\mu,\lambda) = \min_{N} \left(F_{\mathrm{el}}(N,\lambda) - \mu N \right), \tag{4.7}$$

with N the number of electrons, μ the chemical potential, λ a parameter that all thermodynamic potentials have a dependence on, and Ω_{el} the grand canonical equivalent of F_{el}. The dependence of Ω_{el} and F_{el} on the volume V and temperature T has been dropped for simplicity. At the N for which $F_{\mathrm{el}}(N,\lambda) - \mu N$ is minimised,

$$\left(\frac{\partial F_{\mathrm{el}}}{\partial N}\right)_{\lambda} - \mu = 0. \tag{4.8}$$

Expanding F_{el} using the chain rule leads to

$$\mathrm{d}F_{\mathrm{el}} = \left(\frac{\partial F_{\mathrm{el}}}{\partial N}\right)_{\lambda} \mathrm{d}N + \left(\frac{\partial F_{\mathrm{el}}}{\partial \lambda}\right)_{N} \mathrm{d}\lambda, \tag{4.9}$$

and dividing both sides by $\mathrm{d}\lambda$, whilst holding μ constant, gives

$$\left(\frac{\partial F_{\mathrm{el}}}{\partial \lambda}\right)_{\mu} = \left(\frac{\partial F_{\mathrm{el}}}{\partial N}\right)_{\lambda} \left(\frac{\partial N}{\partial \lambda}\right)_{\mu} + \left(\frac{\partial F_{\mathrm{el}}}{\partial \lambda}\right)_{N}. \tag{4.10}$$

An expression for the derivative of Ω_{el} can be found using Eqs. 4.7 and 4.10,

$$\begin{aligned}
\left(\frac{\partial \Omega_{\mathrm{el}}}{\partial \lambda}\right)_{\mu} &= \left(\frac{\partial F_{\mathrm{el}}(N,\lambda) - \mu N}{\partial \lambda}\right)_{\mu} \\
&= \left(\frac{\partial F_{\mathrm{el}}}{\partial N}\right)_{\lambda} \left(\frac{\partial N}{\partial \lambda}\right)_{\mu} + \left(\frac{\partial F_{\mathrm{el}}}{\partial \lambda}\right)_{N} - \mu \left(\frac{\partial N}{\partial \lambda}\right)_{\mu} \\
&= \underbrace{\left[\left(\frac{\partial F_{\mathrm{el}}}{\partial N}\right)_{\lambda} - \mu\right]}_{0} \left(\frac{\partial N}{\partial \lambda}\right)_{\mu} + \left(\frac{\partial F_{\mathrm{el}}}{\partial \lambda}\right)_{N} \\
&= \left(\frac{\partial F_{\mathrm{el}}}{\partial \lambda}\right)_{N},
\end{aligned} \tag{4.11}$$

where the first term in the penultimate line is equal to zero, from Eq. 4.8. By substituting λ for an ionic position $\mathbf{R}_{\alpha}$, the interatomic forces are found.

An analogous expression for the interatomic forces as derivatives of the internal energy

U_{el} in the microcanonical ensemble can be found by expressing $F_{\mathrm{el}}(T)$ as a Legendre transform of $U_{\mathrm{el}}(S)$. This leads to the expected result that the interatomic forces derived using the thermodynamic method above (such that these 'mean' forces can be thought of as ensemble averages of the forces calculated for each electronic quantum state with a given $\mathbf{R}$) are independent of the ensemble that they are measured in. Importantly, though, in the microcanonical ensemble the forces are calculated at constant entropy S, rather than constant T. In theory, an isentropic derivative of U_{el} would give the correct interatomic forces at finite temperature; however, there is no simple way to calculate this, especially in methods such as DFT that fix the temperature rather than the entropy. When also taking into account the issues involved with allowing a fluctuating number of electrons N (see Section 2.7), the derivatives of F_{el} are generally used to evaluate finite-temperature interatomic forces.

4.2 Previous Finite-T Interatomic Potentials

The vast majority of interatomic potentials make the assumption of constant electronic temperature. This can either be zero temperature or some finite temperature around which the potential is to be used. For most purposes, this approximation works well. For instance, a zero electronic temperature potential may be used to study the melting of a solid when ionic effects, such as lattice defects, dominate the phase transition. Using a constant electronic temperature potential to simulate this phase transition is satisfactory as long as the change in the electronic structure and interatomic forces between zero temperature and the melting temperature are negligible. This is true for many simple materials, such as aluminium [21].

For the purpose of simulating the transition from room temperature to WDM, as might occur in a laser-irradiated thin film or the walls of a nuclear fusion reactor, the energies and forces at both low and high temperature must be accurately modelled. Furthermore, a consistent scheme must be devised to allow for the evaluation of energies and forces over

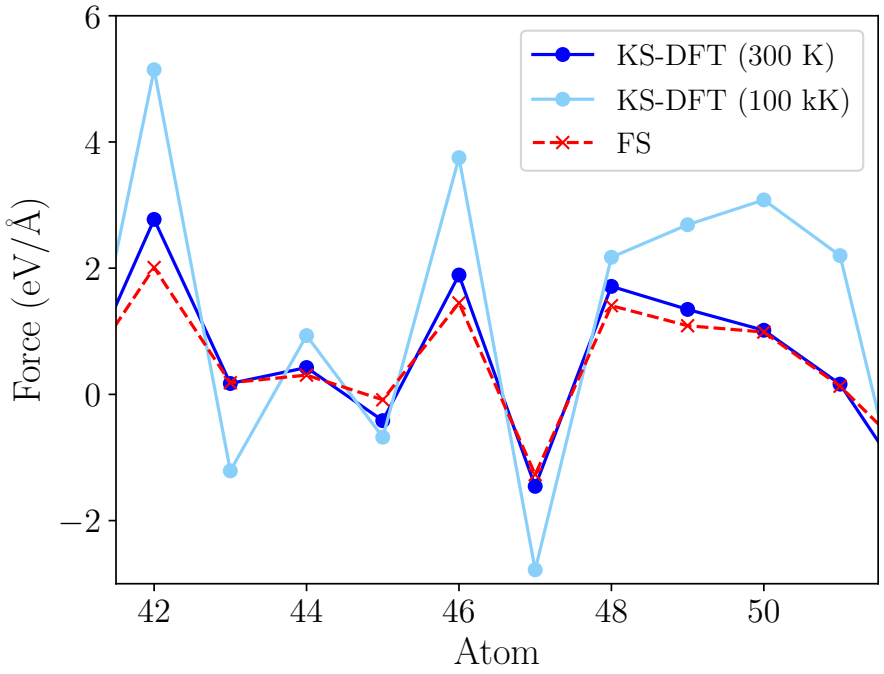

Figure 4.2: The force along the x-axis of a random sample of atoms within a 108 aluminium atom snapshot equilibrated at 10 kK and $\rho = 2.37$ g/cm^3. The dark blue solid lines show the forces predicted by a converged Kohn-Sham calculation with $T_e = 300$ K, the light blue solid lines show the forces predicted by a converged Kohn-Sham calculation with $T_e = 100$ kK, and the dashed red lines show the forces predicted by a zero temperature Finnis-Sinclair potential [136]. The Finnis-Sinclair potential shows qualitative matching with the $T_e = 300$ K MHKS-DFT forces for all atoms, as expected for a potential intended for use up to the melting point. However, the Finnis-Sinclair potential is not suitable for the simulation of a $T_e = 100$ kK system due to the vastly different forces. Note that the atomic labelling is arbitrary and the forces on atoms i and $i + 1$ are joined by a line solely as a visual aid.

the entire intermediate range of temperatures. The hopelessness of attempting to construct a constant temperature potential applicable over such a wide temperature range is made clear by Fig. 4.2. There have been limited investigations into developing electronic-temperature-dependent interatomic potentials for use in molecular dynamics simulations of WDM [137, 138, 139, 140, 141, 142]. To show some of the different approaches, a few of the models will be introduced here.

4.2.1 DeePMD

With the sharp increase in available computing power throughout the last decade, considerable amounts of *ab initio* simulation data can now be readily produced with a fraction of the computational time and resources that were previously needed. This has led to a developing interest in machine learning (ML) potentials that can be fit to the large libraries of available data. Some examples of these ML potentials are the moment tensor potential [143], the spectral neighbour analysis potential [144], the Gaussian approximation potential [145], and the DeePMD potential [146], all with various representations and formulations. These potentials accurately reproduce experimental and *ab initio* simulation results with very small quantitative errors [147], as well as performing well when used in environments they were not fit to.

Three DeePMD potentials for WDM aluminium have previously been fit [46, 148]. Energy and force data from MHKS-DFT-coupled molecular dynamics trajectories were used to train ML potentials at $T_\mathrm{e} = 0.5$, 1, and 5 eV. The potentials were then used to investigate static properties (radial distribution function, isothermal compressibility, etc.) and transport properties (electronic/ionic thermal conductivity), with good matching to *ab initio* results. No method for probing intermediate temperatures was provided.

In the DeePMD method [146], the total energy is expressed as a sum of atomic contributions E_i,

$$E = \sum_i E_i(\{\mathbf{R}\}), \tag{4.12}$$

with $\{\mathbf{R}\}$ the set of atomic coordinates. The atomic contributions are therefore dependent on the local environment of atom i, similar to the Finnis-Sinclair and EAM models [149, 150], and this dependence is what is learned during training.

The method is split into two steps. Firstly, the expected translation, rotation, and permutation symmetries are enforced by creating a local coordinate frame for each atom i. A feature matrix $\mathbf{D}$ is built, with each element $\mathbf{D}_{ij}$ expressing the radial distances and angles between atom i and each of its neighbours j, within some cutoff radius r_c. The

	$\rho = 1.50$ g/cm^3		$\rho = 2.37$ g/cm^3		$\rho = 9.67$ g/cm^3	
Temperature (K)	RMSE	MAE	RMSE	MAE	RMSE	MAE
11600	3190	703	4704	1076	22053	19035
58000	910	518	876	525	36482	32144

Table 4.1: Force RMSE and MAE of the two DeePMD potentials fit in Ref. [46] for aluminium at $\rho = 1.50$, 2.37, and 9.67 g/cm^3 and $T_e = 11600$ and 58000 K. The RMSE and MAE are given in units of meV.

second step uses the feature matrix as the input to a deep neural network, outputting E_i. For each layer in the deep neural network, the transformation

$$\tilde{d}_k = \sum_l w_{kl} d_l^{\text{in}} + b_k \tag{4.13}$$

is applied, with d_l^{in} the input data, w_{kl} the weights, and b_k the biases. Importantly, the weights and biases for all atoms of a particular species must be identical to ensure permutation symmetry [146]. Then, a non-linear function φ (generally the tanh function) is applied to $\tilde{d}_k$ to give the final output of the layer,

$$d_k^{\text{out}} = \varphi(\tilde{d}_k). \tag{4.14}$$

This final step is not applied for the last hidden layer. The training of the deep neural network is achieved by the minimisation of the loss function,

$$L(p_\epsilon, p_f) = p_\epsilon (\Delta\epsilon)^2 + \frac{p_f}{3N} \sum_i |\Delta \boldsymbol{\mathcal{F}}_i|^2, \tag{4.15}$$

with ϵ the energy per atom, $\boldsymbol{\mathcal{F}}_i$ the force on atom i (calculated for the DeePMD potential analytically as the derivative of the energy), Δ the difference between the training and predicted data, N the number of atoms, and p the weights of the error contributions.

The accuracy of the $T_\text{e} = 1$ eV $= 11600$ K DeePMD potential previously trained in Ref. [46] is benchmarked against MHKS-DFT interatomic forces at three densities in Fig. 4.3. The root-mean-square error and mean average error (defined in Appendix B) of the $T_\text{e} = 1$ eV $= 11600$ K and $T_\text{e} = 5$ eV $= 58000$ K DeePMD forces are also shown

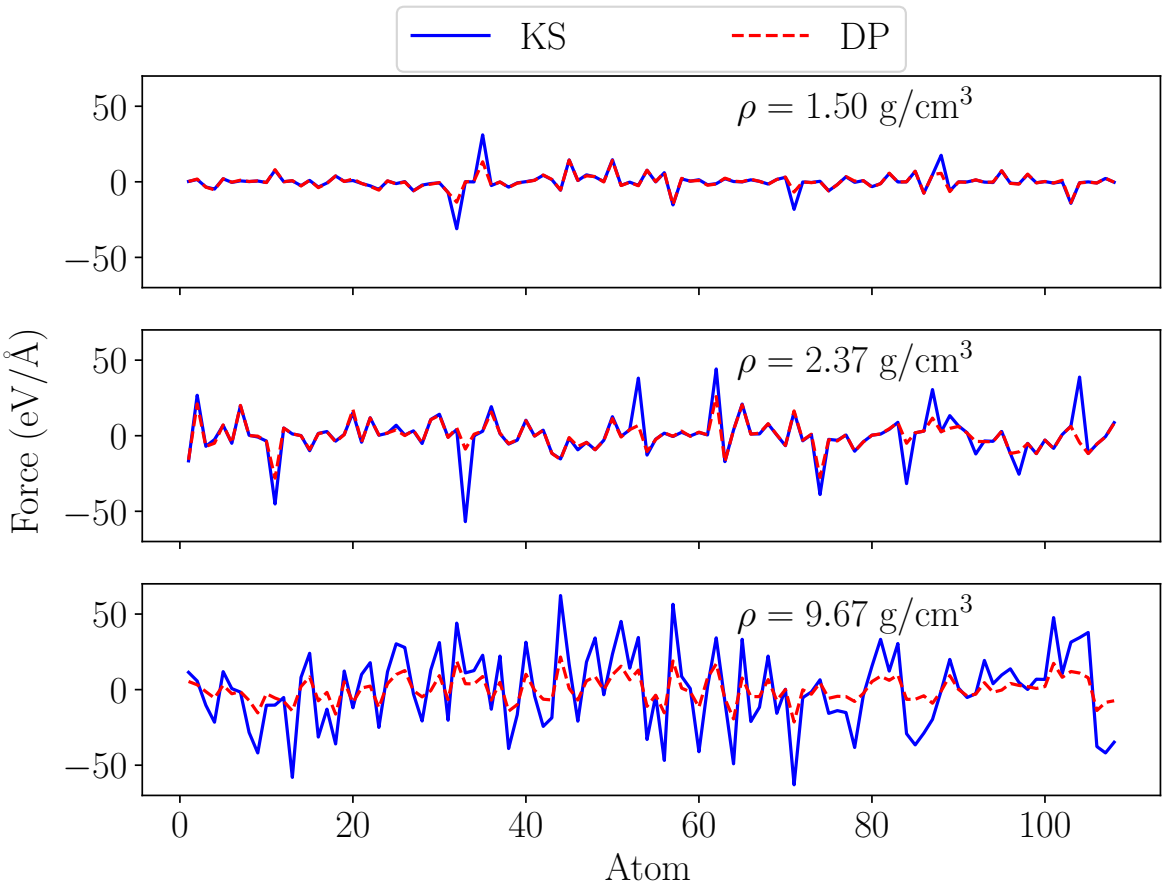

Figure 4.3: The force along the x-axis of each atom within a 108 aluminium atom snapshot equilibrated at 100 kK and with an electronic temperature $T_e = 1$ eV $= 11600$ K. The blue solid lines show the forces predicted by a converged Kohn-Sham calculation, whilst the dashed red lines show the forces predicted by the DeePMD potential fit by Liu et al [46]. The DeePMD forces show a noticeable difference from the KS forces for $\rho = 9.67$ g/cm^3, a result of the potential being fit to only $\rho = 2.70$ g/cm^3 molecular dynamics trajectories. The two methods match reasonably well for the $\rho = 1.50$ g/cm^3 and $\rho = 2.37$ g/cm^3 snapshots; however, the DeePMD potential fails to predict the largest forces accurately. This is likely due to the high equilibration temperature, and therefore kinetic energy, of the snapshots tested here. This allows the atoms to approach much closer to their neighbours than in a respective zero temperature structure for that density. These small interatomic separations are not sampled by the lower temperature ($T_{eq} = 11600$ K) molecular dynamics snapshots used in the training of the DeePMD potentials. Note that the atomic labelling is arbitrary and the forces on atoms i and $i + 1$ are joined by a line solely as a visual aid.

in Table 4.1. Qualitatively, Fig. 4.3 shows that the $T_e = 11600$ K DeePMD potential matches reasonably with the *ab initio* KS data at lower densities. At higher densities, or for small interatomic separations, the DeePMD potential fails to accurately reproduce

the correct forces. This is likely due to the training dataset for the DeePMD potential only including snapshots of $\rho = 2.70$ g/cm^3 aluminium with an equilibration temperature of $T_{\text{eq}} = 11600$ K. The small interatomic separations caused by the high density ($\rho = 9.67$ g/cm^3) and high equilibration temperature ($T_{\text{eq}} = 100$ kK) of the testing snapshot will not be sampled by the training dataset. Therefore, the strong Coulombic repulsion expected from closely separated ions is not reproduced by the DeePMD potential. The root-mean-square error and mean average error of the DeePMD forces are also poor when compared to other available methods (cf. Fig. 6.4). Even at lower densities, both of these metrics are dominated by the large discrepancies when predicting the forces on atoms with a very close nearest neighbour.

It should be noted that there are other differences in the methods used to generate the training data for the DeePMD potential and the testing data produced by MHKS-DFT. These include the pseudopotentials and the XC correlation functionals used. The training data used a 3e projector augmented-wave [151] pseudopotential with the PBE functional [65], whilst the testing data used a 3e norm-conserving pseudopotential with the KSDT functional [103, 104]. The contribution to the error from the difference in pseudopotential and XC functional is expected to be much smaller than that from including only a single material density in the training dataset. This could be confirmed by training a DeePMD potential with only the $\rho = 2.37$ g/cm^3 data produced in Chapter 6 and comparing the forces with MHKS-DFT data.

ML potentials, such as DeePMD, require massive amounts of accurate data to predict chemically accurate energies and forces for a range of systems, due to their extremely general functional form. This is often achievable for low temperature potentials fit to DFT data, but becomes increasingly difficult for elevated temperatures due to the limitations of MHKS-DFT. Furthermore, it can be difficult to gain any physical insight from the potential, especially for those with tens of thousands of fitting parameters. Another drawback of the DeePMD approach is that there is no prescribed method to calculating forces at intermediate temperatures, which would be required for a molecular dynamics simulation of ablation, laser heating, etc. However, a temperature-dependent extension

to DeePMD [152, 153] has been recently developed that incorporates the electronic temperature into the learning of the atomic free energy.

4.2.2 Empirical potentials

Empirical potentials avoid the need for both vast libraries of data and the fitting of myriad weights and biases by substituting the neural network for a simple analytic form, often dependent on only a few parameters. An empirical potential's functional form is commonly motivated by the underlying physics of the system and requires orders of magnitude less data points to fit its parameters. Furthermore, limitations of the functional form can be more easily diagnosed, with extensions to the model developed from physical intuition, rather than by arbitrarily increasing the number of fitting parameters.

Due to the dearth of empirical finite-temperature aluminium potentials, this section will primarily be a general introduction to some functional forms of empirical potentials, along with their strengths and weaknesses for simulating WDM. Previous finite-temperature extensions will be mentioned where appropriate.

Pair potentials

Pair potentials take only the interatomic separation of the two atoms as an input. Often there are also a few fitting parameters that depend on the given atomic species, temperature, etc. Amongst pair potentials, the Lennard-Jones potential is perhaps the simplest and most studied [154]. This breaks down each pairwise interaction into an attractive component and a repulsive component, both of which are described using power laws (see Fig. 4.1). However, the simplicity of the potential limits its use to modelling the dilute noble gases.

Another famous pair potential is the Morse potential [155]. This consists of a sum of exponentials, but with an extra fitting parameter compared to the Lennard-Jones potential. These pair potentials have been extended to finite temperature through scaling

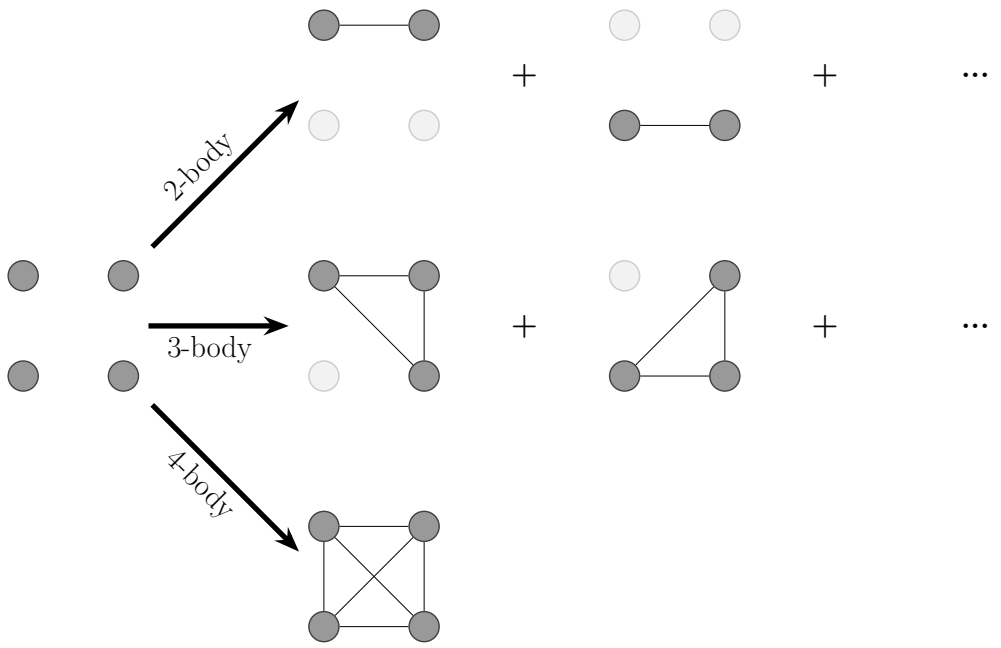

Figure 4.4: A system of four atoms (left) and its description in terms of n-body interactions. The dark grey circles represent the atoms considered in a particular term, whilst the light grey circles represent all other atoms in the system. The lines connecting the atoms show the interactions within a particular term. The top summation shows the two-body contributions with each term an interaction between a pair of atoms. The middle summation shows the three-body contributions consisting of interactions between triplets of atoms. There is also a single four-body contribution.

certain parameters related to the thermal energy or thermal expansion [138, 137, 156]. However, these empirical potentials fit thermodynamic properties with no regard for any possible quantum effects, as well as only fitting to data < 1000 K. Therefore, they will not be suitable for the high temperatures required for WDM, and are unlikely to accurately describe non-equilibrium systems, such as those with 'hot' electrons and 'cold' ions.

The biggest issue with these potentials is that they only consider pairs of atoms in their interactions. The (free) energies and forces therefore only include contributions from the two-body interactions shown in the top line of Fig. 4.4. A three-body potential would also include contributions from the three-body interactions shown in the second line, etc. Whilst it may be that at extremely high temperatures only including pairwise interactions becomes a suitable approximation, a pair potential will not be able to accurately describe the system whilst undergoing heating. Further investigation into the form of the interatomic bonds at WDM conditions must be considered before choosing a functional form that may limit its behaviour, such as the enforcing of the Cauchy relation mentioned earlier.

Many-body potentials

A simple extension to pair potentials is the inclusion of a bond angle between at least three atoms. These many-body potentials better describe materials that may undergo different types of bonding. One of the most widely-used many-body potentials is the Tersoff potential, commonly used for silicon and carbon [157]. Since most of the materials that are likely to be found in WDM conditions are metals, the focus here will be on the embedded atom model (EAM) potential [134, 158, 159] and the similar Finnis-Sinclair potential [149], both of which include some many-body effects vital for describing metallic systems.

The total energy of a system of atoms modelled by the Finnis-Sinclair potential is the sum of the atomic energies. The atomic energy E_i can be expressed as a cohesive embedding

term and repulsive pair potential term,

$$E_i^{\mathrm{FS}} = \sqrt{\rho_i} + \frac{1}{2}\sum_j V(R_{ji}), \tag{4.16}$$

where $\rho_i = \sum_j \phi(R_{ji})$ can be thought of as an approximation to the true local charge density in the EAM paradigm, ϕ and V are some pairwise functions of R_{ji}, often chosen to be polynomials, and R_{ji} is the atomic separation. The replacement of the embedding function $\sqrt{\rho_i}$ by some arbitrary nonlinear function leads to the EAM potential.

A temperature-dependent Finnis-Sinclair potential [26] was developed by altering the embedding function to include the temperature-dependent electronic band energy and entropy from the DFT free energy (Eq. 2.33). By using the Fermi-Dirac distribution and a rectangular model for the density of states (DOS), the approximate scaling of the band energy and entropy with temperature can be found. The remaining DFT free energy was assumed to be temperature independent and contributed to the repulsive pairwise term in the Finnis-Sinclair potential.

For tungsten, the temperature-dependent Finnis-Sinclair potential was fit to DFT data of the body-centred cubic (bcc) free energy against volume at various electronic temperatures. Another potential was fit to DFT data for the pressure of a bcc system with the room temperature equilibrium lattice constant, as the electronic temperature was varied. It was found that the potential's functional form could correctly capture the qualitative effects from both sets of data; however, the functional form of the potential assumes a rectangular DOS, which would not accurately capture the true behaviour at high electronic temperature in noble metals such as gold due to the broadening and shifting of the gold DOS with electronic temperature [21].

Another finite-temperature many-body potential is the gold EAM potential developed by Norman et al [20]. Like the temperature-dependent Finnis-Sinclair potential, this potential was developed to describe non-equilibrium systems with high electronic temperature and low ionic temperature. Rather than using the Fermi-Dirac distribution to derive the

temperature dependence of the energy contributions, a simple parametric dependence of the pairwise functions ϕ and V on the atomic separation R and the electronic temperature T is chosen,

$$\theta(R, T_\mathrm{e}) = \theta_0(R) + \theta_1(R)T_\mathrm{e} + \theta_2(R)T_\mathrm{e}^2, \tag{4.17}$$

with θ either ϕ or V.

Whilst the functional form of the temperature dependence is much simpler than the temperature-dependent Finnis-Sinclair potential, allowing for a faster computational evaluation, it is hard to extract any physical intuition from the fitted potential itself. Instead, Norman et al. used the potential in large-scale molecular dynamics simulations to investigate ablation of gold films when irradiated with a laser. The potential was fit to *ab initio* forces at different electronic temperatures using the force-matching method [160], with errors in the predicted forces of 15-20%. Whilst this level of accuracy may be expected for such a simple functional form, it will be shown later that more recent methods can greatly improve this accuracy without sacrificing the fast evaluation speed required for large-scale simulations.

4.2.3 Ground-state DOS approximation

ML potentials can, in theory, predict arbitrarily accurate energies and forces, but require large amounts of training data which is computationally unfeasible to generate at WDM conditions. The temperature-dependent Finnis-Sinclair potential showed that, for a given DOS, approximate analytic expressions can be derived that predict finite-temperature behaviour at an arbitrary electronic temperature.

A recent paper [27] has shown how finite-temperature effects can be approximated given only the electronic DOS, such that an ML interatomic potential trained on data consistent with the chosen DOS can predict finite-temperature energies and forces. In the method, the DOS is fixed and does not vary with temperature. Instead, the cancellation of certain energy contributions with respect to a change in occupation number f_i allows for the

change in internal energy to be approximated by

$$\Delta U \approx \Delta U_{\mathrm{b}}^{0} = \sum_{i} \varepsilon_{i}^{0} \Delta f_{i}, \tag{4.18}$$

where $U = F + TS$ is the internal energy of the system, U_{b}^{0} is the KS band energy, ε are the KS eigenenergies, and the superscript '0' labels quantities evaluated using zero-temperature eigenenergies. The total free energy is approximated as

$$F(T) \approx U(0) + \Delta U_{\mathrm{b}}^{0}(T) - TS^{0}(T), \tag{4.19}$$

where $U(0)$ is the internal energy calculated by the ML zero-temperature interatomic potential (and thus consistent with the DOS used), and S is the non-interacting entropy.

The forces are then calculated as

$$\boldsymbol{\mathcal{F}}_{\alpha}(T) \approx -\frac{\partial U(0)}{\partial \mathbf{R}_{\alpha}} - \frac{\partial}{\partial \mathbf{R}_{\alpha}} \left[\Delta U_{\mathrm{b}}^{0}(T) - TS^{0}(T) \right]. \tag{4.20}$$

As the second and third terms are analytically approximated using the fixed DOS, the temperature is an external parameter not needed in the training of the ML interatomic potential. The training dataset for the potential therefore only requires data at a single temperature, vastly reducing the computational time required to create the interatomic potential.

In practice, a separate ML model is used to predict the DOS. A drawback of this method is that KS states above the chemical potential $\mu^{0}(T)$ must be included in the training dataset used to learn the DOS. The number of these KS states required to accurately predict the finite-temperature contribution is dependent on the electronic temperature and is not known *a priori*.

As the difference in the probed and reference electronic temperatures increases, the quality of the approximation decreases. To further extend the temperature range of the finite-temperature potential, a new reference state (instead of $T = 0$ K) can be chosen and a

new ML potential and DOS trained on data generated at that temperature. This provides a scheme for the interpolation between electronic temperatures.

4.3 Summary

In this chapter, interatomic potentials have been introduced as a method for calculating energies and interatomic forces of collections of atoms without having to use quantum theory to solve the electronic Schrödinger equation. Empirical potentials, such as the Lennard-Jones and Finnis-Sinclair potentials, often have a simple functional form that is motivated by physical insight with only a few fitting parameters. Conversely, ML potentials use a general form and large set of parameters with the only requirement being invariance under certain symmetry operations (e.g. translation) expected for a physical system. ML potentials require much larger training datasets than empirical potentials, but can, in theory, predict the energy and forces more accurately.

At finite temperature, the derivatives of the Helmholtz free energy F with respect to the ionic positions give the thermodynamically correct interatomic forces. The finite-temperature forces then dictate the motion of the ions during a molecular dynamics simulation. A derivation showing the ensemble-independence of the finite-temperature thermodynamic forces was given.

Several examples of finite-temperature interatomic potentials were discussed, some were designed for use at a single elevated temperature, and some of which were temperature dependent. Whilst the potentials at a single elevated temperature can accurately model WDM conditions, there is no scheme for probing intermediate temperatures and so any simulation must be performed at that single electronic temperature. On the other hand, temperature-dependent potentials allow for a wide range of electronic temperatures to be investigated, but require a procedure to estimate the finite-temperature effects. The chosen procedure may or may not be physically motivated. Two of the potentials introduced approximate the electronic-temperature effects by the Fermi-Dirac smearing of the occu-

pations within the DOS; however, for conditions under which the DOS may drastically change (e.g., phase transitions) the quality of the approximation is likely to diminish.

Chapter 5

Molecular Dynamics

In the preceding chapters, a number of methods for solving the electronic structure problem, and therefore finding the interatomic forces, have been detailed. By treating the ions classically and assuming the Born-Oppenheimer approximation holds, the motion of the ions is then dictated by the interatomic forces calculated for fixed ionic positions.

To simulate this ionic motion, a technique called molecular dynamics (MD) is used. In MD, the ionic subsystem is simulated classically by integrating Newton's laws of motion. If the positions and momenta of the ions are known at time t, MD allows them to be calculated at a later time $t + \Delta t$, given a suitable method to calculate the interatomic forces. The MD process can be repeated *ad infinitum*, with properties of the system calculated as averages over time.

The calculation of useful quantities using MD is dependent upon the ergodic hypothesis; that a system will pass through all accessible phase space, given that it is evolved for an infinite time. If this is true, then time-averaged properties from an MD simulation will be equivalent to ensemble-averaged properties from thermodynamics. It will be assumed that the ergodic hypothesis holds for the systems of interest here [161].

5.1 Calculating statistical quantities

Statistical quantities are measured in MD simulations as functions of the ionic positions, velocities, and forces. For example, the temperature can be calculated using the equipartition theorem,

$$\sum_{i}^{N} \frac{\frac{1}{2} m_i v_i^2}{3N-3} = \frac{1}{2} k_{\mathrm{B}} T, \tag{5.1}$$

with N the number of ions, m the ionic mass, and $v = |\mathbf{v}|$ the ionic velocity. The denominator on the left hand side of the equation is the number of degrees of freedom in 3D, with the three degrees removed due to fixing the total momentum to zero. By rearranging the above equation, the instantaneous temperature at time t can be measured as

$$T(t) = \sum_{i}^{N} \frac{m_i v_i^2(t)}{k_{\mathrm{B}}(3N-3)}. \tag{5.2}$$

The instantaneous pressure of a system can also be calculated as the sum of an ideal gas contribution and virial contribution [161],

$$\begin{aligned} P(t) &= P_{\mathrm{id}}(t) - \frac{\partial U(t)}{\partial V} \\ &= \frac{N k_{\mathrm{B}} T(t)}{V} + \frac{1}{3V} \sum_{i}^{N} \mathbf{r}_i(t) \cdot \boldsymbol{\mathcal{F}}_i(t), \end{aligned} \tag{5.3}$$

with V the volume of the simulation cell, $\mathbf{r}_i$ the position of ion i, and $\boldsymbol{\mathcal{F}}_i$ the total force on ion i. Expressions for periodic systems have also been derived [162].

Whilst both the temperature and pressure can be time averaged, their fluctuations throughout the simulation are often more important, for instance in monitoring the equilibration of the system. An example of an explicitly time-averaged quantity is the diffusion coefficient [161],

$$D = \lim_{t \to \infty} \frac{1}{6t} \left\langle |\mathbf{r}_i(t+\tau) - \mathbf{r}_i(\tau)|^2 \right\rangle, \tag{5.4}$$

where $\langle \dots \rangle$ indicates an average over all ions i and time offsets t. The angle bracket gives the expected mean-square displacement of an atom in time t. The diffusion coefficient

can also be defined as

$$D = \frac{1}{3}\int_0^\infty \langle \mathbf{v}_i(t+\tau)\cdot\mathbf{v}_i(\tau)\rangle \,\mathrm{d}t, \tag{5.5}$$

with the integrand the velocity autocorrelation function. This definition is a *Green-Kubo relation*, an expression that links a macroscopic transport coefficient to an integral over a microscopic time-correlation function [161].

5.2 Anatomy of a time step

A basic MD program contains the following steps:

1. Initialise

Before the first step is taken in an MD simulation, certain input parameters must be defined. These include the time step, temperature, positions, and velocities. Generally, the initial velocities are randomly sampled from a Maxwell-Boltzmann distribution at the desired temperature. In a constant temperature (canonical) simulation, this temperature is often equal to that of the thermostat. The ionic positions and velocities at subsequent time steps are the outputs from the integration of the equations of motion.

2. Calculate forces

The forces on the ions must then be calculated. Depending on the method chosen, the forces can be calculated using MHKS-DFT, OF-DFT, or an interatomic potential. This step is normally the most computationally expensive part of the simulation.

3. Integrate equations of motion

With the positions, velocities, and forces now specified, the classical equations of motion can be integrated to find the ionic positions and velocities at the next time step. The velocity Verlet method is commonly used, due to its speed, memory efficiency, and small energy drift [161]. It also explicitly stores the positions and velocities at each time

step (unlike the Verlet and leapfrog methods), allowing for the consistent calculation of potential, kinetic, and total energies.

The velocity Verlet method is defined by two equations:

$$\mathbf{R}(t+\Delta t) = \mathbf{R}(t) + \mathbf{v}(t)\Delta t + \frac{\boldsymbol{\mathcal{F}}(t)}{2m}\Delta t^2 + \mathcal{O}(\Delta t^3), \tag{5.6}$$

for the positions, and

$$\mathbf{v}(t+\Delta t) = \mathbf{v}(t) + \frac{\boldsymbol{\mathcal{F}}(t+\Delta t) + \boldsymbol{\mathcal{F}}(t)}{2m}\Delta t + \mathcal{O}(\Delta t^3), \tag{5.7}$$

for the velocities. In practice, Eq. 5.6 must be solved first such that $\boldsymbol{\mathcal{F}}(t+\Delta t)$ can be calculated using the updated positions $\{\mathbf{R}(t+\Delta t)\}$.

4. Calculate properties

At the end of each time step the instantaneous temperature and pressure can be calculated using Eqs. 5.2 and 5.3. Contributions to statistical properties, such as the radial distribution functions or diffusion coefficients, are also calculated at this point. In addition, the kinetic and potential energies can be calculated using the velocities and positions, respectively. The sum of these energy contributions gives the total energy, which must be monitored to ensure that there is no energy drift during a microcanonical simulation. When using a thermostat, the sum of the kinetic and potential energies is not conserved; however, the long-time average of the total energy can be used to define when the system is equilibrated, as discussed next.

5.3 Equilibration

Before running an MD simulation, a choice must be made as to the starting configuration of the system. There are a number of options, but usually a lattice structure or random structure is chosen. No matter what is chosen, there will be some bias present that can

potentially skew any time-averaged quantities.

According to the ergodic hypothesis, an ensemble average in thermodynamic equilibrium can be calculated by the time average of an MD simulation. To find the true ensemble average, the quantity should be averaged over an infinite period of time. The starting configuration would therefore be unimportant, as the configurations sampled should be congruent with the partition function in the large time limit. In practice, though, it is impossible to sample an infinite period of time.

Instead, the system is equilibrated first, with the contributions to the time-averaged quantities sampled during a subsequent production run. To equilibrate the system, the MD simulation is run from the initial configuration for a number of time steps. Often, a target temperature or pressure is chosen, with the total energy allowed to fluctuate. For a given starting structure, e.g., an fcc lattice, after a few time steps the system may no longer be identifiable, by eye, as having started from that structure. However, there is likely to still be some bias in the measured energies and properties. Therefore, the end of equilibration is often defined by the point at which certain measured quantities are fluctuating around some average value.

For instance, in a microcanonical simulation the total energy is constant by definition. However, the instantaneous temperature (kinetic energy) and total potential energy fluctuate as the system evolves. When their fluctuations around some average value are small, the system is said to be in equilibrium. For a canonical simulation, the temperature (and therefore kinetic energy) of the thermostat are constant, with the instantaneous temperature of the system fluctuating around the temperature of the thermostat. The potential energy and total energy of the system then fluctuate in time. A system simulated in the canonical ensemble is therefore in equilibrium when the potential and total energies fluctuate around some average value.

Any other property of interest can also be used to assess whether equilibrium has been reached. If the property reaches a near-constant average value, the system is likely to have reached equilibrium. For example, the total pressure (Eq. 5.3) can be measured

throughout the simulation with equilibrium said to be achieved when it reaches a steady state.

In fact, none of these quantities will ever truly be constant, due to numerical error and the stochastic nature of many thermostats and barostats. However, the equilibration process is generally stopped when the fluctuations in the measured quantities are below some chosen threshold. A number of commonly used equilibration tests measure the fluctuations in the instantaneous temperature, plotting the velocity distribution of the ions to ensure a Maxwell-Boltzmann distribution has been reached, and observing the positional disorder of the ions.

The majority of MD simulations carried out in this thesis are used for generating snapshots of atomic configurations. These configurations are then used to compare the various methods of calculating interatomic forces. Once the temperature and total energy have reached a steady state, it is assumed that the MD simulation is adequately equilibrated for this purpose. As the particular configuration is unimportant and the forces will be recalculated with other methods such as MHKS-DFT, OF-DFT, or an interatomic potential, perfect equilibration is not required. All that is necessary is that the snapshots are reasonably realistic samples of the system at the temperature of interest.

Whilst equilibration is important for any MD simulation, here it has been discussed from the perspective of liquid-like structures, which make up the majority of the simulations undertaken in this thesis. In this case, the state after equilibration will be essentially uncorrelated from the initial fcc lattice. In low temperature solids, the experimentally observed structure is often chosen as the starting configuration. The starting structure should therefore be energetically stable and the equilibration simply relaxes the structure (by altering the lattice parameter) and allows the atoms to make small excursions from their equilibrium positions in the perfect crystal lattice.

In Fig. 5.1, the equilibration process and subsequent production run for a system of 108 aluminium atoms at $T_{\mathrm{eq}} = 100$ kK starting in a 3×3×3 fcc supercell configuration is

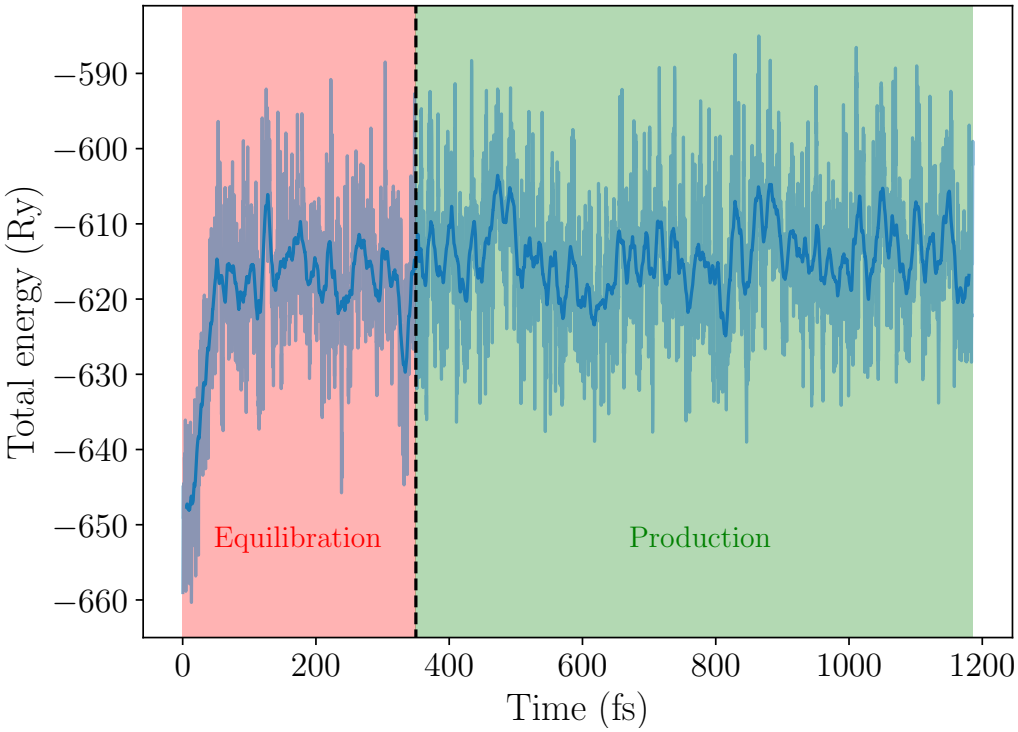

Figure 5.1: The total energy of a thermostatted MD simulation. The light blue line indicates the total energy at each time step, whilst the dark blue line is the centered moving average of $w = 101$ time steps (Eq. 5.8). The system contains 108 aluminium atoms at a density of 2.37 g/cm^3 with an Andersen thermostat set to $T_{\text{eq}} = 100$ kK. The MD simulation was performed using the `PROFESS@QE` program, with the forces at each time step calculated using the non-local SDF OF-DFT functional and the velocity Verlet algorithm used for time integration. Initially, the system is in an fcc supercell configuration and the velocities are taken from a Maxwell-Boltzmann distribution. The system is first equilibrated for 350 fs. The time-averaged properties are then calculated from the 800 fs production run. The temperature is monitored throughout to ensure equilibration has been achieved.

shown. The centered moving average of the total energy has been defined as

$$s_i^w = \frac{1}{w} \sum_{j=-k}^{k} x_{i-j}, \tag{5.8}$$

with i the position of the center time step, w the number of terms in the average, x_i the total energy at time step i, and $k = (w-1)/2$. The initial configuration has a total energy much lower than that found later in the simulation; however, a structure with such high symmetry (fcc) is unlikely to be sampled in a high temperature equilibrated system, due

to the zero ionic entropy required. Instead, the system will spend the majority of the simulation in states that are more abundant in the partition function, and therefore have a higher ionic entropy.

The equilibration run continues until the total energy and temperature reach a steady state. There is no exact definition for when this has been achieved, and from Fig. 5.1 it is obvious that there will always be some fluctuation in the total energy. As the ions move throughout the system, some of the kinetic energy becomes potential energy (and vice versa). If the system were closed, the total energy would be constant (excluding numerical error). However, for a system that is equilibrated at a particular temperature, a thermostat must be used.

5.4 Thermostat

The thermostat attempts to maintain the target temperature by increasing (or decreasing) the kinetic energy of the ions, such that the instantaneous temperature of the system is always close to the target temperature. The thermostat therefore acts as a energy source or sink, changing the total energy in the system and causing the observed fluctuations around the steady state. There is no exact way to model an infinite heat bath, as is assumed in thermodynamics; however, there are a number of schemes that approximate the problem in different ways.

The simplest thermostat is the velocity-scaling method. In this scheme, the velocities of all ions are uniformly scaled at the end of each time step such that the instantaneous temperature, given by Eq. 5.2, is exactly equal to the target temperature. This method does not reproduce the correct canonical ensemble as the kinetic energy is not allowed to fluctuate, as would be expected by statistical mechanics. The arbitrary scaling of the velocities can also slow down the equilibration process as it prevents changes to the spatial temperature gradients.

A more realistic method is the Andersen thermostat [163]. In this scheme, the ions'

velocities are stochastically chosen from a Maxwell-Boltzmann distribution at the target temperature. Rather than reassigning every ion's velocity at every time step, the time between updates for a particular ion is given by the Poisson distribution

$$P(t) = \nu \exp[-\nu t], \tag{5.9}$$

where t is the time and ν is the collision frequency parameter. This is true so long as the probability of an ion being updated in a time step $\mathrm{d}t$ is $\nu \mathrm{d}t$ and the updates are assumed to be uncorrelated.

The temperature in an Andersen thermostatted MD simulation fluctuates and takes a finite time to reach the target temperature. It has also been proven that the Andersen thermostat reproduces the canonical ensemble (so long as the system is in equilibrium), and hence the correct static properties (e.g., pressure) [161]. On the other hand, the lack of momentum conservation leads to unrealistic dynamics, and therefore the mean square displacement and diffusion coefficients are not correctly simulated. The correlated motion of the ions is also disrupted when the non-conservative velocity update occurs, slowing down the equilibration process. This is observed in Fig. 5.2 for different values of the collision frequency parameter ν.

The incorrect diffusion coefficient can be explained as such [165]: the velocity autocorrelation function (as defined in Eq. 5.5) of a single step $\mathrm{d}t$ with initial time τ, can be Taylor expanded to give

$$C(\mathrm{d}t) = C(0) + C'(0)\mathrm{d}t + \mathcal{O}\left((\mathrm{d}t)^2\right), \tag{5.10}$$

where $C'(t)$ is the time derivative of the velocity autocorrelation function. If $t = 0$, the velocity autocorrelation function is simply the mean squared velocity of the ions, which for a system in thermodynamic equilibrium is the mean sqaured velocity of the Maxwell-Boltzmann distribution,

$$C(0) = \frac{3k_\mathrm{B}T}{m}. \tag{5.11}$$

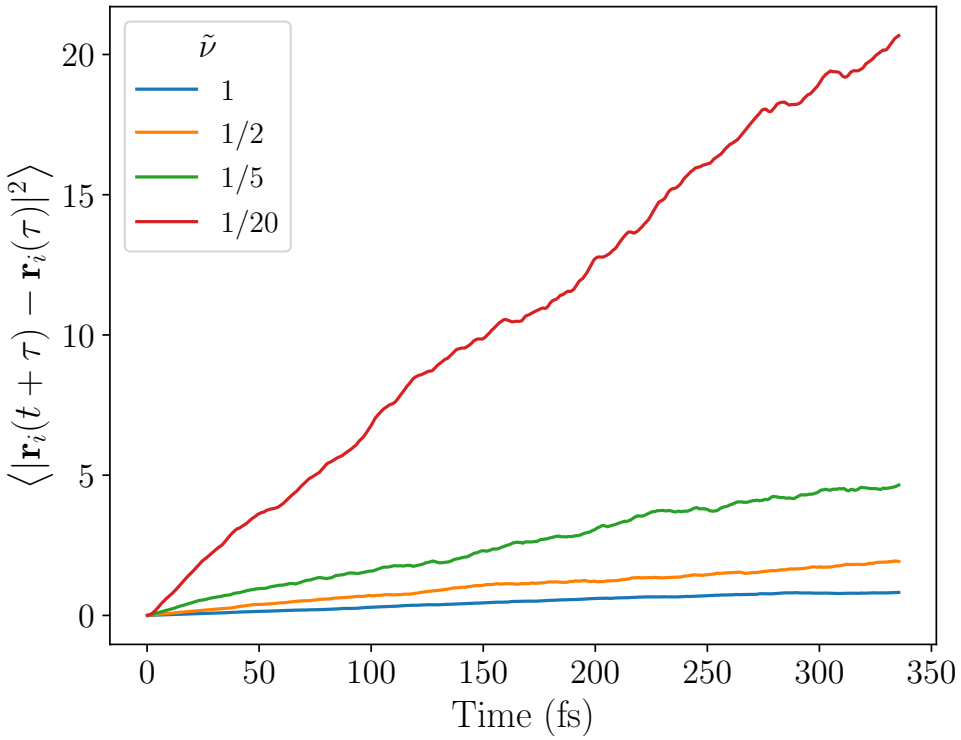

Figure 5.2: Mean square displacement against time for various choices of the collision frequency parameter $\tilde{\nu} = \nu \mathrm{d}t$. The 108 aluminium atom MD simulation was performed using the `PROFESS@QE` program, with the forces at each time step calculated using the semi-local VT84F OF-DFT functional and the velocity Verlet algorithm used for time integration. The initial configuration was a $\rho = 2.37$ g/cm^3 fcc supercell with an equilibration temperature of $T_{\mathrm{eq}} = 50$ kK. The time step was set constant at $\mathrm{d}t = 167$ as, in line with Eq. 5.19. As ν increases, the gradient of the mean square displacement decreases. Since the diffusion coefficient, and therefore the gradient of the mean square displacement, should be independent of ν, the Andersen thermostat cannot reproduce the correct dynamics [164]. See the main text for further discussion.

The time derivative of the velocity autocorrelation function is

$$C'(t) = \langle \mathbf{v}(\tau) \cdot \mathbf{a}(\tau + t) \rangle, \tag{5.12}$$

with $\mathbf{a}$ the acceleration of the atoms. Substituting these two equations into the definition of $C(\mathrm{d}t)$ gives

$$\begin{aligned} C(\mathrm{d}t) &= \frac{3k_{\mathrm{B}}T}{m} + \langle \mathbf{v}(\tau) \cdot \mathbf{a}(\tau) \rangle \mathrm{d}t + \mathcal{O}\left((\mathrm{d}t)^2\right) \\ &= \frac{3k_{\mathrm{B}}T}{m} + \langle \mathbf{v}(\tau) \cdot \boldsymbol{\mathcal{F}}_{\mathrm{tot}}(\tau) \rangle \frac{\mathrm{d}t}{m} + \mathcal{O}\left((\mathrm{d}t)^2\right). \end{aligned} \tag{5.13}$$

Here, the total force on an atom has been defined as

$$\boldsymbol{\mathcal{F}}_{\mathrm{tot}} = \boldsymbol{\mathcal{F}}_{\mathrm{I}} + \nu \mathrm{d}t \boldsymbol{\mathcal{F}}_{\mathrm{T}}, \tag{5.14}$$

with $\boldsymbol{\mathcal{F}}_{\mathrm{I}}$ the force due to the interatomic interactions, $\boldsymbol{\mathcal{F}}_{\mathrm{T}}$ the force due to the interaction with the Andersen thermostat, and the factor of $\nu \mathrm{d}t$ representing the probability of an interaction with the Andersen thermostat during a time step $\mathrm{d}t$. So long as the system (sans the thermostat) conserves the total energy when the atoms are allowed to evolve under the interatomic interactions,

$$\langle \mathbf{v} \cdot \boldsymbol{\mathcal{F}}_{\mathrm{I}} \rangle = 0. \tag{5.15}$$

Since the force due to the interaction with the Andersen thermostat is non-conservative, its contribution does not vanish when averaged. The force due to the thermostat interactions can be written

$$\boldsymbol{\mathcal{F}}_{\mathrm{T}} = m\mathbf{a}_{\mathrm{T}} = \frac{m}{\mathrm{d}t}(\boldsymbol{\epsilon} - \mathbf{v}), \tag{5.16}$$

where $\boldsymbol{\epsilon}$ is a random velocity drawn from a Maxwell-Boltzmann distribution with temperature T after a collision with the Andersen thermostat and $\mathbf{v}$ is the velocity prior to the collision. Substituting the force into Eq. 5.13 leads to

$$\begin{aligned} C(\mathrm{d}t) &= \frac{3k_{\mathrm{B}}T}{m} + \nu \mathrm{d}t \langle \mathbf{v}(\tau) \cdot [\boldsymbol{\epsilon}(\tau) - \mathbf{v}(\tau)] \rangle + \mathcal{O}\left((\mathrm{d}t)^2\right) \\ &= \frac{3k_{\mathrm{B}}T}{m} + \nu \mathrm{d}t \langle \mathbf{v}(\tau) \cdot \boldsymbol{\epsilon}(\tau) \rangle - \nu \mathrm{d}t \langle \mathbf{v}(\tau) \cdot \mathbf{v}(\tau) \rangle + \mathcal{O}\left((\mathrm{d}t)^2\right) \\ &= \frac{3k_{\mathrm{B}}T}{m}(1 - \nu \mathrm{d}t) + \mathcal{O}\left((\mathrm{d}t)^2\right), \end{aligned} \tag{5.17}$$

where the uncorrelated nature of the pre- and post-collision velocities, $\langle \mathbf{v}(\tau) \cdot \boldsymbol{\epsilon}(\tau) \rangle = 0$, and the velocity autocorrelation function with zero time offset (Eq. 5.11) have been used in the final line.

As $\tilde{\nu} = \nu \mathrm{d}t \leq 1$, the choice of collision frequency parameter ν affects the calculated $C(t)$. In the worst case, when $\tilde{\nu} = 1$, the velocity autocorrelation function is zero after only one

time step. From the definition of the diffusion coefficient given in Eq. 5.5, it therefore follows that the measured value of D will decrease as $\tilde{\nu}$ increases, unlike the constant D that would be expected physically.

A simpler argument for the suppressed diffusion coefficient when using the Andersen thermostat can be made by using the random walk. The Andersen thermostat with collision frequency parameter $\tilde{\nu}$ is modelled by a random walk with step size l. The step size l is equivalent to the average distance travelled between collisions with the Andersen thermostat and is therefore inversely proportional to $\tilde{\nu}$.

Assume there are two random walks: one with step size l, and one with step size l/a, where $a > 1$. It is known that the root mean square displacement RMS after N steps is [166]

$$\text{RMS} = \sqrt{N}l. \tag{5.18}$$

If both random walks are simulated for the same total distance Nl, the random walk with step size l/a and Na steps will correspond to a thermostatted system with a times more collisions than that of the random walk with step size l and N steps. The RMS of the two random walks is therefore not equal, with the shorter step size random walk (corresponding to a larger $\tilde{\nu}$) having a smaller RMS. From Eq. 5.4, the diffusion coefficients D are therefore also not equal, with D decreasing as $\tilde{\nu}$ increases.

The Nosé-Hoover thermostat [167, 168] and Nosé-Hoover chains [169] can be used to accurately model dynamical effects by introducing fictional degrees of freedom for the infinite heat bath, conserving the total momentum; however, dynamical properties are not investigated here. Other thermostats, such as the Langevin thermostat [91], have been developed; however, throughout this thesis, both the Andersen and Nosé-Hoover thermostats will be used to calculate equilibrium properties of MD simulations, depending on the availabilty of the method in the software.

5.5 Choosing a time step

The choice of time step is essential to reproducing the correct static and dynamic properties for the system. If the time step is too small, many iterations will be required to explore the phase space, as is required by the ergodic hypothesis. If the time step is too large, ions may approach closer to each other than would be expected realistically or the time integration schemes may become unstable, leading to a drift in the total energy.

The time step for a given system must therefore be tested, prior to the actual simulation. The largest, stable time step will be dependent on numerous factors. The most important factors for the liquid structures investigated here will be the density of the ions ρ and the equilibration temperature T_{eq}.

The simulations reported in this thesis used a time step chosen according to the formula [90],

$$\mathrm{d}t = \mathrm{d}t^{100\mathrm{K}} \left(\frac{100}{T_{\mathrm{eq}}}\right)^{\frac{1}{2}} \left(\frac{1}{\rho}\right)^{\frac{1}{3}}, \tag{5.19}$$

where $\mathrm{d}t^{100\mathrm{K}} = 5$ fs is the time step at 100 K, T_{eq} is the equilibration temperature in Kelvin, and ρ is the material density in g/cm^3. The appropriate choice of $\mathrm{d}t^{100\mathrm{K}}$ is made using the largest vibrational frequency of fcc aluminium at 100 K and the Nyquist theorem. The scaling ensures that, on average, each ion will cover approximately the same fraction of an interatomic distance per time step. An MD simulation without the use of a thermostat was performed for various time steps to demonstrate the instability of the velocity Verlet method for large $\mathrm{d}t$, as shown in Fig. 5.3. Furthermore, MD simulations of all permutations of the minimum and maximum density and temperature used in this thesis were performed at the time step calculated using Eq. 5.19 with the results shown in Fig. 5.4.

All total energies have a slight negative energy drift, with the maximum energy drift per 100 fs for a 100 kK starting temperature approximately 0.02 Ry. This energy loss translates to a lower ionic kinetic energy and instantaneous temperature. From Eq. 5.2, this energy drift corresponds to a decrease in the instantaneous temperature of approximately

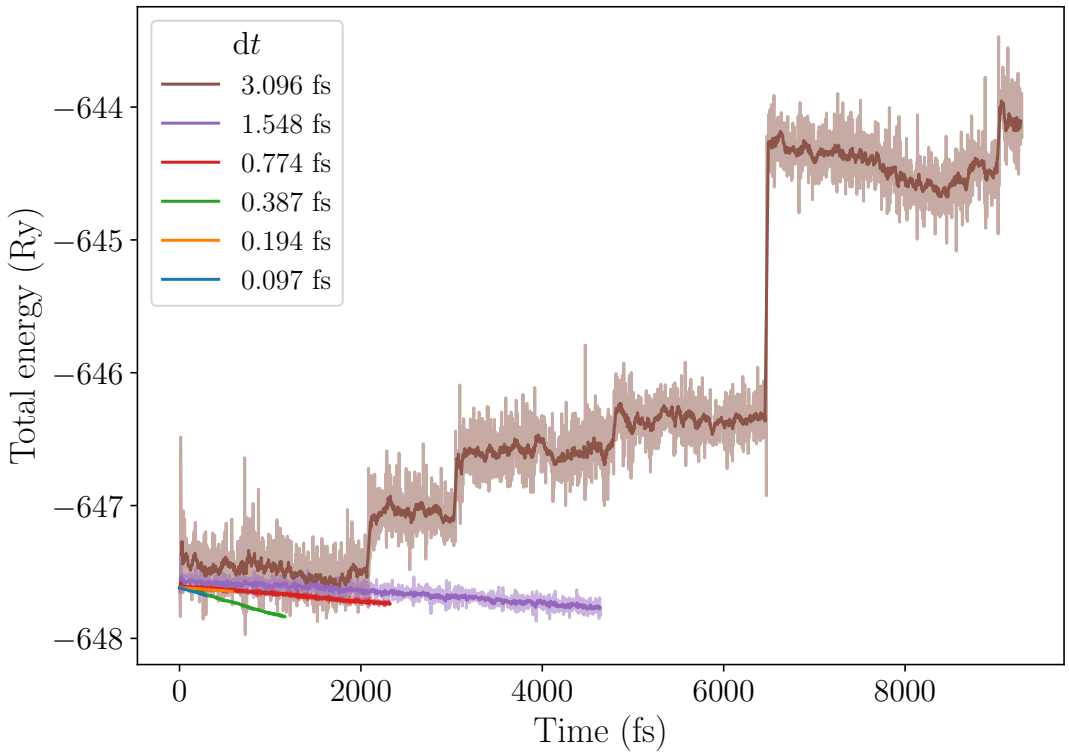

Figure 5.3: Total energy throughout a microcanonical MD simulation for various time steps dt and 3000 iterations. The light coloured lines indicate the total energy at each time step, whilst the dark coloured lines are the centered moving average of $w = 11$ time steps (Eq. 5.8). The smallest time steps (blue and orange) are hidden below the larger time steps. The system contains 108 aluminium atoms with $\rho = 2.37$ g/cm^3 and $T_{\text{eq}} = 100$ kK. The MD simulations were performed using the `PROFESS@QE` program, with the forces at each time step calculated using the semi-local VT84F OF-DFT functional and the velocity Verlet algorithm used for time integration. For the largest time step (d$t = 3.096$ fs), the total energy is unstable with a large energy drift visible. For lower time steps, the total energy still drifts slightly, due to numerical error, but is relatively stable. The time step calculated using Eq. 5.19 (d$t = 0.119$ fs) falls within the stable regime.

20 K, or 0.02%, per 100 fs. The same percentage drop is found for the simulations at 10 kK. Considering the relative size of the energy drift, and the fact that the use of a thermostat will negate the temperature drift given a reasonable number of time steps, this error is acceptable. The relation given by Eq. 5.19 is therefore assumed to be suitable throughout this thesis. The use of a higher-order integrator, such as the Runge-Kutta methods, may lower the energy drift without requiring a smaller time step; however, this will not be investigated here.

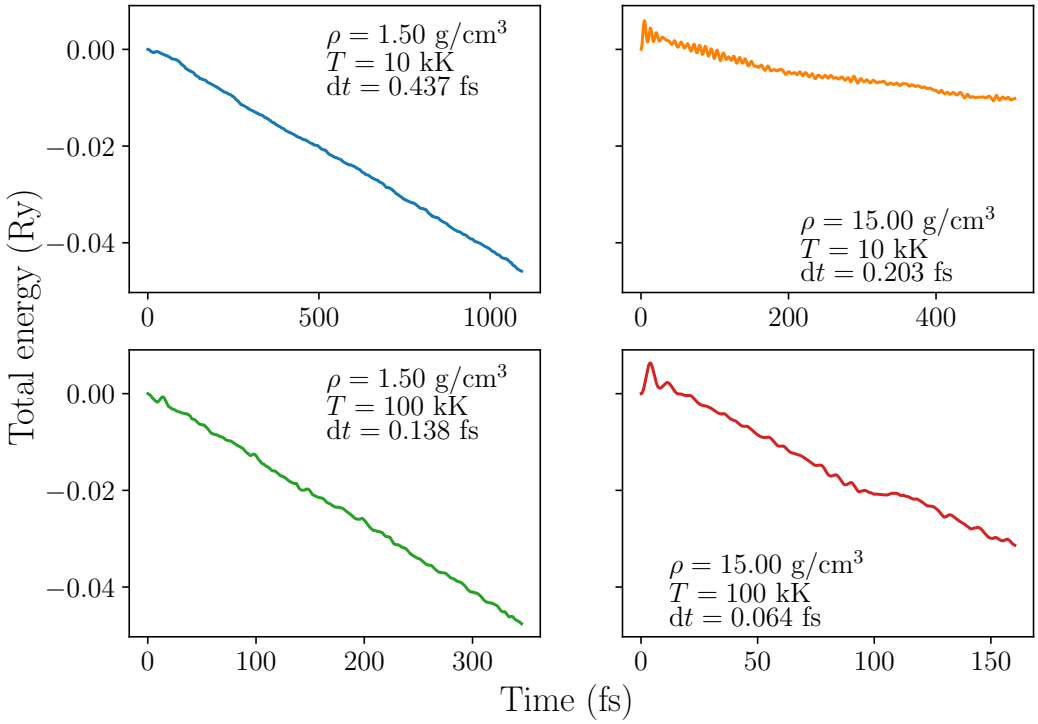

Figure 5.4: Total energy throughout a microcanonical MD simulation for permutations of the minimum and maximum density and temperature investigated in this thesis. All total energies have been shifted to zero energy at time $t = 0$. The time step dt was determined according to Eq. 5.19 and the simulation was run for 2500 iterations. The system contained 108 aluminium atoms for all simulations. The MD simulations were performed using the `PROFESS@QE` program, with the forces at each time step calculated using the semi-local VT84F OF-DFT functional and the velocity Verlet algorithm used for time integration. All simulations show stable total energies with a small energy drift, discussed further in the text.

5.6 Summary

In this chapter, molecular dynamics (MD) has been introduced as a method for simulating the ionic motion of a system of atoms, with the electrostatic and electronic effects calculated by an interatomic potential or DFT method. Equations for calculating the temperature, pressure, and other statistical quantities during an MD simulation have been presented. Although the exact dynamics of a single ion during an MD simulation are potentially unphysical, since the interatomic forces used are the thermodynamic 'mean' forces, the ergodic hypothesis allows for the calculation of thermodynamic properties by a time average over the simulation, so long as the average is taken over a long enough

period.

Before any properties are calculated, the system must first be equilibrated. This removes any exact symmetries or other biases present in the initial configuration. This drastically reduces the simulation time required to calculate equilibrium properties. To equilibrate the system at a specific temperature, a thermostat must be used. Thermostats work by adding or removing kinetic energy from the ions, such that the instantaneous temperature approaches the target temperature. The ionic motion then converts this kinetic energy into potential energy, and vice versa. Certain thermostats conserve different properties and can therefore be used for different purposes; however, for the uses required here, only static properties need to be accurate. This means that any thermostat that accurately reproduces the canonical ensemble in equilibrium can be used.

Finally, the choice of time step was discussed. A balance must be struck between a smaller time step, and therefore more iterations and force calculations, and a larger time step, which can lead to instabilities and energy drift. A scaling formula was presented with a constant average distance travelled for each ion in an iteration, no matter the equilibration temperature or material density.

Chapter 6

Atomic Cluster Expansion

The *Atomic Cluster Expansion* (ACE) is a general and complete descriptor of the local atomic environment derived using single-bond (two-atom) basis functions [50]. Its physical motivation leads to a more intuitive and interpretable functional form than machine-learning potentials, whilst maintaining the accuracy and transferability required for use in multi-scale MD simulations. It has shown successes in modelling materials that have previously been well described by empirical potentials, e.g., copper, as well as materials such as silicon that, until recently, have eluded description by a single functional form [147]. By expressing the atomic contributions to the energy as a polynomial of so-called atomic bases, it can be shown that the effort required to evaluate an ACE scales linearly with the average number of neighbours within the local environment of an atom. Furthermore, a nonlinear functional of ACEs can be constructed to avoid the poor convergence of the linear ACE.

6.1 Single-bond basis functions

A similar derivation to that of Ref. [50] will be followed here. To begin, the total energy of the system is divided into atomic contributions,

$$E = \sum_i E_i, \tag{6.1}$$

with i labelling the atoms. Each atomic energy E_i is then expressed by

$$E_i = V^{(1)}(\mathbf{r}_i) + \frac{1}{2!}\sum_j V^{(2)}(\mathbf{r}_i, \mathbf{r}_j) + \frac{1}{3!}\sum_{jk} V^{(3)}(\mathbf{r}_i, \mathbf{r}_j, \mathbf{r}_k) + \ldots, \tag{6.2}$$

where $V^{(K)}$ represents a general descriptor of the K-body interactions.

In this form, the expansion has two key problems. Firstly, it can give a good description of small clusters; however, for bulk materials terms of $K > 15$ are required to converge the total energy [170]. Secondly, it is computationally prohibitive to include all atoms j, where $j \neq i$, in the summations. It is therefore common to introduce a cutoff radius r_c to limit the expected number of neighbours of each atom to N_c. Tweaking r_c to achieve a reasonable accuracy leads to $N_\mathrm{c} \approx 10^2 - 10^3$, preventing the efficient evaluation of an expansion of order greater than $K = 3$. This is due to the scaling of the computational effort required to evaluate an order K term as $N_\mathrm{c}^{(K-1)}$.

A complete set of orthogonal basis functions $\phi_v(\mathbf{r})$ is introduced, where $v = 0, 1, 2, \ldots$ is the basis function label and $\mathbf{r}$ is a three-component vector. The cluster basis function is defined as

$$\Phi_{\alpha\nu} = \phi_{v_1}(\mathbf{r}_{j_1 i})\phi_{v_2}(\mathbf{r}_{j_2 i}) \ldots \phi_{v_K}(\mathbf{r}_{j_K i}), \tag{6.3}$$

where $\alpha = (j_1 i, j_2 i, \ldots, j_K i)$ labels a cluster of K atoms, $\nu = (v_1, v_2, \ldots, v_K)$ labels the single-bond basis functions within the cluster, and $\mathbf{r}_{ji}$ is the vector from atom i to atom

j in the cluster. By choosing $\phi_0 = 1$, the atomic energy can be expressed as

$$E_i = \sum_{\alpha\nu} J_{\alpha\nu}\Phi_{\alpha\nu}, \tag{6.4}$$

where $J_{\alpha\nu}$ is the expansion coefficient of the cluster basis function $\Phi_{\alpha\nu}$.

For a cluster of atoms of the same element, the energy (or any other observable) is invariant under exchange of bonds, i.e., exchanging bonds ji and ki where atoms j and k are of the same element. Therefore, the dependence of the expansion coefficient $J_{\alpha\nu}$ on α can be reduced to a dependence on the number of bonds K within the cluster α, $J_\nu^{(K)}$. By also choosing $J_0 = 0$ and formulating the sums to be unrestricted over the neighbours j_k, the atomic energy takes the form

$$E_i = \sum_j \sum_v c_v^{(1)}\phi_v(\mathbf{r}_{ji}) + \frac{1}{2}\sum_{j_1 j_2}\sum_{v_1 v_2} c_{v_1 v_2}^{(2)}\phi_{v_1}(\mathbf{r}_{j_1 i})\phi_{v_2}(\mathbf{r}_{j_2 i}) + \ldots, \tag{6.5}$$

where $c_v^{(K)}$ are the updated expansion coefficients.

A direct link to the many-body expansion, introduced in Chapter 9, can be made as each $\phi_v(\mathbf{r})$ corresponds to the interaction of atom i with one of its neighbours. Products of $\phi_v(\mathbf{r})$ incorporate progressively higher order interactions into the expression, with $c_v^{(K)}$ corresponding to contributions to $V^{(K+1)}$.

6.2 Atomic bases

This reformulation hasn't, as of yet, fixed either the poor scaling with N_c or the slow convergence with K; it has simply re-expressed the problem as a function of single-bond basis functions. To tackle the former issue, the atomic base

$$A_{iv} = \langle \varrho_i | \phi_v \rangle = \sum_j \phi_v(\mathbf{r}_{ji}), \tag{6.6}$$

is introduced, where the atomic density is given as

$$\varrho_i = \sum_j \delta(\mathbf{r} - \mathbf{r}_{ji}). \tag{6.7}$$

Substituting this definition into Eq. 6.5 gives

$$E_i = \sum_v c_v^{(1)} A_{iv} + \sum_{v_1 v_2}^{v_1 \geq v_2} c_{v_1 v_2}^{(2)} A_{iv_1} A_{iv_2} + \ldots, \tag{6.8}$$

where the atomic energy is now a simple polynomial of A_{iv}. The sums over neighbours j are now only evaluated when the atomic bases are calculated.

The key reason that Eq. 6.8 is so useful is that the atomic bases can be precalculated. The atomic bases scale linearly with N_c, but only need to be calculated once for a particular cluster and single-bond basis set. The evaluation of Eq. 6.8 is now independent of N_c, allowing the calculation of the energy to scale linearly with N_c for any order expansion. The expected translation, rotation, inversion, and permutation (TRIP) invariance of the energy is enforced by use of the generalised Clebsch-Gordan coefficients to generate an isometry invariant basis,

$$\mathbf{B} = \mathbf{C}\mathbf{A}, \tag{6.9}$$

where $\mathbf{C}$ are the Clebsch-Gordan coefficients, $\mathbf{A}$ is the appropriate product of atomic bases A_{iv}, and $\mathbf{B}$ is the resulting isometry invariant basis. The Clebsch-Gordan coefficients can be recursively generated [171], simplifying the calculation of the $\mathbf{B}$ basis. Further details and discussions relating to the choice of the single-bond basis functions, the Clebsch-Gordan coefficients, and how the forces are analytically evaluated, can be found in Refs. [50] and [147].

6.3 Nonlinear Atomic Cluster Expansion

Expressing the energy in the form of Eq. 6.8 is referred to as a linear ACE. If used as is, there will be a poor convergence with K that, in part, is due to the fact that the linear ACE assumes that the energy can be expressed as a sum of contributions from individual bonds [170]. In reality, chemical bond formation is nonlinear and this approximation breaks down. Instead, the energy can be expressed as a nonlinear function of so-called *atomic properties* chosen such that they can be approximated well by a linear expansion. This lessens the effect of the poor convergence by better representing the many-body interactions.

The expression for the atomic energy is therefore changed from

$$E_i = \varphi_i^{(1)}, \tag{6.10}$$

where $\varphi_i^{(1)}$ is an atomic property expressed by a linear Atomic Cluster Expansion, to the more general

$$E_i = \mathcal{F}(\varphi_i^{(1)}, \ldots, \varphi_i^{(p)}), \tag{6.11}$$

where $\mathcal{F}$ is some nonlinear function of p atomic properties.

As an enlightening example, it will be shown how the Finnis-Sinclair potential can be represented by a nonlinear Atomic Cluster Expansion. The Finnis-Sinclair potential incorporates the finding from the second-moment approximation to quantum mechanical tight-binding theory that the atomic cohesive energy scales like the square root of its atomic coordination [132, 149]. The functional form of the Finnis-Sinclair potential was given in Eq. 4.16. The similar embedded atom method [172, 150, 134] can be found by replacing $\sqrt{\rho_i}$ with some arbitrary nonlinear function.

The Finnis-Sinclair potential can be seen as a nonlinear function of two atomic properties,

each represented by a linear Atomic Cluster Expansion,

$$E_i^{\mathrm{FS}} = \sqrt{\varphi_i^{(1)}} + \varphi_i^{(2)}, \tag{6.12}$$

with

$$\begin{aligned} \varphi_i^{(1)} &= \rho_i \\ \varphi_i^{(2)} &= \frac{1}{2}\sum_j V(R_{ji}), \end{aligned} \tag{6.13}$$

where $\rho_i = \sum_j \phi(R_{ji})$, and ϕ and V are some pairwise functions of the atomic separation R_{ji}. From comparison to Eq. 4.16, the local charge density term and repulsive term have been expressed as Atomic Cluster Expansions, both truncated to only include pairwise contributions. To better reproduce the many-body and angular contributions present in certain materials, higher order terms in the respective Atomic Cluster Expansions of the atomic properties can be included.

Alternatively, a different nonlinear Atomic Cluster Expansion $\mathcal{F}$ can be chosen, either empirically or through physical intuition. For instance, the EAM potential can be expressed by removing the constraint of a square root in Eq. 6.12.

6.4 Fitting a local potential to free energy

The Atomic Cluster Expansion has been derived as a general descriptor of some energy. When modelling forces in warm dense matter, the temperature is non-zero and the energy of interest is therefore the Helmholtz free energy. Whilst the terms "energy" and "free energy" will be used interchangeably here, it is important to understand that the relevant free energy F contains the electronic Helmholtz free energy for fixed ionic positions, calculated assuming the Born-Oppenheimer approximation, along with the Ewald sum for the static ion-ion interactions. Since the ions are held stationary, there is no entropic contribution from the ions included in F. For further discussion, refer to Section 4.1. The

resulting ACE potential is therefore defined to reproduce a free energy F that contains only electronic temperature-dependent contributions. The ionic temperature-dependent contributions then arise from explicitly integrating the ionic equations of motion in the MD simulation.

It is assumed that the energy can be partitioned into an electron gas contribution F_{g}, dependent only on the average electronic density of the system, and a chemical bond term F_{b}. The latter will be modelled by a nonlinear Atomic Cluster Expansion, whilst the former will be expressed analytically. An alternative way of viewing this is as a decomposition into localised and delocalised electronic contributions.

6.4.1 Electron gas contribution

In the derivation of the ACE, a cutoff radius is used to limit the number of neighbours that must be considered. Therefore, to fit an Atomic Cluster Expansion for which a cutoff $E_i(r > r_{\mathrm{c}}) = 0$ is appropriate, it is required that $F_{\mathrm{b}}(V \to \infty) = 0$. Physically, this requirement ensures that there is no bonding at extremely low densities.

The total energy is therefore expressed as

$$F = F_{\mathrm{b}} + F_{\mathrm{g}}, \tag{6.14}$$

and the pressure can be written as

$$P = P_{\mathrm{b}} + P_{\mathrm{g}}, \tag{6.15}$$

where P_{b} can be calculated using Eq. 5.3 as the sum of the ionic ideal gas and virial contributions. The electron gas contribution P_{g} can be found by differentiating F_{g} with respect to V. The force on atom i is simply the ACE potential force,

$$\boldsymbol{\mathcal{F}}_i = \boldsymbol{\mathcal{F}}_{i,\mathrm{b}}, \tag{6.16}$$

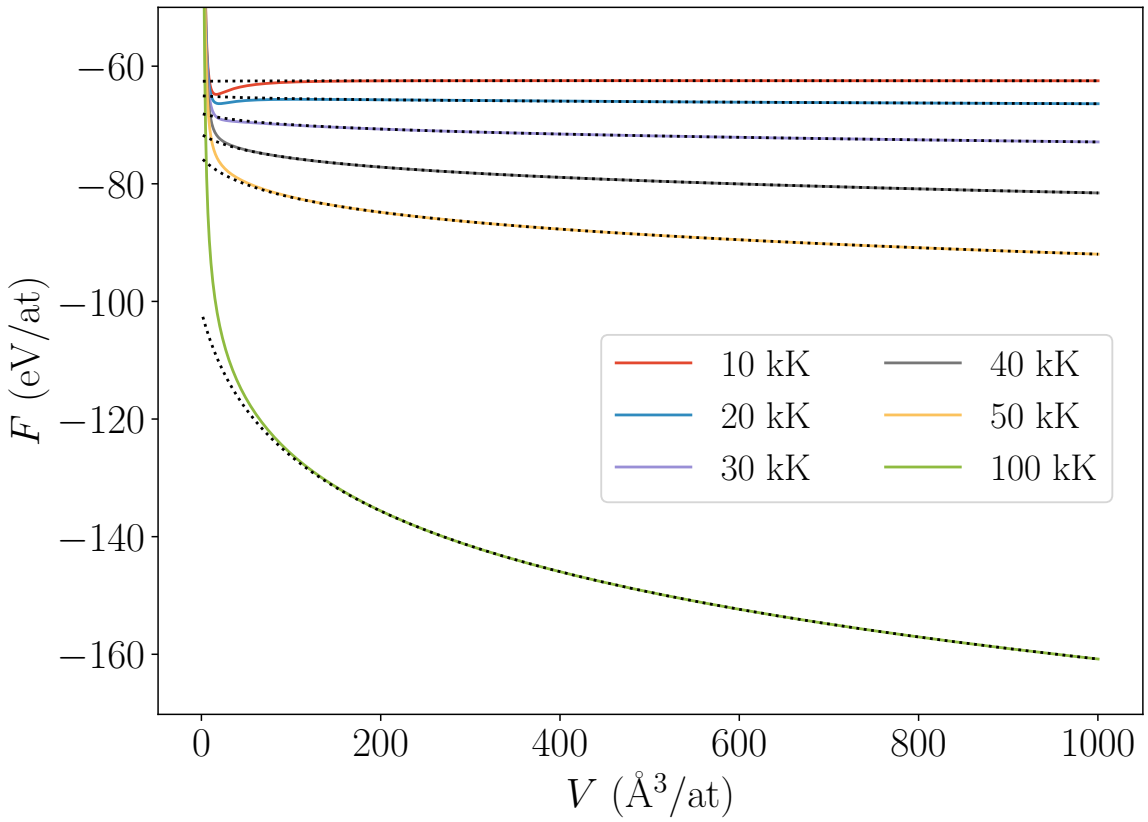

Figure 6.1: MHKS-DFT free energy for varying volume in fcc aluminium. The dotted lines are fits to Eq. 6.21 for each of the electronic temperatures and for data with a primitive fcc unit cell volume $V > 235$ Å^3.

as F_g is assumed to be independent of the ionic positions and so does not contribute to the forces, although it does contribute to the pressure.

Shown in Fig. 6.1 is the variation of the free energy of fcc aluminium with the volume per atom at a range of electronic temperatures, calculated using MHKS-DFT. The fcc data was produced using the same specifics (e.g., psuedopotential, XC functional, etc.) as the rest of the MHKS-DFT data discussed in Section 6.5.1, with the exception of the number of explicit KS orbitals N_{occ} and k-point grid, which were varied to ensure convergence.

Due to the finite electronic temperature, the entropic contribution causes the Helmholtz free energy of the system in Fig. 6.1 to tend to negative infinity as the volume per atom tends to infinity, demonstrating the need for the partition into electron gas and chemical bonding contributions. In fact, above 30 kK there is no local minimum in the free energy, implying that the system has no quasi-equilibrium state, if no external pressure is applied.

Even for those temperatures with a local minimum in the free energy, as V continues to increase the $-TS$ term grows without bound, leading to an increasingly negative free energy.

Perhaps the simplest model of F_{g} would be as the energy of a classical ideal gas. In an ideal gas, the electrons are not only non-interacting, but also do not feel any potential from the positive ions. Modelling the electrons as classical particles is a suitable approximation when the electron density is low enough that the thermal de Broglie wavelength is much smaller than the inter-electron separation. Whilst the electrons should behave classically at large enough V and T, the warm dense regime does not correspond to this limit. Rather, it is the crossover regime between the low-temperature quantum ($k_{\mathrm{B}}T \ll E_{\mathrm{F}}$) and high-temperature classical ($k_{\mathrm{B}}T \gg E_{\mathrm{F}}$) limits. The ideal gas model is used as a first approximation to modelling F_{g} at the largest volumes within the fitting dataset.

The free energy of a system can be expressed as

$$F = U - TS, \tag{6.17}$$

with U the internal energy and S the entropy. For an ideal gas, the internal energy is given by the equipartition theorem,

$$U = \frac{3}{2} N k_{\mathrm{B}} T, \tag{6.18}$$

with N the number of particles. The entropy can be calculated using the Sackur-Tetrode equation [173], derived as the entropy of a monatomic classical ideal gas,

$$\frac{S}{k_{\mathrm{B}} N} = \ln\left[\frac{V}{N}\left(\frac{4\pi m}{3h^2}\frac{U}{N}\right)^{3/2}\right] + \frac{5}{2}, \tag{6.19}$$

where m is the mass of the particle and h is Planck's constant. It is then simple to see that for constant T and N,

$$F \propto -\ln V. \tag{6.20}$$

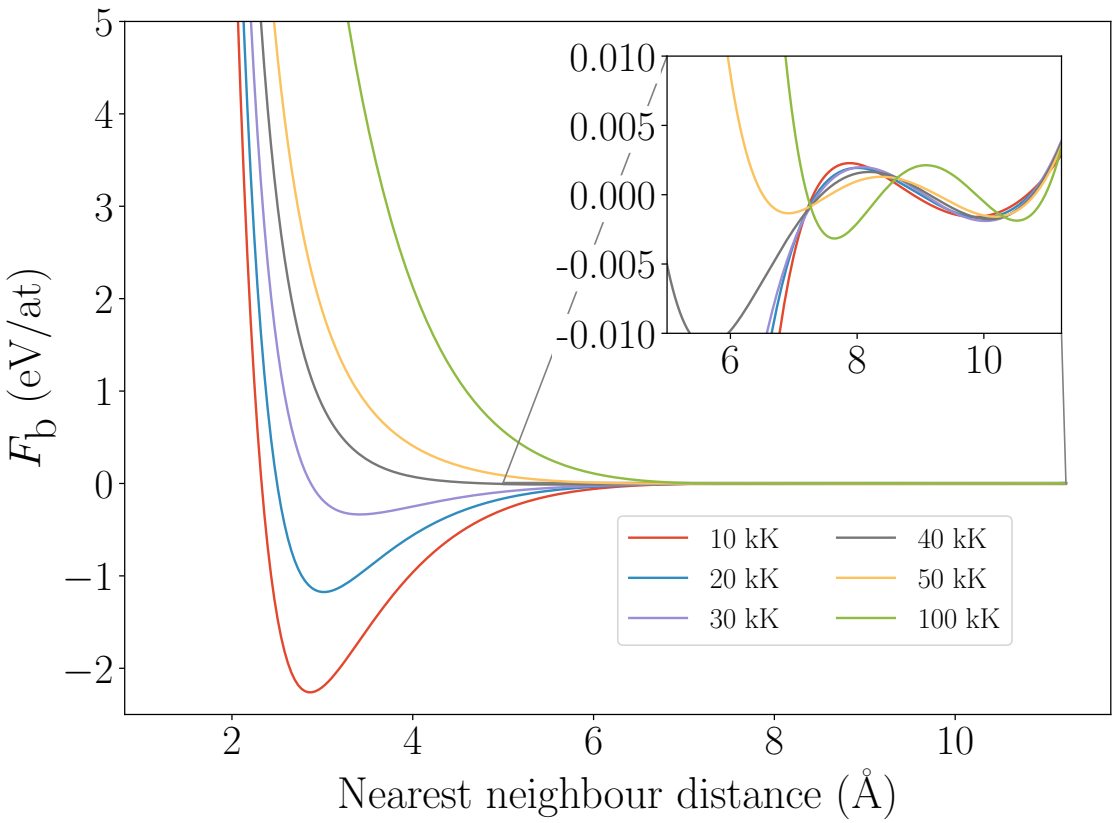

Figure 6.2: Chemical bond energy F_b for varying nearest neighbour distance d in fcc aluminium. The inset plot is a zoom-in on nearest neighbour distance $d > 5$ Å which shows the meV oscillations around zero.

As discussed previously, at large volumes F_g is expected to dominate and so the analytic expression of Eq. 6.20 can be fit to the large volume DFT data of fcc aluminium. When attempting to fit this ideal gas relation to the DFT data for volume per atom $V_{at} > 235$ Å^3, the optimisation either fails, or produces poor results. The following function is therefore used:

$$F_g(V) = a + b \ln\left(1 + \frac{V}{V_0}\right) + cV, \tag{6.21}$$

where a, b, and c are temperature-dependent fitting parameters, the term linear in V can be seen to correct for the non-ideal behaviour, and V_0 is a structure-dependent constant.

The dotted curves in Fig. 6.1 show this fit for constant electronic temperatures of 10, 20, 30, 40, 50, and 100 kK. The analytic function matches well with the DFT data, validating the choice for the functional form of the electron gas contribution. The resulting F_b from Eq. 6.14 is plotted in Fig. 6.2, where the difference from the expected $F_b(V \to \infty) = 0$

can be seen to be of the order of a few meV. From Fig. 6.2, the cutoff radius is chosen to be $r_c = 7.0$ Å. This is because the oscillations in F_b for nearest neighbour distances greater than this are both small in magnitude and likely to be insignificant compared to the error in the approximation for F_g. The chemical bonding energy at all temperatures decays smoothly to zero as the atomic separation r approaches r_c from below.

6.5 Parameterisation

For the fitting of the warm dense aluminium ACE potentials in this thesis, the Finnis-Sinclair nonlinear function of Eq. 6.12 is chosen with Atomic Cluster Expansions including up to four-body contributions ($K_{max} = 3$). A second set of potentials with the same nonlinear function and Atomic Cluster Expansions including only one- and two-body contributions ($K_{max} = 1$) is also fit, to give insight into the importance of K_{max} and the many-body contributions.

The GPU-accelerated fitting of ACE potentials has been implemented by Bochkarev et al. in the `pacemaker` program [174], and the efficient evaluation of energies and forces can be achieved within `LAMMPS` [175] by using the `ML-PACE` library, written by Lysogorskiy et al. [147].

6.5.1 Dataset

To create a dataset, configurations of atoms, referred to as snapshots, must be generated or chosen. The collection of snapshots, along with their corresponding free energies and forces, constitute the dataset. Although stress data was not used in the fitting of the ACE potentials, including this data may improve the accuracy of the predicted pressures. Ideally, if the snapshots are to be generated by MD simulations, the MD simulation would use the most accurate method for calculating the free energies and forces; however, this often requires significant computational resources. Therefore, the snapshots can be

generated using a less computationally expensive method, with the free energies and forces of the snapshot calculated with the more accurate method. If a less accurate method is used to generate the snapshots, there is a risk that the configurations sampled will not be representative of the true dynamics of the system. For instance, if a method is non-ergodic, there will be portions of the phase space which are impossible to sample. To avoid this, an iterative approach could be used: an initial ACE potential could be fit using the configuration generated by the less accurate method, and then the ACE potential used to generate further snapshots.

For low temperature parameterisations, the relevant phases and structures of the material must be carefully selected and included in the training dataset to ensure that ground-state properties are correctly reproduced. Furthermore, surfaces, defects, and randomised MD configurations must also be sampled to improve transferability of the potential [176]. In the warm dense regime, aluminium is a liquid and entropic contributions to the free energy dominate, meaning that structures with symmetry or crystalline order are no longer the lowest free energy configurations. Therefore, the training dataset primarily consists of liquid snapshots from MD simulations at elevated temperatures.

The MD snapshots are generated using `PROFESS@QE` [90], which couples OF-DFT electronic energy minimisations from `PROFESS` [75, 76], to the MD module of `pw.x` within the `Quantum Espresso` suite [105, 106], a combination referred to as OF-MD. The local VT84F functional is included in the most recent release, and I extended the software to include the non-local SDF functional. MHKS-DFT molecular dynamics (MHKS-MD) was not used to generate the snapshots due to the vast computational resources required at the temperatures and densities considered here. The quality of the ACE fits should not be particularly affected by the use of OF-MD, since the energies and forces of the final snapshots will be calculated using MHKS-DFT. The accuracy of the dynamics within the OF-MD simulation is therefore unimportant, so long as the atomic configurations sampled are relatively random and drawn from the correct ensemble, e.g., there are no atoms with close to zero separation. A 3 valence electron (3e) bulk-derived local pseudopotential [177, 178] generated using the Perdew-Zunger XC functional [64] was used for all OF-DFT

calculations, and a plane wave cutoff energy of 750 eV was chosen, which is in line with that given in Ref. [178] such that total energies are converged to within 0.01 meV/atom.

The training dataset contained the fcc data used to fit F_{b}, along with a total of 760 equilibrated snapshots of 108 aluminium atoms with a range of densities (1.50 g/cm^3 - 15.00 g/cm^3) and equilibration temperatures (10 - 100 kK), producing data from a large part of the warm dense regime. For the 108 atom snapshots, the 3×3×3 fcc supercell was chosen as the starting configuration. OF-MD, using either the SDF or VT84F functional, was then used to equilibrate the system in the NVT ensemble using the Andersen thermostat [163]. Only the snapshots with a material density of 2.37 g/cm^3 used the VT84F functional, due to this being the most accurate functional implemented at the time; however, thermodynamic properties such as the radial distribution function were validated against SDF results after the fact and found to match sufficiently. Each snapshot was taken from an independent run to ensure there was no correlation between the configurations. The number of time steps for equilibration was determined manually by observing the total energy throughout the run and ensuring it had reached a steady state. This corresponded to between 4000-10,000 time steps, depending on the temperature and density.

The training and testing datasets were both produced using MHKS-DFT, due to it being the most accurate method of calculating energies, forces, and electronic structure properties from zero temperature up to warm dense matter conditions. All MHKS-DFT calculations were performed using the `pw.x` program in the `Quantum Espresso` (QE) package [105, 106]. The KSDT XC free energy functional was used for the generation of the datasets (both in MHKS-DFT and OF-DFT) to account for the finite-temperature effects often found in WDM; however, it is expected that there would be no noticeable difference if the GDSMFB functional was used instead [179].

A 3e Optimized Norm-Conserving Vanderbilt (ONCV) pseudopotential from `PseudoDojo` [120, 119], generated using the Perdew-Zunger XC functional, was used in all MHKS-DFT calculations. A plane wave cutoff energy of 60 Ry was chosen for the non-local pseudopotential, as suggested by `PseudoDojo` such that the total energy per atom at 300 K was

converged to within 0.2 meV/atom. Two potential issues in this choice of pseudopotential are: 1) that the XC functional used in the calculations is not the same as the XC functional used to generate the pseudopotential, and 2) that using a pseudopotential with 10 electrons in the frozen core limits the range of temperatures and densities that can be studied.

As regards the former issue, Section 3.1 explained that the KSDT XC functional tends to the Perdew-Zunger functional as $T_\mathrm{e} \to 0$ [103]. Also, there is no method, known to the author, to fit a temperature-dependent pseudopotential using a T_e-dependent XC functional. This approximation has also been used previously [101]. As explained in Section 3.2, the severity of the latter issue can be reduced by limiting the systems such that they fall within certain temperature and density constraints. Further discussion on the use of this pseudopotential is presented in Section 8; however, the main aim here is to test the ability of the ACE to fit to and predict finite-temperature data, and the accuracy of the MHKS-DFT data is not expected to affect this.

Enough KS orbitals are included such that the highest energy single-particle KS orbital in each MHKS-DFT calculation has an occupancy $f_\mathrm{min} < 10^{-4}$, as this has been shown to be a requirement for accurate prediction of thermodynamic quantities [67]. For the liquid snapshots, only the Γ point of the Brillouin zone was sampled, as is common for non-crystalline configurations [47, 41]; however, comparison to a $2{\times}2{\times}2$ k-point grid shows convergence of the total free energy to within 2 meV/atom. Note that the total free energy contains a large entropic contribution at high temperatures, leading to larger differences in total free energies than would be expected in total energies at zero temperature.

MHKS-DFT calculations for T_e = 10, 20, 30, 40, 50, and 100 kK were performed on the training structures to produce separate datasets, and therefore ACE potentials, for each T_e. Only structures with $F_\mathrm{b} < 50$ eV/atom were included in the training datasets. The few structures with an energy high enough to be excluded are the lowest volume fcc results, due to the strong Coulomb repulsion present in these high density systems. In addition, structures with a force greater than 150 eV/Å on any atom were also excluded.

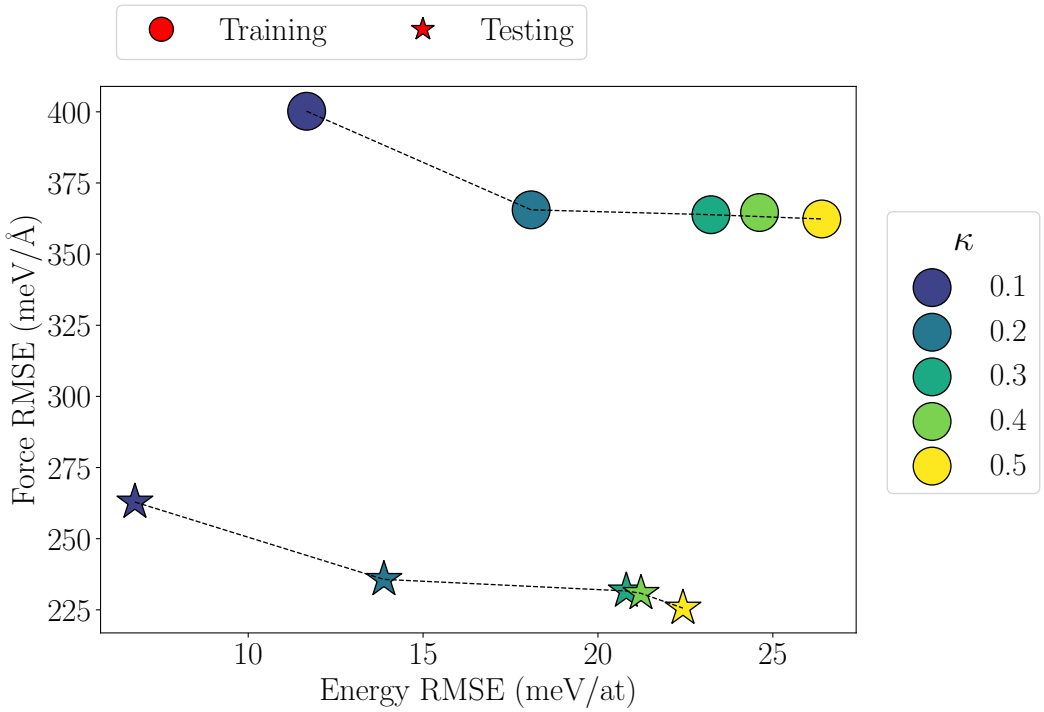

Figure 6.3: Scatter plot of energy and force RMSEs (defined in Appendix B) of a 10 kK ACE potential for different chosen values of κ. The dotted lines represent the Pareto fronts for the training and testing errors.

Without these restrictions, the fitting of the potential to the extreme free energies and forces can cause the overall quality of the fit to suffer.

Overall, there are approximately 82,000 (30,000) atomic environments per T_e in the training (testing) dataset. The testing dataset was generated in an identical manner with the same electronic temperatures; however, since the testing snapshots were generated from new MD simulations, computational constraints limited the dataset to only three densities. The testing dataset also didn't include any fcc snapshots.

6.5.2 Loss function and basis functions

To fit a model to a training dataset, a loss function that quantifies the quality of the fit must be chosen. The aim of the fitting procedure is to minimise this loss function. For the ACE potentials fit here, the loss function is defined as [174]

$$\mathcal{L} = (1-\kappa)(\Delta E)^2 + \kappa(\Delta \boldsymbol{\mathcal{F}})^2 + \Delta_{\text{coeff}} + \Delta_{\text{rad}}, \tag{6.22}$$

where $(\Delta E)^2$ and $(\Delta \boldsymbol{\mathcal{F}})^2$ are the weighted squared energy and force errors, and Δ_{coeff} and Δ_{rad} are the regularisation terms. Δ_{coeff} penalises large expansion coefficients c_v and is defined as [174]

$$\Delta_{\text{coeff}} = L_1 \sum_{\nu p} |c_v^{(p)}| + L_2 \sum_{\nu p} |c_v^{(p)}|^2, \tag{6.23}$$

with $L_1 = 1 \times 10^{-9}$ and $L_2 = 1 \times 10^{-11}$ for the potentials fit here. Δ_{rad} regularises the smoothness of the radial functions and is defined as [174]

$$\begin{aligned} \Delta_{\text{rad}} = \frac{w_0}{r_{\text{c}}^2} \int r^2 \sum_{nl} |R_{nl}(r)| \, \mathrm{d}r + \frac{w_1}{r_{\text{c}}^2} \int r^2 \sum_{nl} \left| \frac{\mathrm{d}R_{nl}(r)}{\mathrm{d}r} \right| \mathrm{d}r \\ + \frac{w_2}{r_{\text{c}}^2} \int r^2 \sum_{nl} \left| \frac{\mathrm{d}^2 R_{nl}(r)}{\mathrm{d}r^2} \right| \mathrm{d}r, \end{aligned} \tag{6.24}$$

with r_c the cutoff radius, R_{nl} the radial functions represented by a linear combination of radial basis functions, and $w_0 = w_1 = w_2 = 1 \times 10^{-8}$ for the potentials fit here. Regularisation will be discussed further in Section 6.5.3.

When fitting an ACE potential, the relative weighting of energy and force errors in the loss function κ dictates which set of errors (energies or forces) to prioritise. There is no *a priori* correct choice, but one suggestion is to plot the energy and force errors for a range of κ, forming a Pareto front [174], whilst another is to balance the variances in the energies and forces [180]. The errors in the energies and forces for preliminary fits with $0.1 < \kappa < 0.5$ at 10 kK are shown in Fig. 6.3.

The training dataset has larger energy and force errors than the testing dataset, likely due to the wider range of densities and structures contained in the training dataset, as discussed above. Since all (but one) values of κ lie on the Pareto front, each value can be said to be Pareto efficient. A value of κ is Pareto efficient if no other choice of κ decreases the force or energy RMSE without increasing the other. Therefore, the Pareto front does not produce a single optimum value of κ, but rather a set of values from which a particular κ can be chosen such that a desired balance of the energy and force RMSEs is achieved.

To decide the value of κ used in the final ACE fits, it is noted that the total energy has been partitioned into electron gas and chemical bonding contributions. The ACE potentials are therefore fit to the exact MHKS-DFT force, but not the total MHKS-DFT energy. Since the partitioning of the energy is an approximation that is used to allow for the fitting of a local potential, the chosen value of κ is biased in favour of the forces, which are known to be exact, insofar as the MHKS-DFT data is exact. Therefore, a value of $\kappa = 0.2$ was chosen.

The combinations of the radial and angular functions that fulfill TRIP invariance (denoted by $\mathbf{B}_{i\nu}$ in Ref. [50]) are referred to as the basis functions of the ACE. The specific choices for the basis functions used in the ACE potentials fit here are shown in Table 6.1. The number of functions in the fitted potentials is noticeably smaller than that of previous potentials [50, 147], due to this investigation acting as a proof of concept for a finite-temperature ACE potential. Even so, a good fit is achieved, as shown in Section 6.6. The robustness of the fitting procedure was tested by optimising from different random starting points. The differences in the energy and force errors of the potentials were negligible.

6.5.3 Optimisation considerations

Further to the choices made above, the optimisation method used is the BFGS algorithm [181], a second-order optimisation algorithm used to solve nonlinear optimisation problems. If a linear ACE functional was chosen, then an analytic solution that minimises the loss function could be found; however, fitting a nonlinear ACE potential to the training data allows for much more flexibility and generally leads to an overall better fit to the data.

A potential issue with any optimisation method is over- or under-fitting to the training data. Over-fitting occurs when the model fits too tightly to the training data, with poor transferability to new data. Under-fitting is the opposite, where the model does not capture the correct behaviours in the training data. A balance must therefore be struck

Functional	Radial basis functions	k	$n_{\max}$	$l_{\max}$	No. of funcs.	κ	r_c (Å)
FS ($K_{\max} = 1$)	Spherical Bessel (cos)	2	30	0	30	0.2	7.0
ACE ($K_{\max} = 3$)	Spherical Bessel (cos)	2	30/4/3	0/4/2	154	0.2	7.0

Table 6.1: Parameters of the ACE functional forms: radial basis functions (and cutoff function), number of radial basis functions (k), maximum principal ($n_{\max}$) and angular momentum ($l_{\max}$) quantum numbers, total number of functions, relative weighting of energy and force errors in the loss function, as defined in Ref. [174] (κ), and cutoff radius r_c.

to find the optimum fit. The aim of the testing dataset is to ensure that this balance is found. A Pareto front, such as in Fig. 6.3, can also be used to ensure that over/under-fitting is avoided. A common method to avoid over-fitting is to use regularisation terms in the loss function. With regularisation, extra terms are added to the loss function that punish both large coefficients (the c_v in Eq. 6.8) and non-smooth radial functions in the fitted potential. Both of these phenomena are associated with over-fitting, as large coefficients or non-smooth radial functions can lead to large changes in the energies and forces for small changes in the ionic positions.

6.6 Results

As a basic test of the quality of the invididual T_e ACE fits, the predicted free energies and forces for a selection of systems will be tested. Later on, the accuracy of the predicted pressures will be benchmarked by equation of state calculations and the finite-temperature effects will be observed in two-temperature MD simulations of laser-heated thin films.

6.6.1 Free energy and forces

By comparing the energies and forces predicted by the newly-fit ACE potentials to those predicted using MHKS-DFT, the quality of the fits can be checked. For the ACE potentials to be a useful method for use in large-scale MD simulations of WDM, they must provide a quantitative improvement on the accuracy of OF-DFT, whilst maintaining the high

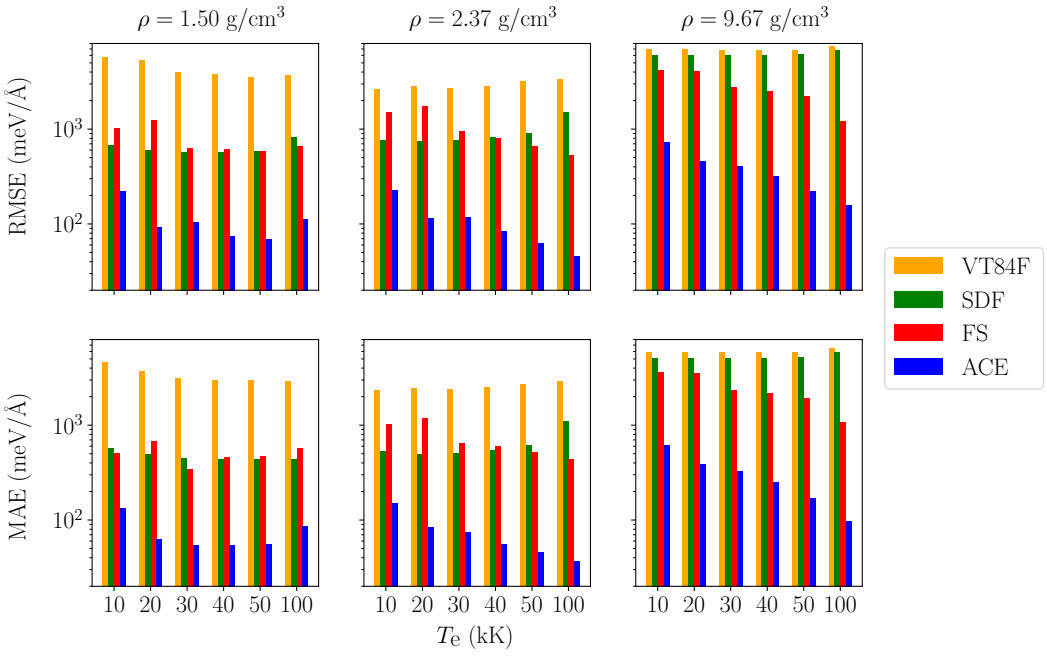

Figure 6.4: RMSE and MAE of forces for various electronic temperatures at three different densities of aluminium. All data points represent an average over 90 snapshots of 108 atoms. Note that the errors are shown on a log scale. Normalised force RMSEs are also shown in Fig. 6.6

computational efficiency and speed. In Figs. 6.4 and 6.5, the root-mean-square error (RMSE) and mean average error (MAE), defined in Appendix B, of the predicted forces and energies per atom are shown on a log scale. The chosen methods compared are OF-DFT with a semi-local (VT84F) functional, OF-DFT with a non-local (SDF) functional, the $K_{\max} = 1$ ('FS') nonlinear ACE potential, and the $K_{\max} = 3$ ('ACE') nonlinear ACE potential. All results are compared with the "exact" forces taken from converged MHKS-DFT calculations. Note that, although at room temperature chemical accuracy is approximately 40 meV/atom, an analagous "chemical accuracy" at finite temperature would be much larger due to the large entropic contribution ($-T_e S$) to the total free energy. A small error in the predicted entropy can therefore lead to a large error in the free energy, explaining the scale of the errors observed here.

The 'ACE' potential can be seen to perform best overall, and is the most accurate method at predicting energies and forces for every temperature at all densities. There are no

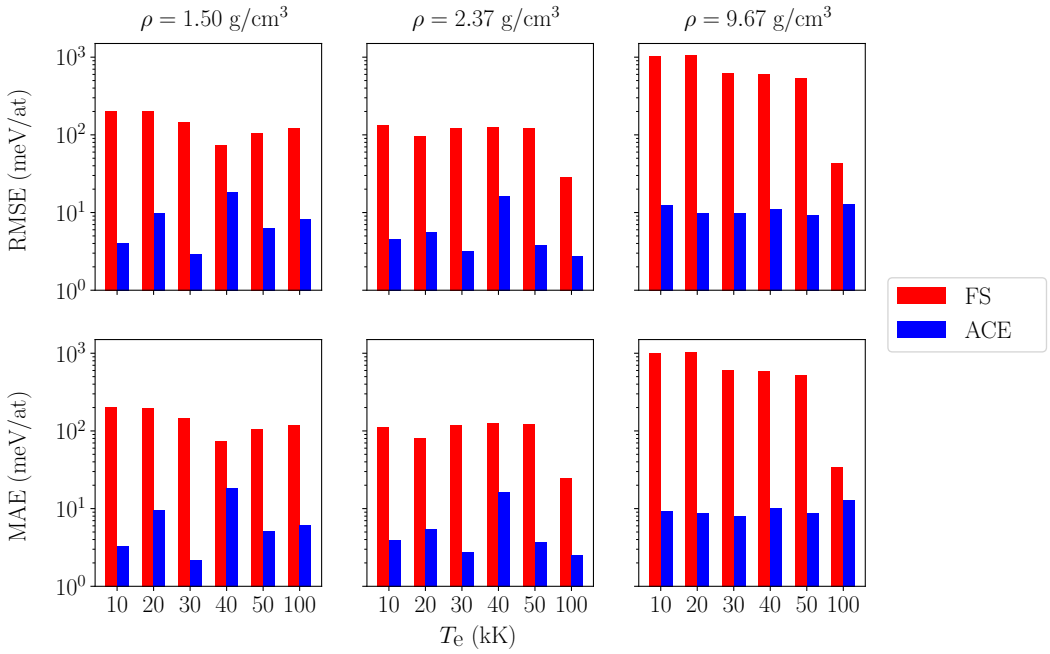

Figure 6.5: RMSE and MAE of energies per atom for various electronic temperatures at three different densities of aluminium. All data points represent an average over 90 snapshots of 108 atoms. Note that the errors are shown on a log scale. Due to the use of a different pseudopotential in the OF-DFT methods, absolute OF-DFT energies cannot be compared with MHKS-DFT, FS or ACE energies.

obvious outliers in the 'ACE' results, showing that good 'ACE' potentials can be obtained at all densities and temperatures considered here. There is approximately an order of magnitude between the 'FS' and 'ACE' RMSEs and MAEs. This shows the importance of including the many-body contributions in the Atomic Cluster Expansions.

The 'ACE' and 'FS' potentials both perform worst at the highest density; however, this pattern also holds for the OF methods. This may be because at higher densities the average interatomic separation is smaller, leading to larger energies and forces. The prediction of these energies and forces will then likely lead to larger errors. Another possible explanation for the reduced accuracy of the 'ACE' and 'FS' potentials at higher densities is that N_c increases with density. The larger number of neighbours may then require more basis functions and higher orders of interaction K (see Eq. 6.5) to fully describe the energies and forces.

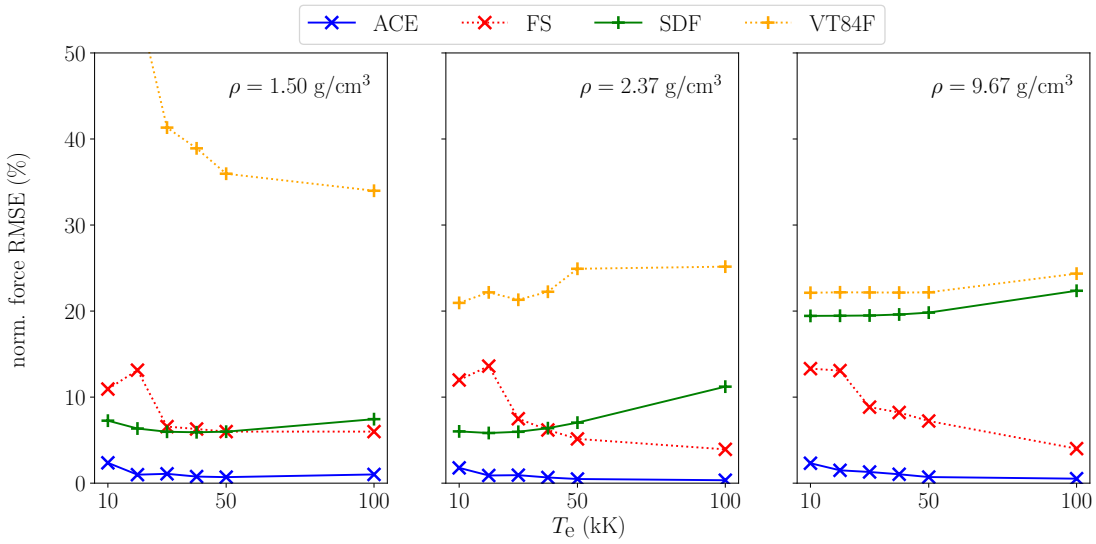

Figure 6.6: The normalised root-mean-square error of the forces, defined in Eq. B.3, for various electronic temperatures at three different densities of aluminium. Pluses indicate OF methods: SDF, solid green line; VT84F, dotted yellow line. Crosses indicate ACE methods: 'ACE', solid blue line; 'FS', dotted red line. All data points at all densities represent an average of 90 snapshots of 108 atoms.

To attempt to elucidate which of these effects is having the greatest impact, the normalised RMSE can be used to compare the relative errors in the forces as a function of temperature and density. The normalised RMSE of the forces is defined as the RMSE divided by the square root of the average squared force. This is shown in Eq. B.3. The normalised RMSE of the forces is plotted for varying T_e and density in Fig. 6.6. From Fig. 6.6, it can be seen that, once again, the 'ACE' potential is highly accurate over the entire range of temperatures and densities, with a normalised RMSE of a few percent in the forces. The 'FS' potential has more anomalies, due to the truncated order of the Atomic Cluster Expansion and small number of basis functions, leading to a worse fit. Still, it always gives results with a normalised RMSE less than 15% in the forces.

On the whole, there is no obvious temperature dependence in the relative accuracy of the 'ACE' results; however the 'FS' potential seems to perform worse at lower temperature. This indicates that the three- and four-body terms may become less important as the electronic temperature increases, as would be expected in a two-component plasma [135]. It is tempting to try and confirm this hypothesis by decomposing the fitted ACE potentials

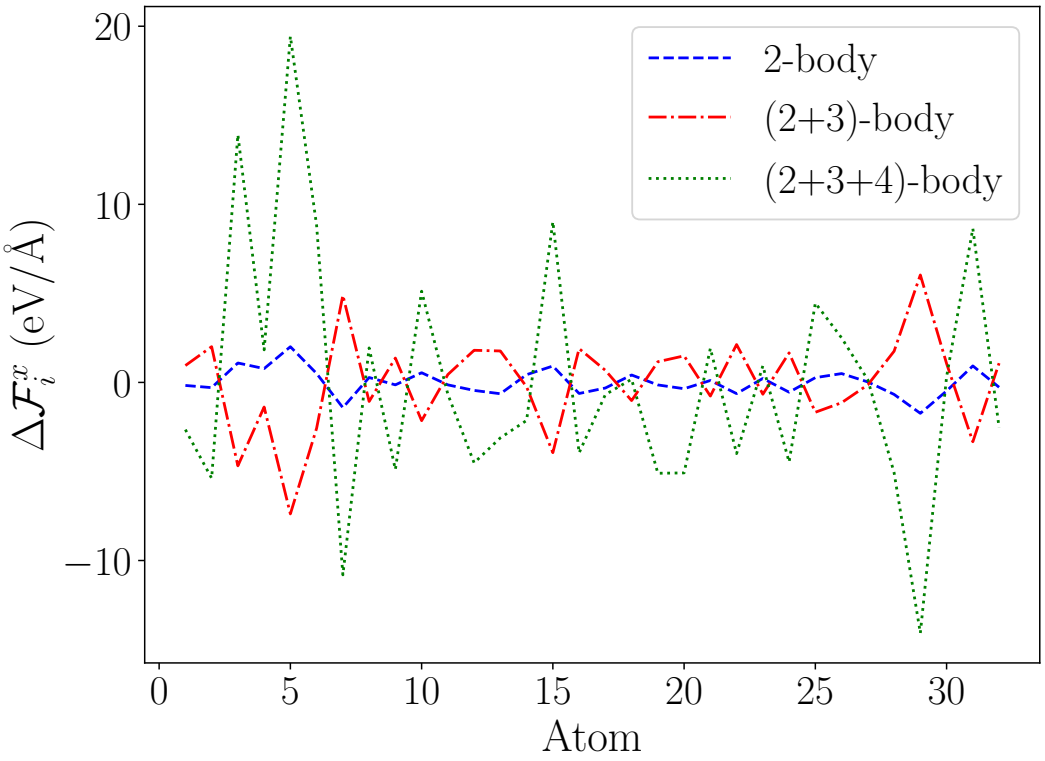

Figure 6.7: The difference in the x-direction force on atom i predicted by the many-body expansion (see Section 9), $\Delta\mathcal{F}_i^x$, in a 32 atom equilibrated aluminium snapshot at 10 kK. The differences are relative to the full 32 atom forces. Note that the n-body contributions to the many-body expansion are not calculated by truncating the ACE, but rather by calculating the interatomic forces within snapshots with only n atoms present. All forces are calculated using the 'ACE' potential in `LAMMPS`. The labelling of the atoms is arbitrary.

into individual K-body interactions using the many-body expansion [182], discussed in Section 9. However, doing so for a 32 atom system gives three- and four-body terms that lead to progressively less accurate predicted forces, as shown in Fig. 6.7. This may be due to the well-known convergence limitations of the many-body expansion in bulk metals [183, 170], or it may be caused by the simple ACE functional form used here.

Although the ACE potentials show good matching with the MHKS-DFT data, the relatively low $K_{\max}$ and small number of functions (see Table 6.1) likely do not provide a large enough basis set to truly capture all of the many-body effects present in warm dense aluminium. Instead, some of the higher body order interactions will be approximated by corrections to the lower order interactions, disrupting the interpretation of the individ-

ual K-body interactions. It is therefore likely that the superior accuracy of the 'ACE' potential is primarily due to the increased basis set size. Whilst elucidating individual K-body interactions to the ACE potentials fitted here proved unfeasible, the impressive accuracy displayed may be a benefit of using a nonlinear function to describe systems with interactions beyond $K_{\max}$. This could be confirmed by fitting a linear ACE potential to the same data and comparing the accuracy of the potentials.

The non-local SDF functional is more accurate at all temperatures and densities than the semi-local VT84F functional, as is to be expected from previous studies [124, 123, 77]. For lower densities, the non-local SDF functional is an order of magnitude more accurate than the semi-local VT84F functional; however, the gain in accuracy diminishes as the density increases. This may be due to the limitation of local pseudopotentials in OF-DFT, which cannot accurately model the interactions between atoms with a small separation. Specifically, the BLPS used here has a large core radius ($r_{\mathrm{c}} = 6.5$ a.u.) which is unlikely to be suitable for high density aluminium. This limitation is discussed further in Chapter 8.

6.6.2 Timing

To benchmark the performance of the methods, MD simulations were performed on an N_{at} atom $\rho = 2.37$ g/cm^3 aluminium system with periodic boundary conditions for N_{ts} timesteps. All methods used a single core, to ensure no overhead from MPI setup and calls was factored in. The MHKS-MD and OF-MD simulations used an Andersen thermostat [163], whereas the ACE-MD simulations used a Nosé-Hoover thermostat [167, 168]. This is not expected to alter the results noticeably.

Due to the computational limitations present, a variable N_{at} and N_{ts} was chosen depending on the method. For MHKS-MD, these were $N_{\mathrm{at}} = 8$ and $N_{\mathrm{ts}} = 1000$. For OF-MD, $N_{\mathrm{at}} = 108$ and $N_{\mathrm{ts}} = 1000$. For ACE-MD, $N_{\mathrm{at}} = 512$ and $N_{\mathrm{ts}} = 20{,}000$. To compare the methods equitably, the scaling relations derived in Section 2.8 were used to approximate the time per MD step for a chosen N_{at}. Although the system sizes were unlikely to be in

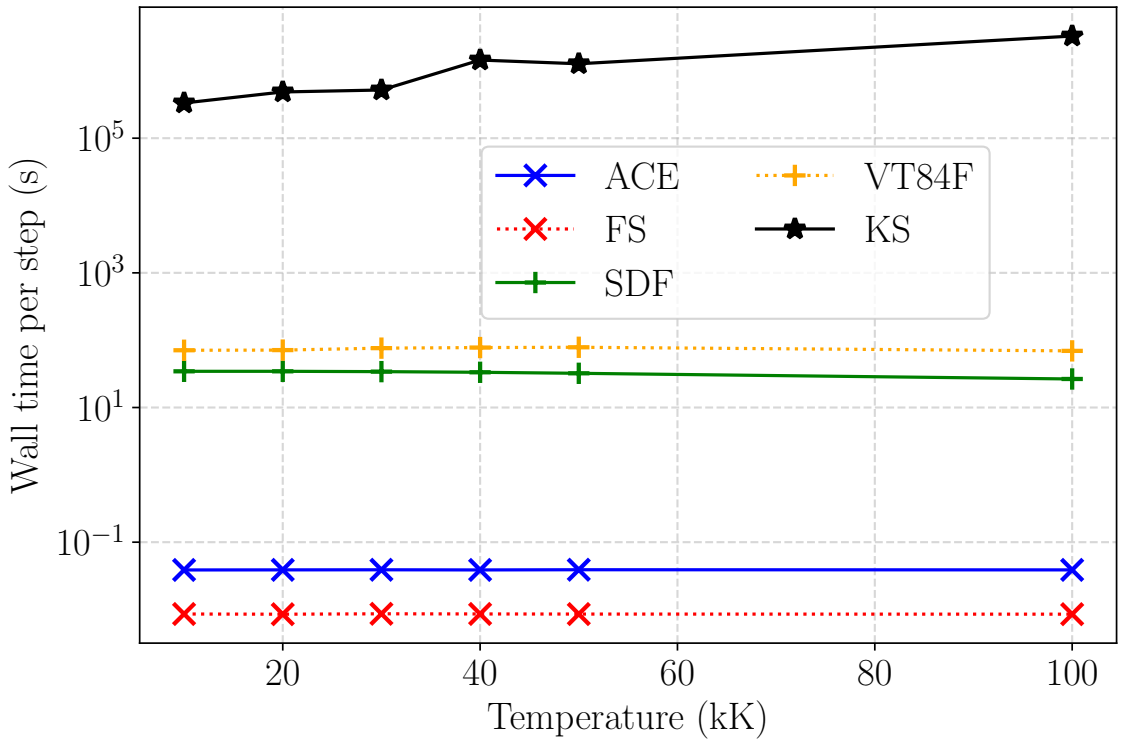

Figure 6.8: Wall time per MD step for various methods of simulating interatomic forces in aluminium at a range of temperatures. All wall times have been extrapolated to $N_{\text{at}} = 512$. The time per MD step of all of the methods, bar MHKS-DFT, is independent of temperature.

the asymptotic regime for which these scaling relations hold, the scaling relations are used here due to the lack of a more appropriate comparative method. Since the primary issue is the suitability of each method for simulating warm dense aluminium in MD simulations, it is logical to extrapolate to the largest system size, $N_{\text{at}} = 512$.

In Fig. 6.8, the wall time per MD step for each of the methods is shown. The only method that has explicit scaling of computational requirements with temperature is MHKS-DFT. MHKS-DFT also has much the largest prefactor, further limiting its potential use in large-scale MD simulations.

In line with expectations, the run times of the OF-DFT and ACE simulations are almost independent of temperature. Although it is expected that a semi-local functional should have a faster evaluation time than a non-local functional, the current implementation of

the VT84F functional is, in fact, slower. This may be because evaluating the VT84F functional requires more FFTs than evaluating the SDF functional. Interestingly, there is a slight decrease in wall time of the OF-DFT methods with increasing temperature. This has been observed previously, with an increasing homogeneity of the electron density being the most likely cause [77].

Within the ACE methods, the 'FS' potential is approximately five times faster than the 'ACE' potential, as is expected from the approximately five times as many basis functions in the 'ACE' potential compared to the 'FS' potential (see Table 6.1). There is a clear separation in the results for the OF-DFT and ACE methods. The ACE methods are, on average, three to four orders of magnitude faster than the OF-DFT methods. This is likely to vary slightly with the material density. At higher densities, evaluation of the ACE energies and forces will slow down. This is due to the increase in N_c, the expected number of neighbours within each atom's cutoff radius. As shown earlier, the computational effort required to evaluate an ACE potential scales linearly with the number of neighbours, explaining this trend. Even at these higher densities, where the ACE methods begin to slow and OF-DFT methods are at their fastest, the ACE potentials should be the most efficient method to calculate the energies and forces. It is also worth noting that the pseudopotential used in OF-DFT is likely to lead to poor results at high densities.

Therefore, these findings show that the ACE potentials are always significantly faster than any currently available OF-DFT method, whilst providing appreciably more accurate forces for warm dense aluminium. This opens the door to efficient, but accurate, MD simulations of the millions of warm dense aluminium atoms required to probe the effects and properties of free-electron laser heating experiments, collision cascades, and planetary cores.

6.7 Summary

The ACE has been introduced as a general and complete descriptor of the local atomic environment using only single-bond basis functions. The ACE avoids the poor scaling of the many-body expansion by using atomic bases which precalculate the contributions from each atom's neighbours. The cost of evaluating an ACE potential therefore scales linearly with the expected number of neighbours N_c. Furthermore, a nonlinear combination of ACEs can be used to better describe atomic bonding, reducing the order of interactions, and therefore the number of terms, required in each ACE. A Finnis-Sinclair-like nonlinear function was used to fit finite-temperature ACE potentials to MHKS-DFT data of equilibrated MD snapshots.

Since the ACE is a local potential, i.e., all neighbours outside of some cutoff radius are ignored, it cannot be fit to raw MHKS-DFT free energies, which tend to negative infinity for increasing volume. Instead, the total free energy must be partitioned into an electron gas term, modelled analytically, and a bonding term, modelled using an ACE. Importantly, only the bonding term contributes to the interatomic forces.

The fits show good matching with MHKS-DFT results, proving that the ACE formalism can reproduce accurate energies and forces for any electronic temperature and implying well-fit final potentials. Comparison to OF-DFT methods show that the ACE potentials are both faster and more accurate when used to simulate the entire range of densities and temperatures found in WDM.

Chapter 7

Temperature Interpolation

One limitation of the current formalism of the Atomic Cluster Expansion is that there is no explicit electronic-temperature dependence. Constructing a single ACE potential that could be used at different temperatures would require the use of temperature-dependent basis functions or fitting parameters, something that has not yet been attempted. Therefore, to allow for the calculation of the interatomic forces and energies at intermediate temperatures, without a significant loss in accuracy or efficiency, an interpolation scheme is required.

7.1 Linear interpolation

The simplest approximation to a true T_e-dependent interatomic potential is a linear interpolation between pairs of ACE potentials. Mathematically, this is given by

$$E(T_\mathrm{I}) = aE(T_\mathrm{L}) + (1-a)E(T_\mathrm{U}), \tag{7.1}$$

ACE temperature (kK)	10	20	30	40	50	100
Interp. temperature (kK)	15				70	

Table 7.1: The electronic temperatures for which an ACE potential has been fit, along with the interpolation temperatures T_I tested here. The interpolation temperatures are shown below the corresponding pair of ACE potentials used in their evaluation.

with T_U and T_L the temperature of the upper and lower bounding ACE potentials, T_I the temperature of interest, E the energy, and the lower fraction

$$a = \frac{T_\mathrm{U} - T_\mathrm{I}}{T_\mathrm{U} - T_\mathrm{L}}. \tag{7.2}$$

This is obviously a crude approximation; however, empirically, it is observed that the bonding energy and forces in aluminium vary monotonically and relatively smoothly with electronic temperature in the warm dense regime. The linear interpolation is likely to break down for any material that undergoes a phase transition or significant change in ionisation over the temperature range of interest, but is likely to work well in most of the warm dense regime of interest in aluminium. This is because the changes in the interatomic forces primarily arise from the smearing of the Fermi-Dirac distribution [21].

To allow for an efficient calculation of energies, forces, pressures, etc., as well as to make use of the previous implementation in `LAMMPS`, I adapted the `PACE` library to allow calculation of the interpolated properties for a given T_e. The scaling with system size is unchanged, and the interpolation only suffers from a doubling of the number of calculations and, therefore, evaluation time, as both $E(T_\mathrm{L})$ and $E(T_\mathrm{U})$ must be evaluated at each step. To test the linear approximation, the interpolated forces in 108 atom snapshots of $\rho = 2.37$ g/cm^3 aluminium are calculated at both 15 and 70 kK. This will gauge the feasibility of the interpolation for closely separated temperatures (10 and 20 kK), but also for the largest separation in temperatures that have been fit (50 and 100 kK). Furthermore, both MHKS-DFT and ACE interpolated forces are compared to the "exact" MHKS-DFT forces, calculated at $T_\mathrm{e} = T_\mathrm{I}$, to investigate both the interpolation in general, and, more specifically, the suitability of using ACE forces in this interpolation. The results are shown in Table 7.2.

$T_e = 15$ kK

Method	norm. RMSE (%)	RMSE (meV/Å)	MAE (meV/Å)
$\mathcal{F}_{KS}(T_L)$	0.732	93.409	83.970
$\mathcal{F}_{KS}(T_U)$	0.752	95.993	86.446
$\mathcal{F}_{ACE}(T_L)$	1.293	165.029	132.359
$\mathcal{F}_{ACE}(T_U)$	1.263	161.097	135.104
$\mathcal{F}_{KS}(T_I)$	0.105	13.407	12.269
$\mathcal{F}_{ACE}(T_I)$	1.038	132.389	101.118

$T_e = 70$ kK

Method	norm. RMSE (%)	RMSE (meV/Å)	MAE (meV/Å)
$\mathcal{F}_{KS}(T_L)$	4.704	613.961	565.136
$\mathcal{F}_{KS}(T_U)$	7.573	988.439	911.835
$\mathcal{F}_{ACE}(T_L)$	4.647	606.529	559.011
$\mathcal{F}_{ACE}(T_U)$	7.632	996.088	918.430
$\mathcal{F}_{KS}(T_I)$	0.583	76.027	67.901
$\mathcal{F}_{ACE}(T_I)$	0.679	88.564	76.469

Table 7.2: Error in the predicted forces of $\rho = 2.37$ g/cm^3 aluminium when approximated by various methods. The first (second) two rows show the error when the forces are taken to be those calculated by MHKS-DFT (ACE) at $T_e = T_{L/U}$. For $T_e = 15$ kK, $T_L = 10$ kK and $T_U = 20$ kK, whilst for $T_e = 70$ kK, $T_L = 50$ kK and $T_U = 100$ kK. The final two rows are the MHKS-DFT and ACE interpolated forces calculated using Eq. 7.1. The errors are relative to the forces calculated using MHKS-DFT at $T_e = T_I$.

At both temperatures, the MHKS-DFT interpolated forces $\mathcal{F}_{\mathrm{KS}}(T_{\mathrm{I}})$ are approximately an order of magnitude more accurate than either $\mathcal{F}_{\mathrm{KS}}(T_{\mathrm{L}})$ or $\mathcal{F}_{\mathrm{KS}}(T_{\mathrm{U}})$, showing the feasibility of a linear interpolation in these warm dense conditions. The ACE interpolated forces $\mathcal{F}_{\mathrm{ACE}}(T_{\mathrm{I}})$ are unsurprisingly worse than those from MHKS-DFT; however, they are consistent with the errors in the non-interpolated ACE fits at $\rho = 2.37$ g/cm^3, shown in Fig. 6.4. Therefore, the combination of the simple linear interpolation, given by Eq. 7.1, and finite-temperature ACE potentials should be a suitable approximation for the range of temperatures studied here.

One drawback of a linear interpolation scheme is that as the temperature of the system crosses one of the temperatures at which an ACE potential was fit, the gradients of the forces will discontinuously jump. The linear interpolation scheme would therefore lead to unrealistic behaviour in, e.g., investigations of finite electronic temperature phonons where the phonons are calculated using the derivatives of the forces (see Chapter 10 and Appendix C). The discontinuous gradients of the forces may also cause issues in two-temperature MD simulations (see Chapter 11) if the electronic temperature passes through one of the ACE temperatures listed in Table 7.1.

To improve the interpolation, a higher-order or spline interpolation could be used. Although the evaluation of the interpolated forces when using either of these methods would take more computational time and resources, the maximum increase in time and resources is proportional to the number of potentials in a specific library. This is because the computational efficiency of the interpolation is dominated by the evaluation of the energy and forces by an ACE potential, rather than the interpolation scheme itself. Furthermore, the use of a higher-order or spline interpolation would allow the gradients (and, if required, the higher-order derivatives) of the forces to be continuous as the electronic temperature crosses a temperature within the potential library. However, these methods do not preserve monotonicity, potentially leading to incorrect predictions of phonon frequencies.

7.2 Future avenues

Although the linear interpolation scheme works for the purposes of this thesis, it provides no further physical insight into the electronic temperature dependence of the interatomic forces. In addition, the energies and forces may not vary slowly with electronic temperature (and so will not be well represented by a linear interpolation), or a larger range of temperatures may be desired (requiring many ACE potentials to be fit to maintain accuracy). Some of the potential avenues for implementing more general electronic-temperature dependence into the Atomic Cluster Expansion will be discussed here.

7.2.1 ACE expansion coefficients

Within the ACE formalism, the atomic energy of atom i is given by Eq. 6.8,

$$E_i = \sum_v c_v^{(1)} A_{iv} + \sum_{v_1 v_2}^{v_1 \geq v_2} c_{v_1 v_2}^{(2)} A_{iv_1} A_{iv_2} + \ldots, \tag{7.3}$$

where v is the basis function label, A are the atomic bases, and c_v are the expansion coefficients. To allow for the parameterisation of the ACE with electronic temperature T_e, the expansion coefficients could be allowed to vary with T_e. This would then allow for T_e to be an input parameter, with the energies and forces only evaluated once, no matter if that electronic temperature is present in the training dataset or not. This could also potentially allow for the modelling of inhomogeneously heated systems, where different atoms have different T_e.

7.2.2 Scaling of fluctuations with T_e

For the (relatively) small range of electronic temperatures fit here (≈ 10 eV), the scale of the fluctuations in the energies and forces does not change much. Even so, the normalised RMSE was introduced earlier to try and remove this temperature scaling and observe the

quality of the ACE fits, independent of electronic temperature. When fitting an interatomic potential over a large range of temperatures (e.g., ≈ 2500 eV), the potential must now accurately describe several orders of magnitude in the fluctuations of the energies and forces. If a single model is fit to both very low and very high temperature data, it may struggle to accurately describe the small change in energy from a different configuration of atoms, due to the much larger change in energy fluctuations arising from the range of temperatures in the training dataset.

To tackle this, inspiration can be taken from the temperature-dependent DeePMD (TD-DPMD) potential [152, 153], which uses a temperature-dependent scaling factor $s(T_\mathrm{e})$ in an attempt to separate the temperature and configuration effects. The motivation for this scaling term is similar to the splitting of the total free energy into an electron gas term and bonding term in Section 6.4 to allow for a better description by a local potential. The scaling factor is fit to the size of the fluctuations in the MHKS-DFT forces for varying temperature,

$$s(T_\mathrm{e}) = \sigma_{\boldsymbol{\mathcal{F}}}(T_\mathrm{e}) = \exp[b] \cdot T_\mathrm{e}^{a}, \tag{7.4}$$

where $\sigma_{\boldsymbol{\mathcal{F}}}$ is the standard deviation of the forces, and a and b are fitting parameters. Since this is an empirical scaling relation, a different functional form for $s(T_\mathrm{e})$ could be chosen depending on how the fluctuations in the energies and forces of the material change with temperature. The total free energy is expressed as

$$E(\{\mathbf{R}\}, T_\mathrm{e}) = s(T_\mathrm{e})\tilde{E}(\{\mathbf{R}\}, T_\mathrm{e}) = s(T_\mathrm{e}) \sum_i \tilde{E}_i(\{\mathbf{R}\}, T_\mathrm{e}), \tag{7.5}$$

with $\tilde{E}$ the rescaled energy, $\tilde{E}_i$ the atomic contributions to the rescaled energy, and $\{\mathbf{R}\}$ the atomic positions. Note that the rescaled energy $\tilde{E}$ still has a dependence on the electronic temperature T_e. The scaling factor does not entirely remove the electronic-temperature dependence of the energies and forces, but rather allows the model for the rescaled energy $\tilde{E}$ to more easily describe the different local environments within the training dataset.

An ACE potential, using the temperature-dependent expansion coefficients $c_v(T_\mathrm{e})$, could be used to model $\tilde{E}$, with the training dataset containing MHKS-DFT free energies and forces that have been reduced by the scaling factor $s(T_\mathrm{e})$.

7.3 Summary

This chapter discussed the question of how to construct temperature-dependent ACE potentials. To carry out an ACE simulation at a temperature other than one of the temperatures in the training dataset, an interpolation scheme must be used to approximate the energy and forces. The approach adopted here is to fit ACE potentials at a set of temperatures within the range of interest. A linear interpolation between pairs of ACE potentials for adjacent temperatures then provides an ACE potential at intermediate temperatures. This holds true no matter the method (e.g., MHKS-DFT, OF-DFT) used to predict the energies and forces.

In the future, it may be possible to use temperature-dependent ACE expansion coefficients to allow for temperature dependence to be explicitly trained. The issue of scale when fitting to a large range of temperatures can be avoided by introducing a scaling parameter that removes a portion of the temperature dependence from the ACE potential. The form of this scaling parameter will likely be empirically chosen as some analytic fitted function.

Part II

Electronic-Temperature Effects on Interatomic Forces

Chapter 8

Equation of State

One of the key tests of a predictive method is to recreate an accurate equation of state (EOS). Libraries of experimental and *ab initio* EOS data in the warm dense regime, e.g., SESAME [184] and QEOS [185], are widely available and often used to benchmark simulation techniques. Theoretical studies primarily use a fixed density MD simulation, coupled to a thermostat at constant temperature, to calculate the average pressure of the system using Eq. 5.3. Due to the importance of ionisation effects in the warm dense regime, MHKS-MD or path-integral Monte Carlo (PIMC) [186, 187] are generally favoured; however, both present computational difficulties related to system size and temperature. To combat this, MHKS-MD is often used at lower temperatures, before interpolating to OF-MD [40, 41] or PIMC [47] once KS-MD becomes intractable. If the chosen method for modelling the interatomic forces does not accurately represent the electronic-temperature effects, the calculated forces and pressures will be incorrect, leading to an EOS that does not match the experimentally observed EOS.

Aluminium has one of the most well-studied EOS [188, 189], in part due to its use as a shock standard [190]. Temperatures up to 10^8 K and compressions ten times that of standard density ($\rho_0 = 2.70$ g/cm^3) have been achieved in simulations, with reasonable agreement between different methods [130, 37, 47]. This data is therefore used to benchmark OF-DFT and the fitted ACE potentials, as well as the 3e pseudopotentials used in

the MHKS-DFT and OF-DFT calculations.

All MD simulations were performed in the canonical emsemble with the pressure measured throughout the simulation. The OF-MD simulations used a 108 atom 3×3×3 fcc supercell as the starting configuration, with the system first equilibrated for 1000 timesteps. This gave reasonable equilibration of the total energy; however, if more computational time and resources were available, an extended equilibration time would be preferred. The pressure was then averaged over the next 1000 timesteps. The timesteps for all methods were, once again, chosen according to Eq. 5.19. The pseudopotential and convergence criteria are the same as those discussed in Section 6.5.1. Only the non-local SDF functional was used, due to the poor accuracy of the semi-local VT84F functional.

The MHKS-MD simulations used the `pw.x` module within `Quantum Espresso` and also used the convergence criteria from Section 6.5.1; however, simulations were also performed using the bulk-derived local pseudopotential (BLPS) that was used in the OF-MD simulations in an attempt to differentiate between errors arising due to the approximate non-interacting free energy functional, and those from the local pseudopotential. The MHKS-MD starting configuration was chosen to be a 64 atom 4×4×4 sc supercell. Previous convergence studies have found that, for the temperatures at interest here, this is the minimum system size for which the pressures are converged well, due to the relative sizes of the kinetic and potential energies [47, 130]. On account of the high computational cost of MHKS-MD, the starting configuration was first pre-equilibrated using OF-MD [191]. The final OF-MD configuration was then re-equilibrated for another 100 timesteps using MHKS-MD (the length of which was once again limited by computational time and resources), to ensure that equilibration with respect to MHKS-DFT had been achieved, before averaging the pressure over 1000 MHKS-DFT timesteps.

The efficiency of the ACE potentials allows for a larger system size and more timesteps to be used in the ACE-MD simulations. Therefore, a random 1024 atom configuration is chosen, which is initially relaxed using a Lennard-Jones potential at 300 K, such that no two atoms are too close together. The configuration is then equilibrated for 5000

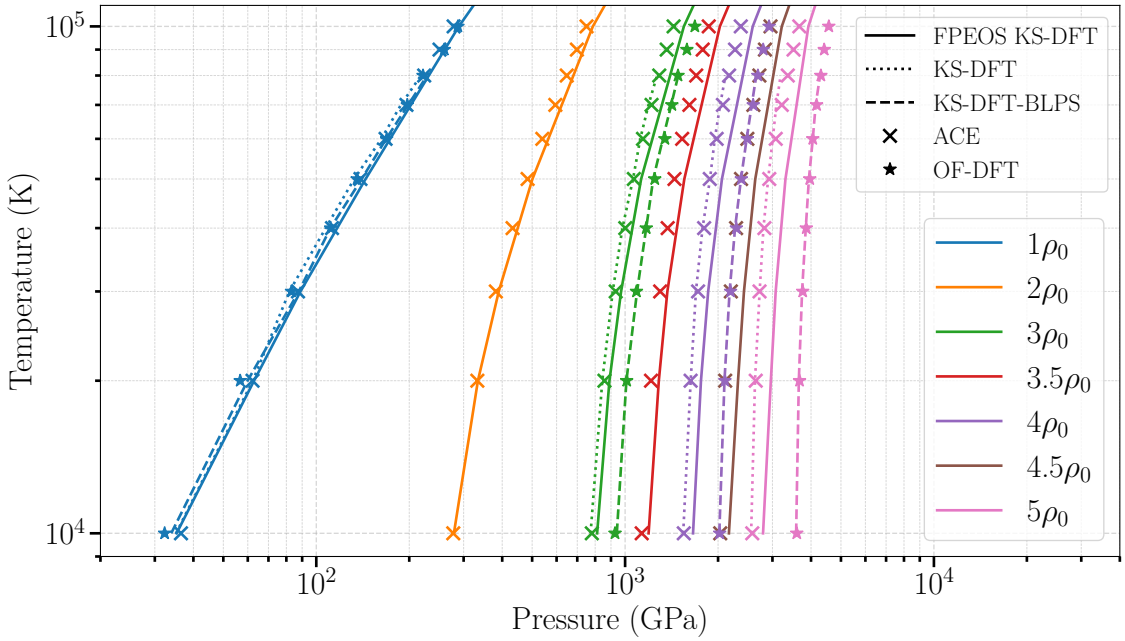

Figure 8.1: Equation of state of warm dense aluminium for various material densities and 10 kK $< T_e = T_i <$ 100 kK. MHKS-DFT and OF-DFT isochores are only plotted for every other density, due to computational limitations. The FPEOS MHKS-DFT data are from Refs. [48] and [47] and use a small-core 11e PAW non-local pseudopotential. The MHKS-DFT data were generated from MHKS-MD simulations using a 3e norm-conserving non-local pseudopotential. The MHKS-DFT-BLPS data were produced similarly to the MHKS-DFT data, but using the BLPS. The ACE data used the fitted ACE potentials and the linear interpolation discussed in Section 7.1 in ACE-MD simulations. Finally, the OF-DFT data used the SDF functional and BLPS in OF-MD simulations. Further details of all methods are given in the text or within references.

timesteps, before averages are taken over the next 5000 timesteps. All of the ACE-MD simulations used `LAMMPS` to solve the ionic equations of motion.

Since the number of timesteps used to calculate the average pressure is relatively small for both the OF- and MHKS-MD methods, there is a chance that the final calculated pressures will not be fully converged. A range of average pressures for each particular density, temperature, and method, can be calculated by taking the average of n steps, with $1 \leq n \leq 1000$. The range of average pressures is relatively small (the largest being a few percent), implying a reasonably slowly varying average pressure, even if convergence cannot be assumed. Even so, the First-Principles Equation of State (FPEOS) [48, 47] data will also be used to ensure that the ACE-MD methods can be compared to fully converged results.

The EOS for each of the methods, along with the FPEOS data, are shown in Fig. 8.1. The ACE-MD and MHKS-MD isochores show excellent correspondence over the entire range of temperatures and densities present in the fitting dataset, demonstrating the transferability of the ACE fits, as well as further proving that the combination of the ACE and the linear interpolation scheme can accurately capture the finite-temperature effects contained within the training dataset.

Limitations arise from the accuracy of the MHKS-DFT training data, primarily due to the use of a 3e pseudopotential. The FPEOS data was generated using MHKS-MD and the zero-temperature LDA [63], but also employed a small-core 11e projector augmented-wave (PAW) pseudopotential. The 3e pseudopotential used in the MHKS-DFT data of Fig. 8.1 cannot describe ionisations and excitations of the 2s and 2p electrons and uses a large core radius, resulting in overlapping frozen cores at higher densities and temperatures. To see if the discrepancy in the pressure between the MHKS-MD results and the FPEOS results is primarily due to the pseudopotential used, a comparison of a 3e and 11e pseudopotential is shown in Fig. 3.5. The 11e pseudopotential can be seen to predict a larger pressure than the 3e pseudopotential, with the difference increasing with rising density. This is in agreement with the findings of Fig. 8.1, and is therefore likely to be the main contribution to the error in the EOS results. Fitting ACE potentials to 11e MHKS-DFT data, or up-fitting the current ACE potentials with limited 11e data, would likely produce a more accurate EOS.

There is unlikely to be a significant pressure difference arising from the choice of XC functional. Previous studies have debated the importance of XC errors [192, 193], with both positive and negative contributions to the pressure being found. Furthermore, the finite-temperature XC contributions have been shown to have a relatively small effect on the EOS and Hugoniot, with pressures changing by only a few percent [101]. The discrepancy between the MHKS-MD EOS and the FPEOS EOS emphasises the importance of using an accurate and complete dataset when fitting an interatomic potential, no matter the quality of the potential's functional form.

The OF-MD EOS shows reasonable agreement with the FPEOS and MHKS-MD data at lower densities, but systematically overestimates the pressure at higher densities. To elucidate the error arising from the BLPS, further MHKS-MD simulations using the BLPS (MHKS-DFT-BLPS) were performed. The EOS that use the BLPS match well, implying that the dominant error in the OF-MD results is not due to the accuracy of the non-interacting free energy functional, but instead the local pseudopotential. It is, however, important to note that the requirement of a local pseudopotential is still an innate limitation of the OF-DFT method. The choice of pseudopotential therefore accounts for most of the differences between methods in Fig. 8.1, further underlining the necessity of using a pseudopotential that is both accurate and transferable across the entire regime of interest.

8.1 Summary

The equation of state for warm dense aluminium has been used as a benchmark for testing the accuracy of OF-DFT and the fitted ACE potentials in modelling finite-temperature effects. The fitted ACE potentials match well with the MHKS-DFT data over the entire range of temperatures and densities. This shows, once again, that the ACE potentials are fit well to the finite-temperature data of warm dense aluminium. Inaccuracies in the ACE and MHKS-DFT EOS are primarily due to the 3e pseudopotential used for these methods, although computational limitations prevent using a more accurate pseudopotential here. The quality of the OF-DFT EOS is adequate at standard density; however, it predicts higher pressures than all other EOS as the material density increases. By calculating a MHKS-DFT EOS using the same pseudopotential as used in OF-DFT, it is shown that the primary source of error arises from the failure of the BLPS to accurately approximate the frozen core in warm dense aluminium.

Chapter 9

Many-body contributions to interatomic forces

As the temperature of the electrons increases, it is expected that the quantum effects become progressively less important, eventually leading to the high-temperature limit where the electrons and ions can be treated as classical particles. Therefore, an interatomic potential for use in a warm dense system may be sufficiently accurate even when only a few orders of interaction (i.e., pair, three-body, etc.) are included. The different orders of interaction for a four-atom system are shown in Fig. 4.4. To investigate this hypothesis, the convergence and accuracy of the many-body expansion is tested for warm dense aluminium.

9.1 Many-body expansion

The well-known many-body expansion allows one to write the energy of a system of N interacting particles with positions $\{\mathbf{R}\}$ as a sum of successive terms, each incorporating a higher order of interactions. It is defined as

$$E\left(\{\mathbf{R}\}\right) = \sum_{i=1}^{N} E_i + \sum_{i=1}^{N} \sum_{j>i} \Delta E_{ij} + \sum_{i=1}^{N} \sum_{j>i} \sum_{k>j} \Delta E_{ijk} + \ldots, \tag{9.1}$$

where $\Delta E_{ij...n}$ can be thought of as the corrections due to the n-body interactions. The two- and three-body contributions take the form

$$\Delta E_{ij} = E_{ij} - E_i - E_j, \tag{9.2}$$

$$\Delta E_{ijk} = E_{ijk} - \Delta E_{ij} - \Delta E_{jk} - \Delta E_{ki} - E_i - E_j - E_k, \tag{9.3}$$

where $E_{ij...n}$ is the energy of the system when only particles i, j, ..., n, are present. Equations for higher order terms can be written in a similar manner. The full summation includes N terms, and is exact in this limit. In practice, calculating all of the terms is intractable and the series must be truncated at some lower order n. The hope is that the sum converges to some reasonable accuracy after only a few terms. For the rest of this chapter, the contributions will be truncated above $n = 3$.

As discussed in Chapter 6, the ACE (Eq. 6.5) is inspired by the many-body expansion (Eq. 9.1); however, the performant implementation of the ACE [147] is not expressed as a sum of the explicit many-body contributions. Therefore, the fitted ACE potentials from Chapter 6 cannot be explicitly decomposed to observe the many-body contributions. The original linear ACE formalism [50] could, in theory, be used to investigate many-body contributions by fitting potentials with increasing $K_{\max}$; however, the many-body expansion is used here instead to investigate the behaviour of the many-body contributions with increasing electronic temperature.

The forces in the many-body expansion are derived as derivatives of the total energy, given by Eq. 9.1. The permutation symmetry of the energy will also be used in the derivation of the forces. In other words, the order of the indices in the energy terms is interchangeable. This means that $E_{ijk} = E_{jik} = E_{kji}$, etc., and this also applies to the corrections, ΔE. The derivative of Eq. 9.1 with respect to the position $\mathbf{R}_a$ of atom a can be expressed by

$$\frac{\partial E}{\partial \mathbf{R}_a} = \frac{\partial \left(\sum_i^N E_i \right)}{\partial \mathbf{R}_a} + \frac{\partial \left(\sum_i^N \sum_{j>i} \Delta E_{ij} \right)}{\partial \mathbf{R}_a} + \frac{\partial \left(\sum_i^N \sum_{j>i} \sum_{k>j} \Delta E_{ijk} \right)}{\partial \mathbf{R}_a}. \tag{9.4}$$

Evaluating the first term on the RHS gives

$$\frac{\partial\left(\sum_i^N E_i\right)}{\partial \mathbf{R}_a} = \frac{\partial E_a}{\partial \mathbf{R}_a} = 0, \tag{9.5}$$

due to the translational symmetry of the one particle system. The second term in Eq. 9.4 can be expressed as

$$\frac{\partial\left(\sum_i^N \sum_{j>i} \Delta E_{ij}\right)}{\partial \mathbf{R}_a} = \frac{\partial\left(\sum_{j>a} \Delta E_{aj}\right)}{\partial \mathbf{R}_a} + \frac{\partial\left(\sum_{i<a} \Delta E_{ia}\right)}{\partial \mathbf{R}_a} = \sum_{j\neq a} \frac{\partial\left(\Delta E_{aj}\right)}{\partial \mathbf{R}_a}, \tag{9.6}$$

where the first equality has one term from $i = a$, and one term from $j = a$. The second equality then makes use of the fact that the dummy indices can be renamed and reordered, as explained above. Taking the derivative of Eq. 9.2 gives

$$\sum_{j\neq a} \frac{\partial\left(\Delta E_{aj}\right)}{\partial \mathbf{R}_a} = \sum_{j\neq a} \left(\frac{\partial E_{aj}}{\partial \mathbf{R}_a} - \cancelto{0}{\frac{\partial E_a}{\partial \mathbf{R}_a}} - \cancelto{0}{\frac{\partial E_j}{\partial \mathbf{R}_a}} \right) = \sum_{j\neq a} \frac{\partial E_{aj}}{\partial \mathbf{R}_a} = -\sum_{j\neq a} \boldsymbol{\mathcal{F}}_{aj}, \tag{9.7}$$

where $\boldsymbol{\mathcal{F}}_{aj}$ is the pairwise force on particle a due to particle j. The final term in Eq. 9.4 can be written as

$$\begin{aligned}
\frac{\partial\left(\sum_i^N \sum_{j>i} \sum_{k>j} \Delta E_{ijk}\right)}{\partial \mathbf{R}_a} =& \frac{\partial\left(\sum_{j>a} \sum_{k>j} \Delta E_{ajk}\right)}{\partial \mathbf{R}_a} + \frac{\partial\left(\sum_{i<a} \sum_{k>a} \Delta E_{iak}\right)}{\partial \mathbf{R}_a} + \\
& \frac{\partial\left(\sum_{i<j} \sum_{j<a} \Delta E_{ija}\right)}{\partial \mathbf{R}_a} \\
=& \frac{\partial\left(\sum_{j>a} \sum_{k>j} \Delta E_{ajk}\right)}{\partial \mathbf{R}_a} + \frac{\partial\left(\sum_{j<a} \sum_{k>a} \Delta E_{ajk}\right)}{\partial \mathbf{R}_a} + \\
& \frac{\partial\left(\sum_{j<k} \sum_{k<a} \Delta E_{ajk}\right)}{\partial \mathbf{R}_a} \\
=& \sum_{j<k}{}' \frac{\partial\left(\Delta E_{ajk}\right)}{\partial \mathbf{R}_a},
\end{aligned} \tag{9.8}$$

where, once again, the indices have been renamed and reordered, and the prime on the

summation indicates that neither j nor k are equal to a. Differentiating Eq. 9.3 gives

$$\begin{aligned}\frac{\partial\left(\Delta E_{ajk}\right)}{\partial \mathbf{R}_a} &= \frac{\partial E_{ajk}}{\partial \mathbf{R}_a} - \frac{\partial\left(\Delta E_{aj}\right)}{\partial \mathbf{R}_a} - \cancelto{0}{\frac{\partial\left(\Delta E_{jk}\right)}{\partial \mathbf{R}_a}} - \frac{\partial\left(\Delta E_{ka}\right)}{\partial \mathbf{R}_a} - \cancelto{0}{\frac{\partial E_a}{\partial \mathbf{R}_a}} - \cancelto{0}{\frac{\partial E_j}{\partial \mathbf{R}_a}} - \cancelto{0}{\frac{\partial E_k}{\partial \mathbf{R}_a}} \\ &= -\boldsymbol{\mathcal{F}}_{ajk} + \boldsymbol{\mathcal{F}}_{aj} + \boldsymbol{\mathcal{F}}_{ak},\end{aligned} \tag{9.9}$$

with $\boldsymbol{\mathcal{F}}_{ajk}$ defined as the three-body force on particle a due to the presence of particles j and k. Therefore, for a many-body expansion including up to three-body interactions, the force on particle a can be expressed as

$$\boldsymbol{\mathcal{F}}_a = \sum_{j\neq a} \boldsymbol{\mathcal{F}}_{aj} + \sum_{j<k}{}' \Delta\boldsymbol{\mathcal{F}}_{ajk}, \tag{9.10}$$

with

$$\Delta\boldsymbol{\mathcal{F}}_{ajk} = \boldsymbol{\mathcal{F}}_{ajk} - \boldsymbol{\mathcal{F}}_{aj} - \boldsymbol{\mathcal{F}}_{ak}. \tag{9.11}$$

A closed formula for the recurrence relation of successive energy contributions to the many-body expansion was derived [194], allowing simple computation of the n^{th} order term from the $(n-1)^{\text{th}}$ order expansion. This relation can be adapted to simplify the calculation of force contributions to the many-body expansion.

9.1.1 Embedding in an HEG environment

The convergence of the many-body expansion is well known to be slow for a system of atoms embedded in a vacuum [183, 195]. Various approaches to improve the convergence have been proposed [182]. Generally, these involve altering the environment in which the atoms are embedded to make it resemble the system of interest more closely. The electrostatically embedded approach [195, 196] is an example of a method based on this idea. The underlying philosophy is not too dissimilar to that of the embedded atom method, whereby the improved description of the environment is hoped to improve the overall energies, forces, etc.

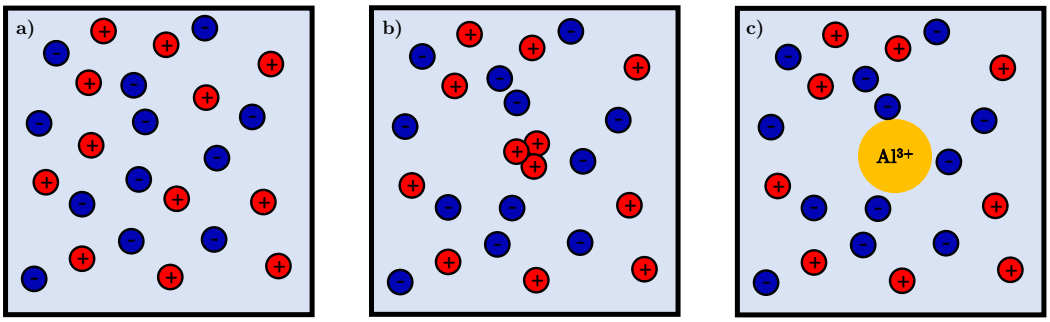

Figure 9.1: Diagrammatic example of embedding a single aluminium atom of charge $Z_{\mathrm{Al}} = 3$ in an HEG, although point charges are used here for visual clarity. **a)** an HEG of density $n_- = n_+ = Z_{\mathrm{Al}} N_{\mathrm{at}}/V$. **b)** Z_{Al} positive charges group up at the embedded aluminium atom's position, with the uniform background reduced everywhere else. **c)** The Z_{Al} positive charges are smeared out to match the local potential of an Al^{3+} pseudopotential. The remaining HEG is allowed to adiabatically equilibrate to its groundstate throughout.

Here, the homogeneous electron gas (HEG) is used to approximate the environment that the atoms are embedded in. This should reasonably describe simple metals with free-electron-like valence electrons, such as aluminium, but may struggle to accurately mimic the environment of more complex materials. To begin, a simulation cell is defined with constant size and total number of atoms N_{at}. The atoms not explicitly involved in the interaction (along with their corresponding valence electrons) are smeared out to create a HEG. This ensures that the total number of valence electrons in the simulation cell is constant, no matter the order of the interaction. For instance, when calculating the pair force on an atom due to a single other atom, two atoms are embedded into a simulation cell where the other $N_{\mathrm{at}} - 2$ ionic cores have been smeared into a static uniform positive background.

An alternative way of viewing this model is to take an HEG with the same number of electrons as the total system and adiabatically perturb the positive background to form ionic pseudopotentials at the required positions in the simulation cell. The system then maintains the same amount of positive and negative charge as in the total system. Here, an ionic pseudopotential, which is the Coulomb potential of a local concentration of

positive background charge, replaces the positive nucleus and core electrons of every atom explicitly considered in a given interaction. Fig. 9.1 shows this for a single aluminium atom embedded in a HEG.

It is important to note, though, that for pseudopotentials with frozen core electrons, the combination of the core electrons and positive ionic core constitute the 'ion' that is being smeared out. For example, if an ionic pseudopotential for aluminium with 13 protons and 10 frozen core electrons is used, the 3 'free' (or valence) electrons contribute to the negative background, with the 3+ 'ion' smeared to make the positive background, given that the ion is not explicitly involved in the interaction.

A question arises as to the number of 'free' electrons Z^* that should be smeared into the HEG. Since DFT treats all non-frozen electrons equally, there is no simple separation of electrons into bound and unbound states. Furthermore, there are multiple ways to define Z^* [197, 198], each of which may lead to a different value for the HEG density. The value of Z^* will also vary with temperature and density through thermal and pressure ionisation. Here, Z^* of aluminium is fixed to 3 for all electronic temperatures, including the 3s and 3p electrons in the HEG density. Using Thomas-Fermi theory [55, 199, 185], average atom models [56] or pressure ionisation models [200], a better approximation to the exact Z^* could be found; however, since Z^* only slightly increases over the range of temperatures studied here [201], the approximation of fixing Z^* is satisfactory for the purposes of elucidating the qualitative size of the many-atom contributions to the interatomic forces.

Furthermore, pseudopotentials are defined for a particular number of valence electrons, with the aluminium pseudopotential used here having 3 valence electrons. If the atoms smeared into the HEG used a value of Z^* different to the number of valence electrons in the pseudopotential, the atoms represented by the HEG would be treated differently to those represented by the pseudopotential. This would lead to inconsistencies in the total number of electrons in the contributions from different orders of interaction.

The total forces are evaluated as in the standard vacuum embedding method. This is

because there are no forces in the unperturbed HEG. However, when calculating the energy of the n-body contributions, there will always be an additional contribution arising from the HEG. To calculate the energy of the system when only the n atoms represented by pseudopotentials are present, the contribution from the HEG formed by smearing $N-n$ atoms must be subtracted,

$$E_{ij\ldots n} = \tilde{E}_{ij\ldots n} - E_{\mathrm{HEG}}(N-n), \tag{9.12}$$

where $E_{ij\ldots n}$ is the energy when only atoms i, j, ..., n, are present, $\tilde{E}_{ij\ldots n}$ is the total energy of the n atoms represented by pseudopotentials and the $N-n$ atoms smeared into the HEG, and E_{HEG} is the energy of the unperturbed HEG. However, the focus for the rest of this chapter will be on the interatomic forces and the sizes of the two- and three-body contributions in the warm dense regime.

9.2 n-body contributions in aluminium

To investigate the n-body contributions in the many-body expansion, an aluminium unit cell containing 8 atoms with periodic boundary conditions is chosen. If the aim of the many-body expansion is to be a practical potential, a high accuracy in the forces must be found for an expansion truncated to only a few orders of interaction.

The two- and three-body contributions to the forces are calculated using the two terms on the right-hand side of Eq. 9.10, with each of the individual components of the summands calculated using MHKS-DFT sampled at the Γ point. A finer mesh of k-points is required to confirm any observed behaviours; however, computational limitations prevented verifying this here. The periodicity is included due to the limitations of the (M)HKS-DFT method. For $T_{\mathrm{e}} > 100$ kK, the extended-FPMD method, introduced in Section 3.4, is used to calculate the forces. The forces are calculated for both the aluminium atoms embedded in a vacuum, as well as within an HEG, as discussed above, to compare accuracy and convergence. The normalised RMSEs of the forces for the two embedding methods

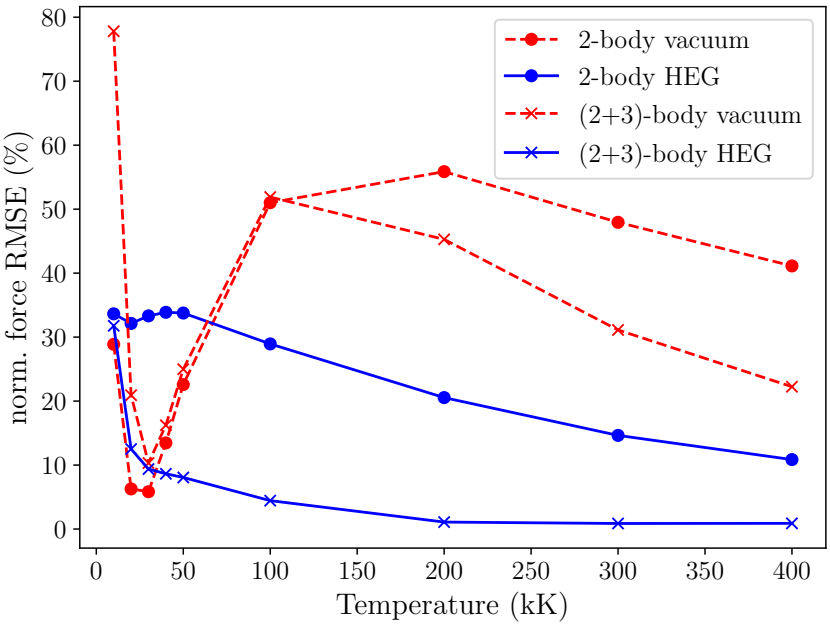

Figure 9.2: Normalised root-mean-square errors in the forces, as defined in Eq. B.3, for the many-body expansion at varying electronic temperature. At each electronic temperature, the forces on the atoms were computed for ten random MD snapshots of a simulation cell containing 8 atoms, equilibrated at $T_{\mathrm{eq}} = 10$ kK under periodic boundary conditions. The RMSE of these forces relative to the corresponding MHKS-DFT forces were then computed. Circles and crosses indicate truncation at pairwise and three-body contributions, respectively. Solid and dashed lines indicate embedding in an HEG and vacuum, respectively.

and two orders of truncation are shown in Fig. 9.2.

It is found that as the electronic temperature increases, the accuracy of low-order expansions improves, in general. Most of the RMSEs do not monotonically decrease throughout the entire temperature range, though. At lower temperatures, substantial many-atom interactions dominate the behaviour and the errors in two- and three-body expansions, whether or not these are constructed using an HEG embedding, are large. For $T_{\mathrm{e}} > 100$ kK, however, the $n > 3$-body effects diminish rapidly, until eventually the pairwise interactions dominate as one would expect in a two-component plasma [135].

The surprisingly high accuracy of the vacuum embedding from 20-30 kK requires explanation. It could be that the two- and three-body expansions systematically underestimate the exact N_{at}-body forces at low temperatures and overestimate them at higher tempera-

tures. Thus, the RMSE drops as the temperature rises and the underestimation reduces, before rising again as the overestimation grows (or vice versa). To test this theory, the sum of signed contributions to the normalised force RMSE can be defined as

$$\Delta\boldsymbol{\mathcal{F}}^2_{\pm} = \frac{\sum_{i,m} \mathrm{sgn}(\Delta\boldsymbol{\mathcal{F}}^m_i) \times (\Delta\boldsymbol{\mathcal{F}}^m_i)^2}{N_\mathrm{s} N_\mathrm{at} \bar{\boldsymbol{\mathcal{F}}}^2}, \tag{9.13}$$

with N_s the total number of snapshots and N_at the total number of atoms in each snapshot. The difference in the MBE and exact force on atom i in snapshot m is defined as

$$\Delta\boldsymbol{\mathcal{F}}^m_i = \boldsymbol{\mathcal{F}}^m_i(\mathrm{MBE}) - \boldsymbol{\mathcal{F}}^m_i(\mathrm{exact}), \tag{9.14}$$

and the average squared force is given as

$$\bar{\boldsymbol{\mathcal{F}}}^2 = \frac{\sum_{m,i} [\boldsymbol{\mathcal{F}}^m_i(\mathrm{exact})]^2}{N_\mathrm{s} N_\mathrm{at}}. \tag{9.15}$$

The sum of signed contributions $\Delta\boldsymbol{\mathcal{F}}^2_{\pm}$ shows whether the contributions to the normalised force RMSE from the underestimation of the forces are larger than the contributions from the overestimation of the forces. In Fig. 9.3, $\Delta\boldsymbol{\mathcal{F}}^2_{\pm}$ is plotted against electronic temperature for the two-body and three-body vacuum and HEG MBEs. Although the three-body vacuum MBE shows the predicted behaviour of an overestimation of the forces at low temperature and an underestimation of the forces at high temperature, interestingly the two-body vacuum MBE does not. In fact, the sum of signed contributions to the two-body vacuum MBE is positive at all temperatures probed. Further investigation is therefore necessary to better understand the high accuracy of the two-body vacuum MBE around 20-30 kK.

When comparing the embedding environments, the HEG embedding is noticeably more accurate at higher temperature, as well as converging faster with the order of the expansion. As would be expected, the HEG is therefore a more realistic environment for warm dense aluminium, especially at the highest temperatures where the valence electrons are expected to be almost entirely delocalised and free-electron-like. It should be noted that,

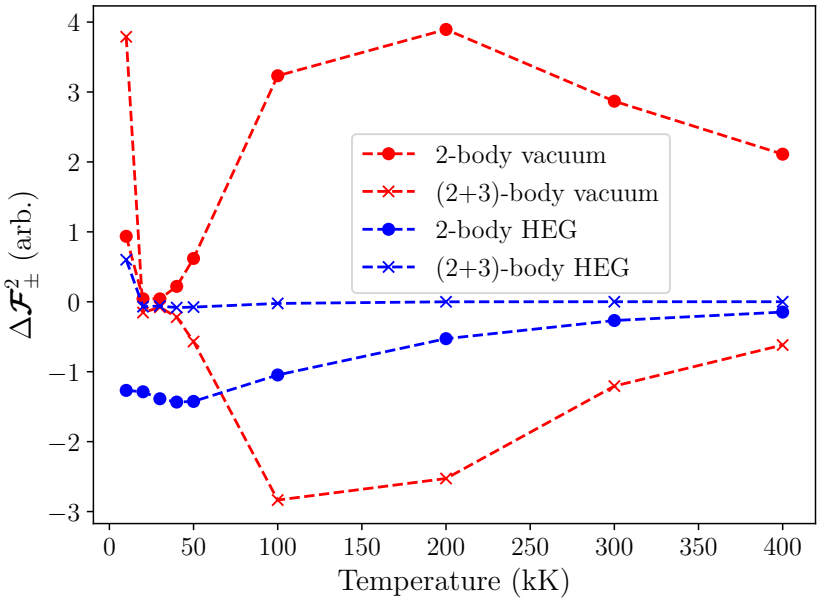

Figure 9.3: The sum of signed contributions to the normalised force RMSE, as defined in Eq. 9.13, for the many-body expansion at varying electronic temperature. At each electronic temperature, the forces on the atoms were computed for ten random MD snapshots of a simulation cell containing 8 atoms, equilibrated at $T_{\mathrm{eq}} = 10$ kK under periodic boundary conditions. The signed contributions to the RMSE of these forces relative to the corresponding MHKS-DFT forces were then computed. Circles and crosses indicate truncation at pairwise and three-body contributions, respectively. Solid and dashed lines indicate embedding in an HEG and vacuum, respectively.

for the results at electronic temperature $T_{\mathrm{e}} > 100$ kK, temperature ionisation is expected to have an effect. As discussed previously, Z^* will increase as the core electrons have enough energy to excite out of the deep core states, altering the forces and energies of the system. Since all of the DFT calculations have used the same 3e pseudopotential, any excitations of core electrons are ignored throughout. These additional excitations may not affect the many-body nature of the interatomic forces strongly, but it is important to understand that the forces obtained may be inaccurate.

Similar trends hold for systems with different numbers of atoms, as well as with different pseudopotentials and XC functionals; however, the rapid increase of computational time required as the number of atoms increases prevents this approach from being used to study systems much larger than those considered here.

9.3 Summary

The many-body expansion is a formally exact method for calculating the energies and forces of a system of N atoms. It has been used here to elucidate the importance of the many-body contributions to the interatomic forces in warm dense aluminium. The method is well known to have poor convergence of the energies and forces with increasing body order when atoms are embedded into a vacuum. To counter this, the embedding environment can be altered to better match the modelled system. In the case of warm dense aluminium, the HEG was chosen to be the embedding environment.

It is shown that the high temperature interatomic forces calculated using a two- or three-body expansion are more accurate when the two- and three-atom clusters are embedded in an HEG than when they are embedded in vacuum. Furthermore, only two- and three-body interactions are required to predict chemically accurate interatomic forces above 200 kK.

Chapter 10

Phonons at finite temperature

Working within the Born-Oppenheimer approximation, which is normally very accurate even for warm dense matter, the effect of the ionic motion on the interatomic forces can be neglected. It follows that the ionic positions may be treated as fixed inputs to the interatomic potential or the electronic minimisation procedure in DFT. The free energy of the electronic degrees of freedom plus the electrostatic ionic contributions, i.e., Eq. 4.2, can then be calculated using the interatomic potential or DFT. However, this is only part of the total free energy of the system, due to the assumption of fixed ions.

The contribution from the ionic motion has been accounted for in previous chapters by an MD simulation. An MD simulation samples the ionic phase space by integrating Newton's laws of motion and does not require a periodic structure. At reasonably low ionic temperatures, an alternative approach uses the phonon spectrum to approximate the contribution to the free energy from the motion of the ions using the harmonic approximation. When discussing phonons, this contribution to the total free energy is referred to as a vibrational contribution F_{vib}. This is because, in a crystalline structure, the atoms oscillate around their equilibrium positions, with an average displacement of zero. This picture does not hold for the liquids studied in the earlier MD simulations, explaining why vibrational contributions to the free energies of liquids were not considered.

Even at zero temperature, the vibrational contribution cannot always be excluded due

to the quantum mechanical zero-point motion. Knowledge of the phonons is vital to understanding the thermodynamic (along with many other) properties of the system at finite temperature [202]. Furthermore, the phonon structure can be used as a test of the accuracy of forces predicted by a given method.

From a physical perspective, as the temperature increases, it is expected that the vibrational contribution quickly becomes the dominant component of the temperature-dependent free energy, from observations such as the Debye model [203]. The temperature-dependence of the vibrational free energy also dictates when a crystalline solid will melt. Therefore, an accurate representation of F_{vib} and the crystal's phonon structure are required to describe the transition from low temperature to the WDM regime, as well as the two-temperature systems with an elevated electronic temperature investigated in Chapter 11. This, in turn, means that the effects due to the finite temperature of the electrons must be properly accounted for.

As was shown in Chapter 2, approximations are required to make the evaluation of the electronic free energy tractable, and the same applies to the evaluation of the free energy contribution from the ionic motion. For instance, the interactions between ions will change when one of the ions is displaced. To fully describe this change, the change in the interaction between the displaced ion and every other ion in the solid must be calculated, as well as knowing the exact form of the interaction between two ions. This is unfeasible for the vast majority of materials. The harmonic approximation is used to simplify this problem by truncating the Taylor expansion of the free energy at the second derivative.

Since the primary reason for investigating phonons in this thesis is as a test of the accuracy of the electronic finite-temperature effects predicted by different methods (e.g., OF-DFT, interatomic potentials), the details of calculating the phonons, as well as how they relate to thermodynamic properties such as F_{vib}, will be discussed in Appendix C.

10.1 Electronic-temperature effects on phonons

Previous chapters have shown that the interatomic forces within a system are dependent on the electronic temperature. This dependence can be observed in systems that are laser irradiated, which causes the electrons to heat up and thermalise to an electronic temperature T_e. For a short time after irradiation, the ionic lattice is still 'cold', whilst the electrons are 'hot'. Therefore, any changes in the interatomic forces during this time must be caused by the finite electronic temperature.

It has been shown in experiments that laser irradiation of semiconductors [204], noble metals [112], and free-electron-like metals [49] can all lead to ultrafast melting of the crystalline structures. However, the melting is not always thermal, i.e., caused by the vibration of the ions. In semiconductors, a high electronic temperature leads to athermal melting, which is the name given to the phase transition caused by the softening of the interatomic forces, rather than heating of the ionic lattice. In noble metals, such as gold, the type of melting is dependent on whether the heating occurs under isochoric conditions [28].

To investigate which materials undergo athermal melting when laser irradiated, the phonons can be calculated for varying T_e. This has previously been investigated using DFPT for a semiconductor (silicon), noble metal (gold), and free-electron-like metal (aluminium) [21]. In Ref. [21], it was found that athermal melting occurs in silicon due to the transverse acoustic mode frequencies becoming imaginary for $T_e > 1.5$ eV. In the harmonic approximation, if any phonon frequency becomes imaginary, the free energy is not at a minimum and therefore the system is in an unstable configuration which will undergo a phase transition to a more stable state [205]. Gold and aluminium did not display athermal melting. The phonon dispersion curve and density of states of aluminium changed very little with temperature. This, argued the authors of Ref. [21], was caused by the absence of localised electrons in the metallic bonding of aluminium. It is therefore expected that laser irradiation of aluminium will not substantially alter the phonon dispersion curve and will not show the bond softening required for athermal melting. Gold showed bond hardening

under isochoric electronic heating, inline with other studies.

Despite its relatively small temperature dependence, the phonon dispersion curve of aluminium is investigated here as a useful test of the accuracy of the various methods used to approximate the electronic contributions to the interatomic forces. Since the phonon frequencies are directly related to the derivatives of the interatomic forces, an accurate interatomic potential should also faithfully recreate the phonon dispersion curve. The phonon dispersion curves for fcc aluminium calculated using the 'direct' method at three different T_e are plotted in Fig. 10.1. Since there is no ACE potential fit to 300 K data, the phonon dispersion cannot be calculated. All of the labelled high symmetry points (Γ, X, and L) are commensurate with the supercells used to calculate the phonon dispersion curves, and therefore the phonon frequencies at these points are 'exact', insofar as the methods themselves are. Furthermore, the phonon dispersions at all T_e have been calculated using the equilibrium lattice constant at 300 K for that method, i.e., under isochoric conditions, as aluminium has no free energy minimum above $T_\mathrm{e} = 30$ kK (see Fig. 6.1).

The results obtained using MHKS-DFT with the non-local pseudopotential and OF-DFT with the SDF functional match the experimental results reasonably well. The results obtained using MHKS-DFT with the bulk-derived local pseudopotential (BLPS) are slightly worse, which may be due to the computationally-limited k-point sampling, combined with the local pseudopotential. Although it is tempting to wholly blame the local pseudopotential for the poor accuracy, the more accurate OF-DFT results also used the same local pseudopotential and the pseudopotential was fit to MHKS-DFT data generated using a non-local pseudopotential. It is therefore odd that the use of the BLPS in MHKS-DFT, where the non-interacting free energy is calculated exactly, would lead to less accurate results that in OF-DFT, where the non-interacting free energy is approximated. It may be that there is a fortuitous cancellation of errors when using the BLPS in OF-DFT; however, this remains an open question.

Increasing T_e to 10 kK shows little change to any of the phonon dispersions, and further increasing T_e to 40 kK shows a slight increase in all frequencies for all methods, excluding

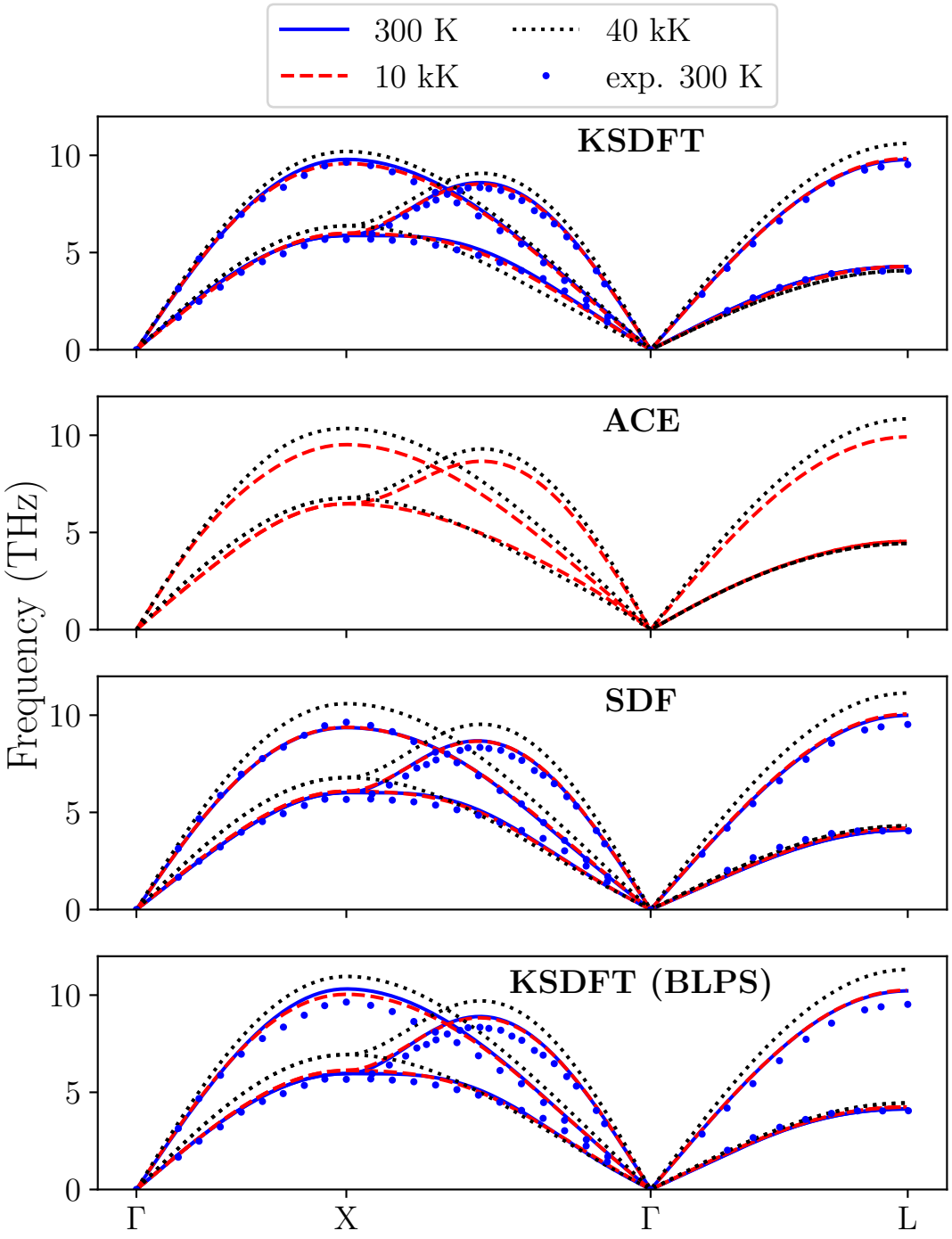

Figure 10.1: Phonon dispersion curves of fcc aluminium along a high symmetry path in the Brillouin zone. All calculations, except ACE, used the 'direct' method on a $2 \times 2 \times 2$ supercell containing 32 atoms with the equilibrium lattice constant a_0 determined by first relaxing the primitive unit cell at 300 K. The ACE calculation used the MHKS-DFT a_0, due to the lack of a 300 K potential, and a $4 \times 4 \times 4$ supercell to give increased accuracy along the path. The phonon dispersion curves were found using `phonopy`, with `Quantum Espresso` used to calculate the MHKS-DFT forces, `PROFESS@QE` for the SDF forces, and `LAMMPS` for the ACE forces. The experimental data points were taken from Ref. [206].

the lower transverse acoustic mode. The slightly larger increase in the SDF X and L frequencies from $T_e = 300$ K to $T_e = 40$ kK, in comparison to those from MHKS-DFT, may be due to the previously mentioned poor accuracy of OF-DFT methods at lower temperatures; however, on comparison to the MHKS-DFT with BLPS results, it seems likely that the main contribution to the difference arises from the pseudopotential used.

The phonon dispersions derived using the ACE potential match well with the MHKS-DFT curves, further proving that the ACE formalism can accurately reproduce electronic finite-temperature effects at arbitrary temperature. The overall results match the previous finding [21] of a weak dependence of the phonons on electronic temperature for this temperature range in aluminium. There is no bond softening present, so no athermal melting is to be expected in aluminium thin films irradiated to $T_e = 40$ kK (see Chapter 11).

10.2 Summary

Phonons have been introduced as an alternative method to calculating the ionic contribution to the total free energy at temperatures below the melting point, but also, more importantly, as another test of the electronic finite-temperature effects on the interatomic forces predicted by the various approaches to solving the electronic subsystem. As the electronic temperature increases, the forces within a material, and therefore the phonon frequencies, can potentially change. This can lead to athermal melting, where the crystalline structure melts due to the weakening of the interatomic forces, rather than from ionic vibrations. Although athermal melting occurs in laser-irradiated silicon, it is not expected to be the method by which laser-irradiated aluminium melts.

The non-local OF-DFT method predicts qualitatively accurate phonons at room temperature and shows similar behaviour to MHKS-DFT for elevated electronic temperature. The ACE phonon dispersion curves faithfully reproduce the MHKS-DFT curves, as expected from the high accuracy of the forces which were studied in Chapter 6.

Chapter 11

Two-temperature molecular dynamics

A simple example of an experimentally realisable system in which T_e-dependent effects can be observed is the heating of a thin film of aluminium by a free electron laser [207]. The laser couples strongly with the electronic subsystem, pumping it with energy that causes its temperature to rise. The stark difference in electron-electron and electron-ion coupling causes the system to reach a nonequilibrium state, where the electronic and ionic subsystems are in thermal equilibrium with themselves, but not each other [110, 111, 23, 26]. The elevated electronic temperature can alter the strength and behaviour of the interatomic forces, the electronic heat capacity, and the electron-phonon coupling constant. These T_e-dependent effects have been previously observed in gold and silicon (see Chapter 10) [19, 20, 21] and can lead to both bond softening (athermal melting) and bond hardening (lattice stabilisation).

The separation of the ionic and electronic temperatures led computational materials scientists first to the adoption of the continuum two-temperature model [208], then later to the coupling of the two-temperature model with molecular dynamics (2T-MD) [23, 24] to more accurately simulate the atomistic behaviour of the ionic subsystem. There have been experiments on laser-irradiated thin films using femtosecond electron diffrac-

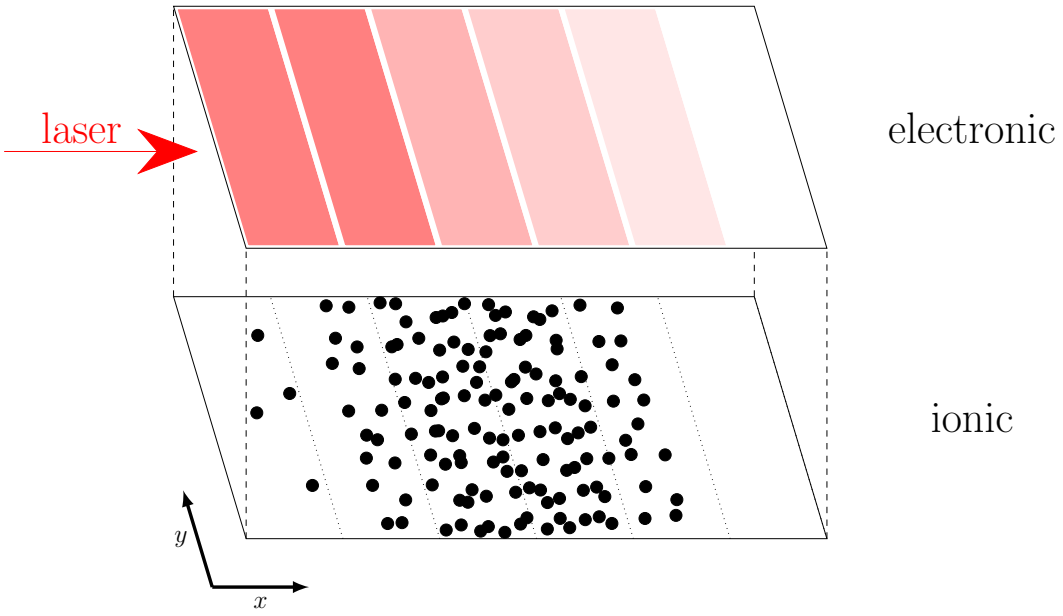

Figure 11.1: A pictorial representation of a 2T-MD simulation of a 2D laser-irradiated thin film. The upper level shows the continuum treatment of the electrons which are modelled by constant electronic temperature cells. The electronic temperature is highest in the darkest cells. The lower level shows the atomistic treatment of the ions by the MD simulation. Each black circle is an individual ion that is coupled to the electronic cell within which it falls. The system is periodic in the y direction with the ions allowed to expand in the x direction. The cell containing no ions is marked as inactive and heat does not flow into or out of it. The laser is heating the electronic system along the positive x direction.

tion [209, 210, 211] that have matched diffraction patterns simulated using 2T-MD [29], whereas the continuum two-temperature model is known to neglect effects such as superheating and recrystallisation [212, 25, 213], further establishing the necessity of using an atomistic model when simulating nonequilibrium heating of aluminium.

11.1 The model

In 2T-MD, the electronic subsystem is coarse grained into cells of constant electronic temperature, whilst the ions are treated atomistically, as shown in Fig. 11.1. Each electronic cell, and the ions contained within it, are then coupled to one another via a Langevin thermostat. The time evolution of the system is expressed by a heat diffusion equation for the

electronic subsystem, coupled to an MD simulation for the ionic subsystem [23, 24, 214]:

$$C_{\mathrm{e}}\frac{\partial T_{\mathrm{e}}}{\partial t} = \boldsymbol{\nabla}\cdot(\kappa_{\mathrm{e}}\boldsymbol{\nabla}T_{\mathrm{e}}) - g_{\mathrm{p}}(T_{\mathrm{e}} - T_{\mathrm{i}}), \tag{11.1}$$

$$m\frac{\partial \mathbf{v}_j}{\partial t} = \boldsymbol{\mathcal{F}}_j - \gamma\mathbf{v}_j + \tilde{\boldsymbol{\mathcal{F}}}, \tag{11.2}$$

with $C = \rho c$ the volumetric heat capacity, c the specific heat capacity, κ the thermal conductivity, g_p the electron-ion coupling constant, T the temperature, m the ionic mass, $\mathbf{v}$ the ionic velocity, $\boldsymbol{\mathcal{F}}_j$ the interatomic force on ion j, $\tilde{\boldsymbol{\mathcal{F}}}$ the stochastic force, γ the friction coefficient, and 'e' and 'i' labelling the electronic and ionic systems, respectively.

For energy conservation within the system, at every time step Δt the energy lost by the ionic subsystem must be gained by the electronic subsystem. For a chosen electronic cell, the energy lost by the ions is [23]

$$\Delta E_{\mathrm{i}}^{J} = \sum_{j\in J}\Delta E_j = \sum_{j\in J}\gamma\mathbf{v}_j\cdot\mathbf{v}_j\Delta t = \Delta t\sum_{j\in J}\gamma v_j^2, \tag{11.3}$$

where ΔE_j is the energy lost by ion j, and the sum is over all ions j within electronic cell J. The energy gained by the electrons can be expressed by

$$\Delta E_{\mathrm{e}}^{J} = g_{\mathrm{p}}T_{\mathrm{i}}V^{J}\Delta t, \tag{11.4}$$

where V^J is the volume of electronic cell J. By equating the energy gain of the electrons with the energy loss of the ions, and using the definition of T_{i} from the equipartition theorem, the electron-ion coupling constant g_{p} and the friction coefficient γ are found to be related by [23]

$$g_{\mathrm{p}} = \frac{3N^{J}k_{\mathrm{B}}\gamma}{V^{J}m}, \tag{11.5}$$

with N^J the number of ions within electronic temperature cell J.

The interatomic forces $\boldsymbol{\mathcal{F}}_j$ are, in general, dependent on the electronic temperature; however, a zero-temperature embedded atom method (EAM) potential [215] will also be used

for comparison. I extended the 2T-MD module [216, 30] present in the October 2021 `LAMMPS` release to calculate the interatomic forces within each electronic cell using that cell's electronic temperature as an input to the temperature-dependent interatomic potential.

The stochastic force $\tilde{\boldsymbol{\mathcal{F}}}$ models the energy input to the ions from the electron-ion coupling [23], and is assumed to have a Gaussian distribution,

$$\langle \tilde{\boldsymbol{\mathcal{F}}}(t) \rangle = 0, \tag{11.6}$$

$$\langle \tilde{\boldsymbol{\mathcal{F}}}(t') \cdot \tilde{\boldsymbol{\mathcal{F}}}(t) \rangle = 2D\delta(t'-t). \tag{11.7}$$

To calculate the strength D of the stochastic force, the fluctuation-dissipation theorem can be used. Following the derivation of Ref. [217], the solution to the Langevin equation (i.e., Eq. 11.2 without the interatomic force $\boldsymbol{\mathcal{F}}_j$) is given as

$$\mathbf{v}(t) = \exp[-\gamma t/m]\mathbf{v}(0) + \int_0^t \mathrm{d}t' \exp[-\gamma(t-t')/m]\delta\tilde{\boldsymbol{\mathcal{F}}}(t')/m. \tag{11.8}$$

When calculating $v(t)^2$ there will be three contributions: the first,

$$\exp[-2\gamma t/m]v(0)^2, \tag{11.9}$$

decays to zero at long times; the second,

$$2\mathbf{v}(0)\exp[-\gamma t/m]\int_0^t \mathrm{d}t' \exp[-\gamma(t-t')/m]\delta\tilde{\boldsymbol{\mathcal{F}}}(t')/m, \tag{11.10}$$

is zero when averaged, by Eq. 11.6; the third,

$$\int_0^t \mathrm{d}t' \exp[-\gamma(t-t')/m]\delta\tilde{\boldsymbol{\mathcal{F}}}(t') \int_0^t \mathrm{d}t'' \exp[-\gamma(t-t'')/m]\delta\tilde{\boldsymbol{\mathcal{F}}}(t'')/m^2, \tag{11.11}$$

is the only non-zero contribution when averaged over a large time. The average of $v(t)^2$

can then be written as

$$\begin{aligned}\langle v(t)^2\rangle &= \exp[-2\gamma t/m]v(0)^2 + \int_0^t \mathrm{d}t' \exp[-\gamma(t-t')/m] \int_0^t \mathrm{d}t'' \exp[-\gamma(t-t'')/m] 2D\delta(t'-t'')/m^2 \\ &= \exp[-2\gamma t/m]v(0)^2 + \int_0^t \mathrm{d}t' \exp[-2\gamma(t-t')/m] 2D/m^2 \\ &= \exp[-2\gamma t/m]v(0)^2 + \frac{D}{m\gamma}\left(1-\exp[-2\gamma t/m]\right) \\ &= \frac{D}{m\gamma},\end{aligned} \tag{11.12}$$

where the first line has substituted Eq. 11.7 into the contribution from Eq. 11.11, the second line has used the integral over the Dirac delta function to remove the integral over t'', the third line has performed the integration over t', and the final line has taken the long time limit. Using the equipartition theorem then gives the relationship between the strength D of the stochastic force and the friction coefficient γ as

$$D = \gamma k_\mathrm{B} T_\mathrm{e}. \tag{11.13}$$

11.1.1 Electron-ion coupling

Many previous 2T-MD simulations [23, 24, 111, 216] have used a constant electron-ion coupling constant g_p. However, *ab initio* calculations [207] have shown that g_p increases by a factor of 1.5 over the temperature range $T_\mathrm{e} = 0$ to 20 kK in aluminium, with similar effects found in other materials. I therefore extended the 2T-MD `LAMMPS` module to allow tabulated data for the electron-ion coupling constant $g_\mathrm{p}(T_\mathrm{e})$ to be used in the model, with each electronic cell using the value of g_p appropriate for its electronic temperature T_e. The values of T_e and g_p will be discontinuous across the edge of the electronic cells, due to the coarse graining.

11.1.2 Surfaces

Special treatment must be given to the surface of the thin film when modelled in 2T-MD. Since the electrons are treated as a continuum, any cell that contains ions (henceforth called an active cell) should have an average electronic density $\rho_e \neq 0$. Any cell that contains no ions (inactive cell) should likewise have zero average electronic density. In the October 2021 version of the 2T-MD `LAMMPS` code, the electronic density of all active cells is constant, no matter the number of ions present in each cell. It is a reasonable assumption that ρ_e is proportional to the number of ions in the cell N_i^{cell}. Therefore, I have adapted the code to calculate ρ_e for each cell such that it is proportional to N_i^{cell} and under the constraint that $\sum \rho_e = N_e$, where N_e is defined as the total number of valence electrons in the system at the start of the simulation, $N_e = ZN_i$, and N_i is the sum of all N_i^{cell}. For all simulations of aluminium thin films, the number of valence electrons per ion was fixed as $Z = 3$.

Another consideration when activating a cell is that the newly active cell should now have a non-zero electronic temperature. In the October 2021 version of the 2T-MD `LAMMPS` module, the initial T_e of any newly active cell is set to some constant value. Instead, I set the initial T_e of the newly active cell to be equal to the T_e of an adjacent cell. This makes physical sense as a cell only becomes active when an ion (and its respective electrons) first enter it. The electrons that enter the cell should therefore be expected to be at the same temperature as the cell from which they have entered. Tracking which cell an ion has entered a new cell from can be complicated, depending on how the ions are stored within the MD code. Furthermore, it is likely unnecessary since all the active neighbouring cells of a newly active cell should be expected to have almost identical T_e. Therefore, the choice of neighbour is largely unimportant to the initial temperature of the newly active cell.

11.1.3 Electronic thermal conductivity

The electronic thermal conductivity dictates how heat transfers between the electrons in adjacent electronic cells. Within the 2T-MD module of `LAMMPS`, the electronic thermal conductivity of an electronic cell is defined as

$$\kappa_{\mathrm{e}}(T_{\mathrm{e}}) = \alpha_{\mathrm{e}}\rho_{\mathrm{e}}c_{\mathrm{e}}(T_{\mathrm{e}}), \tag{11.14}$$

with α_{e} the thermal diffusivity, assumed to be independent of temperature. The temperature independence is argued as follows: The definition of the electronic thermal conductivity within the Drude model [207] is

$$\kappa_{\mathrm{e}}(T_{\mathrm{e}}) = v^2\tau c_{\mathrm{e}}(T_{\mathrm{e}}), \tag{11.15}$$

where v^2 is the mean square velocity of the electrons and τ is the electron scattering time. By assuming v^2 and τ are independent of electronic temperature, Eq. 11.14 is found. However, τ is known to have temperature dependence of the form [218, 207]

$$\frac{1}{\tau} = \frac{1}{\tau_{\mathrm{ee}}} + \frac{1}{\tau_{\mathrm{ei}}} = AT_{\mathrm{e}}^2 + BT_{\mathrm{i}}, \tag{11.16}$$

with τ_{ee} the electron-electron scattering time, τ_{ei} the electron-ion scattering time, and A and B material constants. Furthermore, experimental and simulation data show a clear dependence of the total thermal diffusivity on the temperature [219]. The electronic thermal diffusivity will be assumed constant here, due to the use of an arbitrarily high κ_{e} in the simulations later in this chapter to ensure electronic temperature homogeneity; however, future uses of the 2T-MD code should allow for electronic-temperature dependence of α_{e} to better describe κ_{e}.

At each time step, the evolution of the electronic subsystem is calculated by solving Eq. 11.1 using Euler's method. For a one-dimensional system, the electronic temperature of

cell j at time $n+1$ can be written as [220, 221]

$$T_j^{n+1} = T_j^n + \frac{\Delta t}{(\Delta x)^2}\left(\frac{\tilde{\kappa}_{j+1}^n}{C(T_j^n)}(T_{j+1}^n - T_j^n) + \frac{\tilde{\kappa}_{j-1}^n}{C(T_j^n)}(T_{j-1}^n - T_j^n)\right) + \Delta t\frac{\dot{q}_j^n}{C(T_j^n)}, \quad (11.17)$$

where $\tilde{\kappa}_k$ is the effective electronic thermal conductivity between cells j and k, $\dot{q} = -g_{\mathrm{p}}(T_{\mathrm{e}} - T_{\mathrm{i}})$ is the rate of energy gain/loss of the electronic subsystem, and the subscript 'e' has been dropped for clarity. The time step between times n and $n+1$, Δt, used in the Euler method is not required to be the same as the time step of the MD simulation that evolves the ionic positions. The above expression for T^{n+1} can be easily extended to three dimensions with distinct spatial steps Δx, Δy, and Δz [220].

For energy conservation between two interacting cells, the effective electronic thermal conductivity $\tilde{\kappa}$ must be the same for both cells. If $\tilde{\kappa}$ is chosen naively to be the mean electronic thermal conductivity of the two interacting cells,

$$\tilde{\kappa} = \frac{\kappa_j + \kappa_k}{2}, \quad (11.18)$$

or as

$$\tilde{\kappa} = \kappa\left(T = \frac{T_j + T_k}{2}, \rho = \frac{\rho_j + \rho_k}{2}\right), \quad (11.19)$$

the stability condition of the Euler method (in one dimension),

$$\Delta t < \min_{i=j,k}\left(\frac{(\Delta x)^2}{2\tilde{\alpha}^i}\right), \quad (11.20)$$

with the effective electronic thermal diffusivity of cell i defined as $\tilde{\alpha}^i = \tilde{\kappa}/\rho c^i$, leads to an extremely small Δt for neighbouring cells with vastly different κ.

Most often, this occurs when a cell is switched on as an ion moves into it for the first time. This newly activated (na) cell will have a much smaller ρ, and therefore κ, than its neighbouring (neigh) cells. The effective electronic thermal conductivity of the cells, as

defined by Eq. 11.18, can be approximated as

$$\tilde{\kappa} \approx \frac{\kappa^{\text{neigh}}}{2} \gg \kappa^{\text{na}}, \tag{11.21}$$

and the effective electronic thermal diffusivity of the newly activated cell is given by

$$\tilde{\alpha}^{\text{na}} = \frac{\tilde{\kappa}}{\rho^{\text{na}} c^{\text{na}}} \gg \frac{\kappa^{\text{na}}}{\rho^{\text{na}} c^{\text{na}}} = \alpha. \tag{11.22}$$

The inverse of the thermal diffusivity can be seen as the characteristic timescale for heat flow between interacting cells. Since $\tilde{\alpha}^{\text{na}} \gg \alpha$, if the electronic thermal diffusivity of the cell is chosen to be $\tilde{\alpha}^{\text{na}}$, the time step calculated by Eq. 11.20 will be much smaller than the characteristic time step for stability calculated using α. The characteristic time step is the same for all cells due to the definition of κ_{e} given in Eq. 11.14. If the small time step calculated using Eq. 11.20 is used in the Euler method, many consecutive solutions of Eq. 11.17 are required to span a length of time equal to the MD time step. This is computationally expensive and is the primary bottleneck on the performance of the 2T-MD model when using either of the above definitions for $\tilde{\kappa}$.

To avoid this bottleneck, the effective electronic thermal conductivity is defined by the physically-observed relationship of two thermal conductors in series,

$$\frac{1}{\tilde{\kappa}} = \frac{1}{\kappa_j} + \frac{1}{\kappa_k}, \tag{11.23}$$

which is analogous to the total electrical conductance of electrical conductors connected in series. The effect of this change in definition of $\tilde{\kappa}$ on the final simulated structure of a laser-irradiated thin film of aluminium (details of which are given in Section 11.2) is shown in Fig. 11.2. The run time when using Eq. 11.23 as the definition of $\tilde{\kappa}$ was approximately 70 times shorter than the October 2021 version of `LAMMPS` [216, 30] that uses Eq. 11.19. Note that, when using Eq. 11.19, the vast majority of the computational time was spent on the few time steps after a new cell was activated. Although using Eq. 11.23 leads to a larger time step, it is still small enough to guarantee numerical stability,

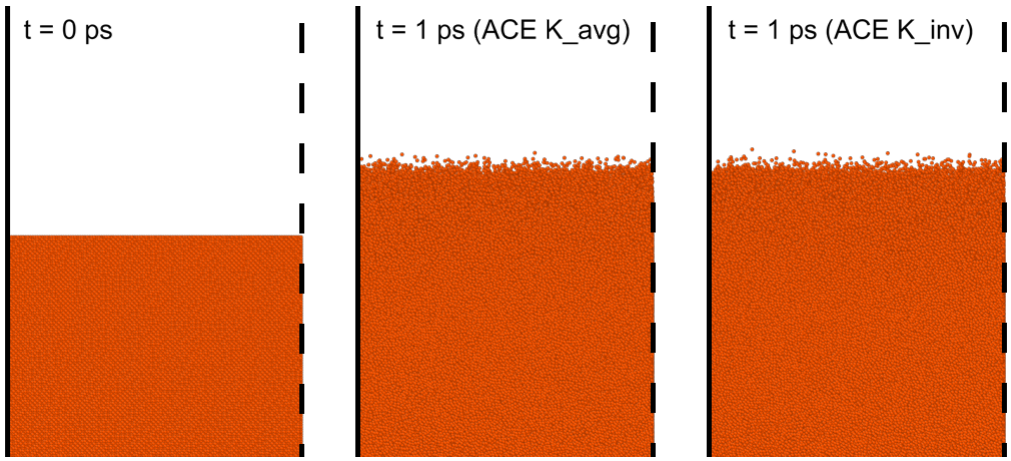

Figure 11.2: Snapshots of a 35×50×50 nm aluminium thin film that has been laser irradiated and is allowed to expand along its x axis (vertical). The initial film was an fcc single crystal with the laser irradiation perpendicular to the (100) plane. The snapshots display only half (25 nm) of the width of the simulation cell in the y direction (horizontal) to allow individual atoms to be distinguished, and periodic boundary conditions are enforced in the y and z directions. The left image shows the equilibrated fcc lattice prior to laser irradiation. The middle image shows the film 1 ps after laser irradiation when using Eq. 11.18 as the effective electronic thermal conductivity. The right image is the same as the middle image, but uses Eq. 11.23 as the definition of the effective electronic thermal conductivity. Both simulations used the T_e-dependent ACE potential to calculate $\boldsymbol{\mathcal{F}}_j$. Both methods gave $T_e(t = 1\text{ps}) \approx 35430$ K for all electronic temperature cells, due to the high electronic thermal conductivity. The final simulated structures are practically identical, with the simulation using Eq. 11.23 approximately 70 times faster than that using Eq. 11.18. All snapshots were plotted using `OVITO` [222] and contained 5.2 million atoms.

reinforcing the idea that averaging the inverse thermal conductivities is the right thing to do. Furthermore, as shown in Fig. 11.2, the simulation remained accurate.

11.2 Laser-irradiated thin film

When a thin film is laser-irradiated, as shown in Fig. 11.1, it is often assumed that the energy from the laser is deposited entirely into the electronic system [213, 29, 49, 223, 16, 224] and, owing to the fast electron thermalisation time relative to the electron-ion coupling rate [113, 225], that the electrons are heated instantaneously. Furthermore, it is assumed here that the thin film is homogeneously heated and that T_e remains spatially homogeneous throughout the simulation.

The homogeneous heating is argued as such: the laser heats the electrons within a skin depth $\lambda_{\text{skin}} < x_{\text{f}}$, where x_{f} is the thickness of the thin film. These electrons then move ballistically, heating the rest of the sample along the direction of the laser [226, 32]. This process has been observed in gold thin films [223, 227] and is very fast.

Taking κ_{e} from Ref. [30] and C_{e} from Refs. [207] and [228], the electronic thermal diffusion coefficient can be calculated using Eq. 11.14 as $\alpha_{\text{e}} \approx \kappa_{\text{e}}/C_{\text{e}} = 7 \times 10^{-4}$ m^{2}s^{-1}. The characteristic time of heating the electrons within a 35 nm thin film can then be approximated as $\Delta t \approx (\Delta x)^2/\alpha_{\text{e}} = 50$ fs, which is short compared to the 1 ps duration of the simulations performed in this chapter. Since the cross-sectional area probed in experiments can be much smaller than the total irradiated region [31, 25], lateral heat diffusion during heating is negligible and the electronic temperature can be assumed homogeneous along all dimensions of the sample. The continued existence of a spatially homogeneous T_{e} after heating is a consequence of the high electronic thermal conductivity of aluminium [229, 230].

A 35×50×50 nm single-crystalline aluminium thin film after laser irradiation, with $T_{\text{e}}(t = 0) = 40$ kK and $T_{\text{i}}(t = 0) = 300$ K, is shown in Fig. 11.3. The size of the film is chosen such that it matches the thickness of the metal thin film in Ref. [29], but is wider to allow for potential voids to form [100]. Prior to the 2T-MD simulation, the starting fcc lattice was equilibrated at 300 K in the NPT ensemble. The T_{e}-dependent values of C_{e} and g_{p} from Refs. [207] and [228] have been used, and all 2T-MD simulations were performed using a locally adapted version of the `ttm/mod` fix [216, 30], available within `LAMMPS`, that incorporates the extended functionality discussed in the preceding sections. Due to the lack of *ab initio* data for g_{p} above 20 kK, and the almost constant value of g_{p} between 5 and 20 kK, the approximation $g_{\text{p}}(T_{\text{e}} > 20 \text{ kK}) \approx g_{\text{p}}(T_{\text{e}} = 20 \text{ kK})$ is assumed to hold.

The impact of using a finite-T_{e} interatomic potential is immediately obvious when comparing the 1 ps snapshots of the EAM and ACE simulations. Both simulations include expansion due to the stochastic force $\tilde{\boldsymbol{\mathcal{F}}}$ that models the energy transport from the hot

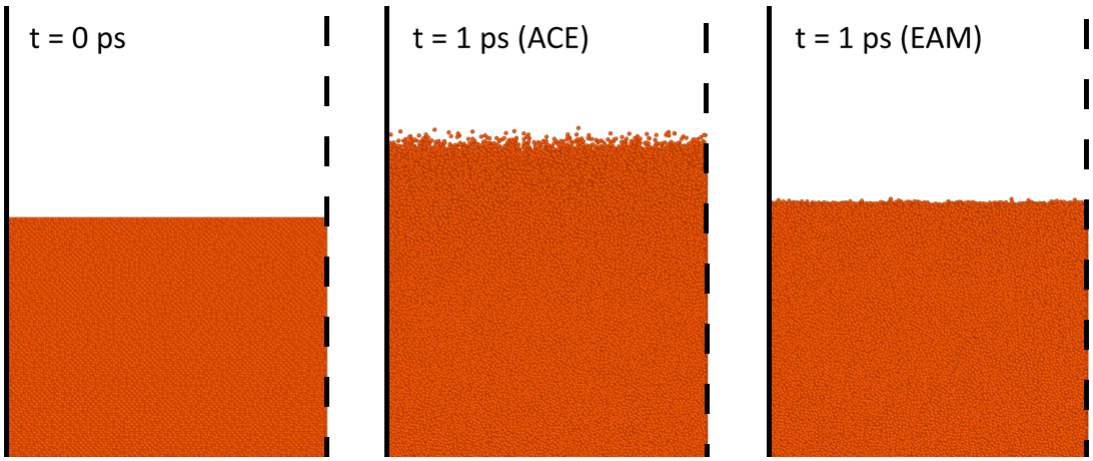

Figure 11.3: Snapshots of a 35×50×50 nm aluminium thin film that has been laser irradiated and is allowed to expand along its x axis (vertical). The initial film was an fcc single crystal with the laser irradiation perpendicular to the (100) plane. The snapshots display only half (25 nm) of the width of the simulation cell in the y direction (horizontal) to allow individual atoms to be distinguished, and periodic boundary conditions are enforced in the y and z directions. The left image shows the equilibrated fcc lattice prior to laser irradiation. The middle image shows the film 1 ps after laser irradiation when the T_e-dependent ACE potential from Chapter 6 is used to calculate $\boldsymbol{\mathcal{F}}_j$ in the simulation. The right image is the same as the middle image, but uses a zero-temperature EAM potential [215] that has previously been used in thin film simulations [49]. All snapshots were plotted using `OVITO` [222] and contained 5.2 million atoms.

electronic subsystem to the cold ions, but only the ACE potential contains T_e dependence of the deterministic interatomic forces $\boldsymbol{\mathcal{F}}_j$. From Eq. 11.1, the characteristic timescale of the electron-ion coupling is given by $t = C_\mathrm{e}/g_\mathrm{p} \approx 1$ ps. As this is of the same order as the length of the simulation, there will be a significant lag time before enough energy is transferred to the ions through $\tilde{\boldsymbol{\mathcal{F}}}$ for the film to expand. In contrast, the finite-T_e effects contained within the ACE potential occur on the timescale of the electron thermalisation (which is approximated in this simulation to be instant) and do not depend on the strength of the electron-ion coupling. The interatomic forces $\boldsymbol{\mathcal{F}}_j$ therefore dictate the short-time behaviour of the ions.

A key limitation of the ACE potentials is that they were not fit to any surface data. Therefore, the behaviour of the ions at the surface of the film may not be entirely correct; however, this issue could be prevented by amending the ACE training dataset to include snapshots of surfaces with elevated electronic temperatures. Alternatively, iterative learning could be used [231] where the surface behaviour is learned after the initial

ACE potential is fit.

There have been previous studies of laser-irradiated aluminium using an electronically-excited interatomic potential [142, 232], where it was found that the melting of the ionic lattice was dominated by electron-ion coupling, rather than the change in interatomic potential due to the thermal electronic excitations. However, these studies approximated the change in the interatomic potential by an effective pairwise interaction that modelled short-lived excitations of 2p electrons, rather than Fermi-Dirac smearing of the occupations of all electronic states. The highest T_e simulated was also 8000 K, lower than the range of T_e studied for the ACE potential here. The use of a temperature-dependent ACE potential fit to *ab initio* data, along with the higher electronic temperatures studied here, clearly enhances the effects arising from the T_e dependence of $\boldsymbol{\mathcal{F}}_j$.

11.3 Femtosecond electron diffraction

Femtosecond (or ultrafast) electron diffraction [210, 211] is a technique used to experimentally observe the evolution of laser-irradiated thin films. Femtosecond electron diffraction experiments allow for the observation of diffraction patterns and ionic structure factors in these nonequilibrium systems [209, 112, 233, 234, 49], which can be compared to diffraction patterns and structure factors calculated from the results of 2T-MD simulations. Furthermore, both femtosecond electron diffraction and 2T-MD can be used to elucidate the transition between heterogeneous and homogeneous melting as the pumping laser intensity increases [29], or to study phenomena such as the breathing motion observed in polyhedral clusters of aluminium [49].

Accurately simulating diffraction patterns observed experimentally is a key test of the 2T-MD method and its input parameters (e.g., g_p and C_e). Of particular note here, the simulated diffraction patterns can also be used to benchmark the importance of electronic-temperature effects in the interatomic potential used. Previously, simulated diffraction patterns of laser-irradiated gold thin films [29] have been matched to exper-

imental data [112] using a zero-temperature EAM potential. It was found that using finite-temperature interatomic potentials produced results with only minor differences in the simulated decay of Laue diffraction peaks and electronic and ionic temperatures; however, the finite-temperature interatomic potentials used were fit to data with a constant electronic temperature much lower than of interest here [20].

Guo et al. [235] determined through measurement of the dielectric constant that aluminium thin films should undergo athermal melting when irradiated with a laser fluence of at least 34 mJ/cm^2; however, a subsequent femtosecond electron diffraction study by Siwick et al. [233] found that even at a laser fluence of 70 mJ/cm^2, the melting dynamics could be described by lattice heating driven by electron-phonon interactions.

A further femtosecond electron diffraction study of aluminium thin films was recently published by Wu et al. [49]. However, the time evolution of the diffraction patterns was only observed for a laser fluence of 500 mJ/cm^2. A laser fluence up to 1250 mJ/cm^2 was used to irradiate aluminium thin films, but only the diffraction patterns at 50 ps were recorded. The authors also used 2T-MD, with a zero-temperature EAM potential [236], to recreate the breathing motion of the first peak of the radial distribution function.

For the linear interpolation scheme and ACE potentials fit in this thesis to be of use in simulating the system probed by Wu et al., the electronic temperature must fall within the range found in the ACE training dataset (10 - 100 kK) for the approximately 1.5 ps that the system takes to melt. Therefore, a 2T-MD simulation using the same parameters and interatomic potential as Ref. [49] was undertaken for both the highest laser fluence (1250 mJ/cm^2) and the laser fluence used to generate the time evolution of the diffraction patterns (500 mJ/cm^2). The electronic temperature was then output by the 2T-MD `LAMMPS` module at particular time intervals. Although a zero-temperature interatomic potential could be used for electronic temperatures lower than 10 kK (since finite-temperature effects will become negligible as $T_\mathrm{e} \to 0$), the main aim of simulating the diffraction patterns is to test the finite-temperature ACE potentials.

For a laser fluence of 1250 mJ/cm^2, the electronic temperature after laser heating reaches

just above 10 kK for approximately 250 fs. However, after this time the electronic temperature falls below 10 kK (the lowest temperature for which an ACE potential was fit), preventing the simulation of diffraction patterns for longer than 250 fs. For a laser fluence of 500 mJ/cm^2, the electronic temperature never reaches 10 kK, and as such the experimentally observed time evolution of the diffraction pattern shown in the paper cannot be reproduced using the ACE potentials fit here.

Therefore, for the fitted ACE potentials to be of use in simulating electron diffraction patterns, either experimental data of the electron diffraction patterns at higher laser fluence (and therefore electronic temperature) must be produced, or lower electronic temperature ACE potentials must be fit. Since the primary interest of this thesis is investigating the electronic-temperature effects on the interatomic forces, the former would be much preferred. Although these elevated electronic temperatures are unlikely to be found in two-temperature systems relevant to real-world applications (e.g., laser etching and inertial confinement fusion reactor walls), these electronic temperatures are expected to be found in planetary cores [237]. The electron diffraction patterns would therefore provide experimental data that could prove useful as a benchmark for the finite-temperature ACE potentials used to model these astrophysical processes.

A laser with lower power could potentially be used to irradiate an aluminium thin film with a higher fluence by increasing the irradiation time, such that a high electronic temperature is achieved; however, the assumption of instant electronic heating used earlier would no longer hold and the finite transition from zero electronic temperature to high electronic temperature would, once again, require an ACE potential that can model interatomic forces all the way down to zero electronic temperature.

At the high laser fluences required for an electronic temperature of order 10 kK to be achieved, ablation is likely to occur. Previously reported values of the absorbed fluence[1] required for ablation are F_{ablation} = 65 - 70 mJ/cm^2 [239, 240]. For a thick enough sample, the core region may be accurately described without taking into account the

[1]Note that the absorption rate of aluminium is approximately 13% [100, 238], i.e., the laser fluence required for ablation is $F^{\text{laser}}_{\text{ablation}} = F_{\text{ablation}}/0.13 \approx 500$ mJ/cm^2.

ablation dynamics that occur at the surfaces. Avoiding laser fluences above the ablation threshold would potentially simplify the understanding of any electronic temperature effects observed; however, it is unlikely that the high electronic temperatures required for electronic temperature effects to become noticeable could be reached with laser fluences lower than the ablation threshold. By expanding the dataset used to fit the ACE potentials to include small clusters of atoms and other configurations representative of ablation, ACE potentials could be fit that will allow the finite-temperature effects at a range of laser fluences to be investigated.

11.4 Summary

This chapter began by explaining the two-temperature molecular dynamics (2T-MD) method, a simulation technique that can model nonequilibrium systems with a high electronic temperature but low ionic temperature. This commonly occurs in laser-irradiated thin films that can also be experimentally probed using femtosecond electron diffraction.

I then extended and adapted a previous implementation of the 2T-MD method to incorporate more accurate models of physical parameters: a temperature-dependent electron-ion coupling, an electronic density proportional to the number of ions within a particular electronic cell, an initial temperature for a newly activated electronic cell equal to that of one of its neighbours, temperature-dependent interatomic forces that are coupled to the electronic temperature of the electronic cell occupied by the ion, and an effective electronic thermal conductivity calculated using a model of electrical conductors in series. Previously unnoticed bugs and inefficiencies in the module were also fixed.

I used the 2T-MD method to simulate laser-irradiated aluminium thin films with both my temperature-dependent ACE potential and a zero-temperature EAM potential, previously used in similar studies. Large differences between the structures of the films 1 ps after irradiation were observed, showing the necessity of including electronic-temperature effects in the simulation of laser-irradiated solids. It is hoped that these results will be validated

by future femtosecond electron diffraction experiments.

Finally, future uses of the 2T-MD method and temperature-dependent ACE potentials in experimentally realisable systems are discussed, along with potential limitations.

Chapter 12

Conclusion

12.1 Summary

In this thesis, the performance of various simulation techniques for use in large-scale MD simulations of warm dense aluminium has been investigated. The free energies, forces, EOSs, and phonon dispersion curves, as well as the scaling of computational and time resources with system size and temperature, were compared against benchmark MHKS-DFT data.

OF-DFT methods scale independently of temperature, whilst also scaling favourably with system size, allowing for the simulation of the high temperature systems found in warm dense matter. Use of a non-local free energy functional, implemented in Chapter 3, may give satisfactory accuracy for limited applications, but the restriction to local pseudopotentials was found to cause noticeable deviations from benchmark calculations. Whether it is possible to construct a local pseudopotential that can reasonably match the accuracy of non-local pseudopotentials in warm dense aluminium is an open question.

In Chapter 6, the Atomic Cluster Expansion (ACE), originally derived by Ralf Drautz [50], was introduced. Due to its general form and high accuracy, it was chosen as the basis for fitting a finite-temperature interatomic potential. Firstly, individual potentials were each

fit to data at a single electronic temperature to ensure the ACE could accurately predict finite-temperature data. Then, free energies and forces predicted by the ACE potentials were compared to MHKS-DFT benchmark data. The resulting potentials predict forces with an error of only a few percent and energies with an error less than 20 meV/atom, much lower than the corresponding OF-DFT errors. Importantly, the evaluation of the ACE potentials requires only a fraction of the computational cost of both MHKS-DFT and OF-DFT.

Temperature dependence was incorporated into the ACE potentials by using a linear interpolation scheme. The free energies and forces at a temperature T_I were calculated by linearly interpolating between the free energies and forces predicted by ACE potentials fit to data at temperatures T_L and T_U, where $T_\mathrm{L} < T_\mathrm{I} < T_\mathrm{U}$. Equations of state for warm dense aluminium were calculated to test the ACE and OF-DFT method, as well as the linear interpolation scheme. This also gave insight into the importance of the pseudopotential used in DFT methods.

The many-body contributions to the interatomic forces were investigated, with embedding in an HEG shown to converge high temperature interatomic forces at a lower order of interaction than embedding in a vacuum. It was also shown that, at high enough temperatures, many-body interactions are expected to become negligible.

Predicting the phonon dispersion curves of nonequilibrium aluminium at finite temperature acted as another test of the accuracy of the finite-temperature ACE potentials and OF-DFT. The resulting phonon dispersion curves confirmed previous findings of a lack of bond hardening or softening in warm dense aluminium.

Finally, the two-temperature molecular dynamics (2T-MD) model was used to simulate laser irradiation of aluminium thin films. Neither MHKS-DFT nor OF-DFT could be used in these simulations, due to the poor computational scaling of the methods; however, the efficient evaluation of the ACE allows systems of millions of atoms to be readily simulated. Adaptations and extensions to the 2T-MD model were made to better match the underlying physics of the system and improve the computational efficiency. A comparison

between the final structures of the thin films, simulated using a zero-temperature EAM interatomic potential and the temperature-dependent ACE potential, showed significant qualitative differences due to the electronic-temperature effects.

12.2 Future Work

In this work, the ACE has been shown to reproduce the free energies and forces of a MHKS-DFT training dataset to a high degree of accuracy, at a fraction of the computational cost of *ab initio* methods. Furthermore, the high accuracy persists no matter the electronic temperature of the fitting data and a linear interpolation scheme allows for probing of systems at intermediate electronic temperatures not contained within the training dataset. However, for systems that may undergo a phase transition or other behaviour not described by the Fermi-Dirac smearing of electronic occupations, this linear interpolation may not hold. The linear interpolation also leads to discontinuous gradients in the free energies and forces when the temperature of the electrons in the system crosses an electronic temperature contained within the training dataset.

Higher-order spline interpolation was suggested as a possible approach that would allow for continuous gradients with only a constant factor increase in the computational time and resources. A better approach would be to allow the expansion coefficients of the ACE to vary with the electronic temperature. A single temperature-dependent ACE potential could therefore be fit to a dataset containing snapshots at a range of electronic temperatures. Potential problems may arise when fitting data from different electronic temperatures. This is because the magnitude of the free energy and force fluctuations can change with electronic temperature. The largest errors, which are assumed to be found where the fluctuations are largest, will dominate the loss function. This effect can be mitigated by use of a scaling factor.

By employing a pseudopotential with a smaller core radius and fewer frozen core electrons, accurate MHKS-DFT data at temperatures and densities higher than those studied here

could be included in the ACE training dataset. This should lead to a better matching of the ACE and FPEOS equations of state in Chapter 8 and a better understanding of the importance of the pseudopotential in DFT methods.

The use of a temperature-dependent ACE potential in the extended 2T-MD `LAMMPS` module would allow for the simulation of electron diffraction patterns in laser-irradiated metals that can be compared to experimentally observed patterns. Expanding the training dataset of the ACE potentials to include configurations representative of low temperatures and those found in ablation processes would make it possible to simulate electron diffraction patterns for the entire duration of the laser irradiation and at the high laser fluences required to observe electronic-temperature effects. In the case of aluminium, this would require the fitting of a 300 K ACE potential, which has not currently been performed; however, fitting this potential should be possible. The comparison with experimental data would provide insight into the transition between heterogeneous and homogenous melting, as well as other atomistic behaviours. The importance of finite electronic temperature effects in accurately describing laser-irradiated systems could be investigated by performing the same 2T-MD simulation using a zero-temperature potential. The combination of 2T-MD and a finite-temperature potential could also be used to investigate the importance of electronic-temperature effects in laser micromachining, where localised heating by a laser can form patterns on the surface of a material through ablative processes.

Finally, both inertial confinement fusion implosions and planetary cores are known to contain warm dense matter [1, 2, 7, 8, 9]. A finite-temperature ACE potential fit to appropriate data could be used to investigate the importance of electronic-temperature effects in these systems. Importantly, the efficient evaluation of the energies and forces in the ACE paradigm would allow large-scale MD simulations of these systems to be performed, something not possible using *ab initio* methods. The results of these simulations could be compared to experimental data [241], providing insight into the electronic-temperature effects.

Bibliography

[1] S X Hu, B Militzer, V N Goncharov, and S Skupsky. First-principles equation-of-state table of deuterium for inertial confinement fusion applications. *Phys. Rev. B*, 84(22):224109, December 2011. 1, 189

[2] I Cook. Materials research for fusion energy. *Nature Materials*, 5:77–80, February 2006. 1, 189

[3] Ralph Ernstorfer, Maher Harb, Christoph T Hebeisen, Germán Sciaini, Thibault Dartigalongue, and R J Dwayne Miller. The Formation of Warm Dense Matter: Experimental Evidence for Electronic Bond Hardening in Gold. *Science*, 323(5917):1033–1037, 2009. 1

[4] Katerina Falk. Experimental methods for warm dense matter research. *High Power Laser Science and Engineering*, 6, 2018/ed. 1

[5] E Zarkadoula, S L Daraszewicz, D M Duffy, M A Seaton, I T Todorov, K Nordlund, M T Dove1, and K Trachenko. Electronic effects in high-energy radiation damage in iron. *J. Phys.: Condens. Matter*, 26(8):85401, 2014. 1

[6] L. B. Fletcher, H. J. Lee, T. Döppner, E. Galtier, B. Nagler, P. Heimann, C. Fortmann, S. LePape, T. Ma, M. Millot, A. Pak, D. Turnbull, D. A. Chapman, D. O. Gericke, J. Vorberger, T. White, G. Gregori, M. Wei, B. Barbrel, R. W. Falcone, C.-C. Kao, H. Nuhn, J. Welch, U. Zastrau, P. Neumayer, J. B. Hastings, and S. H. Glenzer. Ultrabright X-ray laser scattering for dynamic warm dense matter physics. *Nature Photonics*, 9(4):274–279, April 2015. 1

[7] Gilles Chabrier. Quantum effects in dense Coulumbic matter - Application to the cooling of white dwarfs. *The Astrophysical Journal*, 414:695–700, September 1993. 1, 189

[8] Alessandra Benuzzi-Mounaix, Stéphane Mazevet, Alessandra Ravasio, Tommaso Vinci, Adrien Denoeud, Michel Koenig, Nourou Amadou, Erik Brambrink, Floriane Festa, Anna Levy, Marion Harmand, Stéphanie Brygoo, Gael Huser, Vanina Recoules, Johan Bouchet, Guillaume Morard, François Guyot, Thibaut de Resseguier, Kohei Myanishi, Norimasa Ozaki, Fabien Dorchies, Jerôme Gaudin, Pierre Marie Leguay, Olivier Peyrusse, Olivier Henry, Didier Raffestin, Sebastien Le Pape, Ray Smith, and Riccardo Musella. Progress in warm dense matter study with applications to planetology. *Physica Scripta*, T161:014060, May 2014. 1, 189

[9] M D Knudson, M P Desjarlais, R W Lemke, T R Mattsson, M French, N Nettelmann, and R Redmer. Probing the Interiors of the Ice Giants: Shock Compression of Water to 700 GPa and 3.8 g/cm3̂. *Phys. Rev. Lett.*, 108(9):91102, February 2012. 1, 189

[10] T. Sasaki, T. Ohuchi, A. Watabe, S. Sugimoto, K. Takahashi, T. Kikuchi, M. Koga, and S. Fujioka. An Exploding Wire-Compression Method for Evaluating the Electrical Conductivity of Diamond-Like Carbon in a Warm Dense State. *IEEE Transactions on Plasma Science*, 47(2):1477–1481, February 2019. 1

[11] Toru Sasaki, Yuuri Yano, Mitsuo Nakajima, Tohru Kawamura, and Kazuhiko Horioka. Warm-dense-matter studies using pulse-powered wire discharges in water. *Laser and Particle Beams*, 24(3):371–380, September 2006. 1

[12] Shaunak Mukherjee, Florian Libisch, Nicolas Large, Oara Neumann, Lisa V. Brown, Jin Cheng, J. Britt Lassiter, Emily A. Carter, Peter Nordlander, and Naomi J. Halas. Hot Electrons Do the Impossible: Plasmon-Induced Dissociation of H $_2$ on Au. *Nano Letters*, 13(1):240–247, January 2013. 1

[13] S H Glenzer, O L Landen, P Neumayer, R W Lee, K Widmann, S W Pollaine, R J Wallace, G Gregori, A Höll, T Bornath, R Thiele, V Schwarz, W.-D. Kraeft, and R Redmer. Observations of Plasmons in Warm Dense Matter. *Phys. Rev. Lett.*, 98(6):65002, February 2007. 1

[14] Siegfried H. Glenzer and Ronald Redmer. X-ray Thomson scattering in high energy density plasmas. *Reviews of Modern Physics*, 81(4):1625–1663, December 2009. 1

[15] D. Kraus, J. Vorberger, D. O. Gericke, V. Bagnoud, A. Blažević, W. Cayzac, A. Frank, G. Gregori, A. Ortner, A. Otten, F. Roth, G. Schaumann, D. Schumacher, K. Siegenthaler, F. Wagner, K. Wünsch, and M. Roth. Probing the Complex Ion Structure in Liquid Carbon at 100 GPa. *Physical Review Letters*, 111(25):255501, December 2013. 1

[16] B. Mahieu, N. Jourdain, K. Ta Phuoc, F. Dorchies, J.-P. Goddet, A. Lifschitz, P. Renaudin, and L. Lecherbourg. Probing warm dense matter using femtosecond X-ray absorption spectroscopy with a laser-produced betatron source. *Nature Communications*, 9(1):3276, August 2018. 1, 178

[17] Travis Sjostrom and Jérôme Daligault. Ionic and electronic transport properties in dense plasmas by orbital-free density functional theory. *Physical Review E*, 92(6):063304, December 2015. 1, 2, 29, 73

[18] J. Vorberger, K. U. Plageman, and R. Redmer. The structure in warm dense carbon. *High Energy Density Physics*, 35:100737, June 2020. 1

[19] S. V. Starikov, V. V. Stegailov, G. E. Norman, V. E. Fortov, M. Ishino, M. Tanaka, N. Hasegawa, M. Nishikino, T. Ohba, T. Kaihori, E. Ochi, T. Imazono, T. Kavachi, S. Tamotsu, T. A. Pikuz, I. Yu. Skobelev, and A. Ya. Faenov. Laser ablation of gold: Experiment and atomistic simulation. *JETP Letters*, 93(11):642–647, August 2011. 2, 169

[20] G. E. Norman, S. V. Starikov, and V. V. Stegailov. Atomistic simulation of laser ablation of gold: Effect of pressure relaxation. *Journal of Experimental and Theoretical Physics*, 114(5):792–800, May 2012. 2, 55, 92, 169, 182

[21] V. Recoules, J. Clérouin, G. Zérah, P. M. Anglade, and S. Mazevet. Effect of Intense Laser Irradiation on the Lattice Stability of Semiconductors and Metals. *Physical Review Letters*, 96(5):055503, February 2006. 2, 3, 56, 83, 92, 140, 165, 168, 169

[22] Jean Clérouin, Grégory Robert, Philippe Arnault, Christopher Ticknor, Joel D. Kress, and Lee A. Collins. Evidence for out-of-equilibrium states in warm dense matter probed by x-ray Thomson scattering. *Physical Review E*, 91(1):011101, January 2015. 2

[23] D. M. Duffy and A. M. Rutherford. Including the effects of electronic stopping and electron–ion interactions in radiation damage simulations. *Journal of Physics: Condensed Matter*, 19(1):016207, December 2006. 2, 59, 169, 171, 172, 173

[24] A. M. Rutherford and D. M. Duffy. The effect of electron–ion interactions on radiation damage simulations. *Journal of Physics: Condensed Matter*, 19(49):496201, November 2007. 2, 169, 171, 173

[25] Robert Darkins and Dorothy M. Duffy. Modelling radiation effects in solids with two-temperature molecular dynamics. *Computational Materials Science*, 147:145–153, May 2018. 2, 170, 179

[26] S. Khakshouri, D. Alfè, and D. M. Duffy. Development of an electron-temperature-dependent interatomic potential for molecular dynamics simulation of tungsten under electronic excitation. *Physical Review B*, 78(22):224304, December 2008. 2, 59, 92, 169

[27] Chiheb Ben Mahmoud, Federico Grasselli, and Michele Ceriotti. Predicting hot-electron free energies from ground-state data. *Physical Review B*, 106(12):L121116, September 2022. 2, 93

[28] Szymon L. Daraszewicz, Yvelin Giret, Nobuyasu Naruse, Yoshie Murooka, Jinfeng Yang, Dorothy M. Duffy, Alexander L. Shluger, and Katsumi Tanimura. Structural dynamics of laser-irradiated gold nanofilms. *Physical Review B*, 88(18):184101, November 2013. 2, 165

[29] Jacob M. Molina and T. G. White. A molecular dynamics study of laser-excited gold. *Matter and Radiation at Extremes*, 7(3):036901, May 2022. 2, 170, 178, 179, 181

[30] G. E. Norman, S. V. Starikov, V. V. Stegailov, I. M. Saitov, and P. A. Zhilyaev. Atomistic Modeling of Warm Dense Matter in the Two-Temperature State. *Contributions to Plasma Physics*, 53(2):129–139, 2013. 2, 172, 177, 179

[31] R. Darkins, P.-W. Ma, S. T. Murphy, and D. M. Duffy. Simulating electronically driven structural changes in silicon with two-temperature molecular dynamics. *Physical Review B*, 98(2), July 2018. 2, 179

[32] Samuel T. Murphy, Yvelin Giret, Szymon L. Daraszewicz, Anthony C. Lim, Alexander L. Shluger, Katsumi Tanimura, and Dorothy M. Duffy. Contribution of electronic excitation to the structural evolution of ultrafast laser-irradiated tungsten nanofilms. *Physical Review B*, 93(10):104105, March 2016. 2, 179

[33] P. Hohenberg and W. Kohn. Inhomogeneous Electron Gas. *Physical Review*, 136(3B):B864–B871, November 1964. 2, 7

[34] N. David Mermin. Thermal Properties of the Inhomogeneous Electron Gas. *Physical Review*, 137(5A):A1441–A1443, March 1965. 2, 9

[35] W. Kohn and L. J. Sham. Self-Consistent Equations Including Exchange and Correlation Effects. *Physical Review*, 140(4A):A1133–A1138, November 1965. 2, 13

[36] Vincent L. Lignères and Emily A. Carter. An Introduction to Orbital-Free Density Functional Theory. In Sidney Yip, editor, *Handbook of Materials Modeling: Methods*, pages 137–148. Springer Netherlands, Dordrecht, 2005. 2

[37] Shen Zhang, Hongwei Wang, Wei Kang, Ping Zhang, and X. T. He. Extended application of Kohn-Sham first-principles molecular dynamics method with plane wave approximation at high energy—From cold materials to hot dense plasmas. *Physics of Plasmas*, 23(4):042707, April 2016. 2, 73, 75, 147

[38] Phanish Suryanarayana, Phanisri P. Pratapa, Abhiraj Sharma, and John E. Pask. SQDFT: Spectral Quadrature method for large-scale parallel $\mathcal{O}(N)$ Kohn-Sham calculations at high temperature. *Computer Physics Communications*, 224:288–298, March 2018. 2

[39] Flavien Lambert, Jean Clérouin, and Gilles Zérah. Very-high-temperature molecular dynamics. *Physical Review E*, 73(1):016403, January 2006. 2

[40] Travis Sjostrom and Scott Crockett. Quantum molecular dynamics of warm dense iron and a five-phase equation of state. *Physical Review E*, 97(5):053209, May 2018. 2, 64, 147

[41] Travis Sjostrom and Scott Crockett. Orbital-free extension to Kohn-Sham density functional theory equation of state calculations: Application to silicon dioxide. *Physical Review B*, 92(11):115104, September 2015. 2, 126, 147

[42] Valentin V. Karasiev, Debajit Chakraborty, Olga A. Shukruto, and S. B. Trickey. Nonempirical generalized gradient approximation free-energy functional for orbital-free simulations. *Physical Review B*, 88(16):161108, October 2013. 2, 31, 32

[43] Karin M. Carling and Emily A. Carter. Orbital-free density functional theory calculations of the properties of Al, Mg and Al–Mg crystalline phases. *Modelling and Simulation in Materials Science and Engineering*, 11(3):339, April 2003. 2

[44] Junchao Xia, Chen Huang, Ilgyou Shin, and Emily A. Carter. Can orbital-free density functional theory simulate molecules? *The Journal of Chemical Physics*, 136(8):084102, February 2012. 2, 51

[45] T. G. White, S. Richardson, B. J. B. Crowley, L. K. Pattison, J. W. O. Harris, and G. Gregori. Orbital-Free Density-Functional Theory Simulations of the

Dynamic Structure Factor of Warm Dense Aluminum. *Physical Review Letters*, 111(17):175002, October 2013. 2, 29

[46] Qianrui Liu, Denghui Lu, and Mohan Chen. Structure and dynamics of warm dense aluminum: A molecular dynamics study with density functional theory and deep potential. *Journal of Physics: Condensed Matter*, 32(14):144002, January 2020. 2, 85, 86, 87

[47] K. P. Driver, F. Soubiran, and B. Militzer. Path integral Monte Carlo simulations of warm dense aluminum. *Physical Review E*, 97(6):063207, June 2018. 3, 68, 126, 147, 148, 149

[48] Burkhard Militzer, Felipe González-Cataldo, Shuai Zhang, Kevin P. Driver, and François Soubiran. First-principles equation of state database for warm dense matter computation. *Physical Review E*, 103(1):013203, January 2021. 3, 149

[49] Jun Wu, Minxue Tang, Lingrong Zhao, Pengfei Zhu, Tao Jiang, Xiao Zou, Liang Hong, Sheng-Nian Luo, Dao Xiang, and Jie Zhang. Ultrafast atomic view of laser-induced melting and breathing motion of metallic liquid clusters with MeV ultrafast electron diffraction. *Proceedings of the National Academy of Sciences*, 119(4):e2111949119, January 2022. 3, 165, 178, 180, 181, 182

[50] Ralf Drautz. Atomic cluster expansion for accurate and transferable interatomic potentials. *Physical Review B*, 99(1):014104, January 2019. 3, 113, 114, 116, 129, 153, 186

[51] E. Schrödinger. An Undulatory Theory of the Mechanics of Atoms and Molecules. *Physical Review*, 28(6):1049–1070, December 1926. 6

[52] Aurora Pribram-Jones, Stefano Pittalis, E. K. U. Gross, and Kieron Burke. Thermal Density Functional Theory in Context. *arXiv:1309.3043 [cond-mat, physics:physics, physics:quant-ph]*, 96:25–60, 2014. 6, 9

[53] Douglas Rayner Hartree and W. Hartree. Self-consistent field, with exchange, for beryllium. *Proceedings of the Royal Society of London. Series A - Mathematical and Physical Sciences*, 150(869):9–33, May 1935. 6

[54] Igor Ying Zhang and Andreas Grüneis. Coupled Cluster Theory in Materials Science. *Frontiers in Materials*, 6, 2019. 6

[55] R. P. Feynman, N. Metropolis, and E. Teller. Equations of State of Elements Based on the Generalized Fermi-Thomas Theory. *Physical Review*, 75(10):1561–1573, May 1949. 6, 157

[56] Balazs F. Rozsnyai. Relativistic Hartree-Fock-Slater Calculations for Arbitrary Temperature and Matter Density. *Physical Review A*, 5(3):1137–1149, March 1972. 6, 157

[57] Richard M Martin. *Electronic Structure: Basic Theory and Practical Methods*. Cambridge University Press, 2004. 7, 30, 40, 232

[58] M Levy. Universal variational functionals of electron densities, first-order density matrices, and natural spin-orbitals and solution of the v-representability problem. *Proceedings of the National Academy of Sciences of the United States of America*, 76(12):6062–5, December 1979. 7

[59] Elliott H. Lieb. Density functionals for coulomb systems. *International Journal of Quantum Chemistry*, 24(3):243–277, September 1983. 7

[60] Wolfram Koch and Max C. Holthausen. *A Chemist's Guide to Density Functional Theory*. John Wiley & Sons, November 2015. 8

[61] M. Born and R. Oppenheimer. Zur Quantentheorie der Molekeln. *Annalen der Physik*, 389(20):457–484, 1927. 11

[62] M. Bonitz, T. Dornheim, Zh. A. Moldabekov, S. Zhang, P. Hamann, H. Kählert, A. Filinov, K. Ramakrishna, and J. Vorberger. *Ab Initio* simulation of warm dense matter. *Physics of Plasmas*, 27(4):042710, April 2020. 11

[63] D. M. Ceperley and B. J. Alder. Ground State of the Electron Gas by a Stochastic Method. *Physical Review Letters*, 45(7):566–569, August 1980. 14, 150

[64] J. P. Perdew and Alex Zunger. Self-interaction correction to density-functional approximations for many-electron systems. *Physical Review B*, 23(10):5048–5079, May 1981. 14, 58, 64, 124

[65] John P. Perdew, Kieron Burke, and Matthias Ernzerhof. Generalized Gradient Approximation Made Simple. *Physical Review Letters*, 77(18):3865–3868, October 1996. 15, 64, 88

[66] John P. Perdew and Karla Schmidt. Jacob's ladder of density functional approximations for the exchange-correlation energy. *AIP Conference Proceedings*, 577(1):1–20, July 2001. 15

[67] A. Blanchet, M. Torrent, and J. Clérouin. Requirements for very high temperature Kohn–Sham DFT simulations and how to bypass them. *Physics of Plasmas*, 27(12):122706, December 2020. 18, 46, 50, 126

[68] Valentin V. Karasiev, Travis Sjostrom, and S. B. Trickey. Generalized-gradient-approximation noninteracting free-energy functionals for orbital-free density functional calculations. *Physical Review B*, 86(11):115101, September 2012. 18, 31, 32

[69] D. R. Hamann, M. Schlüter, and C. Chiang. Norm-Conserving Pseudopotentials. *Physical Review Letters*, 43(20):1494–1497, November 1979. 21

[70] Fernando Nogueira, Carlos Fiolhais, Jingsong He, John P Perdew, and Angel Rubio. Transferability of a local pseudopotential based on solid-state electron density. *Journal of Physics: Condensed Matter*, 8(3):287–302, January 1996. 22

[71] Mike Finnis. *Interatomic Forces in Condensed Matter*. Oxford Materials, 2003. 22

[72] Paul Bendt and Alex Zunger. Simultaneous Relaxation of Nuclear Geometries and Electric Charge Densities in Electronic Structure Theories. *Physical Review Letters*, 50(21):1684–1688, May 1983. 24

[73] Matyáš Novák, Jiří Vackář, and Robert Cimrman. Evaluating Hellmann–Feynman forces within non-local pseudopotentials. *Computer Physics Communications*, 250:107034, May 2020. 25

[74] Marina Pons, Bruno Juliá-Díaz, Artur Polls, Arnau Rios, and Isaac Vidaña. The Hellmann–Feynman theorem at finite temperature. *American Journal of Physics*, 88(6):503–510, May 2020. 25

[75] Gregory S. Ho, Vincent L. Lignères, and Emily A. Carter. Introducing PROFESS: A new program for orbital-free density functional theory calculations. *Computer Physics Communications*, 179(11):839–854, December 2008. 29, 124

[76] Mohan Chen, Junchao Xia, Chen Huang, Johannes M. Dieterich, Linda Hung, Ilgyou Shin, and Emily A. Carter. Introducing PROFESS 3.0: An advanced program for orbital-free density functional theory molecular dynamics simulations. *Computer Physics Communications*, 190:228–230, May 2015. 29, 124

[77] Kai Luo, Valentin V. Karasiev, and S. B. Trickey. Towards accurate orbital-free simulations: A generalized gradient approximation for the non-interacting free energy density functional. *Physical Review B*, 101(7):075116, February 2020. 29, 49, 135, 137

[78] Kai Luo, Valentin V. Karasiev, and S. B. Trickey. A simple generalized gradient approximation for the noninteracting kinetic energy density functional. *Physical Review B*, 98(4):041111, July 2018. 29

[79] Chen Huang and Emily A. Carter. Toward an orbital-free density functional theory of transition metals based on an electron density decomposition. *Physical Review B*, 85(4):045126, January 2012. 29, 56

[80] V. Recoules and S. Mazevet. Temperature and density dependence of XANES spectra in warm dense aluminum plasmas. *Physical Review B*, 80(6):064110, August 2009. 29

[81] C. F. v. Weizsäcker. Zur Theorie der Kernmassen. *Zeitschrift für Physik*, 96(7):431–458, July 1935. 29

[82] Edward Teller. On the Stability of Molecules in the Thomas-Fermi Theory. *Reviews of Modern Physics*, 34(4):627–631, October 1962. 29

[83] F. Perrot. Gradient correction to the statistical electronic free energy at nonzero temperatures: Application to equation-of-state calculations. *Physical Review A*, 20(2):586–594, August 1979. 30

[84] P. a. M. Dirac. Note on Exchange Phenomena in the Thomas Atom. *Mathematical Proceedings of the Cambridge Philosophical Society*, 26(3):376–385, July 1930. 30

[85] V. V. Karasiev, S. B. Trickey, and Frank E. Harris. Born–Oppenheimer Interatomic Forces from Simple, Local Kinetic Energy Density Functionals. *Journal of Computer-Aided Materials Design*, 13(1):111–129, October 2006. 32

[86] V. V. Karasiev and S. B. Trickey. Issues and Challenges in Orbital-free Density Functional Calculations. *Computer Physics Communications*, 183(12):2519–2527, December 2012. 32

[87] Eunji Sim, Joe Larkin, Kieron Burke, and Charles W. Bock. Testing the kinetic energy functional: Kinetic energy density as a density functional. *The Journal of Chemical Physics*, 118(18):8140–8148, April 2003. 32

[88] Leeor Kronik and Stephan Kümmel. Piecewise linearity, freedom from self-interaction, and a Coulomb asymptotic potential: Three related yet inequivalent properties of the exact density functional. *Physical Chemistry Chemical Physics*, 22(29):16467–16481, July 2020. 32

[89] Alberto Vela, Juan C. Pacheco-Kato, José L. Gázquez, Jorge M. del Campo, and S. B. Trickey. Improved constraint satisfaction in a simple generalized gradient approximation exchange functional. *The Journal of Chemical Physics*, 136(14):144115, April 2012. 32

[90] Valentin V. Karasiev, Travis Sjostrom, and S. B. Trickey. Finite-temperature orbital-free DFT molecular dynamics: Coupling Profess and Quantum Espresso. *Computer Physics Communications*, 185(12):3240–3249, 2014. 33, 109, 124

[91] M. P. Allen and D. J. Tildesley. *Computer Simulation of Liquids*. Oxford University Press, Oxford, United Kingdom, second edition edition, 2017. 39, 40, 108

[92] James W. Cooley and John W. Tukey. An algorithm for the machine calculation of complex Fourier series. *Mathematics of Computation*, 19(90):297–301, 1965. 40

[93] R. J. Needs, Mike Towler, Neil Drummond, and Pablo Lopez Rios. CASINO User's Guide Version 2.13. September 2019. 41

[94] V. R. Saunders, C. Freyria-Fava, R. Dovesi, L. Salasco, and C. Roetti. On the electrostatic potential in crystalline systems where the charge density is expanded in Gaussian functions. *Molecular Physics*, 77(4):629–665, November 1992. 42

[95] Bastian Holst, Martin French, and Ronald Redmer. Electronic transport coefficients from ab initio simulations and application to dense liquid hydrogen. *Physical Review B*, 83(23):235120, June 2011. 45

[96] Stefano Baroni, Stefano de Gironcoli, Andrea Dal Corso, and Paolo Giannozzi. Phonons and related crystal properties from density-functional perturbation theory. *Reviews of Modern Physics*, 73(2):515–562, July 2001. 45

[97] Stefano de Gironcoli. Lattice dynamics of metals from density-functional perturbation theory. *Physical Review B*, 51(10):6773–6776, March 1995. 45

[98] Stefan Goedecker. Linear scaling electronic structure methods. *Reviews of Modern Physics*, 71(4):1085–1123, July 1999. 46

[99] Ernest R. Davidson. The iterative calculation of a few of the lowest eigenvalues and corresponding eigenvectors of large real-symmetric matrices. *Journal of Computational Physics*, 17(1):87–94, January 1975. 46

[100] Sergey V. Starikov and Vasily V. Pisarev. Atomistic simulation of laser-pulse surface modification: Predictions of models with various length and time scales. *Journal of Applied Physics*, 117(13):135901, April 2015. 50, 55, 179, 183

[101] Valentin V. Karasiev, Lázaro Calderín, and S. B. Trickey. Importance of finite-temperature exchange correlation for warm dense matter calculations. *Physical Review E*, 93(6):063207, June 2016. 56, 57, 58, 59, 68, 126, 150

[102] Simon Groth, Tobias Dornheim, Travis Sjostrom, Fionn D. Malone, W. M. C. Foulkes, and Michael Bonitz. *Ab Initio* Exchange-Correlation Free Energy of the Uniform Electron Gas at Warm Dense Matter Conditions. *Physical Review Letters*, 119(13):135001, September 2017. 56, 57

[103] Valentin V. Karasiev, Travis Sjostrom, James Dufty, and S. B. Trickey. Accurate homogeneous electron gas exchange-correlation free energy for local spin-density calculations. *Physical Review Letters*, 112(7), February 2014. 56, 57, 88, 126

[104] Valentin V. Karasiev, James W. Dufty, and S. B. Trickey. Nonempirical Semi-local Free-Energy Density Functional for Matter Under Extreme Conditions. *Physical Review Letters*, 120(7):076401, February 2018. 57, 88

[105] Paolo Giannozzi, Stefano Baroni, Nicola Bonini, Matteo Calandra, Roberto Car, Carlo Cavazzoni, Davide Ceresoli, Guido L. Chiarotti, Matteo Cococcioni, Ismaila Dabo, Andrea Dal Corso, Stefano De Gironcoli, Stefano Fabris, Guido Fratesi, Ralph Gebauer, Uwe Gerstmann, Christos Gougoussis, Anton Kokalj, Michele Lazzeri, Layla Martin-Samos, Nicola Marzari, Francesco Mauri, Riccardo Mazzarello, Stefano Paolini, Alfredo Pasquarello, Lorenzo Paulatto, Carlo Sbraccia, Sandro Scandolo, Gabriele Sclauzero, Ari P. Seitsonen, Alexander Smogunov, Paolo Umari, and Renata M. Wentzcovitch. QUANTUM ESPRESSO: A modular and

open-source software project for quantum simulations of materials. *Journal of Physics Condensed Matter*, 21(39), 2009. 57, 124, 125

[106] P. Giannozzi, O. Andreussi, T. Brumme, O. Bunau, M. Buongiorno Nardelli, M. Calandra, R. Car, C. Cavazzoni, D. Ceresoli, M. Cococcioni, N. Colonna, I. Carnimeo, A. Dal Corso, S. De Gironcoli, P. Delugas, R. A. Distasio, A. Ferretti, A. Floris, G. Fratesi, G. Fugallo, R. Gebauer, U. Gerstmann, F. Giustino, T. Gorni, J. Jia, M. Kawamura, H. Y. Ko, A. Kokalj, E. Kücükbenli, M. Lazzeri, M. Marsili, N. Marzari, F. Mauri, N. L. Nguyen, H. V. Nguyen, A. Otero-De-La-Roza, L. Paulatto, S. Poncé, D. Rocca, R. Sabatini, B. Santra, M. Schlipf, A. P. Seitsonen, A. Smogunov, I. Timrov, T. Thonhauser, P. Umari, N. Vast, X. Wu, and S. Baroni. Advanced capabilities for materials modelling with Quantum ESPRESSO. *Journal of Physics Condensed Matter*, 29(46), October 2017. 57, 124, 125

[107] Susi Lehtola, Conrad Steigemann, Micael J. T. Oliveira, and Miguel A. L. Marques. Recent developments in libxc — A comprehensive library of functionals for density functional theory. *SoftwareX*, 7:1–5, January 2018. 57

[108] Miguel A. L. Marques, Micael J. T. Oliveira, and Tobias Burnus. Libxc: A library of exchange and correlation functionals for density functional theory. *Computer Physics Communications*, 183(10):2272–2281, October 2012. 57

[109] Valentin V. Karasiev. Note on how to use KSDT functional in LibXC. http://www.qtp.ufl.edu/ofdft/research/HOWTO_KSDT_in_LibXC_v5.txt. 57

[110] K. H. Bennemann. Ultrafast dynamics in solids. *Journal of Physics: Condensed Matter*, 16(30):R995–R1056, July 2004. 59, 169

[111] D. M. Duffy, N. Itoh, A. M. Rutherford, and A. M. Stoneham. Making tracks in metals. *Journal of Physics: Condensed Matter*, 20(8):082201, February 2008. 59, 169, 173

[112] M. Z. Mo, Z. Chen, R. K. Li, M. Dunning, B. B. L. Witte, J. K. Baldwin, L. B. Fletcher, J. B. Kim, A. Ng, R. Redmer, A. H. Reid, P. Shekhar, X. Z. Shen, M. Shen,

K. Sokolowski-Tinten, Y. Y. Tsui, Y. Q. Wang, Q. Zheng, X. J. Wang, and S. H. Glenzer. Heterogeneous to homogeneous melting transition visualized with ultrafast electron diffraction. *Science*, 360(6396):1451–1455, June 2018. 59, 165, 181, 182

[113] E. Bévillon, J. P. Colombier, V. Recoules, and R. Stoian. Free-electron properties of metals under ultrafast laser-induced electron-phonon nonequilibrium: A first-principles study. *Physical Review B*, 89(11):115117, March 2014. 59, 178

[114] Michael J. Tambe, Nicola Bonini, and Nicola Marzari. Bulk aluminum at high pressure: A first-principles study. *Physical Review B*, 77(17):172102, May 2008. 60, 63, 64

[115] M. P. Desjarlais, J. D. Kress, and L. A. Collins. Electrical conductivity for warm, dense aluminum plasmas and liquids. *Physical Review E*, 66(2):025401, August 2002. 60

[116] P R Levashov, G V Sin'ko, N A Smirnov, D V Minakov, O P Shemyakin, and K V Khishchenko. Pseudopotential and full-electron DFT calculations of thermodynamic properties of electrons in metals and semiempirical equations of state. *Journal of Physics: Condensed Matter*, 22(50):505501, December 2010. 64

[117] Artem R. Oganov and Peter I. Dorogokupets. All-electron and pseudopotential study of MgO: Equation of state, anharmonicity, and stability. *Physical Review B*, 67(22):224110, June 2003. 64

[118] Alex Willand, Yaroslav O. Kvashnin, Luigi Genovese, Álvaro Vázquez-Mayagoitia, Arpan Krishna Deb, Ali Sadeghi, Thierry Deutsch, and Stefan Goedecker. Norm-conserving pseudopotentials with chemical accuracy compared to all-electron calculations. *The Journal of Chemical Physics*, 138(10):104109, March 2013. 64

[119] M. J. van Setten, M. Giantomassi, E. Bousquet, M. J. Verstraete, D. R. Hamann, X. Gonze, and G. M. Rignanese. The PseudoDojo: Training and grading a 85 element optimized norm-conserving pseudopotential table. *Computer Physics Communications*, 226:39–54, May 2018. 64, 125

[120] D. R. Hamann. Optimized norm-conserving Vanderbilt pseudopotentials. *Physical Review B*, 88(8):085117, August 2013. 64, 125

[121] Martin Schlipf and François Gygi. Optimization algorithm for the generation of ONCV pseudopotentials. *Computer Physics Communications*, 196:36–44, November 2015. 64

[122] L. Harbour, M. W. C. Dharma-wardana, D. D. Klug, and L. J. Lewis. Two-Temperature Pair Potentials and Phonon Spectra for Simple Metals in the Warm Dense Matter Regime. *Contributions to Plasma Physics*, 55(2-3):144–151, 2015. 68

[123] Travis Sjostrom and Jérôme Daligault. Fast and Accurate Quantum Molecular Dynamics of Dense Plasmas Across Temperature Regimes. *Physical Review Letters*, 113(15):155006, October 2014. 70, 73, 135

[124] Travis Sjostrom and Jérôme Daligault. Nonlocal orbital-free noninteracting free-energy functional for warm dense matter. *Physical Review B*, 88(19):195103, November 2013. 70, 71, 135

[125] X. Blanc and E. Cancès. Nonlinear instability of density-independent orbital-free kinetic-energy functionals. *The Journal of Chemical Physics*, 122(21):214106, June 2005. 70

[126] Lin-Wang Wang and Michael P. Teter. Kinetic-energy functional of the electron density. *Physical Review B*, 45(23):13196–13220, June 1992. 70

[127] Yan Alexander Wang, Niranjan Govind, and Emily A. Carter. Orbital-free kinetic-energy density functionals with a density-dependent kernel. *Physical Review B*, 60(24):16350–16358, December 1999. 71

[128] Toshio Fukushima. *Precise and Fast Computaion of Fermi-Dirac Integral of Integer and Half Integer Order by Piecewise Minimax Rational Approximation.* January 2014. 73

[129] Robert Piessens, Elise de Doncker-Kapenga, Christoph W. Überhuber, and David K. Kahaner. *Quadpack*, volume 1 of *Springer Series in Computational Mathematics*. Springer, Berlin, Heidelberg, 1983. 73

[130] A. Blanchet, J. Clérouin, M. Torrent, and F. Soubiran. Extended first-principles molecular dynamics model for high temperature simulations in the Abinit code: Application to warm dense aluminum. *Computer Physics Communications*, 271:108215, February 2022. 74, 147, 148

[131] John Daintith. Lennard-Jones potential. In *A Dictionary of Chemistry*. Oxford University Press, 2008. 77

[132] Mike Finnis. *Interatomic Forces in Condensed Matter*. Oxford University Press, January 2010. 77, 117

[133] Peter Schwerdtfeger, Nicola Gaston, Robert P. Krawczyk, Ralf Tonner, and Gloria E. Moyano. Extension of the Lennard-Jones potential: Theoretical investigations into rare-gas clusters and crystal lattices of He, Ne, Ar, and Kr using many-body interaction expansions. *Physical Review B*, 73(6):064112, February 2006. 77

[134] Murray S. Daw, Stephen M. Foiles, and Michael I. Baskes. The embedded-atom method: A review of theory and applications. *Materials Science Reports*, 9(7):251–310, March 1993. 77, 91, 117

[135] Peter Debye and Erich Hückel. The theory of electrolytes. I. Freezing point depression and related phenomena (Translation). *Physikalische Zeitschrif*, 24:185–206, 1923. 77, 133, 159

[136] M.I. Mendelev, M.J. Kramer, C.A. Becker, and M. Asta. Analysis of semi-empirical interatomic potentials appropriate for simulation of crystalline and liquid Al and Cu. *Philosophical Magazine*, 88(12):1723–1750, April 2008. 84

[137] Arun K. Subramaniyan and C. T. Sun. Engineering molecular mechanics: An efficient static high temperature molecular simulation technique. *Nanotechnology*, 19(28):285706, June 2008. 84, 91

[138] Arun K. Subramaniyan and C. T. Sun. Temperature Dependent Effective Embedded Atom Method Potential for Steady State High Temperature Applications. *Journal of Computational and Theoretical Nanoscience*, 7(1):176–181, January 2010. 84, 91

[139] Samuel T. Murphy, Szymon L. Daraszewicz, Yvelin Giret, Matthew Watkins, Alexander L. Shluger, Katsumi Tanimura, and Dorothy M. Duffy. Dynamical simulations of an electronically induced solid-solid phase transformation in tungsten. *Physical Review B*, 92(13):134110, October 2015. 84

[140] Lalit Shokeen and Patrick K. Schelling. Role of electronic-excitation effects in the melting and ablation of laser-excited silicon. *Computational Materials Science*, 67:316–328, February 2013. 84

[141] John A. Moriarty, Randolph Q. Hood, and Lin H. Yang. Quantum-Mechanical Interatomic Potentials with Electron Temperature for Strong-Coupling Transition Metals. *Physical Review Letters*, 108(3):036401, January 2012. 84

[142] Yudi Rosandi, Fairoja Cheenicode Kabeer, Yaroslav Cherednikov, Eeuwe S. Zijlstra, Martin E. Garcia, Nail A. Inogamov, and Herbert M. Urbassek. Melting of Al Induced by Laser Excitation of 2p Holes. *Materials Research Letters*, 3(3):149–155, July 2015. 84, 181

[143] Alexander V. Shapeev. Moment Tensor Potentials: A Class of Systematically Improvable Interatomic Potentials. *Multiscale Modeling & Simulation*, 14(3):1153–1173, January 2016. 85

[144] A. P. Thompson, L. P. Swiler, C. R. Trott, S. M. Foiles, and G. J. Tucker. Spectral neighbor analysis method for automated generation of quantum-accurate interatomic potentials. *Journal of Computational Physics*, 285:316–330, March 2015. 85

[145] Albert P. Bartók and Gábor Csányi. Gaussian approximation potentials: A brief tutorial introduction. *International Journal of Quantum Chemistry*, 115(16):1051–1057, 2015. 85

[146] Linfeng Zhang, Jiequn Han, Han Wang, Roberto Car, and Weinan E. Deep Potential Molecular Dynamics: A Scalable Model with the Accuracy of Quantum Mechanics. *Physical Review Letters*, 120(14):143001, April 2018. 85, 86

[147] Yury Lysogorskiy, Cas van der Oord, Anton Bochkarev, Sarath Menon, Matteo Rinaldi, Thomas Hammerschmidt, Matous Mrovec, Aidan Thompson, Gábor Csányi, Christoph Ortner, and Ralf Drautz. Performant implementation of the atomic cluster expansion (PACE) and application to copper and silicon. *npj Computational Materials*, 7(1):1–12, June 2021. 85, 113, 116, 123, 129, 153

[148] Qianrui Liu, Junyi Li, and Mohan Chen. Thermal transport by electrons and ions in warm dense aluminum: A combined density functional theory and deep potential study. *Matter and Radiation at Extremes*, 6(2):026902, March 2021. 85

[149] M. W. Finnis and J. E. Sinclair. A simple empirical N-body potential for transition metals. *Philosophical Magazine A*, 50(1):45–55, July 1984. 85, 91, 117

[150] Murray S. Daw and M. I. Baskes. Embedded-atom method: Derivation and application to impurities, surfaces, and other defects in metals. *Physical Review B*, 29(12):6443–6453, June 1984. 85, 117

[151] P. E. Blöchl. Projector augmented-wave method. *Physical Review B*, 50(24):17953–17979, December 1994. 88

[152] Yuzhi Zhang, Chang Gao, Qianrui Liu, Linfeng Zhang, Han Wang, and Mohan Chen. Warm dense matter simulation via electron temperature dependent deep potential molecular dynamics. *Physics of Plasmas*, 27(12):122704, December 2020. 89, 144

[153] Qiyu Zeng, Xiaoxiang Yu, Yunpeng Yao, Tianyu Gao, Bo Chen, Shen Zhang, Dongdong Kang, Han Wang, and Jiayu Dai. Ab initio validation on the connection between atomistic and hydrodynamic description to unravel the ion dynamics of warm dense matter. *Physical Review Research*, 3(3):033116, August 2021. 89, 144

[154] J. E. Jones and Sydney Chapman. On the determination of molecular fields. —II. From the equation of state of a gas. *Proceedings of the Royal Society of London. Series A, Containing Papers of a Mathematical and Physical Character*, 106(738):463–477, October 1924. 89

[155] Philip M. Morse. Diatomic Molecules According to the Wave Mechanics. II. Vibrational Levels. *Physical Review*, 34(1):57–64, July 1929. 89

[156] A. P. Sutton. Temperature-dependent interatomic forces. *Philosophical Magazine A*, 60(2):147–159, August 1989. 91

[157] J. Tersoff. New empirical approach for the structure and energy of covalent systems. *Physical Review B*, 37(12):6991–7000, April 1988. 91

[158] Andrew Ian Duff, Theresa Davey, Dominique Korbmacher, Albert Glensk, Blazej Grabowski, Jörg Neugebauer, and Michael W. Finnis. Improved method of calculating *ab initio* high-temperature thermodynamic properties with application to ZrC. *Physical Review B*, 91(21):214311, June 2015. 91

[159] Andrew Ian Duff, M.W. Finnis, Philippe Maugis, Barend J. Thijsse, and Marcel H.F. Sluiter. MEAMfit: A reference-free modified embedded atom method (RF-MEAM) energy and force-fitting code. *Computer Physics Communications*, 196:439–445, November 2015. 91

[160] F. Ercolessi and J. B. Adams. Interatomic Potentials from First-Principles Calculations: The Force-Matching Method. *Europhysics Letters*, 26(8):583, June 1994. 93

[161] Daan Frenkel and Berend Smit. *Understanding Molecular Simulation: From Algorithms to Applications*. Elsevier, October 2001. 97, 98, 99, 105

[162] Aidan P. Thompson, Steven J. Plimpton, and William Mattson. General formulation of pressure and stress tensor for arbitrary many-body interaction potentials under periodic boundary conditions. *The Journal of Chemical Physics*, 131(15):154107, October 2009. 98

[163] Hans C. Andersen. Molecular dynamics simulations at constant pressure and/or temperature. *The Journal of Chemical Physics*, 72(4):2384–2393, February 1980. 104, 125, 135

[164] H. Tanaka, Koichiro Nakanishi, and Nobuatsu Watanabe. Constant temperature molecular dynamics calculation on Lennard-Jones fluid and its application to watera). *The Journal of Chemical Physics*, 78(5):2626–2634, March 1983. 106

[165] E. A. Koopman. *Simple Numerical Techniques for Mesoscale Polymer Models*. PhD thesis, 2014. 105

[166] W. Smith and M. J. Gillan. INFORMATION QUARTERLY FOR COMPUTER SIMULATION OF CONDENSED PHASES 45. *Daresbury Laboratory*, May 1996. 108

[167] Shuichi Nosé. A unified formulation of the constant temperature molecular dynamics methods. *The Journal of Chemical Physics*, 81(1):511–519, July 1984. 108, 135

[168] William G. Hoover. Canonical dynamics: Equilibrium phase-space distributions. *Physical Review A*, 31(3):1695–1697, March 1985. 108, 135

[169] Glenn J. Martyna, Michael L. Klein, and Mark Tuckerman. Nosé–Hoover chains: The canonical ensemble via continuous dynamics. *The Journal of Chemical Physics*, 97(4):2635–2643, August 1992. 108

[170] R. Drautz, M. Fähnle, and J. M. Sanchez. General relations between many-body potentials and cluster expansions in multicomponent systems. *Journal of Physics: Condensed Matter*, 16(23):3843–3852, May 2004. 114, 117, 134

[171] Giulio Racah. Theory of Complex Spectra. II. *Physical Review*, 62(9-10):438–462, November 1942. 116

[172] Murray S. Daw. Semiempirical, Quantum Mechanical Calculation of Hydrogen Embrittlement in Metals. *Physical Review Letters*, 50(17):1285–1288, 1983. 117

[173] Carl S. Helrich. *Modern Thermodynamics with Statistical Mechanics*. Springer Science & Business Media, November 2008. 121

[174] Anton Bochkarev, Yury Lysogorskiy, Sarath Menon, Minaam Qamar, Matous Mrovec, and Ralf Drautz. Efficient parametrization of the atomic cluster expansion. *Physical Review Materials*, 6(1):013804, January 2022. 123, 127, 128, 130

[175] Aidan P. Thompson, H. Metin Aktulga, Richard Berger, Dan S. Bolintineanu, W. Michael Brown, Paul S. Crozier, Pieter J. in 't Veld, Axel Kohlmeyer, Stan G. Moore, Trung Dac Nguyen, Ray Shan, Mark J. Stevens, Julien Tranchida, Christian Trott, and Steven J. Plimpton. LAMMPS - a flexible simulation tool for particle-based materials modeling at the atomic, meso, and continuum scales. *Computer Physics Communications*, 271:108171, February 2022. 123

[176] Albert P. Bartók, James Kermode, Noam Bernstein, and Gábor Csányi. Machine Learning a General-Purpose Interatomic Potential for Silicon. *Physical Review X*, 8(4):041048, December 2018. 124

[177] Baojing Zhou, Yan Alexander Wang, and Emily A. Carter. Transferable local pseudopotentials derived via inversion of the Kohn-Sham equations in a bulk environment. *Physical Review B*, 69(12):125109, March 2004. 124

[178] Chen Huang and Emily A. Carter. Transferable local pseudopotentials for magnesium, aluminum and silicon. *Physical Chemistry Chemical Physics*, 10(47):7109, 2008. 124, 125

[179] Valentin V. Karasiev, S. B. Trickey, and James W. Dufty. Status of free-energy representations for the homogeneous electron gas. *Physical Review B*, 99(19):195134, May 2019. 125

[180] A. Krishnapriyan, P. Yang, A. M. N. Niklasson, and M. J. Cawkwell. Numerical Optimization of Density Functional Tight Binding Models: Application to Molecules Containing Carbon, Hydrogen, Nitrogen, and Oxygen. *Journal of Chemical Theory and Computation*, 13(12):6191–6200, December 2017. 128

[181] R. Fletcher. *Practical Methods of Optimization*. John Wiley & Sons, June 2013. 129

[182] Ryan M. Richard, Ka Un Lao, and John M. Herbert. Understanding the many-body expansion for large systems. I. Precision considerations. *The Journal of Chemical Physics*, 141(1):014108, July 2014. 134, 155

[183] Andreas Hermann, Robert P. Krawczyk, Matthias Lein, Peter Schwerdtfeger, I. P. Hamilton, and James J. P. Stewart. Convergence of the many-body expansion of interaction potentials: From van der Waals to covalent and metallic systems. *Physical Review A*, 76(1):013202, July 2007. 134, 155

[184] S. P. Lyon and J. D. Johnson. Los Alamos Report No. LA-UR92-3407. 147

[185] R. M. More, K. H. Warren, D. A. Young, and G. B. Zimmerman. A new quotidian equation of state (QEOS) for hot dense matter. *The Physics of Fluids*, 31(10):3059–3078, October 1988. 147, 157

[186] D. M. Ceperley. Path integrals in the theory of condensed helium. *Reviews of Modern Physics*, 67(2):279–355, April 1995. 147

[187] T. Dornheim. Fermion sign problem in path integral Monte Carlo simulations: Quantum dots, ultracold atoms, and warm dense matter. *Physical Review E*, 100(2):023307, August 2019. 147

[188] M. D. Knudson, R. W. Lemke, D. B. Hayes, C. A. Hall, C. Deeney, and J. R. Asay. Near-absolute Hugoniot measurements in aluminum to 500 GPa using a magnetically accelerated flyer plate technique. *Journal of Applied Physics*, 94(7):4420–4431, October 2003. 147

[189] Ryurik F. Trunin. Shock compressibility of condensed materials in strong shock waves generated by underground nuclear explosions. *Physics-Uspekhi*, 37(11):1123, November 1994. 147

[190] M. D. Knudson, M. P. Desjarlais, and Aurora Pribram-Jones. Adiabatic release measurements in aluminum between 400 and 1200 GPa: Characterization of aluminum as a shock standard in the multimegabar regime. *Physical Review B*, 91(22):224105, June 2015. 147

[191] Lenz Fiedler, Zhandos A. Moldabekov, Xuecheng Shao, Kaili Jiang, Tobias Dornheim, Michele Pavanello, and Attila Cangi. Accelerating equilibration in first-principles molecular dynamics with orbital-free density functional theory. *Physical Review Research*, 4(4):043033, October 2022. 148

[192] Travis Sjostrom and Jérôme Daligault. Gradient corrections to the exchange-correlation free energy. *Physical Review B*, 90(15):155109, October 2014. 150

[193] J.-F. Danel, L. Kazandjian, and R. Piron. Equation of state of warm dense deuterium and its isotopes from density-functional theory molecular dynamics. *Physical Review E*, 93(4):043210, April 2016. 150

[194] Ilya G. Kaplan, Ruben Santamaria, and Octavio Novaro. Non-additive forces in atomic clusters. *Molecular Physics*, 84(1):105–114, January 1995. 155

[195] Omar Demerdash and Teresa Head-Gordon. Convergence of the Many-Body Expansion for Energy and Forces for Classical Polarizable Models in the Condensed Phase. *Journal of Chemical Theory and Computation*, 12(8):3884–3893, August 2016. 155

[196] Erin E. Dahlke and Donald G. Truhlar. Electrostatically Embedded Many-Body Expansion for Simulations. *Journal of Chemical Theory and Computation*, 4(1):1–6, January 2008. 155

[197] R. Piron and T. Blenski. Variational-average-atom-in-quantum-plasmas (VAAQP) code and virial theorem: Equation-of-state and shock-Hugoniot calculations for warm dense Al, Fe, Cu, and Pb. *Physical Review E*, 83(2):026403, February 2011. 157

[198] M. Z. Mo. Measurements of ionization states in warm dense aluminum with betatron radiation. *Physical Review E*, 95(5), 2017. 157

[199] P. Fromy, C. Deutsch, and G. Maynard. Thomas–Fermi-like and average atom models for dense and hot matter. *Physics of Plasmas*, 3(3):714–730, March 1996. 157

[200] A.l. Khomkin and A.s. Shumikhin. Equation of state and transport properties of metals in warm dense matter regime. *Contributions to Plasma Physics*, 58(2-3):143–149, 2018. 157

[201] L. Harbour, G. D. Förster, M. W. C. Dharma-wardana, and Laurent J. Lewis. Ion-ion dynamic structure factor, acoustic modes, and equation of state of two-temperature warm dense aluminum. *Physical Review E*, 97(4):043210, April 2018. 157

[202] K. Parlinski. Phonons calculated from first-principles. *École thématique de la Société Française de la Neutronique*, 12:161–166, 2011. 164, 232, 233

[203] P. Debye. Zur Theorie der spezifischen Wärmen. *Annalen der Physik*, 344(14):789–839, 1912. 164

[204] A. M. Lindenberg, J. Larsson, K. Sokolowski-Tinten, K. J. Gaffney, C. Blome, O. Synnergren, J. Sheppard, C. Caleman, A. G. Macphee, D. Weinstein, D. P. Lowney, T. K. Allison, T. Matthews, R. W. Falcone, A. L. Cavalieri, D. M. Fritz, S. H. Lee, P. H. Bucksbaum, D. A. Reis, J. Rudati, P. H. Fuoss, C. C. Kao, D. P. Siddons, R. Pahl, J. Als-Nielsen, S. Duesterer, R. Ischebeck, H. Schlarb, H. Schulte-Schrepping, Th Tschentscher, J. Schneider, D. von der Linde, O. Hignette, F. Sette, H. N. Chapman, R. W. Lee, T. N. Hansen, S. Techert, J. S. Wark, M. Bergh, G. Huldt, D. van der Spoel, N. Timneanu, J. Hajdu, R. A. Akre, E. Bong, P. Krejcik, J. Arthur, S. Brennan, K. Luening, and J. B. Hastings. Atomic-scale visualization of inertial dynamics. *Science (New York, N.Y.)*, 308(5720):392–395, April 2005. 165

[205] Duane C. Wallace. Thermodynamics of Crystals. *American Journal of Physics*, 40(11):1718–1719, November 1972. 165

[206] R. Stedman and G. Nilsson. Dispersion Relations for Phonons in Aluminum at 80 and 300\ifmmode\^circ\else\textdegree\fi{}K. *Physical Review*, 145(2):492–500, May 1966. 167

[207] Zhibin Lin, Leonid V. Zhigilei, and Vittorio Celli. Electron-phonon coupling and electron heat capacity of metals under conditions of strong electron-phonon nonequilibrium. *Physical Review B*, 77(7):075133, February 2008. 169, 173, 175, 179

[208] S. I. Anisimov, B. L. Kapeliovich, and T. L. Perel'Man. Electron emission from metal surfaces exposed to ultrashort laser pulses. *Soviet Journal of Experimental and Theoretical Physics*, 39:375–377, August 1974. 169

[209] Mianzhen Mo, Zhijiang Chen, and Siegfried Glenzer. Ultrafast visualization of phase transitions in nonequilibrium warm dense matter. *MRS Bulletin*, 46(8):694–703, August 2021. 170, 181

[210] H. Park, X. Wang, S. Nie, R. Clinite, and J. Cao. Direct and real-time probing of both coherent and thermal lattice motions. *Solid State Communications*, 136(9):559–563, December 2005. 170, 181

[211] C. J. K. Richardson and J. B. Spicer. Short-time thermoelastic contributions to picosecond-time scale reflectivity measurements of metals. *Applied Physics Letters*, 80(16):2895–2897, April 2002. 170, 181

[212] S Klaumünzer. Thermal-spike models for ion track physics: A critical examination. *Matematisk-Fysiske Meddelelser*, 52:293–328, 2006. 170

[213] Dmitriy S. Ivanov and Leonid V. Zhigilei. Combined atomistic-continuum modeling of short-pulse laser melting and disintegration of metal films. *Physical Review B*, 68(6):064114, August 2003. 170, 178

[214] William J. Weber, Dorothy M. Duffy, Lionel Thomé, and Yanwen Zhang. The role of electronic energy loss in ion beam modification of materials. *Current Opinion in Solid State and Materials Science*, 19(1):1–11, February 2015. 171

[215] Xiang-Yang Liu, Furio Ercolessi, and James B. Adams. Aluminium interatomic potential from density functional theory calculations with improved stacking fault energy. *Modelling and Simulation in Materials Science and Engineering*, 12(4):665–670, May 2004. 171, 180

[216] V. V. Pisarev and S. V. Starikov. Atomistic simulation of ion track formation in UO$\less$sub$\greater$2$\less$/sub$\greater$. *Journal of Physics: Condensed Matter*, 26(47):475401, October 2014. 172, 173, 177, 179

[217] Robert Zwanzig. *Nonequilibrium Statistical Mechanics*. OUP USA, May 2001. 172

[218] Zhibin Lin and Leonid V. Zhigilei. Temperature dependences of the electron–phonon coupling, electron heat capacity and thermal conductivity in Ni under femtosecond laser irradiation. *Applied Surface Science*, 253(15):6295–6300, May 2007. 175

[219] Y. S. Touloukian, R. W. Powell, C. Y. Ho, and M. C. Nicolaou. Thermophysical Properties of Matter-The TPRC Data Series. Volume 10. Thermal Diffusivity. Technical report, January 1974. 175

[220] I. T. Todorov, W. Smith, and U. K. Cheshire. The DL POLY 4 user manual. *STFC, STFC Daresbury Laboratory, Daresbury, Warrington, Cheshire, WA4 4AD, United Kingdom, version*, 4(0), 2011. 176

[221] Ilian T. Todorov, William Smith, Kostya Trachenko, and Martin T. Dove. DL_POLY_3: New dimensions in molecular dynamics simulations via massive parallelism. *Journal of Materials Chemistry*, 16(20):1911–1918, May 2006. 176

[222] Alexander Stukowski. Visualization and analysis of atomistic simulation data with OVITO–the Open Visualization Tool. *Modelling and Simulation in Materials Science and Engineering*, 18(1):015012, December 2009. 178, 180

[223] Tadashi Ogitsu, Yuan Ping, Alfredo Correa, Byoung-ick Cho, Phil Heimann, Eric Schwegler, J. Cao, and Gilbert W. Collins. Ballistic electron transport in non-equilibrium warm dense gold. *High Energy Density Physics*, 8(3):303–306, September 2012. 178, 179

[224] Yu. V. Petrov, K. P. Migdal, N. A. Inogamov, and V. V. Zhakhovsky. Two-temperature equation of state for aluminum and gold with electrons excited by an ultrashort laser pulse. *Applied Physics B*, 119(3):401–411, June 2015. 178

[225] B. Y. Mueller and B. Rethfeld. Relaxation dynamics in laser-excited metals under nonequilibrium conditions. *Physical Review B*, 87(3):035139, January 2013. 178

[226] P. Musumeci, J. T. Moody, C. M. Scoby, M. S. Gutierrez, and M. Westfall. Laser-induced melting of a single crystal gold sample by time-resolved ultrafast relativistic electron diffraction. *Applied Physics Letters*, 97(6):063502, August 2010. 179

[227] J. Hohlfeld, S. S. Wellershoff, J. Güdde, U. Conrad, V. Jähnke, and E. Matthias. Electron and lattice dynamics following optical excitation of metals. *Chemical Physics*, 251(1):237–258, January 2000. 179

[228] E. Bévillon, J. P. Colombier, V. Recoules, and R. Stoian. First-principles calculations of heat capacities of ultrafast laser-excited electrons in metals. *Applied Surface Science*, 336:79–84, May 2015. 179

[229] D. V. Knyazev and P. R. Levashov. Transport and optical properties of warm dense aluminum in the two-temperature regime: Ab initio calculation and semiempirical approximation. *Physics of Plasmas*, 21(7):073302, July 2014. 179

[230] N. A. Inogamov and Yu. V. Petrov. Thermal conductivity of metals with hot electrons. *Journal of Experimental and Theoretical Physics*, 110(3):446–468, March 2010. 179

[231] Cas van der Oord, Matthias Sachs, Dávid Péter Kovács, Christoph Ortner, and Gábor Csányi. Hyperactive learning for data-driven interatomic potentials. *npj Computational Materials*, 9(1):1–14, September 2023. 180

[232] Yudi Rosandi and Herbert M. Urbassek. Melting of Al by ultrafast laser pulses: Dynamics at the melting threshold. *Applied Physics A*, 110(3):649–654, March 2013. 181

[233] Bradley J. Siwick, Jason R. Dwyer, Robert E. Jordan, and R. J. Dwayne Miller. An Atomic-Level View of Melting Using Femtosecond Electron Diffraction. *Science*, 302(5649):1382–1385, November 2003. 181, 182

[234] Renkai Li, Chuanxiang Tang, Yingchao Du, Wenhui Huang, Qiang Du, Jiaru Shi, Lixin Yan, and Xijie Wang. Experimental demonstration of high quality MeV ultrafast electron diffraction. *Review of Scientific Instruments*, 80(8):083303, August 2009. 181

[235] C. Guo, G. Rodriguez, A. Lobad, and A. J. Taylor. Structural Phase Transition of Aluminum Induced by Electronic Excitation. *Physical Review Letters*, 84(19):4493–4496, May 2000. 182

[236] X.-Y. Liu, Wei Xu, S. M. Foiles, and J. B. Adams. Atomistic studies of segregation and diffusion in Al-Cu grain boundaries. *Applied Physics Letters*, 72(13):1578–1580, March 1998. 182

[237] Jiayu Dai, Yong Hou, Dongdong Kang, Huayang Sun, Jianhua Wu, and Jianmin Yuan. Structure, equation of state, diffusion and viscosity of warm dense Fe under the conditions of a giant planet core. *New Journal of Physics*, 15(4):045003, April 2013. 183

[238] Yu Meng, Pengfei Ji, Lan Jiang, Gen Lin, and Jianwu Guo. Spatiotemporal insights into the femtosecond laser homogeneous and heterogeneous melting aluminum by atomistic-continuum modeling. *Applied Physics A*, 128(6):520, May 2022. 183

[239] S. I. Anisimov, N. A. Inogamov, Yu. V. Petrov, V. A. Khokhlov, V. V. Zhakhovskii, K. Nishihara, M. B. Agranat, S. I. Ashitkov, and P. S. Komarov. Interaction of short laser pulses with metals at moderate intensities. *Applied Physics A*, 92(4):939–943, September 2008. 183

[240] Chengping Wu and Leonid V. Zhigilei. Microscopic mechanisms of laser spallation and ablation of metal targets from large-scale molecular dynamics simulations. *Applied Physics A*, 114(1):11–32, January 2014. 183

[241] S. H. Glenzer, L. B. Fletcher, E. Galtier, B. Nagler, R. Alonso-Mori, B. Barbrel, S. B. Brown, D. A. Chapman, Z. Chen, C. B. Curry, F. Fiuza, E. Gamboa, M. Gauthier, D. O. Gericke, A. Gleason, S. Goede, E. Granados, P. Heimann, J. Kim, D. Kraus, M. J. MacDonald, A. J. Mackinnon, R. Mishra, A. Ravasio, C. Roedel, P. Sperling, W. Schumaker, Y. Y. Tsui, J. Vorberger, U. Zastrau, A. Fry, W. E. White, J. B. Hasting, and H. J. Lee. Matter under extreme conditions experiments at the Linac Coherent Light Source. *Journal of Physics B: Atomic, Molecular and Optical Physics*, 49(9):092001, April 2016. 189

[242] K. Parlinski, Z. Q. Li, and Y. Kawazoe. First-Principles Determination of the Soft Mode in Cubic ${\mathrm{ZrO}}_{2}$. *Physical Review Letters*, 78(21):4063–4066, May 1997. 232, 233

[243] Atsushi Togo and Isao Tanaka. First principles phonon calculations in materials science. *Scripta Materialia*, 108:1–5, November 2015. 233, 234, 235

[244] M. Born and E. Brody. Über die spezifische Wärme fester Körper bei hohen Temperaturen. *Zeitschrift für Physik*, 6(1):132–139, 1921. 235

[245] B. Grabowski, L. Ismer, T. Hickel, and J. Neugebauer. Ab initio up to the melting point: Anharmonicity and vacancies in aluminum. *Physical Review B*, 79(13):134106, April 2009. 235

[246] A. Glensk, B. Grabowski, T. Hickel, and J. Neugebauer. Understanding Anharmonicity in fcc Materials: From its Origin to *ab initio* Strategies beyond the Quasiharmonic Approximation. *Physical Review Letters*, 114(19):195901, May 2015. 235

[247] Albert Glensk, Blazej Grabowski, Tilmann Hickel, Jörg Neugebauer, Jürgen Neuhaus, Klaudia Hradil, Winfried Petry, and Michael Leitner. Phonon Lifetimes

throughout the Brillouin Zone at Elevated Temperatures from Experiment and *Ab Initio*. *Physical Review Letters*, 123(23):235501, December 2019. 235

Appendix A

Finding the ground-state density

In the Thomas-Fermi-Dirac model, the total electronic energy of a system at zero temperature can be expressed by

$$E = \mathcal{T}_{\mathrm{TF}} + U + E_{\mathrm{x}}, \tag{A.1}$$

where $\mathcal{T}_{\mathrm{TF}}$ is the non-interacting kinetic energy of the electrons, U is the Coulomb energy of the electron-electron interactions and electron-ion interactions, and E_{x} is the Dirac exchange energy of the electrons. To find the ground-state density, the total electronic energy must be minimised with respect to the electron density $n(\mathbf{r})$ whilst that

$$\int n(\mathbf{r})\mathrm{d}\mathbf{r} = N, \tag{A.2}$$

where N is the total number of electrons. First, the functional derivatives of the energy components must be calculated, e.g.,

$$\begin{aligned}
\delta\mathcal{T}_{\mathrm{TF}} &= \mathcal{T}_{\mathrm{TF}}[n(\mathbf{r}) + \delta n(\mathbf{r})] - \mathcal{T}_{\mathrm{TF}}[n(\mathbf{r})] \\
&= C_{\mathcal{T}} \int [n(\mathbf{r}) + \delta n(\mathbf{r})]^{5/3} - n^{5/3}(\mathbf{r})\mathrm{d}\mathbf{r} \\
&= C_{\mathcal{T}} \int \frac{5}{3} n^{2/3}(\mathbf{r}) \cdot \delta n(\mathbf{r})\mathrm{d}\mathbf{r} + \mathcal{O}(\delta n^2),
\end{aligned} \tag{A.3}$$

giving a functional derivative of $\mathcal{T}_{\mathrm{TF}}$ as

$$\frac{\delta \mathcal{T}_{\mathrm{TF}}}{\delta n(\mathbf{r})} = \frac{5}{3} C_{\mathcal{T}} n^{2/3}(\mathbf{r}). \tag{A.4}$$

Similar derivations provide the functional derivatives of E_{x} and U. To ensure the total number of electrons is fixed, the constraint given in Eq. A.2 is then used to define a Lagrangian whose minimum with respect to the electron density will be found when $n(\mathbf{r})$ is equal to the ground-state density. This can be expressed by the Euler (or Thomas-Fermi) equation

$$\frac{\delta \left(E - \mu [\int n(\mathbf{r}) \mathrm{d}\mathbf{r} - N] \right)}{\delta n(\mathbf{r})} = \frac{\delta \mathcal{T}_{\mathrm{TF}}}{\delta n(\mathbf{r})} + \frac{\delta E_{\mathrm{x}}}{\delta n(\mathbf{r})} + \frac{\delta U}{\delta n(\mathbf{r})} - \mu = 0, \tag{A.5}$$

where μ is a Lagrange multiplier representing the chemical potential.

It is important to note that at equilibrium μ should be constant in space (to ensure no movement of electron density). Computationally, since μ is a constant, it will be discarded when the $\mathbf{G} = \mathbf{0}$ are set to zero.

A.1 Perturbative approach

For now, the ground-state density satisfying Eq. A.5 cannot be easily found. There are still two missing pieces, namely a functional form for $n(\mathbf{r})$, and a method for minimising the equation. The electron density is commonly expressed in a plane wave basis due to its expected smoothness. To minimise the equation, a program was developed that used an iterative method by substituting

$$n_{i+1}(\mathbf{r}) = n_i(\mathbf{r}) + \delta n(\mathbf{r}), \tag{A.6}$$

where $\delta n(\mathbf{r})$ is assumed to be a small perturbation which sums over the unit cell to zero, into Eq. A.5 and expanding to first order in $\delta n(\mathbf{r})$. For analytic simplicity, only the

kinetic and exchange terms will be explicitly used here; however, it should be noted that the Coulomb terms must also be accounted for when applying the method.

If Eq. A.6 is substituted into Eq. A.5, the kinetic energy term becomes

$$\begin{aligned}\frac{5}{3}C_{\mathcal{T}}\left(n_i(\mathbf{r})+\delta n(\mathbf{r})\right)^{2/3} &= \frac{5}{3}C_{\mathcal{T}}n_i(\mathbf{r})^{2/3}\left(1+\frac{2}{3}\frac{\delta n(\mathbf{r})}{n_i(\mathbf{r})}+\mathcal{O}(\delta n^2)\right)\\ &\approx \frac{5}{3}C_{\mathcal{T}}n_i(\mathbf{r})^{2/3}+\frac{10}{9}C_{\mathcal{T}}\frac{\delta n(\mathbf{r})}{n_i(\mathbf{r})^{1/3}}.\end{aligned} \tag{A.7}$$

Both terms can be expanded in a plane-wave basis (see Eq. 2.70) to give

$$f_{\mathcal{T}}(\mathbf{r}) = \frac{5}{3}C_{\mathcal{T}}n_i(\mathbf{r})^{2/3} = \sum_{\mathbf{G}} f_{\mathcal{T}}(\mathbf{G})\exp\{i\mathbf{G}\cdot\mathbf{r}\}, \tag{A.8}$$

$$g_{\mathcal{T}}(\mathbf{r}) = \frac{10}{9}C_{\mathcal{T}}\frac{1}{n_i(\mathbf{r})^{1/3}} = \sum_{\mathbf{G}} g_{\mathcal{T}}(\mathbf{G})\exp\{i\mathbf{G}\cdot\mathbf{r}\}, \tag{A.9}$$

along with the density perturbation which can be expressed as

$$\delta n(\mathbf{r}) = \sum_{\mathbf{G}} \delta n(\mathbf{G})\exp\{i\mathbf{G}\cdot\mathbf{r}\}. \tag{A.10}$$

Eq. A.7 then reads

$$\begin{aligned}\frac{5}{3}C_{\mathcal{T}}\left(n_i(\mathbf{r})+\delta n(\mathbf{r})\right)^{2/3} &= f_{\mathcal{T}}(\mathbf{r})+g_{\mathcal{T}}(\mathbf{r})\delta n(\mathbf{r})\\ &= f_{\mathcal{T}}(\mathbf{r})+\left(\sum_{\mathbf{G}'} g_{\mathcal{T}}(\mathbf{G}')\exp\{i\mathbf{G}'\cdot\mathbf{r}\}\right)\left(\sum_{\mathbf{G}}\delta n(\mathbf{G})\exp\{i\mathbf{G}\cdot\mathbf{r}\}\right)\\ &= f_{\mathcal{T}}(\mathbf{r})+\sum_{\mathbf{G},\mathbf{G}''} g_{\mathcal{T}}(\mathbf{G}''-\mathbf{G})\delta n(\mathbf{G})\exp\{i\mathbf{G}''\cdot\mathbf{r}\},\end{aligned} \tag{A.11}$$

where $\mathbf{G}'' = \mathbf{G}+\mathbf{G}'$.

Using a similar method, the exchange term in Eq. A.5 can be expressed as

$$\frac{4}{3}C_{\mathrm{x}}\left(n_i(\mathbf{r})+\delta n(\mathbf{r})\right)^{1/3} = f_{\mathrm{x}}(\mathbf{r})+g_{\mathrm{x}}(\mathbf{r})\delta n(\mathbf{r}), \tag{A.12}$$

with

$$f_{\mathrm{x}}(\mathbf{r}) = \frac{4}{3} C_{\mathrm{x}} n_i(\mathbf{r})^{1/3} = \sum_{\mathbf{G}} f_{\mathrm{x}}(\mathbf{G}) \exp\{i\mathbf{G}\cdot\mathbf{r}\}, \tag{A.13}$$

$$g_{\mathrm{x}}(\mathbf{r}) = \frac{4}{9} C_{\mathrm{x}} \frac{1}{n_i(\mathbf{r})^{2/3}} = \sum_{\mathbf{G}} g_{\mathrm{x}}(\mathbf{G}) \exp\{i\mathbf{G}\cdot\mathbf{r}\}, \tag{A.14}$$

and

$$g_{\mathrm{x}}(\mathbf{r})\delta n(\mathbf{r}) = \sum_{\mathbf{G},\mathbf{G}''} g_{\mathrm{x}}(\mathbf{G}''-\mathbf{G})\delta n(\mathbf{G}) \exp\{i\mathbf{G}''\cdot\mathbf{r}\}. \tag{A.15}$$

All of the calculated Fourier components (which would normally include the Coulomb Fourier components) can be combined into a single Fourier expansion of Eq. A.5. This then reads

$$\begin{aligned} &\sum_{\mathbf{G}} \left(f_{\mathcal{T}}(\mathbf{G}) + f_{\mathrm{x}}(\mathbf{G}) + \delta_{\mathbf{G},\mathbf{0}}\mu(\mathbf{G}=\mathbf{0}) + \dots\right) \exp\{i\mathbf{G}\cdot\mathbf{r}\} \\ &+ \sum_{\mathbf{G},\mathbf{G}'} \left(g_{\mathcal{T}}(\mathbf{G}-\mathbf{G}')\delta n(\mathbf{G}') + g_{\mathrm{x}}(\mathbf{G}-\mathbf{G}')\delta n(\mathbf{G}')\right) \exp\{i\mathbf{G}\cdot\mathbf{r}\} = 0, \end{aligned} \tag{A.16}$$

where an ellipsis is included to remind the reader of the missing Coulomb contributions, and the single Fourier component of μ is included using $\delta_{\mathbf{G},\mathbf{0}}$. From now, all of the $\mathbf{G}=\mathbf{0}$ components will be set to zero, effectively removing this μ contribution. One of the core reasons for using a plane-wave basis is the orthogonality of the plane waves. This means that when calculating $\delta n(\mathbf{G})$, only the contributions from that $\mathbf{G}$ vector to the sums in Eq. A.16 are required. However, there is still the sum over $\mathbf{G}'$ that must be evaluated for each $\mathbf{G}$.

This leads to a set of coupled equations that can be formulated into a matrix equation of the form

$$\underline{\underline{\mathbf{A}}}\,\underline{\mathbf{x}} + \underline{\mathbf{b}} = \underline{\mathbf{0}}, \tag{A.17}$$

where, for simplicity, a 1D system with $\mathbf{G} = \frac{2\pi m_1}{L}\hat{\mathbf{x}}$ and $-N/2 \leq m_1 \leq N/2$ will be

considered. The vectors and matrix are defined as

$$\underline{\mathbf{x}} = \begin{pmatrix} \delta n(\mathbf{G}(m_1 = -N/2)) \\ \delta n(\mathbf{G}(m_1 = -N/2+1)) \\ \vdots \end{pmatrix}, \tag{A.18}$$

$$\underline{\mathbf{b}} = \begin{pmatrix} b(\mathbf{G}(m_1 = -N/2)) \\ b(\mathbf{G}(m_1 = -N/2+1)) \\ \vdots \end{pmatrix}, \tag{A.19}$$

where $b(\mathbf{G})$ is defined as

$$b(\mathbf{G}) = f_{\mathcal{T}}(\mathbf{G}) + f_{\mathrm{x}}(\mathbf{G}), \tag{A.20}$$

and

$$\underline{\underline{\mathbf{A}}} = \begin{pmatrix} a(0) & a(-1) & a(-2) & \dots \\ a(1) & a(0) & a(-1) & \dots \\ a(2) & a(1) & a(0) & \dots \\ \vdots & \vdots & \vdots & \ddots \end{pmatrix}, \tag{A.21}$$

where a shorthand notation of $a(N/2) = a(\mathbf{G}(m_1 = N/2))$ has been used, with $a(\mathbf{G})$ defined as

$$a(\mathbf{G}) = g_{\mathcal{T}}(\mathbf{G}) + g_{\mathrm{x}}(\mathbf{G}). \tag{A.22}$$

The Fourier components of δn in $\underline{\mathbf{x}}$ are then added to the initial density to find n_{i+1}, which is then used as the initial density in the next iteration loop. This is continued until some condition, generally the difference of total energy between iterations, is within some threshold. As with conventional HKS-DFT, the Hohenberg-Kohn theorems ensure that the electron density found at the energy minimum is the ground-state density.

This method of treating the minimisation of the energy by finding a perturbed density that solves the Thomas-Fermi equation turned out to be not only extremely unstable, but relatively slow.

Due to the use of FFTs to transform between real and reciprocal space, the computational

efficiency is primarily limited by the filling and solving of the matrix $\underline{\underline{\mathbf{A}}}$. This matrix is of size $N^3 \times N^3$, where N is the number of reciprocal lattice vectors along one dimension. This is because the m_1, m_2, and m_3 integers of the possible $\mathbf{G}$ vectors have to be unravelled into a single dimension, for each of $\mathbf{G}$ and $\mathbf{G}'$, to allow the canned matrix solver to work.

Linear stability analysis was performed that found that the method should be stable, subject to the usual caveat of choosing the initial density to not be too far from the ground-state density. However, the only way to find a stable result is by including a positive background charge n_0 that is much larger than the charge of the ions. The additional electrons, needed to cancel the charge from the positive background, may act to make the relative size of the perturbations in the electron density, due to the added atoms, smaller, limiting the computational problems mentioned below. It should be noted, though, that changing n_0 will change the total number of electrons in the periodic unit cell, in turn affecting the total energy of the system.

The instability seems to arise primarily from problems with the density. Firstly, although the density should be real and positive for all $\mathbf{r}$, it often contains small, but not always negligible, imaginary components. Whilst negligible imaginary terms can be expected from the FFTs, these will often grow throughout the iterations causing unphysical behaviour. This was fixed by throwing away the imaginary components after each inverse FFT, thereby not allowing these spurious imaginary terms to grow. Secondly, and most importantly, the density would at times becomes negative. Apart from this behaviour being unphysical, it would also cause the program to fail when fractional powers of the density, e.g., Eq. A.4, are calculated. This seems to be a limitation of the naive implementation used in this first program.

A.2 Direct minimisation

A second program fixed these problems by introducing the OF-DFT wave function $\psi(\mathbf{r})$, such that

$$n(\mathbf{r}) = \psi(\mathbf{r})^2. \tag{A.23}$$

By optimising with respect to $\psi(\mathbf{r})$, instead of $n(\mathbf{r})$, the density is guaranteed to always be positive and real.

The largest difference between the two programs is that the second program directly minimises the energy, rather than using a perturbative approach. This works through a canned optimiser. The functional derivatives are still useful, though, as the Jacobian can be fed in to the optimiser to improve the efficiency of the minimisation process.

The program also introduced a normalisation process by which, at each step, the density is renormalised to avoid the number of electrons within the unit cell changing. If it was allowed to change freely as the minimiser wanted, the energy would also change. Practically, this then means that the program minimises the energy in the space of constant electron number. Since the density will always be renormalised, the program freely changes the number of electrons throughout. To incentivise only small changes in the number of electrons, a cost function can be added that punishes large deviations from the correct normalisation. This was chosen as a simple harmonic well.

In this method there is no matrix that needs to be manually filled. As this was the limiting step in the previous program, this method is far quicker for a comparable number of $\mathbf{G}$ and $\mathbf{R}$ vectors. If the matrix filling was performed in Fortran 90, rather than Python, the difference in speed between the methods is likely to decrease (since the second method uses in-built functions that already written in Fortran 90/C).

As an example, Fig. A.1 shows the thermal-equilibrium electron density obtained using OF-DFT with two "bolonium" ions in the unit cell. "Bolonium" is simply some unspecified ion that has three valence electrons and can be described by using a regularised Coulomb

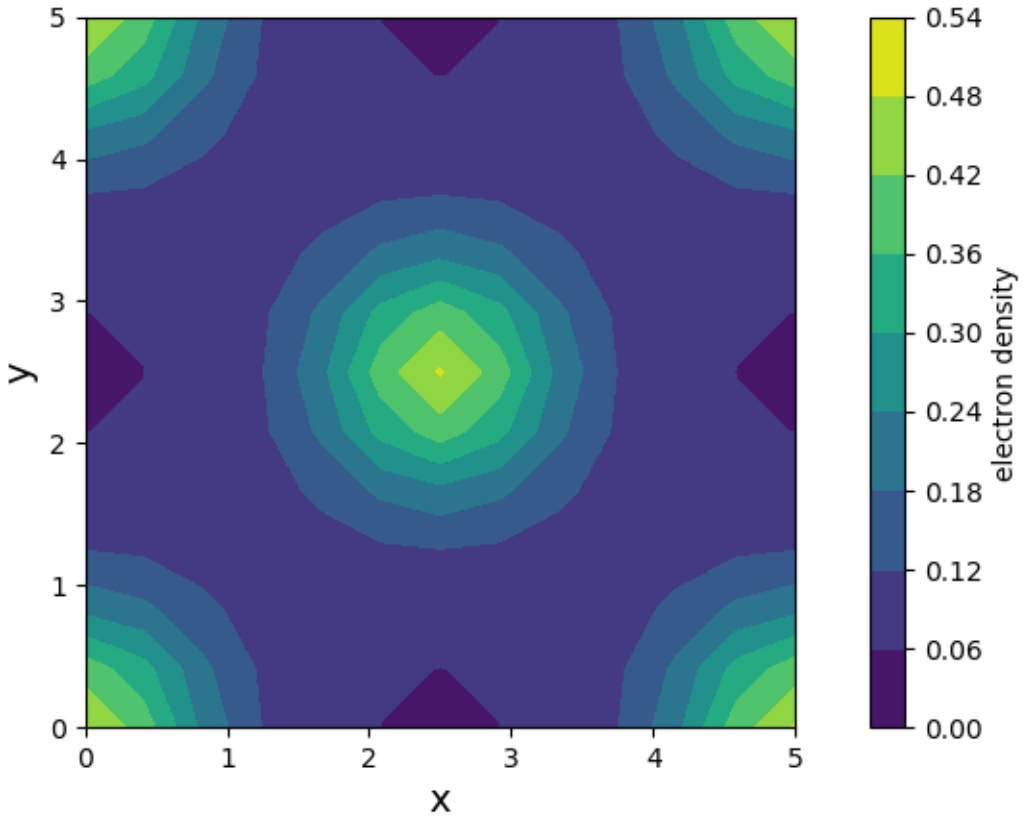

Figure A.1: Heat plot of the thermal-equilibrium electron density in a slice $z = 0$ for a periodic unit cell containing a bolonium ion at $[0, 0, 0]$ and $[2.5, 2.5, 0]$, produced using our OF-DFT program. The box size is 5 a.u., $T = 5$ K, a background charge density of $n_0 = 0.03$ is included, and there are $12 \times 12 \times 12$ real grid points used in the minimisation. The pseudopotential used is the regularised Coulomb potential with $\sigma = 0.5$.

potential as its pseudopotential. The regularised Coulomb potential is the convolution of the Coulomb potential and a Gaussian of standard deviation σ. The quantitatively correct behaviour of the electron density can be observed, however bonding between the ions is not predicted due to the lack of the von Weizsacker correction.

Appendix B

Error metrics

The most common metric for assessing the quality of an interatomic potential is the root-mean-square error (RMSE). The RMSE quantifies the difference between some predicted values and their corresponding exact values. Here, the RMSE is used to compare the (M)HKS-DFT energies and forces with those predicted by the other methods introduced in the thesis.

The RMSE may be defined in one of two ways; either per component, or per vector. When used in this thesis, the RMSE is defined in its per vector form, in other words

$$\mathrm{RMSE} = \sqrt{\frac{\sum_{n,i} \left(\Delta \boldsymbol{\mathcal{F}}_i^n\right)^2}{N_\mathrm{s} N_\mathrm{at}}}, \tag{B.1}$$

with N_s the number of snapshots, N_at the number of atoms per snapshot, n and i the snapshot and atom index, respectively, and

$$\Delta \boldsymbol{\mathcal{F}}_i^n = \boldsymbol{\mathcal{F}}_i^n(\mathrm{predicted}) - \boldsymbol{\mathcal{F}}_i^n(\mathrm{exact}) \tag{B.2}$$

the difference in the predicted and exact force on atom i in snapshot n.

The normalised RMSE is defined such that different T_e can be compared on the same footing. This is required as the magnitude of the forces varies with electronic temperature,

which then affects the RMSE. This, in turn, makes it difficult to judge the quality of fits at different T_e. The normalised RMSE is defined as

$$\text{norm. RMSE } (\%) = 100 \times \frac{\text{RMSE}}{\sqrt{\bar{\boldsymbol{\mathcal{F}}}^2}}, \tag{B.3}$$

with the average squared force given as

$$\bar{\boldsymbol{\mathcal{F}}}^2 = \frac{\sum_{n,i} \left[\boldsymbol{\mathcal{F}}_i^n(\text{exact})\right]^2}{N_\mathrm{s} N_\mathrm{at}}. \tag{B.4}$$

Analogously to the RMSE, the mean average error (MAE) is defined in its per vector form,

$$\text{MAE} = \frac{1}{N_\mathrm{s} N_\mathrm{at}} \sum_{n,i} \sqrt{(\Delta \boldsymbol{\mathcal{F}}_i^n)^2}. \tag{B.5}$$

The MAE is another useful measure of the errors associated with some predictor; the main difference being that the RMSE grows more quickly when predicted values are far from the exact values.

Replacing $\boldsymbol{\mathcal{F}}_i^n$ by the free energy per atom F_i^n in the above equations gives the error metrics for the energies.

Appendix C

Phonons

The derivation of the phonons will begin by assuming the ions are in their equilibrium configuration with zero temperature. Since the equilibrium configuration must correspond to a minimum in the energy, if a small enough perturbation is applied to the configuration, the change in the total energy can be approximated by a truncated Taylor expansion.

The condition for equilibrium is that the force acting on each ion I in each direction α is zero, i.e.,

$$\mathcal{F}_{I,\alpha} = -\frac{\partial E(\mathbf{R})}{\partial R_{I,\alpha}} = 0, \tag{C.1}$$

where E is energy at zero temperature or the free energy at finite temperature and $\mathbf{R}_I$ is an ionic position. The energy of a particular configuration $E(\mathbf{R})$ can be expressed as a Taylor expansion around the minimum energy that is truncated at second order,

$$E(\mathbf{R}_0 + \mathbf{U}) = E(\mathbf{R}_0) + \sum_{I,\alpha}\sum_{J,\beta} \frac{U_{I,\alpha}U_{J,\beta}}{2} \frac{\partial^2 E}{\partial R_{I,\alpha}\partial R_{J,\beta}}\bigg|_{\mathbf{R}=\mathbf{R}_0}, \tag{C.2}$$

where $\mathbf{R}_0 = \{\mathbf{R}_{I,0}, \mathbf{R}_{J,0}, \dots\}$ is the set of equilibrium positions of the ions, $U_{I,\alpha}$ is a small perturbation in direction α of ion I, where a set of perturbations can be combined into a perturbation matrix defined as $\mathbf{R} = \mathbf{R}_0 + \mathbf{U}$, and the definition of the force at equilibrium is used to exclude the first derivative of the energy.

For the rest of this Appendix, only perturbations of a single ion in a single direction, i.e. $\mathbf{U} = U_{I,\alpha}$, will be used. The truncation of higher than second order terms is called the harmonic approximation [57]. This approximation leads to the forces following Hooke's Law, that is that they are linear with respect to the perturbation.

C.1 Calculating the interatomic force constants

The matrix of second derivatives in Equation C.2 is the Hessian, and is often called the matrix of interatomic force constants (IFCs), $C^{IJ}_{\alpha\beta}$. These IFCs are used to evaluate the change in energy due to an arbitrary perturbation, as well as find the phonon frequencies. Symmetries of the system are vital to increase the efficiency in any method of calculating the IFCs, but will not be explicitly discussed here. The IFCs can be calculated using density functional perturbation theory (DFPT), which will be not discussed here, or by the 'direct' method of calculating the interatomic forces for a perturbed structure.

C.1.1 'Direct' method

The 'direct', or finite difference, method involves creating a supercell by combining multiple unit cells into a larger structure. This is necessary as otherwise periodic boundary conditions would cause all periodic images of the perturbed ion to also move.

When calculating the interatomic forces of the perturbed structure, the number of unit cells within the supercell must be limited due to computational constraints. For instance, most (M)HKS-DFT programs scale as N^3, where N is the total number of ions in the supercell. Furthermore, $C^{IJ}_{\alpha\beta}$ is expected to reduce with increasing distance between ions I and J [202]. In contrast to this, a supercell should be as large as possible, as only the phonon frequencies at $\mathbf{q}$ points (where the notation $\mathbf{q}$ is from convention when dealing with phonons) commensurate with the supercell [202, 242] will be exact. Between these $\mathbf{q}$ points, the phonon frequencies must be interpolated under symmetry constraints.

The most widespread program incorporating this method is `phonopy` [243]. The IFCs are defined as

$$C_{\alpha\beta}^{IJ} \approx -\frac{\mathcal{F}_{J,\beta}(\mathbf{R}_0 + U_{I,\alpha}) - \mathcal{F}_{J,\beta}(\mathbf{R}_0)}{U_{I,\alpha}}, \tag{C.3}$$

where $\mathcal{F}_{I,\alpha}(\mathbf{R})$ is the force on ion I along direction α for a configuration $\mathbf{R}$. The size of the perturbation, $U_{I,\alpha}$, must be chosen wisely, as if it is too large the finite difference method will produce a gradient with a large truncation error, whereas if it is too small the difference between the forces will be comparable to that of the error from calculating the interatomic forces. `phonopy` then uses the modified Parlinski-Li-Kawazoe method [242], which involves turning the above equation into a matrix equation, to calculate the IFCs.

C.2 Finding the phonon frequencies

The dynamical matrix is then constructed, which gives the dynamical properties of the system, as the Fourier transform of the IFCs,

$$D_{\alpha\beta}^{IJ}(\mathbf{q}) = \frac{1}{\sqrt{M_I M_J}} \sum_l C_{\alpha\beta}^{I'J(l)} \exp\{i\mathbf{q} \cdot [\mathbf{R}_{J(l)} - \mathbf{R}_{I'}]\}, \tag{C.4}$$

where the sum over l refers to summing the contribution from ion J in every periodic unit cell l, and the explicit dependence of the J terms on l is shown by $J(l)$. The notation I' represents the ion within the original unit cell and M_I is the mass of ion I.

An equation of motion is then formed to find the phonon frequencies $\omega_{\mathbf{q}\nu}$ for a given wave vector $\mathbf{q}$ and band index ν,

$$\sum_{\beta J'} D_{\alpha\beta}^{I'J'}(\mathbf{q}) e_{\mathbf{q}\nu}^{\beta J'} = \omega_{\mathbf{q}\nu}^2 e_{\mathbf{q}\nu}^{\alpha I'}, \tag{C.5}$$

with both indices I' and J' now representing ions in the original unit cell, and $e_{\mathbf{q}\nu}^{\alpha I'}$ the elements of the vector that describe the pattern of displacements in the normal mode of wavevector $\mathbf{q}$ and polarisation ν [243, 202]. These phonon frequencies are commonly

plotted through a path in $\mathbf{q}$ space to produce a phonon dispersion curve.

C.3 Thermodynamic properties

Many thermodynamic properties can be constructed from the phonon frequencies. Some of the more useful definitions will be given here without derivation [243]. These definitions are all given in the canonical ensemble (i.e., constant temperature and particle number) within the harmonic approximation. All results are given in atomic units.

The vibrational internal energy is defined as

$$E_{\text{vib}} = \sum_{\mathbf{q}\nu} \omega_{\mathbf{q}\nu} \left[\frac{1}{2} + \frac{1}{\exp\{\omega_{\mathbf{q}\nu}/k_B T\} - 1} \right], \tag{C.6}$$

with T the temperature of the ions. From this, the vibrational free energy F_{vib}, the entropy S, and the constant volume heat capacity C_V of the phonons can be derived,

$$F_{\text{vib}} = \frac{1}{2} \sum_{\mathbf{q}\nu} \omega_{\mathbf{q}\nu} + k_B T \sum_{\mathbf{q}\nu} \ln\left[1 - \exp\{-\omega_{\mathbf{q}\nu}/k_B T\}\right], \tag{C.7}$$

$$S = -\frac{\partial F}{\partial T} = \frac{1}{2T} \sum_{\mathbf{q}\nu} \omega_{\mathbf{q}\nu} \coth\{\omega_{\mathbf{q}\nu}/2k_B T\} - k_B \sum_{\mathbf{q}\nu} \ln\left[2\sinh\{\omega_{\mathbf{q}\nu}/2k_B T\}\right], \tag{C.8}$$

$$C_V = \left(\frac{\partial E}{\partial T}\right)_V = \sum_{\mathbf{q}\nu} k_B \left(\frac{\omega_{\mathbf{q}\nu}}{k_B T}\right)^2 \frac{\exp\{\omega_{\mathbf{q}\nu}/k_B T\}}{[\exp\{\omega_{\mathbf{q}\nu}/k_B T\} - 1]^2}. \tag{C.9}$$

This is just a selection of properties that show why accurate phonon frequencies are essential to modelling materials at finite temperature.

C.4 Anharmonicities

The investigation into finite temperature phonons, so far, has only used the harmonic approximation to calculate phonon frequencies. In reality, most materials, such as met-

als, require the higher order terms excluded from Eq. C.2 to describe the experimental behaviour [244]. These are collectively known as anharmonicities.

The first step into including anharmonic effects is the quasi-harmonic approximation [243]. This is the assumption that the lattice parameter is allowed to vary (which ensures thermal expansion can be properly modelled) whilst the harmonic approximation holds at each value of the lattice parameter. The phonon frequencies, and therefore properties, are then functions of the volume. The quasi-harmonic approximation, at best, describes the majority of the missing contributions; however, as the temperature approaches the melting point of the material, the higher order anharmonicities begin to dominate [245].

Further anharmonic terms are required to describe behaviours such as phonon-phonon interactions and electron-phonon interactions, and these often require taking into account vacancies within the larger atomic structure, and using molecular dynamics to sample the configuration space [245, 246, 247]. Anharmonicities are not expected to be important when investigating electronic finite-temperature phonons.